Springer ThesesRecognizing Outstanding Ph.D. Research

Lutz Fechner

High-Resolution Experiments on Strong-Field Ionization of Atoms and Molecules

Test of Tunneling Theory, the Role of Doubly Excited States, and Channel-Selective Electron Spectra



Springer Theses

Recognizing Outstanding Ph.D. Research

Aims and Scope

The series "Springer Theses" brings together a selection of the very best Ph.D. theses from around the world and across the physical sciences. Nominated and endorsed by two recognized specialists, each published volume has been selected for its scientific excellence and the high impact of its contents for the pertinent field of research. For greater accessibility to non-specialists, the published versions include an extended introduction, as well as a foreword by the student's supervisor explaining the special relevance of the work for the field. As a whole, the series will provide a valuable resource both for newcomers to the research fields described, and for other scientists seeking detailed background information on special questions. Finally, it provides an accredited documentation of the valuable contributions made by today's younger generation of scientists.

Theses are accepted into the series by invited nomination only and must fulfill all of the following criteria

- They must be written in good English.
- The topic should fall within the confines of Chemistry, Physics, Earth Sciences, Engineering and related interdisciplinary fields such as Materials, Nanoscience, Chemical Engineering, Complex Systems and Biophysics.
- The work reported in the thesis must represent a significant scientific advance.
- If the thesis includes previously published material, permission to reproduce this must be gained from the respective copyright holder.
- They must have been examined and passed during the 12 months prior to nomination.
- Each thesis should include a foreword by the supervisor outlining the significance of its content.
- The theses should have a clearly defined structure including an introduction accessible to scientists not expert in that particular field.

More information about this series at http://www.springer.com/series/8790

Lutz Fechner

High-Resolution Experiments on Strong-Field Ionization of Atoms and Molecules

Test of Tunneling Theory, the Role of Doubly Excited States, and Channel-Selective Electron Spectra

Doctoral Thesis accepted by the Ruperto Carola University of Heidelberg, Germany



Author
Dr. Lutz Fechner
Department of Quantum Dynamics and Control
Max Planck Institute for Nuclear Physics Heidelberg
Germany Supervisor
Priv.-Doz. Dr. Robert Moshammer
Department of Quantum Dynamics
and Control
Max Planck Institute for Nuclear Physics
Heidelberg
Germany

ISSN 2190-5053 ISSN 2190-5061 (electronic) Springer Theses ISBN 978-3-319-32045-8 ISBN 978-3-319-32046-5 (eBook) DOI 10.1007/978-3-319-32046-5

Library of Congress Control Number: 2016935217

© Springer International Publishing Switzerland 2016

This work is subject to copyright. All rights are reserved by the Publisher, whether the whole or part of the material is concerned, specifically the rights of translation, reprinting, reuse of illustrations, recitation, broadcasting, reproduction on microfilms or in any other physical way, and transmission or information storage and retrieval, electronic adaptation, computer software, or by similar or dissimilar methodology now known or hereafter developed.

The use of general descriptive names, registered names, trademarks, service marks, etc. in this publication does not imply, even in the absence of a specific statement, that such names are exempt from the relevant protective laws and regulations and therefore free for general use.

The publisher, the authors and the editors are safe to assume that the advice and information in this book are believed to be true and accurate at the date of publication. Neither the publisher nor the authors or the editors give a warranty, express or implied, with respect to the material contained herein or for any errors or omissions that may have been made.

Printed on acid-free paper

This Springer imprint is published by Springer Nature
The registered company is Springer International Publishing AG Switzerland

Supervisor's Foreword

The interaction of strong laser pulses with atoms and molecules has been subject of scientific interest for decades. A large manifold of interesting phenomena arise from the quantum nature of the systems, their strong modification by the laser electric field and—after ionization—from the acceleration of the freed electrons in the laser field. Beside computationally highly demanding quantum calculations, various theoretical models have been developed that are able to approximately describe the dynamics in many cases.

In order to gain insight into the details of the processes and to refine and adapt the existing models accordingly, precise measurements have to be performed and suitable experimental setups are requested. The detection of all charged particles created in a certain process and the precise determination of their three-dimensional momentum vectors became possible with the invention of the Reaction Microscope. These spectrometers provide a very high resolution and are capable of performing true multi-particle coincidence measurements on a shot-to-shot basis with very low background. Data selection according to, e.g., the masses and charge states of the created ions or the kinetic energy released in a process can yield channel-selective data and thus helps to answer the open questions in the field.

An atom exposed to a very strong laser field typically experiences a large deformation of the binding Coulomb potential. As a consequence, a potential barrier is formed where electrons may tunnel out. Thus, a very fundamental quantum process is triggered by the laser pulse. In order to relate the experimental observable—the final momentum of the electron—to the process and its dynamics, the further interaction of the freed electron with the laser field has to be taken into account: In the vicinity of its parent ion, the electron is driven back and forth by the laser. Depending on the laser electric field at the moment of ionization and the initial momentum the electron had right after tunneling, a certain trajectory and final momentum results. Theoretical models suggest that the initial momentum distribution of the freed electrons depends on the shape of their bound state wave function prior to the tunneling process. Although used in many theoretical and

experimental works, this dependence has never been shown directly in any experiment before.

In this thesis, ionization processes of rare gas atoms and hydrogen molecules are experimentally investigated. Using few-cycle laser pulses in a pump-probe scheme and argon as target, the dependence of the final electron momentum distribution on the bound state wave function is directly proven. Highly resolved electron momentum distributions are obtained for rare gas atoms and molecular hydrogen along the transition from the multiphoton to the tunneling regime, using laser pulses over a large range of wavelengths. Unique fingerprints of autoionizing Rydberg states in argon and krypton are identified. For hydrogen, different reaction channels in terms of ionization and dissociation of the molecule are isolated using the unique features of the Reaction Microscope. This provides a set of channel-resolved benchmark data for future theoretical calculations and models.

Heidelberg, Germany January 2016 Priv.-Doz. Dr. Robert Moshammer

Abstract

In this thesis, the ionization of atoms and small molecules in strong laser fields is experimentally studied by utilization of a reaction microscope.

The fundamental process of tunnel ionization in strong laser fields is subject of investigation in a pump-probe experiment with ultrashort laser pulses. A coherent superposition of electronic states in singly charged argon ions is created within the first, and subsequently tunnel-ionized with the second pulse. This gives access to state-selective information about the tunneling process and allows to test common models.

Moreover, the ionization of krypton and argon at different wavelengths is studied, from the multiphoton to the tunneling regime. The population of autoionizing doubly excited states in the laser fields is proven and a possible connection to the well-known dielectronic recombination processes is discussed. The wavelength-dependent investigations are furthermore extended to molecular hydrogen. In addition to ionization, this system might undergo different dissociative processes. Channel-selective electron momentum distributions are presented and compared to each other.

Contents

1			on	1 4
•				
2		_	er Fields and Ultrashort Laser Pulses	5
	2.1		ematical Description of Laser Pulses	5
		2.1.1	Laser Pulses as Superpositions of Resonator Modes	7
		2.1.2	Dispersion in Matter	12
		2.1.3	General Properties of Focussed Laser Beams	13
	2.2		Pulse Generation and Manipulation	16
		2.2.1	The Femtosecond Laser System	16
		2.2.2	Generation of Few-Cycle Pulses	17
		2.2.3	Setup for Pump-Probe Measurements	20
		2.2.4	Frequency Doubling and Mixing	21
		2.2.5	Wavelength Tuning Using an OPA System	23
	Refe	erences		25
3	Ioni	zation	in Strong, Ultrashort Laser Pulses	29
	3.1	Multip	photon and Tunnel Ionization: The Keldysh Parameter	29
	3.2	Standa	ard Tunneling Theory: The ADK Theory	32
	3.3	Quasi-	-free Electrons in Strong Laser Fields	33
		3.3.1	The Three-Step Model	34
		3.3.2	Interference Structures in Electron Spectra	37
	3.4	The R	ole of Excited States	39
		3.4.1	Freeman Resonances	40
		3.4.2	RESI	40
		3.4.3	Population and Stabilization of Excited States	41
	3.5	Molec	rular Hydrogen in Strong Laser Fields	42
		3.5.1	Ionization and Dissociation Channels	42
		3.5.2	The Floquet Picture	44
		3.5.3	Bond Softening and Molecular Stabilization	46
	ъс	erences		48

x Contents

4	The	Reaction Microscope	53
	4.1	Setup	53
		4.1.1 The Spectrometer and Detectors	55
		4.1.2 Preparation of the Gas Jet	59
	4.2	Data Processing	60
		4.2.1 Momentum Reconstruction	61
		4.2.2 Solid-Angle Correction	66
		4.2.3 Calibration of the REMI	67
	4.3	Performance of the System	71
		4.3.1 Acceptance	71
		4.3.2 Resolution	72
		4.3.3 General Limitations and the Importance of Excellent	
		Vacuum Conditions	73
	Refe	erences	74
5	Tun	nel Ionization from a Coherent Superposition in Ar ⁺	77
	5.1	Spin-Orbit Wave Packets in Noble Gas Ions	77
	5.2	A SOWP in Ar ⁺ as Initial State for Further Tunnel Ionization	80
		5.2.1 Estimation of the Laser Intensity	84
		5.2.2 The "Scaled Hydrogen" Model	86
		5.2.3 Transverse Momentum Distributions	89
		5.2.4 Time-Resolved Momentum Distributions	91
	Refe	erences	93
6	Pop	ulation of Doubly Excited States in Strong Laser Pulses	97
	6.1	Noble Gas Rydberg Atoms	98
		6.1.1 Doubly Excited States and Autoionization	100
	6.2	Population of DES at Different Wavelengths	101
		6.2.1 Angular Distributions	114
	6.3	Considerations About Lifetimes and Pump-Probe	
		Measurements	115
	6.4	Other Targets: Neon and Molecular Nitrogen	119
	Refe	erences	120
7	Cha	nnel-Selective Electron Spectra for H ₂ at Different	
		velengths	123
	7.1	Separation of the Different Reaction Channels	123
	7.2	Experimental Setup and Measurement of the Wavelengths	126
	7.3	Changes in the Ion Momentum Distributions	127
	7.4	Electron Momentum Distributions	130
	Refe	erences	136

Contents	
	Al

	Conclusion and Outlook	
Ap	pendix A	145

Nomenclature

ADC Analog-to-digital converter
ADK Ammosov-Delone-Krainov
ARS Autoionizing Rydberg state
ATI Above-threshold ionization

BBO Barium borate
CE Coulomb explosion
CEP Carrier-envelope phase

COLTRIMS Cold target recoil ion momentum spectroscopy

CPA Chirped pulse amplification CVA Coulomb-Volkov approximation

cw Continuous-wave

DEC Doubly excited complex
DES Doubly excited state

DFG Difference frequency generation
DR Dielectronic recombination
EBIT Electron beam ion trap
FEL Free-electron laser
FSR Free spectral range

FTI Frustrated tunneling ionization
FWHM Full width at half maximum
GVD Group velocity dispersion
HeNe Laser Helium-neon laser
HHG High harmonic generation
KER Kinetic energy release
KLM Kerr lens mode-locking

laser Light amplification by stimulated emission of radiation

MCP Micro-channel plate MPI Multiphoton ionization

NSDI Non-sequential double ionization OPA Optical parametric amplifier

REMI Reaction microscope

xiv Nomenclature

RESI Recollision excitation with subsequent ionization

SAE Single-active-electron

SESAM Semiconductor saturable absorber mirror

SFA Strong-field approximation
SFG Sum frequency generation
SHG Second harmonic generation
SOWP Spin-orbit wave packet
SPM Self-phase modulation

TEM Mode transverse electromagnetic mode Ti:sapphire Titanium-doped sapphire (Ti:Al₂O₃)

TOD Third-order dispersion VMI Velocity-map imaging

Chapter 1 Introduction

The wave-character of light and the particle-character of matter seemed disparate until the last century, when physics proved the opposite: Light and matter may likewise be described as particles and waves, a fact commonly known as *wave-particle duality* and also valid for larger, massive objects [11]. Despite this common ground, in everyday life as well as in most experiments, light and matter act completely different and can be distinguished well by their diverse properties. This was also emphasized in the 2012 Nobel Prize in Physics press release: "David Wineland traps electrically charged atoms, or ions, controlling and measuring them with light, or photons. Serge Haroche takes the opposite approach: he controls and measures trapped photons, or particles of light, by sending atoms through a trap. Both Laureates work in the field of quantum optics studying the fundamental interaction between light and matter, a field which has seen considerable progress since the mid-1980s." [16].

Indeed, nowadays, the interaction of light and matter is the subject of investigation in a large variety of experiments. Decisive for the development of the field was the invention of the laser¹ [9]. The unique properties of laser light, for example its spectral narrowness, are in fact mandatory for many experiments and exploited in a manifold of different techniques from laser cooling of atoms [15] to high resolution spectroscopy [13].

Despite the scientific potential comprised in the interaction processes, their mathematical treatment is—at first glance—fairly simple and often relies on quantum mechanical perturbation theory. In fact, the interaction of monochromatic light with an atom is one of the basic examples of such approach in undergraduate textbooks. The approach uses the fact that the electric field associated with the light is small compared to the electric field that keeps the electrons bound.

In laboratories, this condition is often, but not always fulfilled. Remarkably soon after the invention of the laser itself, techniques were invented allowing the temporal confinement of the emitted laser radiation and thus the creation of "giant" light pulses [10]. Additional spatial confinement by focusing these pulses onto a target

¹Light amplification by stimulated emission of radiation.

[©] Springer International Publishing Switzerland 2016

L. Fechner, High-Resolution Experiments on Strong-Field Ionization of Atoms and Molecules, Springer Theses, DOI 10.1007/978-3-319-32046-5_1

2 1 Introduction

soon provided intensities with corresponding electric fields that were equal to or even exceeded the atomic fields. It is no surprise that a perturbative treatment of the interaction between the laser field and an atom breaks down in this situation, and the seemingly simple task to describe the problem becomes tremendously complicated.

Although quantum mechanics provides the appropriate equation to describe the problem, the time-dependent Schrödinger equation, finding its full numerical solution is—even with today's fastest computers—only possible for very specific, fairly simple problems. In addition, if such a solution is found, the calculation usually only returns a final result rather than an intuitive picture of the underlying processes. However, those simple pictures are desirable since they often help to predict and understand important aspects of the light-matter interactions.

In 1965, Keldysh investigated the ionization process in strong electromagnetic fields using an alternative approach of treating the laser field classically [7]. In this work, the area of strong-field physics was divided into two regimes, a separation which still persists. One side, commonly known as the *multiphoton regime*, is associated with rather low intensities and/or short wavelengths. Here, the binding energy of the electron is large compared to the *ponderomotive energy*, the cycle-averaged kinetic energy of a free electron in the laser field. The opposite is the case for high intensities and/or long wavelengths in the *tunneling regime*. As suggested by the names, the characteristics of the ionization process can be described most appropriately either by the absorption of several photons or a tunneling process of the electron, respectively.

Since then, much effort has been spent to refine and extend the classical treatment of the interaction. In the tunneling regime, the interaction between the laser and the electron after the tunneling process turned out to be extremely important for understanding the strongly enhanced rates for double and multiple ionization obtained in moderately intense laser fields [8]. Usually, the full treatment still involves quantum mechanical tunneling as a first step and a subsequent classical treatment of the freed electron which resembles a fairly good approximation. Due to this combination of quantum mechanics and classical physics, the approaches are commonly referred to as "semi-classical models". Important milestones are the ADK theory, e.g. [1, 12, 14], and the extension to three steps in the *three-step model* [3] that also considers the possible recollision of the electron with its parent ion. It is this recollision which gives rise to the enhanced rates for double and multiple ionization as well as to other interesting phenomena, such as the generation of highly energetic radiation and the formation of extremely short light pulses with durations of down to 100 as² and below [17].

Despite the progress, many questions remain. One of them is related to the region "in between" the two regimes, in which neither the tunneling nor the multiphoton picture seems to be valid and where, in fact, most of the experiments are carried out. When coming from the tunneling regime and approaching shorter wavelengths and thus faster and faster oscillation of the field, one may ask, up to which point tunneling

²One attosecond (as) equals 10⁻¹⁸ s.

1 Introduction 3

can be treated adiabatically, hence neglecting the temporal variation of the field during the process. This question is still controversially discussed [2, 6]. Another question is related to the momentum distribution of the electrons right after the tunneling process, before being accelerated by the laser field. Although different models predict certain momentum distributions, their explicit experimental validation is pending.

However, promising new experimental techniques such as the *attoclock* technique [5], provide an astonishing level of detail on information about the process of tunnel ionization. For example, few tens of attoseconds were experimentally found as an upper limit for the *tunneling time*—the time the electron needs to tunnel out—in helium [4]. Similar to conventional streaking techniques, the temporal information is mapped onto spatial coordinates. For each time of ionization, associated coordinates can be calculated and the experimental data are interpreted with the reversed relation. These calculations require detailed knowledge about the initial momenta of the electrons which is—as described above—currently only available in terms of theoretical predictions from models. One of the aims of this work is to experimentally test these models.

In this thesis, the ionization of atoms and small molecules in strong laser fields is experimentally investigated by utilization of a highly advanced momentum spectrometer: the reaction microscope. Chapter 2 gives a brief overview about the mathematical description of ultrashort, strong laser pulses and their technical creation. Furthermore, the specific laser system and the pulse manipulation techniques utilized throughout this work are described. Following this, Chap. 3 focusses on the interaction of intense laser pulses with matter, in particular on the description of ionization processes in atoms and molecules. The reaction microscope and its working principle is treated in Chap. 4.

Afterwards, the experimental results are presented, divided into three parts. In the first, Chap. 5, common theoretical models about the electron momentum distribution directly after the tunneling process are explicitly tested. This is done by using ultrashort pulses in a pump-probe scheme and a coherent superposition of electronic states in singly ionized argon as initial state for further tunnel ionization.

The subject of the second experimental part, presented in Chap. 6, is the interaction of strong laser pulses of different wavelengths with noble gas atoms, namely krypton and argon. Tuning the wavelength by utilizing an optical parametric amplifier and nonlinear crystals for frequency mixing enables the observation of characteristic changes in the electron momentum distributions and the ionization process while approaching the tunneling regime. Furthermore, the excitation of doubly-excited states of the atoms is proven and investigated.

In the last part, presented in Chap.7, a similar investigation is performed for the most simple molecule existing, H₂. In addition to pure ionization, this system features different dissociation channels. The reaction microscope enables their separation and thus offers channel-selected electron momentum distributions at different wavelengths. The results of all experiments presented in this thesis are summarized in Chap. 8, where future perspectives are also discussed.

4 1 Introduction

References

 M.V. Ammosov et al., Tunnel ionization of complex atoms and of atomic ions in an alternating electromagnetic field. Sov. Phys. JETP 64, 1191–1194 (1986)

- 2. R. Boge et al., Probing nonadiabatic effects in strong-field tunnel ionization. Phys. Rev. Lett. 111, 103003 (2013). doi:10.1103/PhysRevLett.111.103003
- P.B. Corkum, Plasma perspective on strong-field multiphoton ionization. Phys. Rev. Lett. 71, 1994–1997 (1993). doi:10.1103/PhysRevLett.71.1994
- 4. P. Eckle et al., Attosecond ionization and tunneling delay time measurements in helium. Science 322, 1525–1529 (2008). doi:10.1126/science.1163439
- P. Eckle et al., Attosecond angular streaking. Nat. Phys. 4, 565–570 (2008). doi:10.1038/ nphys982
- I.A. Ivanov, A.S. Kheifets, Strong-field ionization of He by elliptically polarized light in attoclock configuration. Phys. Rev. A: At. Mol. Opt. Phys. 89, 021402(R) (2014). doi:10.1103/ PhysRevA.89.021402
- L.V. Keldysh, Ionization in the field of a strong electromagnetic wave. Sov. Phys. JETP 20, 1307–1314 (1965)
- 8. A. L'Huillier et al., Multiply charged ions formed by multiphoton absorption processes in the continuum. Phys. Rev. Lett. 48, 1814–1817 (1982). doi:10.1103/PhysRevLett.48.1814
- T.H. Maiman, Stimulated optical radiation in ruby. Nature 187, 493–494 (1960). doi:10.1038/ 187493a0
- F.J. McClung, R.W. Hellwarth, Giant optical pulsations from ruby. J. Appl. Phys. 33, 828–829 (1962). doi:10.1063/1.1777174
- O. Nairz et al., Quantum interference experiments with large molecules. Am. J. Phys. 71, 319–325 (2003). doi:10.1119/1.1531580
- 12. A.I. Nikishov, V.I. Ritus, Ionization of systems bound by short-range forces by the field of an electromagnetic wave. Sov. Phys. JETP 23, 168–177 (1966)
- C.G. Parthey et al., Improved measurement of the hydrogen 1S-2S transition frequency. Phys. Rev. Lett. 107, 203001 (2011). doi:10.1103/PhysRevLett.107.203001
- A.M. Perelomov et al., Ionization of atoms in an alternating electric field. Sov. Phys. JETP 23, 924–934 (1966)
- 15. W.D. Phillips, Laser cooling and trapping of neutral atoms. Rev. Mod. Phys. **70**, 721–741 (1998). doi:10.1103/RevModPhys.70.721
- RSAS. The 2012 Nobel Prize in Physics Press Release. Nobelprize.org. Nobel Media AB 2014 (2012). http://www.nobelprize.org/nobel_prizes/physics/laureates/2012/press.html. Accessed 15 Sep 2014
- 17. G. Sansone et al., High-energy attosecond light sources. Nat. Photon. 5, 655–663 (2011). doi:10.1038/nphoton.2011.167

Chapter 2 Strong Laser Fields and Ultrashort Laser Pulses

The creation of strong laser fields is closely related to the formation of short laser pulses giving access to very high intensities while keeping the average power of the laser system on a moderate and thus experimentally feasible level. Usually, in addition to this strong temporal confinement of the energy, the laser beam is also focussed spatially. This chapter gives an overview about ultrashort laser pulses and the strong fields they are associated with. It is organized as follows: First, in Sect. 2.1 the mathematical framework as commonly used for the description of short laser pulses is summarized. It also covers the properties and the description of electromagnetic fields in laser resonators and in particular the concepts underlying *mode-locking* as a key technique in modern ultrashort pulse generation. Here, the focus lies on *Kerr-lens mode-locked Ti:sapphire*¹ laser systems since these represent the standard table-top system used in many laboratories as well as in the experimental setup used in this work. Then, in Sect. 2.2, the specific laser system and subsequent pulse manipulation techniques as used in this work are discussed involving also the treatment of important nonlinear effects in matter.

2.1 Mathematical Description of Laser Pulses

This section gives a short summary about the mathematical description of short laser pulses. It follows the descriptions which can be found in standard laser physics textbooks, e.g. [4, 8, 11, 21, 40]. Particular information about ultrashort laser pulses and the associated phenomena are reviewed e.g. in [5, 10, 18, 22].

If the polarization and transverse properties of a laser beam are neglected, monochromatic light emitted from a laser system can be characterized at any (fixed) point in space by its oscillating electric field $E(t) = \text{Re}\{E \exp[i\omega t]\}$ [9, Sect. 7.3] where E is the field amplitude and ω_L the angular laser frequency. The continuous wave

¹Titanium-ion doped sapphire (Ti:Al₂O₃).

[©] Springer International Publishing Switzerland 2016

oscillates with constant amplitude and the laser thus represents the extreme antonym of a suitable system for the generation of ultrashort pulses. In fact, lasers with an emission characteristic close to this hypothetical system, as e.g. the Helium-neon laser (HeNe laser) are commonly referred to as *continuous-wave* (cw) laser systems. To extend the description to non-monochromatic laser sources, an arbitrary spectral amplitude $\tilde{E}(\omega)$ of finite width is introduced and the resulting field may be described as, see e.g. [40, appendix G],

$$E(t) = \text{Re}\left\{\frac{1}{\sqrt{2\pi}} \int_{-\infty}^{\infty} d\omega \tilde{E}(\omega) \exp[i\omega t]\right\}$$
 (2.1)

$$= \operatorname{Re} \left\{ \frac{1}{\sqrt{2\pi}} \int_{-\infty}^{\infty} d\omega \tilde{A}(\omega) \exp[i(\omega t + \varphi(\omega))] \right\}, \tag{2.2}$$

where the factor $1/\sqrt{2\pi}$ preceding the integral is arbitrarily chosen. The complex field amplitude $\tilde{E}(\omega) = \tilde{A}(\omega) \exp[i\varphi(\omega)]$ is not accessible in the experiment, however, the spectral intensity $I(\omega) = E^*(\omega) E(\omega)$ may be measured with a spectrometer. In contrast, $\tilde{A}(\omega)$ is real, representing the modulus of a complex number. In particular Eq. (2.2) allows a fairly intuitive interpretation: The total electric field E(t) is formed by a continuous superposition of harmonically oscillating fields with individual contributions to the total field characterized by an amplitude $\tilde{A}(\omega)$. In addition, each of the contributing fields may have an individual phase shift $\varphi(\omega)$. Equation (2.1) can be directly identified with the Fourier transform [6, Sect. 15.3.1.2], relating E(t) in the time domain with $\tilde{E}(\omega)$ in the frequency domain:

$$E(t) = \mathcal{F}\left\{\tilde{E}(\omega)\right\}. \tag{2.3}$$

The inverse transformation is then given by

$$\tilde{E}(\omega) = \mathcal{F}^{-1} \left\{ E(t) \right\} = \frac{1}{\sqrt{2\pi}} \int_{-\infty}^{\infty} dt E(t) \exp[-i\omega t]. \tag{2.4}$$

The special case of monochromatic radiation can easily be obtained from Eq. (2.4) with $\tilde{E}(\omega) = \frac{\delta(\omega - \omega_L)}{\sqrt{2\pi}}$. Further details about the mathematical treatment can be found in literature, e.g. in [10, 40], and will not be discussed here in detail.

The Fourier transform, connecting the spectral and the temporal representation of the laser field, causes an intrinsic and fundamental connection between the spectral width 2 $\Delta \omega$ and the minimum pulse duration $\Delta \tau_{\rm F}$ achievable. If Gaussian profiles are presumed, $E(t) \propto \exp\left[-4\ln(2)t^2/\Delta \tau_{\rm F}^2\right]$ and $\tilde{E}(\omega) \propto \exp\left[-4\ln(2)\omega^2/\Delta \omega^2\right]$, Eq. (2.1) yields

$$\Delta \tau_{\rm F}' = \frac{8 \ln(2)}{\Delta \omega'}.\tag{2.5}$$

²The term "width" is used here and in the following as a synonym for "full width at half maximum" (FWHM).

However, due to the important role of the intensity $I=E^2$ in the interaction with atoms and molecules, see Sect. 3.1, often the temporal and spectral distributions I(t) and $I(\omega)$ are of more interest than the electric fields. If the width of these distributions is denoted with $\Delta \tau_{\rm F}$ and $\Delta \omega$, respectively, it follows directly from the properties of the Gaussian distribution $\Delta \tau_{\rm F}' = \sqrt{2} \Delta \tau_{\rm F}$ and $\Delta \omega' = \sqrt{2} \Delta \omega$ and thus with Eq. (2.5):

$$\Delta \tau_{\rm F} = \frac{4 \ln(2)}{\Delta \omega}.\tag{2.6}$$

Although discussed here for the special case of Gaussian profiles, similar relations of the form $\Delta \tau_F = ^{\rm const}/\Delta \omega$ can be established for other distributions, see e.g. [40, Sect. 8.6.1]. It can be concluded that the duration of the pulses is generally limited by the spectral width of the laser system. It should be noted that $\tilde{E}(\omega)$ was chosen as a real value, thus $\varphi(\omega) \equiv 0$. As will be shown in the following section, any other choice of the phase will either not influence or lengthen the pulse duration. In the example above, however, the pulse duration is limited *only* by the bandwidth of the laser and the mathematical property of the Fourier transform, therefore such ideal laser pulses are commonly called *Fourier-limited pulses*. The discussion of the monochromatic laser at the beginning of this section can now be put in simple equations: From $\Delta \omega = 0$ follows with Eq. (2.6) $\Delta \tau_F = \infty$.

2.1.1 Laser Pulses as Superpositions of Resonator Modes

For the generation of short laser pulses, the additional constraints arise due to the resonator introducing boundary conditions for the electric field. In a resonator of optical length d with infinitely large planar end-mirrors the condition is simply given by $\omega/2\pi = qc/2d$ where q>0 is an integer number and c the speed of light in vacuum [8, Sect. 2.1]. The stationary field configurations in the resonator, commonly known as resonator eigenmodes or simply resonator modes, are given by standing plane waves fulfilling the condition for an arbitrary choice of q. In addition, the resonator modes are fully characterized by this number. However, for resonators with finite mirror diameters, the situation is substantially different. Caused by continuous diffraction losses which depend on the distance to the resonator axis, planar waves are no longer eigenmodes, see e.g. [8, Sect. 5.2.2].

For symmetric *confocal resonators* with spherical mirrors, where d is twice the focal length of the mirrors, new solutions have been found analytically, first for the special case of identical square resonator mirrors [2], later for more general configurations including circular shaped mirrors [3]. These solutions are commonly referred to as *transverse electromagnetic modes* (TEM modes), characterized by three integer numbers q, m, n > 0 and denoted as $\text{TEM}_{m,n,q}$, see e.g. [8, Sect. 5.2.3]. The transverse field amplitude in the modes is characterized by m and n and is of Gaussian shape for all $\text{TEM}_{0,0,q}$ modes which are usually called *fundamental modes*.

The frequency depends on all three numbers and is, in the case of identical circular resonator mirrors in confocal configuration, given by [2, 3]

$$\frac{\omega}{2\pi} = \frac{c}{2d} \cdot \begin{cases} q + \frac{1}{2}(2m + n + 1) & \text{circular mirrors} \\ q + \frac{1}{2}(m + n + 1) & \text{square mirrors.} \end{cases}$$
 (2.7)

Obviously, in both cases, different $\text{TEM}_{m,n,q}$ modes comprise the same frequency and thus are energetically degenerated. Compared to the hypothetical case of infinitely large mirrors mentioned before, new frequencies are accessible for appropriate combinations of m and n with 2m+n+1 and m+n+1 being odd for circular and square mirrors, respectively. These frequencies are centered right in the middle between those of the fundamental modes. Thus, the frequency difference between two adjacent modes of the resonator, the *free spectral range* (FSR) is given by [8, Sect. 5.2.8]

$$\frac{\delta\omega_{\rm FSR}}{2\pi} = \frac{c}{4d}.\tag{2.8}$$

Since non-fundamental modes exhibit intensity profiles less confined on the resonator axis, an appropriate aperture or choice of the ratio between the mirror diameters and d can be used to increase their relative diffraction losses and thus to force the laser into the fundamental modes, see e.g. [21, Sect. 8.1.]. For convenience, the absence of non-fundamental modes is assumed in the following, $m = n \equiv 0$. The frequency difference between two adjacent *fundamental* modes oscillating in the resonator is given by [8, Sect. 5.2.8]

$$\frac{\delta\omega}{2\pi} = 2\frac{\delta\omega_{\rm FSR}}{2\pi} = \frac{c}{2d}.$$
 (2.9)

Provided, the amplification by the active laser medium is sufficiently high, all resonator modes in a certain spectral range may contribute to the formation of the overall electric field emitted by the system. If the emission spectrum of the active medium is assumed to be of Gaussian shape centered around ω_0 with a width $\Delta\omega$ fulfilling $\delta\omega\ll\Delta\omega\ll\omega_0$ and the phase relation between adjacent modes is further assumed to be constant, $\delta\varphi=$ const, the total field Eq. (2.2) can be written as [40, Sect. 8.6.1.]

$$E(t) = \operatorname{Re}\left\{\frac{1}{\sqrt{2\pi}} \sum_{l=-\infty}^{\infty} \tilde{A}(\omega_0 + l\delta\omega) \exp\left[i((\omega_0 + l\delta\omega)t + l\delta\varphi)\right]\right\}$$

$$= \operatorname{Re}\left\{\frac{1}{\sqrt{2\pi}} \left(\sum_{l=-\infty}^{\infty} \tilde{A}(\omega_0 + l\delta\omega) \exp\left[il\delta\varphi\right] \exp\left[il\delta\omega t\right]\right) \exp\left[i\omega_0 t\right]\right\}$$

$$= \operatorname{Re}\left\{\frac{1}{\sqrt{2\pi}} A(t) \exp\left[i\omega_0 t\right]\right\}. \tag{2.10}$$

In the last step, the expression in brackets was identified as a discrete version of the Fourier transform and the existence of an appropriate function A(t) was deduced.

As derived e.g. in [40, Sect. 8.6.1.], the electric field is oscillating with a *carrier* frequency ω_0 and is modulated in amplitude by a time-dependent function A(t) commonly referred to as pulse envelope. Further, for the separation of the pulses in time τ and their duration $\Delta \tau$ it can be derived [40, Sect. 8.6.1.]

$$\tau = 2\pi/\delta\omega \tag{2.11}$$

$$\Delta \tau = 4\ln(2)/\Delta\omega. \tag{2.12}$$

From Eqs. (2.11) and (2.9) follows $\tau=2d/c$ meaning that the repetition rate of the laser system is simply determined by the round-trip time of the laser pulses in the resonator [40, Sect. 8.6.2]. Equation (2.12) is identical to the previously found general expression, Eq. (2.6). From this it can be concluded that the superposition of resonator modes with constant phase differences of adjacent modes produces Fourier limited pulses. This situation is commonly referred to as *mode-locked* operation of the laser. In suitable materials, as e.g. Ti:sapphire crystals, $\Delta\omega$ can be large enough to cause simultaneously significant amplification for a certain wavelength λ_1 and even its second harmonic $\lambda_2=2\lambda_1$ [12] which is commonly called an *octave-spanning* spectrum. In this situation, $\Delta\tau_F$ can become very short, even of the same order of the oscillation period of the electromagnetic wave itself. Such pulses are commonly referred to as *few-cycle pulses* [5]. It is noteworthy that the peak intensity in such laser pulses is proportional to the square of the number of modes contributing, see e.g. [40, Sect. 8.6.1.].

The most general form for the phase $\varphi(\omega)$ guaranteeing the generation of Fourier limited pulses is given by

$$\varphi(\omega) = \varphi(\omega_0) + a \cdot (\omega - \omega_0), \qquad (2.13)$$

where a is a constant and the function $\varphi(\omega)$ is only evaluated for the discrete resonator frequencies. This equation may be interpreted as a Taylor series [6, Sect. 6.1.4.5] of an arbitrary function $\varphi(\omega)$ around ω_0 up to the first order. It is self-evident and often also convenient to extend this to

$$\varphi(\omega) = \varphi(\omega_0) + \frac{\partial \varphi(\omega)}{\partial \omega} \bigg|_{\omega = \omega_0} (\omega - \omega_0) + \frac{1}{2} \frac{\partial^2 \varphi(\omega)}{\partial \omega^2} \bigg|_{\omega = \omega_0} (\omega - \omega_0)^2 + \mathcal{O}(\omega^3),$$
(2.14)

see e.g. [35, Sect. 9.1]. The influence of the different terms on the shape of the generated pulses are displayed in Fig. 2.1 calculated for a model resonator and active medium. Although the number of modes contributing is much less than in a typical laser setup for ultrashort laser pulses, general qualitative features can be studied. The figure depicts eight spectral field distributions $\tilde{A}(\omega)$ of Gaussian shape evaluated at the positions of the resonator modes (blue line and dots in left pictures). The spectral phase $\varphi(\omega)$ is shown in green. E(t) is then calculated with Eq. (2.10), where the summation can be restricted to a finite number of modes with significant amplitudes

without noticeable change of the result. E(t) is shown on the right as a blue line, while the red line shows the envelope function calculated by replacing Re{} by Abs{} in Eq. (2.10).

In Fig. 2.1a, the width of the emission spectrum is fairly narrow such that only three modes significantly contribute to the total electric field, resulting in a beat frequency. The phase in this example is globally set to zero, $\varphi(\omega) \equiv 0$. If the spectrum is chosen broader and broader along (b) and (c), well separated pulses arise which become shorter and shorter. The electric field shown in (c) represents a few-cycle Fourier limited pulse. If a constant global phase is added as done in (d), where $\varphi(\omega) = -\pi$, the envelope and thus the pulse duration is not affected. However, the phase offset between the carrier wave and the envelope, commonly referred to as carrier-envelope phase (CEP), see e.g. [5, 29, 32], is altered. Since CEP effects are not explicitly studied in this work and their presence only used as an indicator for the pulse duration, see Sect. 2.2.2, the influence of the constant phase on the electric field is ignored in the following.

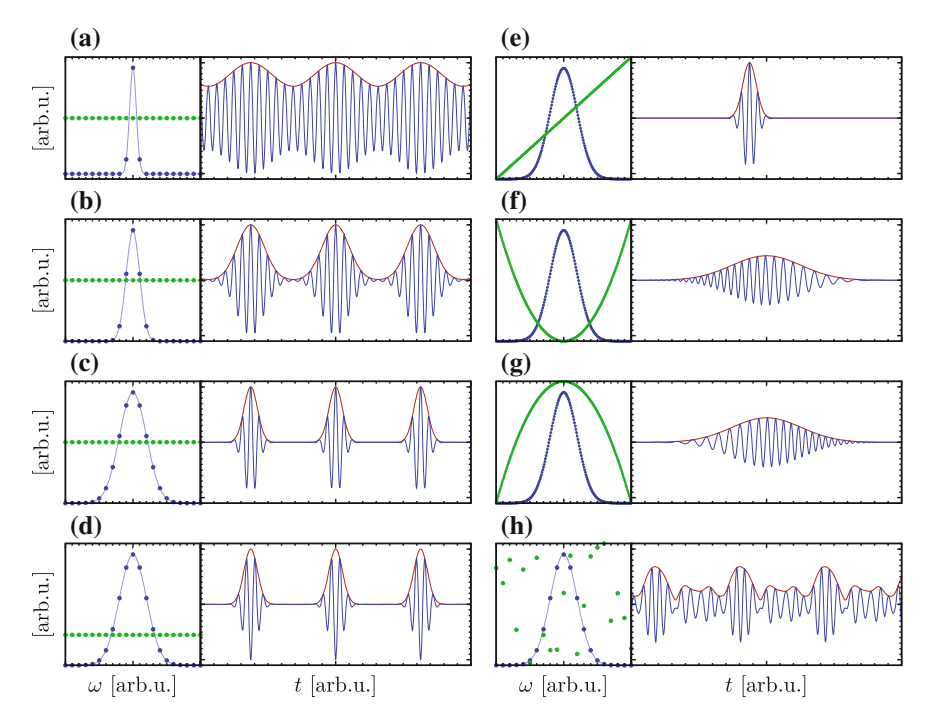


Fig. 2.1 Examples for electric fields created by superpositions of resonator modes. Each figure contains of two plots: In the *left*, the spectral amplitude $\tilde{A}(\omega)$ and the spectral phase $\varphi(\omega)$ are shown in *blue* and *green*, respectively. The functions are evaluated at the discrete frequencies of the resonator modes. In the *right* picture, the resulting electric field is shown in *blue*, the envelope function in *red*, see text for details

As discussed earlier, even a linear trend in $\varphi(\omega)$ guarantees the generation of Fourier limited pulses, see Eq. (2.13). This situation is depicted in Fig. 2.1e, where the pulses from (c) are exactly reproduced despite being shifted on the absolute timescale. Apart from this, the spacing between the modes was decreased, modeling a lengthening of the resonator, see Eq. (2.9). Consequently the round-trip time increases such that the preceding and the following pulses are not visible in the picture any further. For a quadratic trend in $\varphi(\omega)$, however, the situation changes substantially. Even though the spectral amplitudes are identical to the previous case, this phase relation leads to much longer pulses as depicted in Fig. 2.1f, g. In addition, the frequency of the carrier wave changes along the pulse which is commonly known as chirp, see e.g. [35, Sect. 9.1]. Finally the case of a random phase relation is shown in (h). The electric field produced seems to be chaotic, nevertheless it is still periodic and each of the occurring peak-like structures has a duration comparable to the well separated, Fourier limited pulses in (c), see e.g. [40, Sect. 8.6]. In order to make the effects more visible, the frequency spacing of the modes is chosen larger again, as in (a)–(d).

In conclusion, the generation of ultrashort laser pulses requires not only the contribution of many modes with different frequencies but also a fixed phase relation between the different modes as close as possible to Eq. (2.13), the ideal mode-locking condition. In reality, the situation becomes more difficult since optical elements in the beam path and even the air traversed on the way to the actual experiment will certainly change the phase relations due to dispersion, see Sect. 2.1.2.

Kerr Lens Mode-Locking

Different techniques have been developed to obtain mode-locked laser operation for the generation of ultrashort pulses. For an historical review see e.g. [18]. One example mentioned there is the *Kerr lens mode-locking* (KLM), an approach based on the nonlinear optical Kerr-effect in suitable transparent materials. It is widely exploited in Ti:sapphire laser systems and will be discussed in the following.

Although mode-locking is defined and described in the frequency domain, namely with the condition from Eq. (2.13) for adjacent resonator modes, it is feasible and convenient to switch to the time-domain picture: As shown in the previous section, perfect mode-locking occurs if, and only if, the associated laser pulses are Fourier limited. Therefore, if a process inside the resonator is capable of shortening the pulses such that their duration approaches the Fourier limit, the phase relation between the modes will adapt and converge to the associated phase relation.

The basic idea for efficient mode-locking is therefore to artificially lower the quality of the resonator and thus increase the losses for any continuous components of the wave, currently present in the resonator [40, Sect. 8.6.3.2 and Appendix F.2]. Any spiked structure generated in the initially random spontaneous emission of the active medium will gain energy quickly and—after some round-trips in the resonator—may form a short stable pulse. The largely differing peak intensity in the pulsed field configuration can be utilized in this respect in different *passive mode-locking* techniques. For example, a suitable absorbing material, a *fast saturable absorber*, may be inserted into the resonator, absorbing the laser radiation but being saturated and thus

transparent for high intensities [40, Sect. 8.6.3.2 and Appendix F.2]. The saturable absorbance may also be included in the resonator end-mirrors using *semiconductor saturable absorber mirrors* (SESAM) [20].

KLM is likewise a passive mode-locking technique but relies on the non-linear optical Kerr-effect, see e.g. [40, Sect. 8.6.3.2] and thus on refraction rather than absorption. For low field intensities the definition of the refractive index $n_0 = c/v_{\rm ph}(\lambda)$ as a function of the phase velocity of the light $v_{\rm ph}(\lambda)$ and therefore the wavelength λ is a very good approximation. In contrast, in very strong fields, the refractive index shows an additional dependence on the laser intensity I(t) and is given by [40, Sect. 8.6.3.2]

$$n(t) = n_0 + n_2 I(t). (2.15)$$

The second order index of refraction n_2 in this expression is a (very small) positive constant. Typical values are around 10^{-13} cm²/W to 10^{-17} cm²/W, see e.g. [4, table 4.1.2], such that the second order term is negligible for low intensities.

With increasing intensity, however, the influence of the second terms grows and for ultrashort strong field can become significant. If a $\text{TEM}_{0,0,q}$ pulse with a Gaussian transverse intensity distribution travels through a non-linear medium inside the resonator, Eq. (2.15) causes a refractive index that changes over the transverse coordinate. Effectively, for $n_2 > 0$ a spherical lens is formed, focusing the beam towards the resonator axis [40, Sect. 8.6.3.2]. This is commonly referred to as *self-focusing*. An aperture or an appropriate geometry of the resonator itself can be used in order to suppress any continuous field components.

If an aperture is present or the geometry of the resonator itself is appropriately chosen, the focusing is required for a sufficient reduction of losses and therefore pulsed field components are favored in the resonator. In each round trip of the pulse, the leading and trailing edge are suppressed due to their lower intensity and the pulse gets shortened [21, Sect. 10.2.2]. One advantage of KLM is the almost instantaneous response of the medium [40, Sect. 8.6.3.2]. Moreover, in particular for Ti:sapphire laser systems, it is beneficial that the laser crystal itself may serve as a non-linear medium for the optical Kerr-effect [19].

2.1.2 Dispersion in Matter

In particular for short laser pulses, dispersion in matter is an important issue due to their large bandwidth according to Eq. (2.12). While traveling along \hat{e}_z through a transparent material, a short laser pulse accumulates a spectral phase of [35, Sect. 7.2]

$$\Phi(\omega) = \frac{n(\omega)\,\omega}{c}z,\tag{2.16}$$

where $n(\omega)$ is the refractive index of the material and c the speed of light in vacuum. Since the carrier frequency ω_0 even of few-cycle pulses is large compared to their

Quantity		Relation			
Phase velocity	$v_{ m ph}$	ω_0/A			
Group velocity	v_{g}	1/B			
Group velocity dispersion	GVD	C			

Table 2.1 Definition of phase velocity, group velocity and group velocity dispersion and the relation of this values to (Eq. 2.17) as found e.g. in [35, Sect. 9.1]

spectral width $\delta\omega$ and the refractive index usually sufficiently smooth, this expression can be approximated by a Taylor expansion, cf. [35, Sect. 9.1]

$$\Phi(\omega) = \underbrace{\Phi(\omega_0)}_{A} + \underbrace{\frac{\partial \Phi(\omega)}{\partial \omega} \Big|_{\omega = \omega_0}}_{B} (\omega - \omega_0) + \frac{1}{2} \underbrace{\frac{\partial^2 \Phi(\omega)}{\partial \omega^2} \Big|_{\omega = \omega_0}}_{C} (\omega - \omega_0)^2 + \mathcal{O}(\omega^3).$$
(2.17)

The three factors A, B and C depend on the characteristics of $n(\omega)$ and are—for fixed ω_0 —material constants. Usually, the related quantities listed in Table 2.1 are used for characterization.

The influence of such phase functions on the pulses and their duration was already depicted in Sect. 2.1.1. In particular in the design of femtosecond laser systems also higher orders as the *third order dispersion* (TOD) have to be considered and compensated as accurately as possible, see e.g. [5]. Furthermore, if the phase function is not sufficiently smooth on the scale given by $\Delta\omega$, a (low-order) Taylor expansion might be a less good approximation. Instead, $\Phi(\omega)$ can be derived from $n(\omega)$ which is often well characterized. The pulse shape and duration can then numerically be calculated according to Eq. (2.2). After all, dispersion in media may lead to temporal broadening of short pulses and therefore has to be compensated (or precompensated) in order to obtain short pulses in the experiment.

2.1.3 General Properties of Focussed Laser Beams

Laser beams can be focussed onto a well defined spot using lenses or curved mirrors. Not only the maximum intensity achievable but also a detailed knowledge about the intensity distribution near the focus, the "shape" of the focal volume, is desirable for two reasons: First, the interaction processes between light and matter strongly depends on the intensity, see e.g. Sect. 3.1. Thus, in the case of a gas jet of finite diameter where the laser is focussed on (see Chap. 4), not all atoms will experience the same laser intensity. In fact, an intrinsic averaging over different intensities is present which has to be considered in the interpretation of the data, see e.g. [30]. Second, the geometry of the laser focus is important for the experiment since it defines the interaction region as the spatial overlap with the usually much more extended gas jet, see Sects. 4.1.2 and 4.3.

The intensity of a laser beam can, if exclusively fundamental modes are considered, be described by a Gaussian transverse profile as seen in Sect. 2.1.1. In case of a focussed beam this still holds at any position z_0 along the laser propagation direction \hat{e}_z . However the beam diameter then depends on z_0 . A focussed beam can therefore be described with [11, Sects. 12.2 and 12.3]

$$I_{z_0}(r) = I_{z_0}^{\text{max}} \cdot \exp\left[-\frac{2r^2}{w^2(z_0)}\right]$$
 (2.18)

with

$$w(z) = w_0 \sqrt{1 + z^2/z_R^2}, (2.19)$$

$$w_0 = \lambda f / \pi R_L, \tag{2.20}$$

$$z_R = w_0^2 \pi / \lambda. \tag{2.21}$$

Here, r is the transverse spatial coordinate perpendicular to \hat{e}_z , λ the wavelength in the beam, f the focal length of the lens or mirror, R_L the radius of the laser before focusing and z_R the *Rayleigh length*, the distance along \hat{e}_z between the waist of the focus and the point, where its diameter has increased by a factor of $\sqrt{2}$. At this position the intensity has decreased to 1/2 of the peak intensity as present in the center of the focus. In contrast to this, $w_0 = w(z=0)$ describes the transverse distance from the center of the focus to the radius, where the intensity has decreased to $1/e^2 \approx 1/7.4$. Although both parameters describe the dimensions of the laser focus it is important to keep in mind that they can not simply be related to each other.

 $I_{z_0}^{\max}$ denotes the intensity on the beam axis in the plane defined by $z=z_0$. An integration of Eq. (2.18) over φ and r in each of this planes has to yield the same value since the total power of the radiation is preserved. Therefore it is $I_{z_0}^{\max}=(w_0/w_{(z_0)})^2 I^{\max}$ where $I^{\max}=I_{z_0=0}^{\max}$ is the global maximum of the laser intensity. The intensity distribution in the laser focus is thus given by [31, Sect. 2.2]

$$I(z,r) = I^{\max} \left(\frac{w_0}{w(z)} \right)^2 \exp \left[-\frac{2r^2}{w^2(z)} \right]. \tag{2.22}$$

This expression is plotted in Fig. 2.2 for typical parameters of the experiment, namely $\lambda=790\,\mathrm{nm},\,f=7\,\mathrm{cm},\,R_L=0.5\,\mathrm{cm}.$ Solid red lines represent w(z). The intensity distribution is much more elongated in the propagation direction of the laser than perpendicular to it. Note that the distance shown along z in Fig. 2.2 is 20 times larger than the one shown along r. To emphasize this characteristic feature of laser foci, curves of equal intensity can be calculated. Demanding $I(z,r)=\alpha I^{\mathrm{max}}$ with $\alpha\in[0,1]$ in Eq. (2.22) yields [31, Sect. 2.2]³

³The original equation contains a typing error which is corrected here.

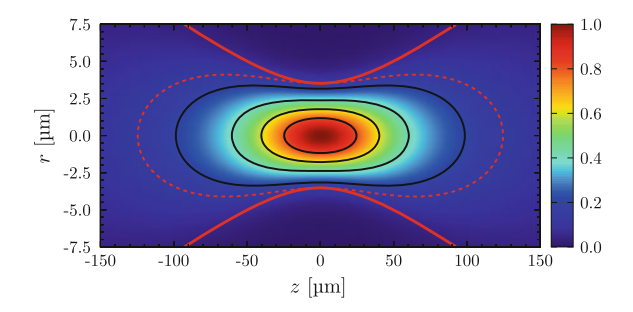


Fig. 2.2 Intensity distribution in a Gaussian laser focus according to Eq. (2.22) with lines of equal intensity (black solid lines) calculated with Eq. (2.23) for (from origin) $\alpha = 0.8$, 0.6, 0.4, 0.2, respectively. The positions where the intensity has dropped to $^{1}/e^{2}$ is shown as red dashed line. The parameters used in the calculations are $\lambda = 790 \, \text{nm}$, $f = 7 \, \text{cm}$, $R_L = 0.5 \, \text{cm}$. The red solid lines denote w(z) calculated with Eq. (2.19). A similar calculation and illustration of the contour lines can be found in [31, Sect. 2.2]

$$r^{\alpha}(z) = \pm \operatorname{Re} \left\{ \sqrt{\frac{1}{2} w^{2}(z) \ln \left[\frac{1}{\alpha} \left(\frac{w_{0}}{w(z)} \right)^{2} \right]} \right\}.$$
 (2.23)

The contour lines defined by this relation are shown in Fig. 2.2—starting from the origin outwards—for $\alpha=0.8,\,0.6,\,0.4,\,0.2$, respectively. The typical extent of the focus with respect to z and r can be calculated with $\alpha_0=1/e^2$, shown as dashed red line. The condition $r^{\alpha_0}(z)=0$ and the calculation of $r^{\alpha_0}(0)$ thus yields

$$\Delta r = 2w_0 \approx 7.0 \,\mu\text{m},$$

$$\Delta z = 2z_R \sqrt{\left(e^2 - 1\right)} \approx 250 \,\mu\text{m}.$$
(2.24)

Note that Δr also denotes the *diameter* of the laser focus in radial direction rather than the radius. After all, the circumference of the focus along the direction of propagation is much larger than its transverse diameter. As can be seen from Eq. (2.20) and Eq. (2.21), both quantities are proportional to λ . Therefore, light with shorter wavelengths can be focussed "harder", in the case of $\lambda=395$ nm for example, onto a spot of half the extension in each direction. The relations in this section are only valid for laser beams with perfect Gaussian beam profile. However, real laser beams often show deviations from this ideal situation which is usually described by a value $M^2 \geq 1$ (= 1 for a Gaussian profile), see e.g. [11, Sect. 12.5]. As a consequence, the focus dimensions are usually larger than described by Eq. (2.24). Since the aim of this section is more the qualitative description than the derivation of exact numbers, this more complex situation is not treated here.

2.2 Laser Pulse Generation and Manipulation

For the different experiments presented in this thesis, laser pulses of different duration and central wavelength are required. However, in each case, the first step is the generation of strong ultrashort pulses with a commercial femtosecond laser system. These pulses are then modified in different subsequent processes in order to achieve e.g. shorter pulse durations or a different central wavelength.

2.2.1 The Femtosecond Laser System

In all experiments presented in this thesis a commercial *FEMTOLASERS* "FEMTOPOWER compact PRO HP/HR" Ti:sapphire⁴ laser system is used as a source for strong and ultrashort laser pulses. General information about Ti:sapphire laser systems can be found e.g. in [10, Sect. 6.7.2] and [40, Sect. 9.2.8]. The specific information about the system used in the experiments are compiled from [14, 15]. The system consists of a mirror-dispersion controlled Ti:sapphire oscillator [37] producing ultrashort (\lesssim 10 fs), close to Fourier limited, but weak pulses at a high repetition rate. These pulses are stretched in time and subsequently amplified in a second Ti:sapphire crystal in a *chirped pulse amplification* (CPA) scheme [39]. With this technique, damage of the Ti:sapphire crystal in the amplification stage is prevented as it would occur otherwise due to the extreme intensities and thereby caused non-linear effects.

In a multi-pass setup, the laser beam is guided through the amplifier crystal. After the fourth pass, the repetition rate is reduced to around 3 kHz by a Pockels cell. Thus, most of the pulses are suppressed and only one pulse is further amplified in every shot of the pump laser. A description of a very similar amplifier system can be found in [25]. The strong but temporally stretched pulses are compressed in a subsequent prism compressor where a complex interplay of optical prisms and chirped mirrors provide a negative refraction index and at the same time correct for higher order dispersion [36]. The pulse duration is specified to less than 30 fs, the pulse energy to larger than 800 mJ. *Gain narrowing*, the reduction of the spectral width in the amplification process, see e.g. [10, Sect. 7.2.2], mainly causes the increase of the pulse duration compared with the output of the oscillator. In Fig. 2.4a and b, the two spectra can be compared. The overall dispersion of the laser pulses is controlled by third-order dispersion (TOD) precompensation after the oscillator and careful adjustment of the compressor stage. Thus, close to Fourier limited pulses are emitted by the laser system.

⁴Titanium-doped sapphire (Ti:Al₂O₃).

2.2.2 Generation of Few-Cycle Pulses

In the pulses emitted by the laser system, the electric field fulfills more than ten oscillations with a periodicity of approximately 2.6 fs. Even shorter, *few-cycle pulses*, where the pulse duration is in the same order of the field periodicity, see e.g. [5], can be generated in a subsequent process [33]: Since the minimum pulse duration of the pulses delivered by the laser system is limited mainly by the width of the spectral profile, the first step towards shorter pulses is the generation of additional wavelength components. For this, a nonlinear optical effect namely *self-phase modulation* (SPM), see e.g. [4, Sect. 7.5], in a gaseous medium is utilized. Afterwards the pulses can be compressed with specifically designed *chirped mirrors*.

Spectral Broadening by Self-Phase Modulation

In Sect. 2.1, the optical Kerr effect was discussed causing an intensity-dependent refractive index, Eq. (2.15):

$$n(t) = n_0 + n_2 I(t) .$$

If the dispersion experienced by an initially Fourier limited $\text{TEM}_{0,0,q}$ pulse, while traveling through a medium of length L with $n_2 > 0 \in \Re$, is neglected, the accumulation of a phase is the only remaining effect [4, Sect. 7.5]:

$$\Phi(t) = -n_2 \frac{\omega_0 L}{c_0} I(t) \tag{2.25}$$

This time-dependent phase shifts the frequencies in the pulse resulting in [4, Sect. 7.5]

$$\omega(t) = \omega_0 + \frac{d\Phi(t)}{dt}$$

$$= \omega_0 \left(1 - n_2 \frac{L}{c_0} \frac{dI(t)}{dt} \right), \qquad (2.26)$$

where $\omega(t)$ is referred to as the *instantaneous frequency* in the pulse. In the leading edge of the pulse, where ${}^{dI(t)}/{}_{dt} > 0$, the frequency is shifted towards lower values while higher frequencies are generated in the trailing edge. Thus, the spectrum of the pulse is broadened and the pulse itself is positively chirped although the temporal pulse shape is not changed in the first instance [10, Sect. 8.1.1]. However, it is of course affected by the usual dispersion in the material. In reality, the situation is much more complex due to effects as self-steepening [4, Sect. 13.3] or finite non-linear response times [4, table 4.1.1] neglected here. A consequence is e.g. the non-symmetric broadening of the spectrum visible in Fig. 2.4 not covered by Eq. (2.26) for Fourier limited pulses with symmetric envelope. The enhanced spectral width of the laser light forms the basis of the generation of even shorter pulses.

In the experimental setup schematically shown in Fig. 2.3, the pulses delivered by the laser system are focussed onto a hollow-core glass fiber with an inner diameter of $250 \,\mu m$. By using a lens with a large focal length of about 1.5 m, the laser

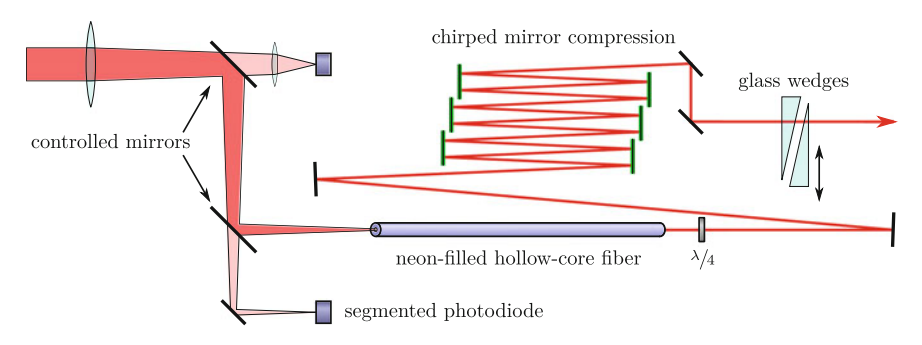


Fig. 2.3 Schematic overview about the setup used for the generation of few-cycle laser pulses. The pulses delivered by the femtosecond laser system are focussed onto a neon-filled hollow-core fiber filled with neon. The beam is spatially stabilized using two controlled mirrors and two segmented photodiodes, see text for details. After spectral broadening by SPM in the neon gas, the laser pulses pass a λ /4-plate ensuring linear polarization. Chirped mirrors temporally compress the pulses and also precompensate for the dispersion on the path to the REMI. Fine-adjustment of the overall dispersion and pulse-duration is performed by movable glass-wedges

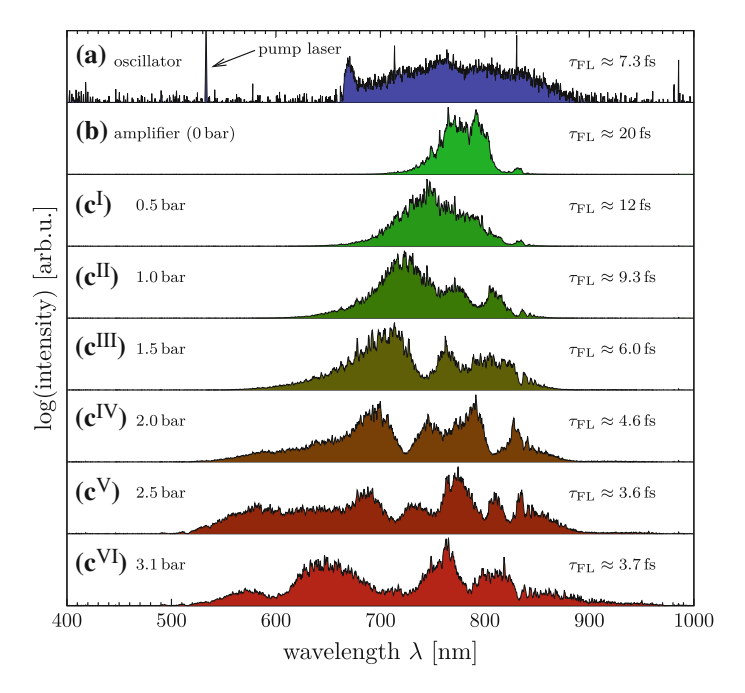


Fig. 2.4 Typical laser spectra obtained at different steps of the ultrashort pulse generation and their Fourier limits. **a** In the oscillator. **b** After the chirped mirrors and the Mach–Zehnder interferometer with an empty fiber. Apart from (*small*) losses on the optical elements this spectrum resembles the output spectrum of the femtosecond laser system. (e^{I-VIII}) Same as (**b**) but with nonzero, different absolute neon pressures in the fiber. SPM broadens the spectrum and thus reduces the Fourier limit of the pulses. In the region of short wavelengths the spectrum is suppressed by the low reflectivity of the chirped mirrors used

focus created is very elongated (see Sect. 2.1.3) and—since additionally confined in the hollow center of the fiber—extends to the full fiber length of about 1 m. Over this distance, the light can interact with neon atoms inside the hollow core, which represent the nonlinear medium for the SPM process. Since the optimal and stable incoupling into the fiber is crucial, small spatial drifts of the laser beam over time have to be efficiently compensated. For this purpose, a focus stabilization system was built [24]. It contains two four-fold segmented photodiodes where small parts of the beam are focussed on and thus small drifts can be detected. A computer can react by small adjustments with two motorized mirrors. A */4-plate after the fiber is used to ensure linear polarization of the light.

Chirped Mirror Compression

Due to the extremely broad spectrum, the laser pulses are very sensitive to dispersion. While traveling through optical elements and the air on the way to the spectrometer, see Chap. 4, the different frequencies in the pulses gather an individual phase, see Sect. 2.1.2. In order to compensate for this, *chirped mirrors* with an effective negative dispersion are used [41]. These mirrors are specially designed and coated such that the red components of the beam can penetrate deeper into the material and thus travel a longer distance compared to the blue. Three matched pairs of chirped mirrors are used in the experiment while each mirror is hit twice by the laser beam resulting in twelve reflexions in total. Fine tuning of the overall dispersion is performed with an additional small amount of glass, a pair of movable wedges.

Figure. 2.4b and c^{I-VIII} show spectra obtained after the chirped mirrors for different pressures of neon in the fiber. Apart from (small) losses on the optical elements, (b) resembles the output spectrum of the femtosecond laser system described in Sect. 2.2.1. However, short wavelengths around 500 nm and below are suppressed due to insufficient reflectivity of the chirped mirrors in this range. An approximation for the Fourier limit of the pulses is given for each of the spectra in Fig. 2.4, as it can be obtained by a calculation of the temporal shape of the electric field according to Eq. $(2.4)^5$ and a subsequent Gaussian fit to the temporal intensity distribution associated.

The duration of the pulses delivered by the system was measured to be around 6 fs before, see [16, 23], using autocorrelation and ZAP-SPIDER⁶ techniques [1]. However, in order to obtain information about the pulse duration during the alignment of the setup for few-cycle pulses, in this work a *single-shot Stereo-ATI* ⁷ *phasemeter* [42] was utilized. Detailed information about the setup can be found in [17]. Since the quality of the CEP-signal delivered by this device depends crucially on the pulse duration [34], it can be used as a qualitative indicator for the pulse duration at least for alignment purposes, where no accurate value has to be extracted.

⁵The integral in the expression is replaced by a sum over the binned spectrum.

⁶Zero-additional-phase spectral phase interferometry for direct electric field reconstruction.

⁷Above-threshold ionization.

2.2.3 Setup for Pump-Probe Measurements

For the time-resolved *pump-probe measurements* presented in Chap. 5, two pulses are required with an adjustable time delay with respect to each other. In such experiments, the first "pump" pulse is used to start dynamics in the target system while the second pulse "probes" the state of the system after a defined and adjustable time period, during which the system is allowed to evolve freely, see e.g. [28, 38]. For the creation of the pulse-pair and the adjustment of the time-delay, a *Mach–Zehnder interferometer* is used. Detailed information about the setup can be found in [13]. Starting from a single laser pulse, a thin beam splitter is used to create two identical pulses. Each pulse travels along one of the two arms of the interferometer, see Fig. 2.5. One of the arms is equipped with a piezo-driven stage to move two mirrors and to adjust the distance s the specific pulse has to travel before the two beams are recombined by a second beam splitter. The time delay between the pulses can be controlled with high precision and a spatial shift of the stage by Δs leads to a shift in time of

$$\Delta t = 2\frac{\Delta s}{c},\tag{2.27}$$

where c is the speed of light in air. The setup works for both ultrashort pulses from the fiber and the pulses delivered directly from the femtosecond laser system.

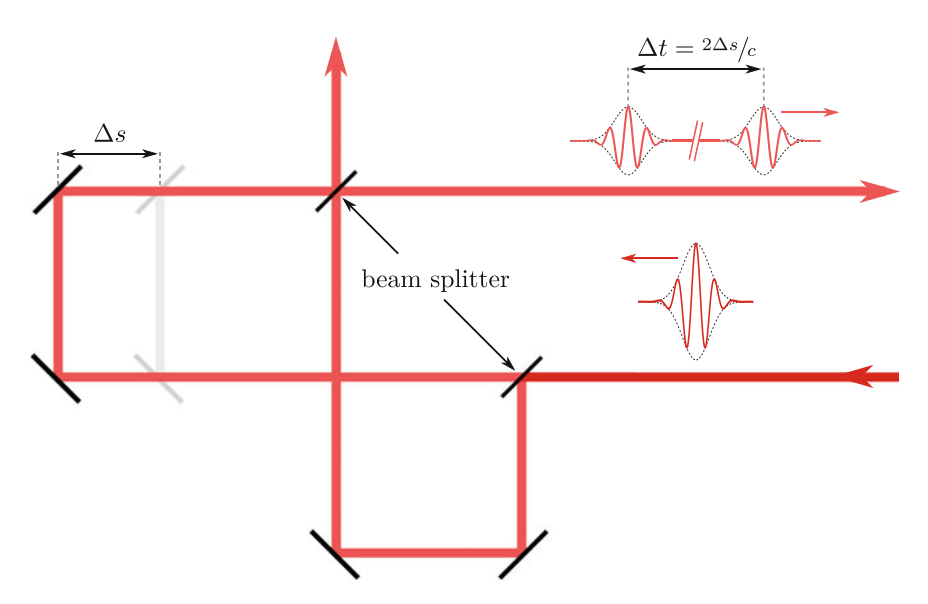


Fig. 2.5 Schematic picture of the Mach–Zehnder interferometer. The incoming pulses are split into two identical copies. The time delay of one pulse with respect to the other can be controlled by adjusting the length of one arm of the spectrometer

2.2.4 Frequency Doubling and Mixing

Nonlinear effects in suitable materials can be used to generate coherent and intense pulses at wavelengths not accessible directly for the laser system. Exposed to the strong fields of a (linearly polarized) intense laser, the electron clouds of the atoms in a nonlinear medium—e.g. a crystal made from β -barium borate (BBO)—are collectively driven back and forth. If the strength of the laser field is in the same order as the intrinsic atomic electric fields, large amplitudes are achieved in the driven oscillation. In contrast to very small amplitudes, where the oscillation has approximately harmonic character, higher orders of the effective potentials become significant. For a lossless and dispersionless medium, the polarization is given by [4, Sect. 1.1]

$$P(t) = \chi^{(1)} E(t) + \chi^{(2)} E^{2}(t) + \chi^{(3)} E^{3}(t) + \cdots$$

= $P^{(1)}(t) + P^{(2)}(t) + P^{(3)}(t) + \cdots,$ (2.28)

where $\chi^{(1)}$ is the linear and $\chi^{(2)}$ and $\chi^{(3)}$ the second- and third-order nonlinear susceptibilities. This relation can be utilized in different experimental schemes to generate new frequency components, initially not present in the laser spectrum. For simplicity the following discussion is restricted to monochromatic fields but can in principle be extended to the broader spectrum of short laser pulses: The phase matching conditions mentioned are then only fulfilled perfectly for the carrier frequency ω_0 . However, for frequencies sufficiently close to ω_0 , the processes may take place, although with reduced efficiency [4, Sects. 2.2 and 2.7]. Thus, few-cycle pulses with their very broad spectra are not suitable and in the experiments exclusively the direct output of the femtosecond laser system is utilized.

Second Harmonic Generation (SHG)

In the simplest scheme possible, the laser pulses delivered by the laser are directly focussed into the nonlinear crystal. If the electric field is described as $E(t) = E \exp(-i\omega_0 t) + \text{c.c.}$, Eq. (2.28) yields [4, Sect. 1.2]

$$P^{(2)}(t) = 2\chi^{(2)}EE^* + \left[\chi^{(2)}E^2e^{-2i\omega_0t} + \text{c.c.}\right]. \tag{2.29}$$

The spectrum of the time-dependent polarization comprises components with a frequency of $2\omega_0$ and so does the light emitted. For this reason the process is known as second harmonic generation (SHG). As depicted in Fig. 2.6, this can be understood as a transformation of two photons of the incident beam into one photon of the doubled frequency. In addition to the conservation of energy, a special form of momentum conservation has to be considered: For an efficient generation of second harmonic

⁸Since *E* and *P* are treated as scalar quantities, the tensor-nature of the susceptibilities $\chi^{(i)}$ is omitted [4, Sect 1.1].

⁹This description of the total electric field as a sum of a complex field and its complex conjugated expression, $E(t) = \varepsilon(t) + \text{c.c.}$, is mathematically equivalent to the description $E(t) = \text{Re}\{\varepsilon(t)\}$ used in Sect. 2.1.

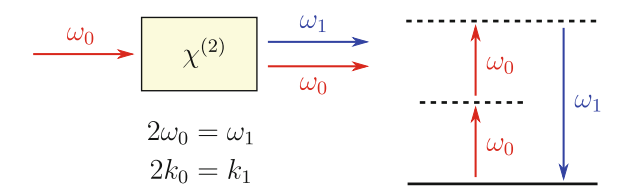


Fig. 2.6 Scheme for SHG in a nonlinear crystal. Two photons of the incident laser beam are converted into one photon of twice the frequency and energy ω_1 . In the energy diagram on the right the *solid line* represents the ground state while virtual states, only existent in the presence of the laser field, are displayed as *dashed lines*. In addition, the phase matching condition, Eq. (2.30), is displayed. Scheme according to [4, Fig. 1.2.1]

radiation it is necessary that the *wavevector mismatch* vanishes [4, Sects. 2.2 and 2.6]:

$$\Delta k = 2k_0 + k_1 = 2\frac{n_0\omega_0}{c} + \frac{n_1\omega_1}{c} = 0,$$
(2.30)

where $\omega_1 = 2\omega_0$ and n_i is the refractive index of the nonlinear material for the respective frequency. This situation is commonly referred to as *phase matching* and Eq. (2.30) is the associated *phase matching condition*.

In particular for nonlinear crystals, birefringent properties of the material may be utilized for this purpose: By aligning the optical axis of the crystal with respect to the propagation direction of the light, n_i can be adjusted [4, Sect. 2.7].

In the experiment, a BBO crystal is used to generate second harmonic radiation from the fundamental 790 nm pulses delivered by the femtosecond laser system. Thus, pulses with a carrier wavelength of 395 nm close at the high-frequency edge of the visible and the beginning of the ultraviolet spectrum are generated. On one hand, the SHG process can only be efficient for a relatively narrow spectral region around the central carrier frequency, which suggests a longer duration for the pulses compared with those in the incoming beam. On the other hand, SHG is a nonlinear process and hence depends strongly on the laser intensity. Therefore the leading and trailing edges of the pulse can be expected to be suppressed and the pulse shortened.

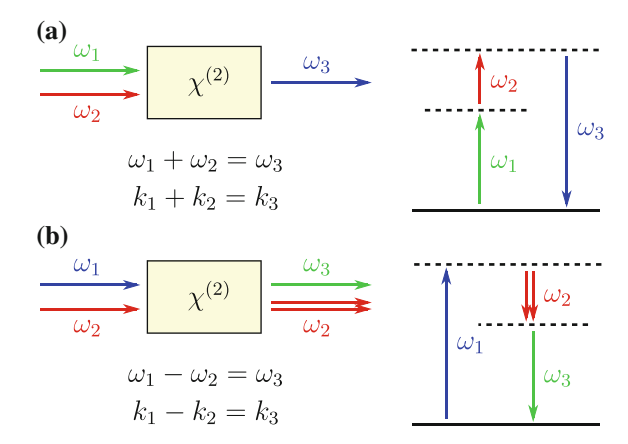
Frequency Mixing: Generation of Sum and Difference (SFG and DFG)

In a modified scheme, laser pulses of two different frequencies, ω_1 and ω_2 ($\omega_1 > \omega_2$) can be focussed simultaneously into the nonlinear crystal. For the moment, the availability of pulses with two different carrier frequencies is simply postulated and will be elucidated later in Sect. 2.2.5. In analogy to the treatment of SHG, the incident beam can be described by $E(t) = E_1 \exp(-i\omega_1 t) + E_2 \exp(-i\omega_2 t) + \text{c.c.}$ and Eq. (2.28) yields [4, Sect. 1.2]

$$P^{(2)}(t) = 2\chi^{(2)} \left(E_1 E_1^* + E_2 E_2^* \right) + \left[\chi^{(2)} \left(E_1^2 e^{-2\omega_1 t} + E_2^2 e^{-2\omega_2 t} \right) + \text{c.c.} \right]$$

$$+ \left[2\chi^{(2)} \left(E_1 E_2 e^{-2(\omega_1 + \omega_2)t} + E_1 E_2^* e^{-2(\omega_1 - \omega_2)t} \right) + \text{c.c.} \right].$$
 (2.31)

Fig. 2.7 Frequency mixing with a SFG and b DFG in a nonlinear crystal with according phase matching conditions, Eq. (2.32). DFG contains a stimulated process where the irradiated radiation of lower frequency ω_2 is coherently amplified. Schemes according to [4, Fig. 1.2.2] for (a) and [4, Fig. 1.2.3] for (b), respectively



The first two terms reflect SHG processes simultaneously but independently taking place for the two different frequencies, while the last term is arising from an interplay between them. It introduces components in the oscillations of the time-dependent polarization with both the sum $\omega_3 = \omega_1 + \omega_2$ and the difference $\omega_3 = \omega_1 - \omega_2$ of the two frequencies initially present. Thus, radiation with theses frequencies may be emitted, provided that the respective phase matching condition is met [4, Sects. 2.4 and 2.5]

$$k_1 \pm k_2 = k_3 \text{ for } \omega_3 = \omega_1 \pm \omega_2$$
 (2.32)

The processes are referred to as *sum frequency generation* (SFG) and *difference frequency generation* (DFG), respectively, and depicted in Fig. 2.7. The latter is remarkable in one important aspect: DFG contains a stimulated process where the radiation of the incident lower frequency ω_2 is coherently amplified. This unique feature of DFG offers an efficient way for the creation of arbitrary frequencies, technically utilized as described in the following section.

2.2.5 Wavelength Tuning Using an OPA System

For creation of pulses with arbitrary carrier frequencies directly from the pulses delivered by the femtosecond laser system, several nonlinear effects may be combined, namely SPM followed by DFG and optional subsequent SHG, SFG or DFG. The experimental scheme presented in the following is refereed to as *optical parametric amplifier* (OPA). Here, only a brief description of the working principle is given, composed from [7] and [4, Sect. 2.8].

As discussed in Sect. 2.2.2, SPM in non-linear materials can be used for the generation of frequency components initially not present in the laser beam. Thus, a continuum of white light can be produced by focusing a part of the laser beam into

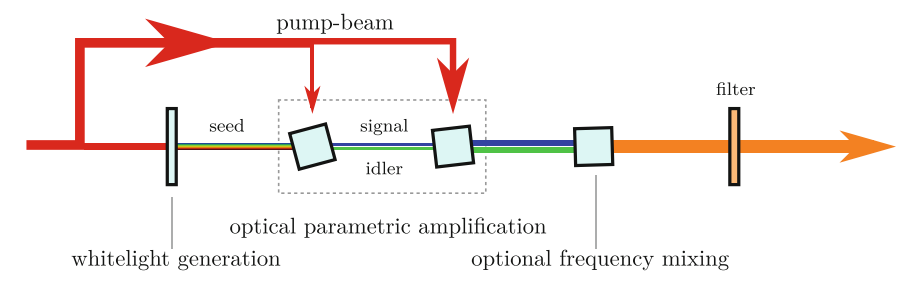


Fig. 2.8 Working principle of the OPA system: The pump beam is delivered by the femtosecond laser system. A small part of the beam creates a continuum of *white* light due to SPM in a sapphire plate. Any frequency generated can serve as seed for an DFG process in a nonlinear crystal. Here, the energy of one pump photon is used for the amplification of the seed beam and additional generation of an idler photon. The signal beam is further amplified in a second OPA stage, again producing an additional strong idler beam. Subsequent frequency doubling (SHG) or mixing (SFG, DFG) of residual pump, signal and idler beam is optionally possible. A filter finally removes the undesired frequencies before the pulses are guided to the experiment

e.g. a sapphire plate. A desired wavelength of this continuum may be used together with radiation of the initial wavelength of 790 nm for a DFG process in a nonlinear crystal. Since energy conservation has to be fulfilled, the chosen wavelength has to be larger than 790 nm. In this context it is convenient to refer to the different beams coupled into the crystal as *seed* and *pump* beam, respectively, see Fig. 2.8. A part of the energy of one photon from the pump beam is used for amplification of the seed beam by stimulated emission. In addition, a second photon of a different wavelength is formed using the remaining energy. The process may also be carried out in a two-step amplification scheme involving two nonlinear crystals, representing a pre- and a power amplifier. Hence, a *signal* and *idler* beam are generated where one is the amplified seed. In the following—as commonly defined—the signal represents the beam with the higher photon energy.

By rotation of the nonlinear crystal and thereby achieving phase matching for a particular combination of signal and idler wavelengths, the carrier frequency of the generated pulses can be controlled over a large range. After the OPA, pulses with three different carrier frequencies are usually available: The remaining part of the pump beam delivered by the laser as well as the signal and the idler beam. Subsequent frequency doubling or mixing by SHG, SFG or DFG may be used and extends the region of accessible wavelengths.

In the experiment a commercial *Light Conversion* "TOPAS-C" OPA system is used containing two OPA amplification stages and subsequent optional frequency doubling (SHG) or mixing (SFG, DFG) [26]. Downstream filters containing highly reflective mirrors for the desired wavelength ensure sufficient suppression of other radiation. The polarization of the emitted radiation depends on the generation mechanism and is either horizontal or vertical after the OPA. Two different periscopes are used to guide the beam to the REMI such that the polarization is finally aligned along the spectrometer axis in either case as shown in Fig. 4.1.

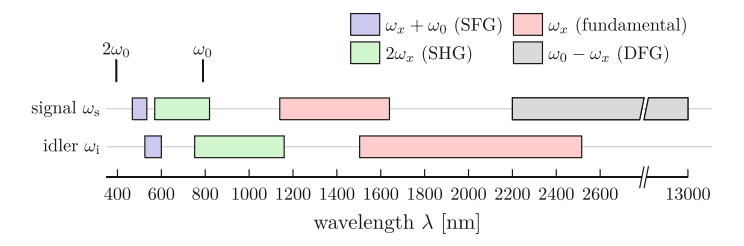


Fig. 2.9 Wavelengths accessible with the OPA system for pump wavelength of $\omega_0=790\,\mathrm{nm}$. Different production schemes deliver wavelengths over the full visible to infrared spectrum (ranges according to "WinTOPAS 3.0.12" control software delivered with the system). In addition, the harmonic frequency $2\omega_0$ is shown accessible by SHG of ω_0

Figure 2.9 gives an overview about the different production mechanisms made available by the OPA and the accessible wavelengths. It is noteworthy that—in principle—the full range from around 470 nm to around 13000 nm can be accessed. However, due to strongly deviating efficiencies of the different processes, strong-field experiments are restricted to a region below approximately 1600 nm. Before entering the OPA, the spectrum of the femtosecond laser system is slightly narrowed to a width of about 30 nm around the central wavelength in order to facilitate the overall phase matching. The signal and idler pulses are expected to have a duration of 0.7-1 times the duration of the pump pulses [27]. Thus, the pulse duration can be roughly estimated to be at least about 20 fs or longer.

References

- P. Baum et al., Zero-additional-phase SPIDER: full characterization of visible and sub-20-fs ultraviolet pulses. Opt. Lett. 29, 210–212 (2004). doi:10.1364/OL.29.000210
- G.D. Boyd, J.P. Gordon, Confocal multimode resonator for millimeter through opticalwavelength masers. Bell Syst. Tech. J. 40, 489–508 (1961). doi:10.1002/j.1538-7305.1961. tb01626.x
- G.D. Boyd, H. Kogelnik, Generalized confocal resonator theory. Bell Syst. Tech. J. 41, 1347– 1369 (1962). doi:10.1002/j.1538-7305.1962.tb03281.x
- 4. R.W. Boyd, Nonlinear Optics (Academic Press, Boston, 2003)
- T. Brabec, F. Krausz, Intense few-cycle laser fields: frontiers of nonlinear optics. Rev. Mod. Phys. 72, 545–591 (2000). doi:10.1103/RevModPhys.72.545
- 6. I.N. Bronstein et al., Taschenbuch der Mathematik (Europa-Lehrmittel, 2005)
- G. Cerullo, S. De Silvestri, Ultrafast optical parametric amplifiers. Review of Scientific Instruments 74, 1–18 (2003). doi:10.1063/1.1523642
- 8. W. Demtröder, Laser Spectroscopy (Springer, Berlin, 2003)
- 9. W. Demtröder, Experimentalphysik 2: Elektriziät und Optik (Springer-Verlag, Berlin Heidelberg New York, 2004)
- 10. J.C. Diels, W. Rudolph, Ultrashort Laser Pulse Phenomena (Academic Press, Boston, 2006)
- J. Eichler, H.J. Eichler, Laser—Bauformen, Strahlführung, Anwendungen (Springer, New York, 2010)
- 12. R. Ell et al., Generation of 5-fs pulses and octave-spanning spectra directly from a Ti:sapphire laser. Opt. Lett. 26, 373–375 (2001). doi:10.1364/OL.26.000373

- T. Ergler, Zeitaufgelöste Untersuchungen zur Fragmentationsdynamik von H₂ (D₂) in ultrakurzen Laserpulsen. Ph.D. thesis. Ruperto-Carola University of Heidelberg, Germany. URN: urn:nbn:de:bsz:16-heidok-67240 (2006)
- User's manual for Mirror-dispersion-controlled Ti:Sapphire Oscillator FEMTOSOURCE Rainbow seed. FEMTOLASERS Produktions GmbH (2006)
- FEMTOPOWER compact pro CE-PHASE HP/HR Femtosecond Multi-pass Amplifier USER'S MANUAL v. 3.2. FEMTOLASERS Produktions GmbH
- B. Fischer, Time resolved studies of H₂⁺ dissociation with phase-stabilized laser pulses. Ph.D. thesis. Ruperto-Carola University of Heidelberg, Germany. URN: urn:nbn:de:bsz:16-heidok-107569 (2010)
- C. Hofrichter, A stereo electron spectrometer for carrier-envelope phase measurements of fewcycle laser pulses, MA thesis. Ruperto-Carola University of Heidelberg, Germany (2009)
- 18. U. Keller, Ultrafast solid-state laser oscillators: a success story for the last 20 years with no end in sight. Appl. Phys. B: Lasers Opt. 100, 15–28 (2010). doi:10.1007/s00340-010-4045-3
- 19. U. Keller et al., Femtosecond pulses from a continuously self-starting passively mode-locked Ti:sapphire laser. Opt. Lett. 16, 1022–1024 (1991). doi:10.1364/OL.16.001022
- Ursula Keller et al., Semiconductor saturable absorber mirrors (SESAM's) for femtosecond to nanosecond pulse generation in solid-state lasers. IEEE J. Sel. Top. Quantum Electron. 2, 435–453 (1996). doi:10.1109/2944.571743
- 21. Fritz Kurt Kneubühl and Markus Werner Sigrist. Laser. Vierweg + Teubner (2008)
- 22. F. Krausz et al. (ed.), Ultrafast Optics IV (Springer, LLC, New York, 2004)
- M. Kremer, Einfluß der Träger-Einhüllenden-Phase auf die Wechselwirkung ultrakurzer Laserpulse mit Molekülen, Ph.D. thesis. Ruperto-Carola University of Heidelberg, Germany. URN: urn:nbn:de:bsz:16-heidok-100544 (2009)
- A. Krupp, Untersuchung der Pulsdauer und Langzeitstabilisierung eines Hohlfaserkompressors, BA thesis. Ruperto-Carola University of Heidelberg, Germany (2011)
- M. Lenzner et al., Sub-20-fs, kilohertz-repetition-rate Ti:sapphire amplifier. Opt. Lett. 20, 1397–1399 (1995). doi:10.1364/OL.20.001397
- TOPAS-C, Traveling-wave Optical Parametric Amplifier of Superfluorescence, User's Manual. Light Conversion Ltd. (2006)
- TOPAS-C specification sheet. http://www.lightcon.com/upload/iblock/a86/a86f4da6ccbf3c
 724a18148a8cc852a3.pdf, Accessed 22 July 2014. Light Conversion Ltd. (2014)
- 28. A. Mokhtari et al., Direct femtosecond mapping of trajectories in a chemical reaction. Nature **348**, 225–227 (1990). doi:10.1038/348225a0
- 29. G.G. Paulus et al., Absolute-phase phenomena in photoionization with few-cycle laser pulses. Nature **414**, 182–184 (2001). doi:10.1038/35102520
- J.H. Posthumus, The dynamics of small molecules in intense laser fields. Rep. Progr. Phys. 67, 623–665 (2004). doi:10.1088/0034-4885/67/5/R01
- J.H. Posthumus, J.F. McCann, Diatomic molecules in intense laser fields. In: *Molecules and Clusters in Intense Laser Fields*, ed. by J. Posthumus (Cambridge University Press, Cambridge, 2001). Chap. 2, pp. 27–77
- 32. T. Rathje et al., Review of attosecond resolved measurement and control via carrier-envelope phase tagging with above-threshold ionization. J. Phys. B: Atom. Mol. Opt. Phys. **45**, 074003 (2012). doi:10.1088/0953-4075/45/7/074003
- 33. S. Sartania et al., Generation of 0.1-TW 5-fs optical pulses at a 1-kHz repetition rate. Opt. Lett. **22**, 1562–1564 (1997). doi:10.1364/OL.22.001562
- 34. A.M. Sayler et al., Real-time pulse length measurement of few-cycle laser pulses using above-threshold ionization. Opt. Exp. 19, 4464–4471 (2011). doi:10.1364/OE.19.004464
- 35. A.S. Siegmann, Lasers (University Science Books, USA, 1986)
- Ch. Spielmann et al., Compact, high-throughput expansion-compression scheme for chirped pulse amplification in the 10 fs range. Opt. Commun. 120, 321–324 (1995). doi:10.1016/0030-4018(95)00494-S
- A. Stingl et al., Sub-10-fs mirror-dispersion-controlled Ti:sapphire laser. Opt. Lett. 20, 602–604 (1995). doi:10.1364/OL.20.000602

References 27

38. Albert Stolow et al., Femtosecond time-resolved photoelectron spectroscopy. Chem. Rev. **104**, 1719–1758 (2004). doi:10.1021/cr020683w

- 39. Donna Strickland, Gerard Mourou, Compression of amplified chirped optical pulses. Opt. Commun. **56**, 219–221 (1985). doi:10.1016/0030-4018(85)90120-8
- 40. O. Svelto, in *Principles of Lasers*, ed. by David C. Hanna. (Plenum Press, New York, 1998)
- 41. R. Szipöcs et al., Chirped multilayer coatings for broadband dispersion control in femtosecond lasers. Opt. Lett. **19**, 201–203 (1994). doi:10.1364/OL.19.000201
- 42. T. Wittmann et al., Single-shot carrier-envelope phase measurement of few-cycle laser pulses. Nat. Phys. **5**, 357–362 (2009). doi:10.1038/nphys1250

Chapter 3 Ionization in Strong, Ultrashort Laser Pulses

With the invention of the laser in 1960 [65] and the rapid development of the new techniques in the following decades, extremely strong alternating electric fields became available. For the first time, electrons in atoms and molecules could be exposed to fields in the same order of magnitude as the ones binding them to the nuclei. In this section, the basic theories developed in the last decades describing atoms and molecules in strong laser fields are briefly summarized. Section 3.1 treats the common classification of strong-field ionization processes by the definition of two regimes characterized by the *Keldysh parameter: Multiphoton ionization* and *tunnel ionization*. Section 3.2 gives a short overview about the standard theory used to describe the latter in terms of ADK^1 -theory. Then, in Sect. 3.4, the role of excited states in ionization and excitation processes is discussed followed by a compilation of different mechanisms leading to atomic stabilization—or ionization suppression—of atoms and molecules in strong laser fields. Finally, the interaction of molecular hydrogen with a strong laser field is treated in Sect. 3.5.

3.1 Multiphoton and Tunnel Ionization: The Keldysh Parameter

The treatment of the interaction of electromagnetic fields with atoms or molecules is often possible in terms of lowest order (time-dependent) perturbation theory, see e.g. [58, Chap. VI], [70]. Such a description requires the external fields acting on the particle to be sufficiently small compared to the atomic fields. In case of the hydrogen atom, the latter is simply calculated from the definition of the system of atomic units to be in the order of 10^{11} V/m, see Appendix A.1. A typical value for atoms is in general 10^9 V/m [52]. These values exceed the typical field strengths conventionally available in laboratories by orders of magnitude thus perturbation theory is

¹Ammosov-Delone-Krainov.

[©] Springer International Publishing Switzerland 2016

widely applicable to a manifold of experiments and effects. The ionization of atoms by weak electromagnetic radiation is another example, where perturbation theory is well applicable in terms of *Fermi's golden rule*, see e.g. [21, Sect. I.B.2]. However, ultrashort laser pulses provide electric fields which typically are in the same order of magnitude or even exceed the atomic fields. At an intensity of 10^{15} W/cm² for example, commonly available from modern table-top laser systems, the associated electric field strength is about 10^7 V/m. A description within the framework of perturbation theory is not possible any more and different methods have to be applied.

Typically, in strong-field laser-ionization of atoms and molecules, the ionization potential E_i is large compared to the photon energy delivered by the laser system, $E_i \gg \omega_0$.² Single-photon ionization of the system thus is simply forbidden energetically.³ The ionization processes taking place in this situation fundamentally depend on both the intensity and the wavelength: As it was shown in [52] mainly two ionization mechanisms are possible, commonly known as *tunnel ionization* and *multiphoton ionization* (MPI), see e.g. [34], each dominating in its "regime" separated from each other by the *Keldysh (adiabaticity) parameter* given by

$$\gamma = \omega_0 \sqrt{\frac{2E_i}{I}}. (3.1)$$

In this expression, I denotes the laser intensity. The processes underlying the ionization are fundamentally different in the multiphoton regime ($\gamma \gg 1$) compared to the tunneling regime ($\gamma \ll 1$). For example, expressions for the ionization probability derived in [52] for $\gamma \ll 1$ and $\gamma \gg 1$ are significantly diverse. In addition the question arises, how systems behave in the "intermediate" regime with $\gamma \approx 1$. Due to the typical parameters of real laser systems widely used in experiments, this question is far from being a theoretical problem: Fig. 3.1 shows the Keldysh parameters which can be computed using Eq. (3.1) and atomic data from Table A.2 for an argon atom exposed to typical laser radiation, cf. Sect. 2.2. In fact, typical strong-field experiments are carried out around $\gamma \approx 1$ where both mechanisms can be expected to perform comparably well (or badly). For example, the adiabatic treatment of the usually slowly varying laser field in the tunneling regime breaks down and non-adiabatic effects have to be considered, see e.g. [6, 47]. However, the question, up to which Keldysh parameter adiabatic models perform well, is still heavily debated, compare e.g. [11] with [49]. It also has to be noted that the description of the phenomena by only one dimensionless parameter might not be sufficient: While $\gamma \to 0$ can according to Eq. (3.1) be realized either with $I \to \infty$ or with $\omega_0 \to 0$, the physical processes caused by respective radiation clearly differ, hence at least two dimensionless parameters are required for a characterization [82, 83].

²Atomic units a.u. with $\hbar = e = m_e = 1$ are used if not stated otherwise, see Appendix A.1.

³Such processes are possible and investigated at synchrotron and free-electron laser (FEL) facilities or with table-top high harmonic generation (HHG) techniques, where sufficiently high photon energies can be provided, see e.g. [88], [84] and [2], respectively.

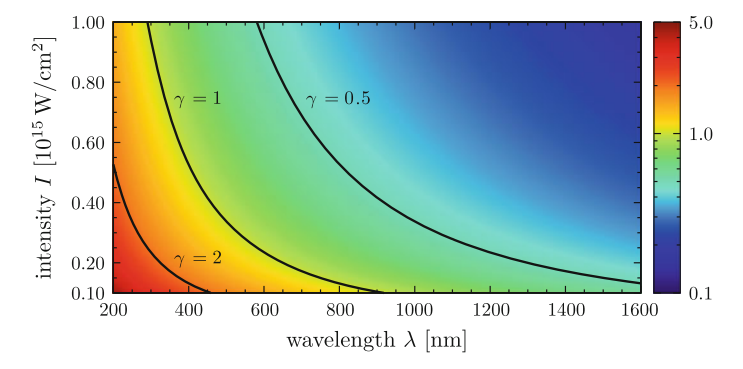


Fig. 3.1 Keldysh parameter for argon as a function of wavelength and intensity. For typical wavelengths and intensities commonly accessible in experiments γ is around 1. Ionization thus often takes place neither in the "deep tunneling" nor in the pure multiphoton regime

Considering the cycle averaged kinetic energy of a free electron in a laser field, the classical *ponderomotive energy* $U_{\rm p}=I/4\omega_0^2$, the expression Eq. (3.1) can be rewritten as

$$\gamma = \sqrt{\frac{E_{\rm i}}{2U_{\rm p}}},\tag{3.2}$$

see e.g. [9], showing an exclusive dependence of γ on the ratio between the binding energy and the energy of the freed electron in the laser field. Figure 3.2 depicts schematically the two different ionization mechanisms often referred to as "vertical" (multiphoton) and "horizontal" (tunneling) channels, see e.g. [50]: In the first, the electron is excited by a subsequent absorption of several photons and thus experiences an excitation along the (vertical) energy axis, see Fig. 3.2a. In contrast, tunnel ionization frees the electron by an extensive, varying modification of the binding potential, see Fig. 3.2b: Due to the comparable strength of the laser and the atomic field, the combined potential is lowered to a large extend such that the bound electron can tunnel through the barrier and therefore moves along a "horizontal" trajectory. The energy of the electron is then changed within the subsequent motion in the laser field, see e.g. [24]. This motion and in particular the possibility for the electron to recollide with its parent ion gives rise to interesting phenomena, see Sect. 3.3.1. For completeness it should be mentioned that for too strong fields the tunnel ionization turns into a third possible mechanism, the over-the-barrier ionization, see e.g. [13]: The barrier is lowered to a very large extent which allows the electron to simply leave the atom horizontally "above" the barrier.

As mentioned in [79], the accessible values for γ are limited towards both sides if in an experiment the laser frequency is fixed and only the intensity is varied: According to Eq. (3.1), a large γ requires very low intensities which causes low count rates and thus poor statistics or simply does not allow the process of interest to take place. In the opposite direction, towards small values for γ , where very high

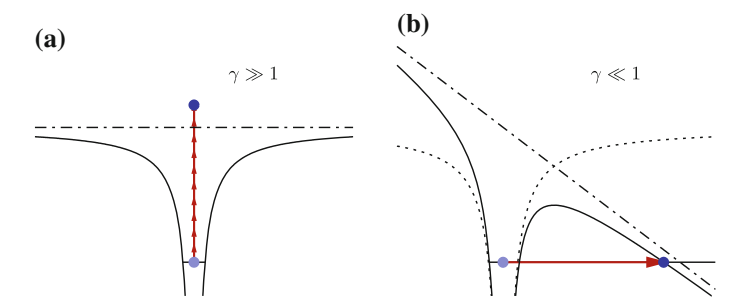


Fig. 3.2 Schematic representation of the different ionization mechanisms as found in many references, e.g. [13, 81]. **a** Multiphoton ionization along the "vertical" channel by simultaneous absorption of several photons. **b** Tunneling ionization of an electron through the "horizontal" channel by laser-induced modification of the attractive Coulomb potential

intensities are needed, saturation effects become distracting: A significant or even dominating part of the atoms may be ionized with an intensity considerably lower than the desired intensity either in the outer spatial regions of the laser focus, see Sect. 2.1.3, or already in the (temporal) leading edge of the pulses. For this reason, as will be shown in Chaps. 6 and 7, a transition from the multiphoton to the tunneling regime can be performed more conveniently in an experiment by variation of the wavelength.

The treatment of ionization in the multiphoton regime is closely related to lowest order perturbation theory of the interaction between atoms and light, see e.g. [41]. One prediction of such calculations is the characteristic dependence of the cross-section—or ion yield—on the intensity, see e.g. [41],

$$\Gamma \sim I^n,$$
 (3.3)

were n is the number of photons absorbed. As mentioned in [41], most experimental results indicate the perturbative approach to be inappropriate and in particular a dependence as predicted by Eq. (3.3) could only be observed for fairly low laser intensities [32, 57, 63].

3.2 Standard Tunneling Theory: The ADK Theory

Based on the work of Keldysh, a lot of theoretical work was performed in order to understand the tunnel ionization of atoms and molecules in strong laser fields, see e.g. [26, 27, 78] for a review and a historical overview. In the following, the most fundamental and relevant conclusions will be briefly summarized. The standard equations used to describe tunnel ionization are most often referred to as *ADK theory*, named after the authors Ammosov, Delone and Krainov of [3]. However, it has to be noted that very similar results had been published decades before, in [67, 68, 73–75], see also [78, Appendix 13.3] for further details on the relation between the

equations in these publications and those known as "ADK theory". Nevertheless, due to its prevalence in literature, the expression "ADK theory" is used along with the associated equations in the following.

The ionization rate in the tunneling regime depends fundamentally different on the intensity as it is the case in the multiphoton regime given by Eq. (3.3). For linearly polarized light and not too strong fields the rate of ionization from an atomic state characterized by the main quantum number n, the angular quantum number l and the magnetic quantum number m can (provided $l \ll n$ and $n \gg 1$) be expressed as [3]

$$\Gamma = \sqrt{\frac{3Fn^{*3}}{\pi Z^{3}}} \frac{Z^{2}}{4\pi n^{*3}} \left(\frac{2e}{n^{*}}\right)^{2n^{*}} \frac{(2l+1)(l+|m|)!}{2^{|m|}(|m|)!(l-|m|)!} \times \left(\frac{2Z^{3}}{Fn^{*3}}\right)^{2n^{*}-|m|-1} \exp\left[-\frac{2Z^{3}}{3n^{*3}F}\right], \tag{3.4}$$

where $F = \sqrt{I}$ is the strength of the laser field and $n^* = Z/\sqrt{2E_i}$ the effective main quantum number, considering the situation in complex atoms $(n^* = n$ for atomic hydrogen). In particular, for l = 1 follows [3]

$$\frac{\Gamma_{m=0}}{\Gamma_{|m|=1}} = \frac{2Z^3}{Fn^{*3}} = \frac{2}{F} (2E_i)^{3/2} \gg 1.$$
 (3.5)

The tunneling process thus heavily favors ionization of electrons from the m=0 orbital which will become important for the experiment and model presented in Chap. 5.

The photoelectron momentum distribution can be written as [26, 27]

$$\Gamma(p_{\parallel}, p_{\perp}) \propto \exp\left[-\frac{\omega_0^2 (2E_{\rm i})^{3/2}}{3F^3} p_{\parallel}^2\right] \exp\left[-\frac{(2E_{\rm i})^{1/2}}{F} p_{\perp}^2\right],$$
 (3.6)

where p_{\parallel} denotes the momentum component in the direction of the laser polarization and p_{\perp} the component perpendicular to this direction. The three-dimensional distribution which can be obtained is therefore of Gaussian shape with different widths parallel and perpendicular to the polarization of the laser. Particularly interesting is the component p_{\perp} since, in this direction, the electrons are not accelerated by the laser.

3.3 Quasi-free Electrons in Strong Laser Fields

As already seen in Sect. 3.1, electrons gain no energy "during" the tunneling process and therefore undergo a "horizontal" ionization scheme. In fact, the electron velocity in the direction of the laser polarization is often assumed to be exactly zero in the moment right after the tunneling process, see e.g. [8, 12, 23, 29, 62, 71]. The electrons'

energy then matches the potential energy curve, see Fig. 3.2. However, alternative assumptions also exist as e.g. the presence of a certain momentum distribution of finite width [48, 76] and even a dependence of the respective distribution on the bound state [50]. However, after the tunneling, the electron is able to gain energy from the laser field and finally escapes with a finite velocity. Of course, this process needs to fulfill both momentum and energy conservation. The first is the reason why the presence of the parent ion is mandatory and the process is not possible for an electron far away. The sum of the final momenta of electron and ion in the rest frame vanishes and the two observables are anticorrelated.

Despite the importance of the parent ion, its influence on the electron trajectory is often neglected in order to simplify the mathematical treatment. This assumption is based on the argument that the laser field dominates over the attractive Coulomb field in the relevant spatial regions which is known as *strong-field approximation* (SFA), see e.g. [9]. It is obvious that this assumption is in particular good far away from the ion and for very strong fields while it breaks down for weaker fields and electron trajectories sufficiently close to the nucleus. However, these trajectories are of special importance as will be briefly discussed in the following and—despite the preceding remarks—often are treated within the SFA. Detailed information about the topics may be found e.g. in [8, 9, 13, 34].

3.3.1 The Three-Step Model

After tunneling induced by a linearly polarized laser, the electron undergoes a sinusoidal quiver motion in the field with a mean kinetic energy of U_p and may either drift away from its parent ion or recollide with it. The phase of the laser in the moment of ionization is determining the subsequent trajectory of the electron which is utilized in "conventional" streaking experiments, e.g. [53], as well as the recently invented attoclock-technique [29, 30]. Assuming a vanishing initial momentum along the direction of the laser polarization, the electron momentum in this direction at a time t_1 can be written in the SFA as, see e.g. [8],

$$p(t_1) = \int_{t_0}^{t_1} dt E(t)$$

= $A(t_0) - A(t_1)$, (3.7)

where A(t) is the vector potential associated with the laser field by $E(t) = -\partial A(t)/\partial t$ and usually chosen such that $A(t \to \infty) \to 0$. In the moment of recollision t_c , the kinetic energy of the electron is therefore simply given by, see e.g. [8],

$$E_{\rm c}(t_{\rm c}) = \frac{p^2(t_{\rm c})}{2} = \frac{1}{2} \left[A(t_0) - A(t_{\rm c}) \right]^2.$$
 (3.8)

This expression is maximized to a value of about $3.17U_p$ for an ionization time of $t_c \approx 0.05T$ after a field maximum [23], where $T = 2 \pi/\omega_0$ is the periodicity of the laser field. If the electrons are back-scattered from the ion in the first recollision and accelerated further during the next period of the field, energies of up to $10U_p$ can be obtained [71].

The whole process of ionization and recollision can consequently be described as a sequence of three steps as proposed in [23] and schematically shown in Fig. 3.3c:

1st step: Tunnel ionization The electron is tunneling out of the atomic potential and appears outside with vanishing kinetic energy.

2nd step: Laser-driven classical motion The electron is accelerated in the field and gains kinetic energy.

3rd step: Recollision The electron recollides with its parent ion.

Since the first step of the sequence is obviously of quantum-nature while the others are treated purely classically, calculations within the three-step model are often called *semi-classical*, see e.g. [8]. The energy released in the last step depends in general on the trajectory of the individual electron and U_p , and is often large enough to initiate further ionization of the system in a *non-sequential double ionization* (NSDI) process, see e.g. [8, 9, 34]. If the energy is not sufficient for a direct second ionization, the atom may still be excited and subsequently ionized in the presence of the field, a process which is commonly called *recollision excitation with subsequent ionization* (RESI) [33], see Sect. 3.4.2. Also, high energetic radiation may be emitted which is utilized in *high harmonic generation* (HHG) techniques and the closely connected creation of attosecond pulses, see e.g. [2].

Figure 3.3 depicts possible scenarios for quasi-free electrons driven by the laser field after ionization. The electric field and the associated vector potential are shown in (a). The trajectories of three electrons, ionized at different phases of the laser field $(-\pi/8, 0 \text{ and } +\pi/8 \text{ with respect to an electric field maximum)}$ are exemplarily shown in (b). While the electron ionized before the maximum (red curve) is drifting away from the parent ion, the others recollide later. For the electron ionized exactly at the field maximum (green curve), the recollision energy calculates to zero with Eq. (3.8) since the vector potentials in the moment of tunneling and recollision are identical. The electron ionized after the field maximum (blue curve) is recolliding earlier and with a finite energy. The situation at four selected points in time, t_1 to t₄ marked in (b), is schematically depicted in (c). The lengths of the arrows are proportional to the electrons' instantaneous velocity and the temporal gradient of the field respectively. The electrons' positions are marked with dots in the same color code as in (b). Electrons not shown in the last two pictures already recollided with the parent ion. Note that t_4 resembles the situation exactly one laser period after t_1 . The electron subsequently undergoes the same acceleration again but starts already at a larger distance to the ion. Thus, while oscillating it drifts away from the parent ion.

In the first instance, the sum of the ionization potential and the ponderomotive potential $E_i + U_p$ has to be invested to free the electron, see e.g. [14]. However, the final electron energy is according to Eq. (3.7) independent of U_p and simply given

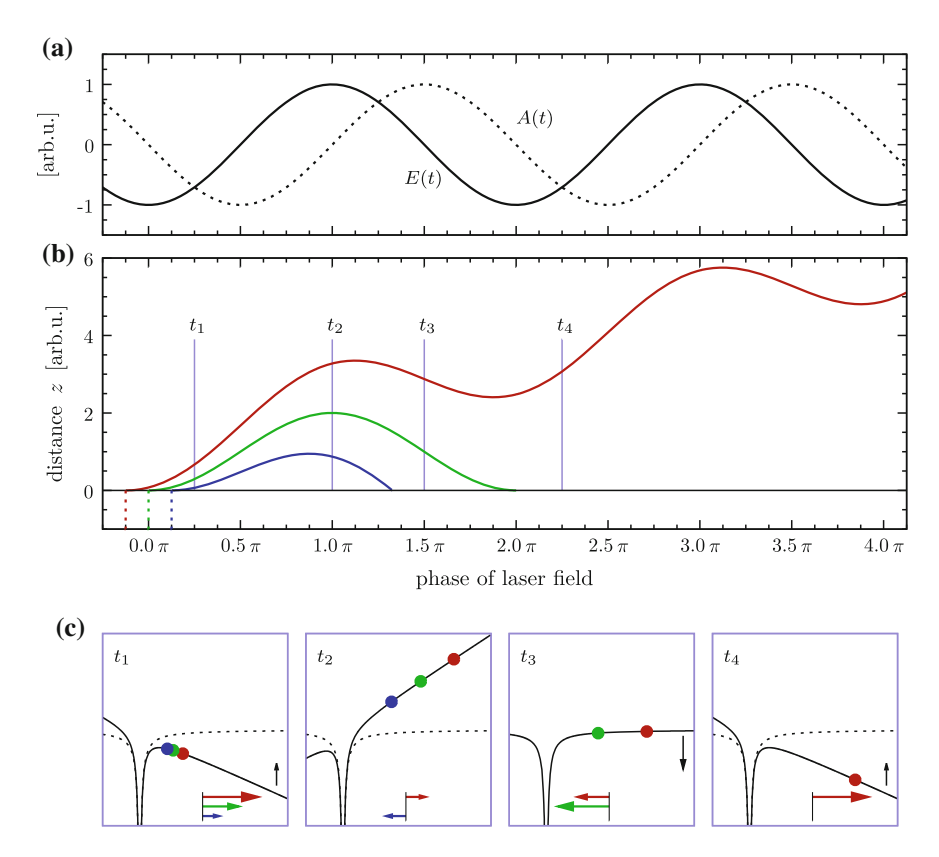


Fig. 3.3 Possible scenarios for quasi-free electrons driven by the laser field after ionization. **a** Electric field E(t) and associated vector potential A(t). **b** Trajectories for electrons ionized at three different phases of the laser electric field. **c** Schematic representation of the situations at four selected times t_1 to t_4 marked in (**b**). See text for detailed description

by the value of the vector potential in the moment of ionization $A(t_0)$. Indeed, this behavior could be experimentally confirmed and explained as follows [14, 39, 40]:

After being freed, the electron leaves the laser focus and enters a field-free environment. In the gradient of the intensity and the associated decrease of $U_{\rm p}$ experienced in this process, the quiver motion of the electron is transformed into a directed drift motion. This compensates for the initial loss of available kinetic energy due to the enhancement of the ionization potential. For pulse durations of about 1 ps and below, the situation is substantially different. Since there is not enough time for the electron to escape from the focus before the laser pulse is over, the final kinetic energy *does* depend on $U_{\rm p}$ [35, 40]. However, also for long pulses, the ponderomotive potential has an influence on the ionization process, as can be seen e.g. in a clear dependence of the photoelectron angular distributions on $U_{\rm p}$ [39].

3.3.2 Interference Structures in Electron Spectra

If experimental photoelectron momentum spectra are investigated, a simple Gaussian distribution as predicted by Eq. (3.6) is in fact barely observed. Instead, a manifold of different structures appear, some independent of wavelength or intensity, some changing position and shape with variation of these parameters. While the first class can usually be related to resonances in the atoms or molecules (see Sect. 3.4), the latter arises from quantum interference, a very general and important consequence of the quantum nature of the particles.

Interference effects may arise in general if a system can follow different paths transforming its initial state into a certain final state without revealing to any observer which path was taken. The most simple and prominent example is Young's doubleslit experiment, see e.g. [20, Sect. I.A.2], where the paths are in fact given by spatial trajectories. Emitted particles might go through any of the two slits and afterwards hit a screen where they are detected. Originally, the experiment was performed with photons but works in the same manner also for massive particles as electrons due to the wave-particle duality, see e.g. [20, Sect. I.A.2]. It is important to note that although the interference is spatially visible—it in fact appears in the momentum domain: Before the particles reach the slit, their momentum is much better known than their location. The slits confine the wave functions associated with the particles on a small spatial volume and at the same time blur the information about the particles' momentum due to the uncertainty principle, see e.g. [20, Sect. I.C.3]. Consequently the information about the direction of the momentum vector is lost, which results in waves emerging radially from each of the slits. These waves interfere and an interference pattern appears on the screen. As a summary, the spatial double-slit causes interference effects in the associated Fourier domain.

In case of strong-field ionization of atoms something similar may arise: In the SFA, as treated in the previous section, the final state, characterized by the electron momentum, is identical for electrons ionized at different times within the laser cycle: As can be derived from Eq. (3.7), all electrons ionized in the presence of the same vector potential $A(t_0)$ have the same final momentum. In Fig. 3.3a it can be easily seen that identical values for $A(t_0)$ are periodically found in subsequent cycles of the laser, and also within any of the cycles. In this sense, a temporal double-slit or—in the case of several laser periods contributing—a "grating" is created, see e.g. [4]. Thus, interference structures in the momentum domain can be observed, see e.g. [46, 61], which can be attributed to interference of electrons ionized in the same cycle (intracycle interference) or of electrons ionized in different cycles, separated in time by exactly one laser period (intercycle interference) [4]. In the case of infinitely long pulses the final electron momentum distribution can be written as [4]

$$W(\vec{p}) = 4\Gamma(\vec{p}) \underbrace{\cos^2\left(\frac{\Delta S}{2}\right)}_{F(\vec{p})} \underbrace{\left[\frac{\sin(N\tilde{S}/2)}{\sin(\tilde{S}/2)}\right]^2}_{B(p)},$$
(3.9)

where

$$\begin{split} \tilde{S} &= (2\pi/\omega_0) \left(E + U_{\rm p} + E_{\rm i} \right), \\ \Delta S &= - \left(2U_{\rm p}/\omega_0 \right) \left[\left(1 + 2|\tilde{\kappa}|^2 \right) {\rm sgn}(\kappa_z) \arccos \left({\rm sgn}(\kappa_z) \tilde{\kappa} \right) - \left(4\kappa_z - \tilde{\kappa} \right) \sqrt{1 - \tilde{\kappa}^2} \right], \\ \tilde{\kappa} &= \kappa_z + i \sqrt{\gamma^2 + \kappa_\rho^2} \quad \text{and} \quad \vec{\kappa} = \left(\kappa_\rho, \kappa_z \right) = \omega_0 \vec{p} / \sqrt{I}. \end{split}$$

In these expressions, γ denotes the Keldysh parameter as defined in Eq. (3.2) and $\Gamma(\vec{p})$ the momentum-resolved ionization rate given by Eq. (3.6) within the ADK model. The first interference factor in Eq. (3.9), $F(\vec{p})$, is caused by intracycle interference and the second, B(p), arises from intercycle interference of electron trajectories. The form of the latter resembles the commonly known equation describing interference effects caused by an ideal spatial grating with infinitely narrow slits, see e.g. [28, Sect. 10.5.3].

In Fig. 3.4a, Eq. (3.9) is plotted for a laser wavelength of 790 nm, an intensity of 3×10^{14} W/cm² and five optical cycles (of constant intensity), contributing to the intercycle interference. Figure 3.4b shows the distribution with neglected intercycle interference effects ($F(\vec{p}) \equiv 1$ in (3.9)). The intercycle interferences give rise to above-threshold ionization (ATI) structures, see e.g. [41], visible as rings separated by the ω_0 , the photon energy of the laser radiation. The electron absorbs more photons than needed for an ionization, modifying Eq. (3.10) to [40]

$$E = (n+s)\omega - E_i, \tag{3.10}$$

with $s \ge 0$ the integer number of additionally absorbed photons. A review about this topic can be found in [41].

However, in an experiment the situation is quite different. In contrast to the simulation, due to the characteristic intensity distribution in the laser focus (see Sect. 2.1.3), shot-to-shot fluctuations or long-term drifts of the laser system, a certain intensity distribution has to be assumed. The influence on the distributions is visualized in Fig. 3.4c, where a Gaussian intensity distribution with a relative width of only 5% is assumed around the intensity of 3×10^{14} W/cm² used in (a). 10^5 random intensities are considered and the calculated full momentum distributions, including again intercycle interference effects, are superimposed. Clearly the structure changes dramatically. The situation becomes even more complicated if—beyond SFA—the influence of the Coulomb field is considered as done in [4] by using both a more sophisticated model (CVA⁴) and solving the TDSE: Although the distributions change dramatically, the authors can show the robustness of the ATI rings' positions.

⁴Coulomb-Volkov approximation.

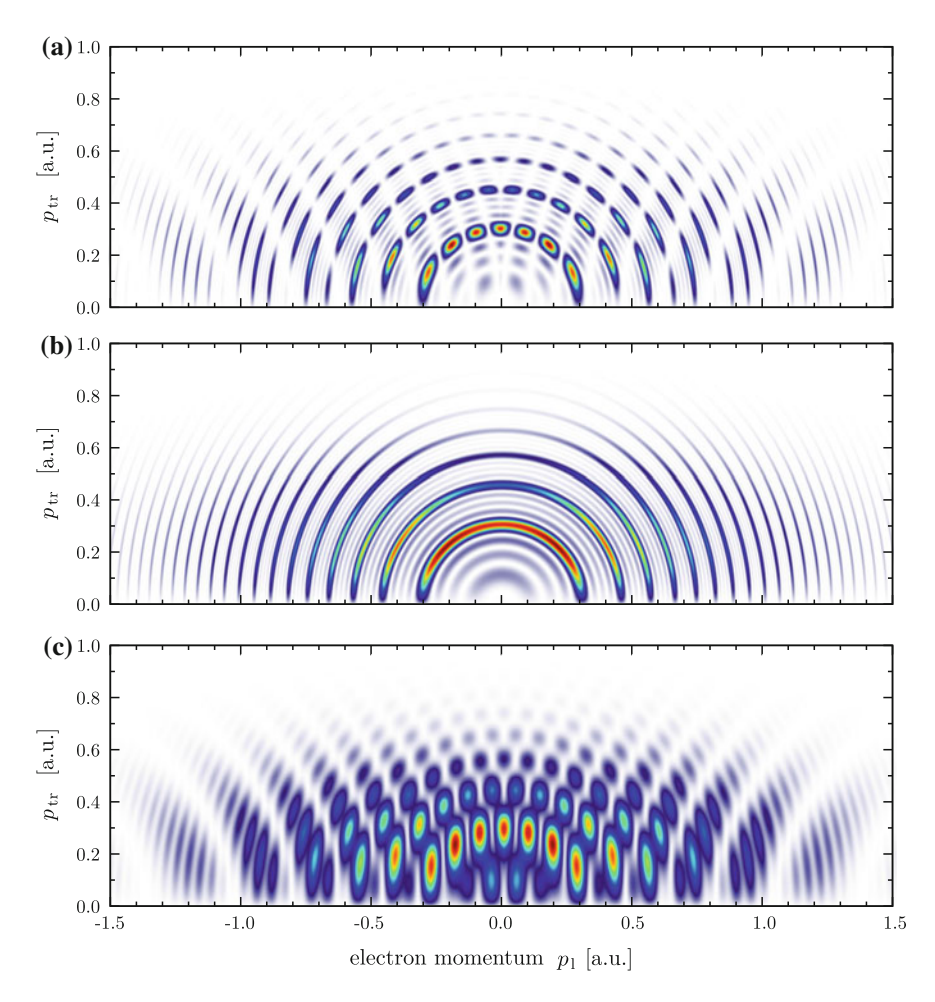


Fig. 3.4 Electron momentum distributions with interference structures. a Distribution calculated with (3.9) for ionization of argon with 790 nm radiation and an intensity of 3×10^{14} W/cm². Intracycle interference of five periods in the laser field is considered. b Same as for (a) but neglected intercycle interference effects. c Same as (a) but with a simple intensity averaging, see text for more details. The linear color scale used is displayed in Fig. A.1 (a)

3.4 The Role of Excited States

Although the equations presented in the last sections are commonly used and often yield satisfactory results, they in fact mostly disregard the inner structure of the atoms in terms of excited states. However, even the simplest atoms contain a large manifold of excited states which can be expected to play an important role in the interaction and to contribute to the ionization processes. Some aspects and their usual treatment will be discussed in the following sections.

3.4.1 Freeman Resonances

In the end of the last section, the appearance of ATI structures in the photoelectron spectra was discussed. As can be seen in Fig. 3.4, the distinct rings comprise no further structure. In the energy spectrum associated, each ring translates simply to a broad peak which is in agreement with early experimental findings [1], where laser pulses with a duration longer than 10 ns were used. However, if ultrashort pulses of about 1 ps or shorter are utilized for ionization, the appearance of a sub-structure in each of the peaks can be observed and be identified as arising from enhanced ionization caused by excited states [40]: Due to the strong AC-Stark shift associated with the extreme electric fields present in the pulse, excited states of the atom are shifted into resonance with an integer number of photons n' < n. Since the field strength smoothly in- and decreases before and after the pulse maximum, this holds usually for many states of different energies. It is the compensation of the ponderomotive momentum shift by the subsequent motion in the laser field (cf. Sect. 3.3.1) which suppresses the substructure in the final electron energy spectrum in the case of the longer pulses [40].

In general, the Stark shift of a certain atomic state is larger, the closer the unshifted state is situated below the continuum such that the energetic difference between the ground state and highly excites states is enlarged in the presence of the laser field, see e.g. [14]. For a deeply bound state with a binding energy E_i fulfilling $E_i \gg \omega_0$, the magnitude of this shift is given by [41]

$$U_{\rm p}' = U_{\rm p} \left(\frac{\omega_0}{E_{\rm i}}\right)^2 \approx 0. \tag{3.11}$$

While the atomic ground state is therefore hardly affected, excited states close to the threshold shift almost identical to the continuum such that the ionization potential for these stats essentially stays constant over the full laser pulse. As shown in [10], such a state may—after being efficiently populated in the specific moment of resonance—be ionized immediately or at any later time in the pulse resulting in practically the same final electron energy. As discussed in Sect. 3.4.3 the atom also may resist the ionization completely and "survive" the laser pulse.

3.4.2 RESI

As discussed in Sect. 3.3, electrons freed at certain phases of the oscillating laser field will gain energy and return to their parent ion where they recollide. As discussed in Sect. 3.3.1 energies of up to $3.17U_p$ can be released. In contrast, electrons freed very close to a field maximum recollide with relatively low kinetic energies such that NSDI is energetically forbidden. Nevertheless, excitation of the parent ion may still be possible resulting in a (doubly) excited atom. Due to the lowered ionization

potential of the system, the laser pulse still present may easily cause ionization which is called *recollision excitation with subsequent ionization* (RESI) [33]. The dynamics of a *doubly excited* (*Coulomb*) *complex* (DEC) formed as a transition state in a RESI process was recently investigated using the laser system and the REMI also used in this work [17].

3.4.3 Population and Stabilization of Excited States

The appearance of Freeman resonance as described above already shows the possibility of Rydberg states being populated within short laser pulses. In case of the ionization and formation of the characteristic structures in the photoelectron energy spectrum, the population of these states provides a first step in the ionization scheme, effectively lowering the ionization potential of the atom and enhancing the ionization probability. Apart from the possibility of direct ionization of the excited atoms in the same laser pulse, e.g. a different laser can be utilized to trigger this ionization [10], or the excited atoms may resist any further ionization with strong fields [10, 51]. In this case, the atom "survives" as neutral, excited species. In case of [51], the same laser pulse was used to first excite the atom and to afterwards ionize it. The loosely bound electron resists the ionization by a laser field which is strong enough to overcome the large excitation energy in the first place.

Frustrated Tunnel Ionization

The population of Rydberg states within a strong laser pulse has recently been embedded into the three three-step model [69]: Recolliding electrons with very low recollision energy may be recaptured by their parent ion, forming a Rydberg atom in the *frustrated tunneling ionization* (FTI). Consequently, a sharp dependence on the laser ellipticity, namely a strong decrease of the efficiency towards elliptical polarization, could be observed due to a lower probability for the electrons to revisit their parent ion [59]. As noted in [69], FTI might happen for a "substantial fraction" of the electrons and thus could be one of the dominant processes described by the three-step-model, although widely unexplored in experiments due to the neutral species produced. The concept of FTI was also expanded to dissociation processes in molecules H₂ [66], and lately to the single ionization of noble gas dimers [91].

Strong-Field Stabilization

The investigation of stabilization effects in strong laser fields was mainly carried out theoretically in the first place and different stabilization mechanisms were proposed both for the interaction of atoms with intense laser fields in the range of 10^{15} W/cm², and the interaction with "super-intense" laser pulses of 10^{17} W/cm² and above [16]. The latter is omitted in the following since it has no relevance for the experiments carried out in this work, a more recent review can be found in [42].

For the experimentally accessible intensities, two different classes of stabilization processes were found, namely *interference stabilization* of Rydberg states involving different types of Raman-transitions via the continuum and *adiabatic* stabilization mechanisms, see [77] for a review. Recently, the survival of Rydberg states in strong laser fields has been investigated with a new experimental technique, allowing to directly measure the actual ionization intensity of the individual atoms and thus to rule out spatial and temporal variations [31]. In this work, the stability of the atoms was proven up to an intensity of more than 10^{15} W/cm² and the results interpreted using both solution of the full TDSE and a SAE⁵ approximation.

3.5 Molecular Hydrogen in Strong Laser Fields

The complexity of mechanisms taking place in the interaction of atoms with strong laser fields is evident from the discussions in the last section although within this thesis, only the main aspects can briefly be summarized. The situation gets even more complicated if—instead of atomic targets—molecules are exposed to the radiation. For example in H₂, the most simple neutral molecule, the presence of two nuclei causes an additional degree of freedom, the internuclear separation. Within the Born-Oppenheimer approximation, see e.g. [94, Sect. 2.2], this distance can be regarded as a parameter, "tuning" the energy-levels of the system: For each (fixed) internuclear distance R the associated Schrödinger equation can be solved numerically and the total energy of the system E(R), depending also on the electronic state of the system characterized by appropriate quantum numbers, can be calculated [54–56]. Single ionization of the hydrogen molecule leads—in the first instance—to H₂⁺, for which the same calculations have been performed [85]. The potential curves for the lowest electronic states are shown in Fig. 3.5. Double ionization of the H₂ produces two protons, which could—as long as their distance from each other is comparable to the internuclear distance of H₂⁺—be called H₂⁺⁺ "system". However, the repulsive Coulomb force between the protons leads to rapid Coulomb explosion, see e.g. [80, Sect. 2.5].

3.5.1 Ionization and Dissociation Channels

The dissociation of molecular hydrogen in strong laser fields was subject of a manifold of theoretical and experimental studies, see e.g. [45, 79] for reviews. Before a detailed picture about the strong-field induced processes in H_2 is given in Sect. 3.5.2, the basic different ionization and dissociation scenarios will be discussed considering only the few potential curves shown in Fig. 3.5. Neglecting pure excitation, the hydrogen molecule may be singly ionized in a $H_2 \longrightarrow H_2^+ + e^-$ process,

⁵Single-active-electron.

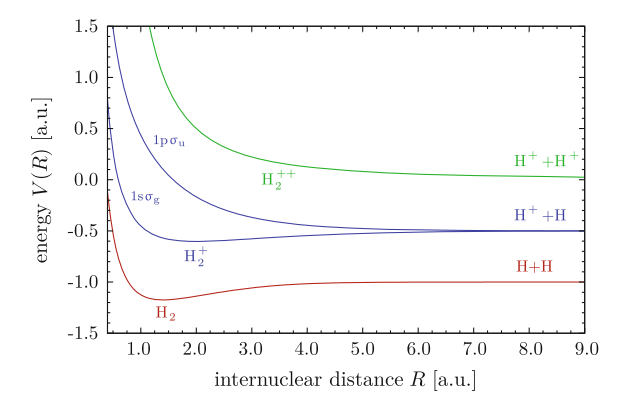


Fig. 3.5 Potential energy curves for the neutral and ionized hydrogen molecule. Data points for the H_2 and the H_2^+ potential curves can be found in [54] and [85], respectively. For the picture, a cubic interpolation between the points given in the reference was performed. The repulsive Coulomb force between the two protons determines the potential curve after double ionization of the H_2 molecule, see e.g. [80, Sect. 2.5]

leaving the molecular ion either in the *gerade*1s σ_g or the *ungerade*1p σ_u state. While the gerade state offers a molecular binding in several vibrational states [22], which are typically populated simultaneously in tunnel ionization [90], the ungerade state is purely repulsive and its population thus leads to the dissociation of the molecule $(H_2 \longrightarrow H_2^+ + e^- \longrightarrow H^+ + H + e^-)$, see e.g. [36, 43, 87]. Laser-induced transitions between the gerade and the ungerade states are also possible as will be described in Sect. 3.5.2.

Another possible channel is the double ionization of H_2 , although much more energy is needed. Such a process resulting in H_2^{++} subsequently dissociating, $H_2 \longrightarrow H_2^{++} + 2e^- \longrightarrow 2H^+ + 2e^-$, is commonly known as *Coulomb explosion* (CE) of the molecule, see e.g. [72]. These processes can in principle be distinguished from the dissociation of H_2^+ e.g. by the number of particles produced and the higher final kinetic energy of the protons, the kinetic energy release (KER) [60]. Moreover, the protons produced in the Coulomb explosion process are correlated in momentum which is visible e.g. in ion-ion covariance or coincidence mapping, see e.g. [38, 89], [25, Sect. 3.2]. In addition, the processes turn out to be very selective on the molecular orientation, usually favoring their parallel orientation with respect to the laser polarization, see e.g. [19, 45]. Therefore, the ions are dissociating along the spectrometer axis, see Sect. 4.1, and the different processes discussed and summarized in Table 3.1 can be identified already in the simple time-of-flight spectra recording the ionic products of H_2 after ionization, see e.g. [89]. Figure 3.6 exemplarily shows the respective part of a spectrum obtained with a wavelength of about 570 nm.

Process	Neutrals created	Ions created	KER	Electrons freed
Single ionization	_	H_2^+	_	1
Single ionization and dissociation	Н	H ⁺	Small	1
Double ionization and Coulomb explosion	_	2H ⁺	Large	2
- F				

Table 3.1 Possible ionization and dissociation scenarios starting from neutral H₂, see e.g. [89]

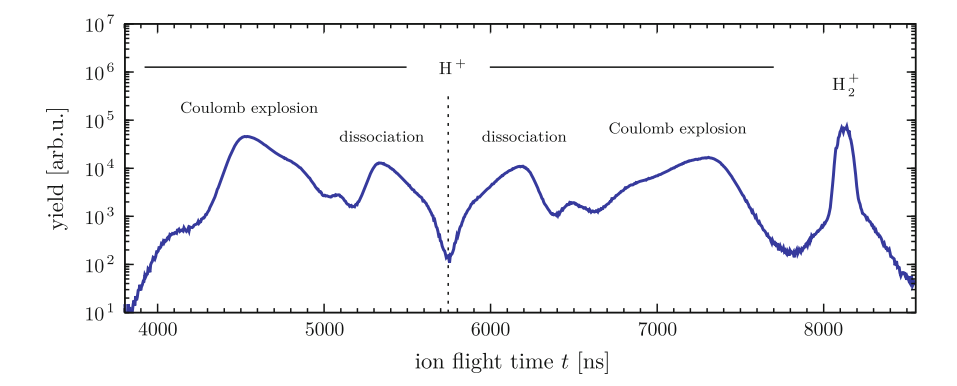


Fig. 3.6 Typical ion time-of-flight distribution in an experiment with H_2 at a central wavelength of about 570 nm. The individual peaks can be assigned to the processes listed in Table 3.1, see e.g. [89] for a similar picture and assignment: The dashed vertical line close to 5750 ns marks the flight time for a H^+ ion with vanishing initial momentum. Two pairs of peaks are visible distributed around this value, consisting of H^+ ions which gained momentum in a dissociative process and thus were accelerated either towards (smaller flight time) or away from the detector (larger flight time). The larger the time difference to the vertical line, the higher the KER of the underlying process. This allows the assignment of the peaks to the dissociation and the Coulomb explosion

3.5.2 The Floquet Picture

Although a description of the processes taking place in the interaction of strong laser fields with H₂ in the framework of the unperturbed molecular potential curves and vertical transitions in the Born-Oppenheimer approximation is possible to some extent, it is certainly not sufficient. Phenomena such as *molecular stabilization*, see Sect. 3.5.3, can not be explained. In fact, a more successful description is procurable in a picture, which treats the molecule and the laser field as one system, the *Floquet picture*, named after the *Floquet theorem* [37] exploited in the mathematical treatment [18]: New potential curves are calculated, resembling *dressed* states which only exist for the combined system of molecule and laser field. In the following, the concept is briefly summarized following the description in [72]. More detailed information also about other theoretical approaches can be found e.g. in [5, 45, 79, 80, 94].

If the Hamiltonian of an unperturbed, field-free molecule is denoted with $\hat{H}_0(\vec{r}, \vec{R}, t)$, the respective operator in presence of the laser field may be written in dipole approximation as [18]

$$\hat{H}(\vec{r}, \vec{R}, t) = \hat{H}_0(\vec{r}, \vec{R}) + \hat{\mu}(\vec{r}, \vec{R}) \cdot \vec{E}_0 \cos(\omega_0 t). \tag{3.12}$$

Here, \vec{r} and \vec{R} represent the coordinates of the electrons and nuclei, respectively, and $\hat{\mu}$ is the electric dipole operator. In case of H_2^+ , \vec{R} reduces to a scalar, namely the internuclear distance and \vec{r} describes the three coordinates of the remaining electron with respect to the center of mass of the two nuclei. The evolution of the molecule in the laser field can in principle be obtained by solving the respective TDSE, given by [18]

$$i\frac{\partial\Psi(\vec{r},\vec{R},t)}{\partial t} = \hat{H}(\vec{r},\vec{R},t)\Psi(\vec{r},\vec{R},t). \tag{3.13}$$

It can be shown that this problem is—due to the Hamiltonians' periodicity in time—equivalent to the solution of a different Schrödinger equation with a time-independent Floquet Hamiltonian $\hat{H}_F(R)$ represented by an infinite matrix [86]. In the case of Eq. (3.12) and for a unperturbed system containing two electronic states of energy $V_1(R)$ and $V_2(R)$, the Floquet Hamiltonian is given by [18]

$$\hat{H}_{F}(R) = \begin{pmatrix} \vdots & \vdots & \vdots & \vdots & \vdots & \vdots & \vdots \\ \dots & V_{1}(R) + 2\omega_{0} & \Lambda_{12}(R) & 0 & 0 & 0 & 0 & \dots \\ \dots & \Lambda_{21}(R) & V_{2}(R) + \omega_{0} & \Lambda_{12}(R) & 0 & 0 & 0 & \dots \\ \dots & 0 & \Lambda_{21}(R) & V_{1}(R) & \Lambda_{12}(R) & 0 & 0 & \dots \\ \dots & 0 & 0 & \Lambda_{21}(R) & V_{2}(R) - \omega_{0} & \Lambda_{12}(R) & 0 & \dots \\ \dots & 0 & 0 & 0 & \Lambda_{21}(R) & V_{1}(R) - 2\omega_{0} & \Lambda_{12}(R) & \dots \\ \dots & 0 & 0 & 0 & 0 & \Lambda_{21}(R) & V_{2}(R) - 3\omega_{0} & \dots \\ \vdots & \vdots & \vdots & \vdots & \vdots & \vdots & \ddots \end{pmatrix},$$

$$(3.14)$$

where $\Lambda_{ij}(R) = \vec{\mu}_{ij}(R) \cdot \vec{E}_0 \cos(\omega_0 t)/2$. The eigenvalues obtained by (numerical) diagonalization of $\hat{H}_F(R)$ form the new potential curves $\tilde{V}(R)$ for the combined system of molecule and laser field commonly referred to as *dressed* states, see e.g. [18]. In such calculations, only a finite number of matrix elements can be considered. Although it is in principle possible to calculate the results using only one diagonal Floquet block (shown in red in Eq. (3.14)), convergence is usually achieved only with larger matrices. However, modern desktop computers can perform this in seconds even for 100×100 matrices and larger. The Floquet method can be utilized if the field period is much shorter than the dissociation [79] and ideal for not too short pulses [64]. If these conditions are not fulfilled, other approaches like *wave-packet calculations* are more applicable, see e.g. [45, 64].

Within the simplified picture of the H_2^+ molecule discussed in the previous section, $V_1(R)$ and $V_2(R)$ can be identified with the attractive and repulsive $1 \text{s } \sigma_g$ and $1 \text{p } \sigma_u$ states, respectively, shown in Fig. 3.5. If only one Floquet block is considered, the dressed states can be derived analytically, see e.g. [72]:

$$\tilde{V}_{\pm}(R) = \frac{V_{\rm g}(R) + V_{\rm u}(R) - \omega_0}{2} \pm \frac{1}{2} \sqrt{\left[V_{\rm g}(R) - V_{\rm u}(R) + \omega_0\right]^2 + \omega_{\rm R}^2(R)}.$$
(3.15)

Here, $\Lambda_{ij}(R) = \Lambda_{ji}(R) = \omega_R(R)$ with ω_R being the Rabi frequency, was used. The latter is linked to the electric field by the dipole moment $\vec{d}(R)$ according to $\omega_R(R) = \vec{E_0}\vec{d}(R)$ [5, Sect. 3.1]. Although this expression is a very crude approximation due to the small Floquet Hamiltonian used, it shows the influence of the orientation of the molecule with respect to the laser polarization: A non-parallel alignment results simply in a smaller effective electric field $E'_0 = E_0 \cos(\theta)$ respectively in a lower intensity $I' = I \cos^2(\theta)$, hence a lower chance for the molecule to dissociate, see e.g. [94, Sect. 2.4].

Figure 3.7b shows the dressed states calculated within the Floquet picture and compares the situation to the model treating the molecule as unaffected by the field and the interaction with the laser as transitions between the potential curves as discussed in Sect. 3.5.1, Fig. 3.7a. For $\omega_R(R) \equiv 0$, the dressed curves cross each other at the internuclear separation where the energetic difference of the former unperturbed curves is resonant with the photon energy, see blue dashed line in (b). However, for high laser intensities, the curves couple and they do not intersect any more. Instead, at the internuclear distance of the former crossing R_0 , where $V_g(R_0) = V_u(R_0) - \omega_0$, Eq. (3.15) yields a separation of the dressed curves by $\omega_R(R_0)$, an avoided crossing. This is proportional to the square root of the laser intensity, see e.g. [72]. The transition between the states can be described in the Floquet picture by the evolution of the system along paths on the dressed potential curves where the probability for each path can be derived from Landau-Zener theory, see e.g. [93].

3.5.3 Bond Softening and Molecular Stabilization

With increasing laser intensity and likewise increasing separation between the \tilde{V}_{\pm} curves, molecules initially bound in vibrational states of the $1s\,\sigma_g$ state my dissociate. Although this is also evident in the picture of the unperturbed potential curves by considering the absorption of a photon, see Fig. 3.7a, a new aspect arises in the Floquet picture, namely a possible tunneling character of the process, see e.g. [43], [94, Sect. 2.4]. Ionization from a vibrational state is possible even if the remaining potential would classically forbid the process. This is commonly referred to as *bond softening*, see e.g. [15, 79, 93], [80, Sect. 2.4], [94, Sect. 2.4]. In some respects, the Floquet picture in Fig. 3.7b bears analogy to the common picture of tunnel

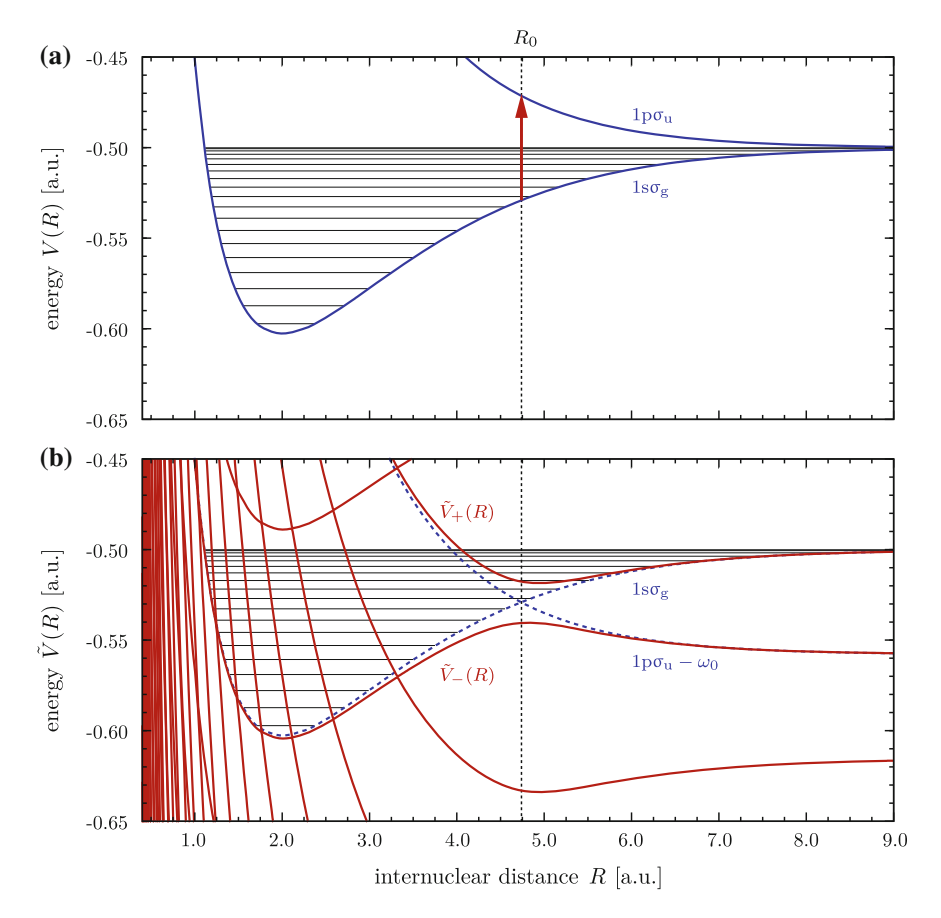


Fig. 3.7 Comparison of unperturbed and dressed potential curves, adapted from [72]. The data points of the unperturbed curves are generated from the points given in [85] by cubic interpolation, the vibrational energy levels for the $1 \text{s} \sigma_g$ state taken from [22]. **a** Unperturbed potential curves with laser-induced transition. The wavelength of the laser is 790 nm thus the resonance appears at an internuclear distance of $R = R_0 \approx 4.74$ a.u. **b** Dressed potential curves calculated for a laser intensity of 5×10^{14} W/cm² and the same wavelength as in (**a**) considering 201 Floquet blocks (a 402×402 Floquet matrix). The Rabi-frequencies $\omega_R(R)$ needed for the calculation are generated from data points given in [7] by cubic interpolation

ionization, see Fig. 3.2b. The counterpart, namely the treatment of unchanged potentials and photon-induced transitions is associated with the multiphoton picture, Figs. 3.7a and 3.2a.

Since some field-induced potential curves, e.g. \tilde{V}_+ in Fig. 3.7, exhibit a minimum, new bound states can be created by the presence of the laser, see e.g. [94, Sect. 2.4]. Population may occur due to resonance between field-free vibrational levels with this laser-induced states. The molecule is then "actively" stabilized by the laser and will not dissociate before the intensity drops. This is known as *molecular stabilization* or—in analogy to the effect described above—*bond hardening*, see e.g. [44, 92], [5, Sect. 3.8].

References

- P. Agostini et al., Free-free transitions following six-photon ionization of xenon atoms. Phys. Rev. Lett. 42, 1127–1130 (1979). doi:10.1103/PhysRevLett.42.1127
- P. Agostini, L.F. DiMauro, The physics of attosecond light pulses. Rep. Prog. Phys. 67, 813–855 (2004). doi:10.1088/0034-4885/67/6/R01
- 3. M.V. Ammosov et al., Tunnel ionization of complex atoms and of atomic ions in an alternating electromagnetic field. Sov. Phys. JETP **64**, 1191–1194 (1986)
- D.G. Arbó et al., Doubly differential diffraction at a time grating in above-threshold ionization: intracycle and intercycle interferences. Nucl. Instrum. Methods Phys. Res. Sect. B: Beam Interact. Mater. Atoms 279, 24–30 (2012). doi:10.1016/j.nimb.2011.10.030
- 5. A.D. Bandrauk et al., Theory of molecules in intense laser fields (Chap. 3), in *Molecules in Laser Fields*, ed. by A.D. Bandrauk (Macel Dekker Inc., New York, 1994), pp. 109–179
- I. Barth, O. Smirnova, Nonadiabatic tunneling in circularly polarized laser fields: physical picture and calculations, *Physical Review A: Atomic, Molecular, and Optical Physics*, vol. 84 (2011), 063415. doi:10.1103/PhysRevA.84.063415
- 7. D.R. Bates, The oscillator strength of H_2^+ , $1s\sigma 2p\sigma$. J. Chem. Phys. **19**, 1122–1124 (1951). doi:10.1063/1.1748487
- W. Becker, H. Rottke, Many-electron strong-field physics. Contemp. Phys. 49, 199–223 (2008). doi:10.1080/00107510802332908
- W. Becker et al., Theories of photoelectron correlation in laser-driven multiple atomic ionization. Rev. Mod. Phys. 84, 1011–1043 (2012). doi:10.1103/RevModPhys.84.1011
- M.P. de Boer, H.G. Muller, Observation of large populations in excited states after short-pulse multiphoton ionization. Phys. Rev. Lett. 68, 2747–2750 (1992). doi:10.1103/PhysRevLett.68. 2747
- 11. R. Boge et al., Probing nonadiabatic effects in strong-field tunnel ionization. Phys. Rev. Lett. 111, 103003 (2013). doi:10.1103/PhysRevLett.111.103003
- T. Brabec et al., Coulomb focusing in intense field atomic processes. Phys. Rev. A: Atomic Mol. Opt. Phys. 54, R2251–R2254 (1996). doi:10.1103/PhysRevA.54.R2551
- T. Brabec, F. Krausz, Intense few-cycle laser fields: frontiers of nonlinear optics. Rev. Mod. Phys. 72, 545–591 (2000). doi:10.1103/RevModPhys.72.545
- P.H. Bucksbaum et al., Role of the ponderomotive potential in above-threshold ionization. J. Opt. Soc. Am. B: Opt. Phys. 4, 760–764 (1987). doi:10.1364/JOSAB.4.000760
- P.H. Bucksbaum et al., Softening of the H⁺₂ molecular bond in intense laser fields. Phys. Rev. Lett. 64, 1883–1886 (1990). doi:10.1103/PhysRevLett.64.1883
- K. Burnett et al., Atoms in ultra-intense laser fields. J. Phys. B: At. Mol. Opt. Phys. 26, 561–598 (1993). doi:10.1088/0953-4075/26/4/003
- N. Camus et al., Attosecond correlated dynamics of two electrons passing through a transition state. Phys. Rev. Lett. 108, 073003 (2012). doi:10.1103/PhysRevLett.108.073003
- S.-I. Chu, Floquet theory and complex quasivibrational energy formalism for intense field molecular photodissociation. J. Chem. Phys. 75, 2215–2221 (1981). doi:10.1063/1.442334
- K. Codling et al., Multiphoton ionisation of H₂ and D₂ using an intense sub-picosecond laser.
 J. Phys. B: At. Mol. Opt. Phys. 21, L433–L438 (1988). doi:10.1088/0953-4075/21/15/003
- 20. C. Cohen-Tannoudji et al., Quantum Mechanics (Hermann and Wiley, New York, 1977)
- 21. C. Cohen-Tannoudji et al., Atom-Photon Interactions (Wiley, New York, 1998)
- S. Cohen et al., Vibrational States of the hydrogen molecular ion. Phys. Rev. 119, 1025–1027 (1960). doi:10.1103/PhysRev.119.1025
- P.B. Corkum, Plasma perspective on strong-field multiphoton ionization. Phys. Rev. Lett. 71, 1994–1997 (1993). doi:10.1103/PhysRevLett.71.1994
- P.B. Corkum et al., Above-threshold ionization in the long-wavelength limit. Phys. Rev. Lett. 62, 1259–1262 (1989). doi:10.1103/PhysRevLett.62.1259
- C. Cornaggia, Small polyatomic molecules in intense laser fields (Chap. 3), in *Molecules and Clusters in Intense Laser Fields*, ed. by J. Posthumus (Cambridge University Press, Cambridge, 2001), pp. 84–113

References 49

 N.B. Delone, V.P. Krainov, Tunneling and barrier-suppression ionization of atoms and ions in a laser radiation field. Physics-Uspekhi 41, 469–485 (1998). doi:10.1070/ PU1998v041n05ABEH000393

- 27. N.B. Delone, V.P. Krainov, Multiphoton Processes in Atoms (Springer, Berlin, 2000)
- 28. W. Demtröder, Experimentalphysik 2: Elektriziät und Optik (Springer, Berlin, 2004)
- 29. P. Eckle et al., Attosecond ionization and tunneling delay time measurements in helium. Science **322**, 1525–1529 (2008). doi:10.1126/science.1163439
- P. Eckle et al., Attosecond angular streaking. Nat. Phys. 4, 565–570 (2008). doi:10.1038/ nphys982
- 31. U. Eichmann et al., Observing Rydberg atoms to survive intense laser fields. Phys. Rev. Lett. 110, 203002 (2013), doi:10.1103/PhysRevLett.110.203002
- 32. F. Fabre et al., Multiphoton above-threshold ionisation of xenon at 0.53 and 1.06μm. J. Phys. B: At. Mol. Phys. **15**, 1353–1369 (1982). doi:10.1088/0022-3700/15/9/012
- B. Feuerstein et al., Separation of recollision mechanisms in nonsequential strong field double ionization of Ar: the role of excitation tunneling. Phys. Rev. Lett. 87, 043003 (2001). doi: 10.1103/PhysRevLett.87.043003
- C. Figueira de Morisson Faria, X. Liu, Electron-electron correlation in strong laser fields. J. Mod. Opt. 58, 1076–1131 (2011). doi:10.1080/09500340.2010.543958
- E. Fiordilino, M.H. Mittleman, Kinematics of multiphoton ionisation in a laser pulse. J. Phys. B: At. Mol. Phys. 18, 4425–4431 (1985). doi:10.1088/0022-3700/18/22/011
- B. Fischer, Time resolved studies of H₂⁺ dissociation with phase-stabilized laser pulses. Ph.D. thesis. Ruperto-Carola University of Heidelberg, Germany. URN: urn:nbn:de:bsz:16-heidok-107569 (2010)
- G. Floquet, Sur les équations différentielles linéaires à coefficients périodiques. Annales scientifiques de l'École Normale Supérieure 12, 47–88 (1883)
- L.J. Frasinski et al., Molecular H₂ in intense laser fields probed by electron-electron, electronion, and ion-ion covariance techniques. Phys. Rev. A: At. Mol. Opt. Phys. 46, R6789–R6792 (1992). doi:10.1103/PhysRevA.46.R6789
- R.R. Freeman et al., Pondermotive effects on angular distributions of photoelectrons. Phys. Rev. Lett. 57, 3156–3159 (1986). doi:10.1103/PhysRevLett.57.3156
- R.R. Freeman et al., Above-threshold ionization with subpicosecond laser pulses. Phys. Rev. Lett. 59, 1092–1095 (1987). doi:10.1103/PhysRevLett.59.1092
- R.R. Freeman, P.H. Bucksbaum, Investigations of above-threshold ionization using subpicosecond laser pulses. J. Phys. B: At. Mol. Opt. Phys. 24, 325 (1991). doi:10.1088/0953-4075/24/2/004
- 42. M. Gavrila, Atomic stabilization in superintense laser fields. J. Phys. B: At. Mol. Opt. Phys. 35, R147–R193 (2002). doi:10.1088/0953-4075/35/18/201
- A. Giusti-Suzor et al., Above-threshold dissociation of H⁺₂ in intense laser fields. Phys. Rev. Lett. 64, 515–518 (1990). doi:10.1103/PhysRevLett.64.515
- 44. A. Giusti-Suzor, F.H. Mies, Vibrational trapping and suppression of dissociation in intense laser fields. Phys. Rev. Lett. **68**, 3869–3872 (1992). doi:10.1103/PhysRevLett.68.3869
- A. Giusti-Suzor et al., Dynamics of H⁺₂ in intense laser fields. J. Phys. B: At. Mol. Opt. Phys. 28, 309–339 (1995). doi:10.1088/0953-4075/28/3/006
- R. Gopal et al., Three-dimensional momentum imaging of electron wave packet interference in few-cycle laser pulses. Phys. Rev. Lett. 103, 053001 (2009). doi:10.1103/PhysRevLett.103. 053001
- 47. T. Herath et al., Strong-field ionization rate depends on the sign of the magnetic quantum number. Phys. Rev. Lett. **109**, 043004 (2012). doi:10.1103/PhysRevLett.109.043004
- 48. C. Hofmann et al., Comparison of different approaches to the longitudinal momentum spread after tunnel ionization. J. Phys. B: At. Mol. Opt. Phys. 46, 125601 (2013). doi:10.1088/0953-4075/46/12/125601
- I.A. Ivanov, A.S. Kheifets, Strong-field ionization of He by elliptically polarized light in attoclock configuration. Phys. Rev. A: At. Mol. Opt. Phys. 89, 021402(R) (2014). doi:10.1103/PhysRevA.89.021402

- R.R. Jones et al., Anatomy of strong field ionization. J. Mod. Opt. 52, 165–184 (2005). doi:10.1080/0950034042000275360
- R.R. Jones et al., Population trapping in Kr and Xe in intense laser fields. Phys. Rev. A: At. Mol. Opt. Phys. 47, R49–R52 (1993). doi:10.1103/PhysRevA.47.R49
- L.V. Keldysh, Ionization in the field of a strong electromagnetic wave. Sov. Phys. JETP 20, 1307–1314 (1965)
- R. Kienberger et al., Atomic transient recorder. Nature 427, 817–821 (2004). doi:10.1038/ nature02277
- 54. W. Kołos, L. Wolniewicz, Potential-energy curves for the $X^1\sum_g^+$, $b^3\sum_u^+$, and $C^1\Pi_u$ states of the hydrogen molecule. J. Chem. Phys. **43**, 2429–2441 (1965). doi:10.1063/1.1697142
- W. Kołos, L. Wolniewicz, Improved theoretical ground-state energy of the hydrogen molecule.
 J. Chem. Phys. 49, 404–410 (1968). doi:10.1063/1.1669836
- W. Kołos, L. Wolniewicz, Improved potential energy curve and vibrational energies for the electronic ground state of the hydrogen molecule. J. Mol. Spectrosc. 54, 303–311 (1975). doi:10.1016/0022-2852(75)90083-1
- 57. P. Kruit et al., Absorption of additional photons in the multiphoton ionisation continuum of xenon at 1064, 532 and 440 nm. J. Phys. B: At. Mol. Phys. 14, L597–L602 (1981). doi:10.1088/0022-3700/14/19/003
- 58. L.D. Landau, E.M. Lifschitz, *Lehrbuch der Theoretischen Physik*, Band III, Quantenmechanik (Akademie-Verlag, Berlin, 1965)
- A.S. Landsman et al., Rydberg state creation by tunnel ionization. New J. Phys. 15, 013001 (2013). doi:10.1088/1367-2630/15/1/013001
- J. Laskin, C. Lifshitz, Kinetic energy release distributions in mass Spectrometry. J. Mass Spectrom. 36, 459–478 (2001). doi:10.1002/jms.164
- F. Lindner et al., Attosecond double-slit experiment. Phys. Rev. Lett. 95, 040401 (2005). doi:10.1103/PhysRevLett.95.040401
- C. Liu, K.Z. Hatsagortsyan, Origin of unexpected low energy structure in photoelectron spectra induced by midinfrared strong laser fields. Phys. Rev. Lett. 105, 113003 (2010). doi:10.1103/ PhysRevLett.105.113003
- L.A. Lompré et al., Laser-intensity effects in the energy distributions of electrons produced in multiphoton ionization of rare gases. J. Opt. Soc. Am. 2, 1906–1912 (1985). doi:10.1364/ JOSAB.2.001906
- L.B. Madsen et al., Multiphoton ionization of H₂⁺ by intense light: a comparison of Floquet and wavepacket results. Phys. Rev. A: At. Mol. Opt. Phys. 58, 456–465 (1998). doi:10.1103/ PhysRevA.58.456
- T.H. Maiman, Stimulated optical radiation in ruby. Nature 187, 493–494 (1960). doi:10.1038/ 187493a0
- B. Manschwetus et al., Strong laser field fragmentation of H₂: Coulomb Explosion without Double Ionization. Phys. Rev. Lett. 102, 113002 (2009). doi:10.1103/PhysRevLett.102.113002
- 67. A.I. Nikishov, V.I. Ritus, Ionization of systems bound by short-range forces by the field of an electromagnetic wave. Sov. Phys. JETP 23, 168–177 (1966)
- 68. A.I. Nikishov, V.I. Ritus, Ionization of atoms by an electromagnetic-wave field. Sov. Phys. JETP **25**, 145–156 (1967)
- T. Nubbemeyer et al., Strong-field tunneling without ionization. Phys. Rev. Lett. 101, 233001 (2008). doi:10.1103/PhysRevLett.101.233001
- J. Paldus, Perturbation theory (Chap. 5), in Springer Handbook of Atomic, Molecular, and Optical Physics [online], ed. by G.W.F. Drake (Springer Science+Buisiness Media Inc., New York, 2006), pp. 101–114. doi:10.1007/978-0-387-26308-3
- G.G. Paulus et al., Rescattering effects in above-threshold ionization: a classical model. J. Phys. B: At. Mol. Opt. Phys. 27, L703–L708 (1994). doi:10.1088/0953-4075/27/21/003
- 72. D. Pavičić, Coulomb explosion and intense-field photodissociation of ion-beam H_2^+ and D_2^+ . Ph.D. thesis. LMU der Ludwig-Maximilians-Universität München, Germany. URN: urn:nbn:de:bvb:19-21593 (2004)

73. A.M. Perelomov et al., Ionization of atoms in an alternating electric field. Sov. Phys. JETP 23, 924–934 (1966)

- A.M. Perelomov et al., Ionization of atoms in an alternating electric field: II. Sov. Phys. JETP 24, 207–217 (1967)
- A.M. Perelomov, V.S. Popov, Ionization of atoms in an alternating electrical field. III. Sov. Phys. JETP 25, 336–349 (1967)
- A.N. Pfeiffer et al., Probing the longitudinal momentum spread of the electron wave packet at the tunnel exit. Phys. Rev. Lett. 109, 083002 (2012). doi:10.1103/PhysRevLett.109.083002
- A.M. Popov et al., Strong-field atomic stabilization: numerical simulation and analytical modelling. J. Phys. B: At. Mol. Opt. Phys. 36, R125–R165 (2003). doi:10.1088/0953-4075/36/10/201
- 78. V.S. Popov, Tunnel and multiphoton ionization of atoms and ions in a strong laser field (Keldysh theory). Physics-Uspekhi 47, 855–885 (2004). doi:10.1070/PU2004v047n09ABEH001812
- J.H. Posthumus, The dynamics of small molecules in intense laser fields. Rep. Prog. Phys. 67, 623–665 (2004). doi:10.1088/0034-4885/67/5/R01
- J.H. Posthumus, J.F. McCann, Diatomic molecules in intense laser fields (Chap. 2), in *Molecules and Clusters in Intense Laser Fields*, ed. by J. Posthumus (Cambridge University Press, Cambridge, 2001), pp. 27–77
- M. Protopapas et al., Atomic physics with super-high intensity lasers. Rep. Prog. Phys. 60, 389–486 (1997). doi:10.1088/0034-4885/60/4/001
- H.R. Reiss, Effect of an electromagnetic field on a weakly bound system. Phys. Rev. A: At. Mol. Opt. Phys. 22, 1786–1813 (1980). doi:10.1103/PhysRevA.22.1786
- H.R. Reiss, Limits on tunneling theories of strong-field ionization. Phys. Rev. Lett. 101, 043002 (2008). doi:10.1103/PhysRevLett.101.043002
- A. Rudenko et al., Exploring few-photon, few-electron reactions at FLASH: from ion yield and momentum measurements to time-resolved and kinematically complete experiments. J. Phys. B: At. Mol. Opt. Phys. 43, 194004 (2010). doi:10.1088/0953-4075/43/19/194004
- 85. T.E. Sharp, Potential-energy curves for molecular hydrogen and its ions. At. Data Nucl. Data Tables **2**, 119–169 (1970). doi:10.1016/S0092-640X(70)80007-9
- J.H. Shirley, Solution of the Schrödinger Equation with a Hamiltonian Periodic in Time. Phys. Rev. 138, B979–B987 (1965). doi:10.1103/PhysRev.138.B979
- 87. K. Sändig, H₂⁺ in intensiven Lichtfeldern. Ph.D. thesis. LMU der Ludwig-Maximilians-Universität München, Germany. URN: urn:nbn:de:bvb:19-4400 (2000)
- 88. L. Spielberger et al., Double and Single Ionization of Helium by 58-keV X Rays. Phys. Rev. Lett. 76, 4685–4688 (1996). doi:10.1103/PhysRevLett.76.4685
- M.R. Thompson et al., One and two-colour studies of the dissociative ionization and Coulomb explosion of H₂ with intense Ti:sapphire laser pulses. J. Phys. B: At. Mol. Opt. Phys. 30, 5755–5771 (1997). doi:10.1088/0953-4075/30/24/014
- X. Urbain et al., Intense-laser-field ionization of molecular hydrogen in the tunneling regime and its effect on the vibrational excitation of H₂⁺. Phys. Rev. Lett. 92, 163004 (2004). doi:10.1103/PhysRevLett.92.163004
- A. von Veltheim et al., Frustrated tunnel ionization of noble gas dimers with rydberg-electron shakeoff by electron charge oscillation. Phys. Rev. Lett. 110, 023001 (2013). doi:10.1103/ PhysRevLett.110.023001
- G. Yao, S.-I. Chu, Laser-induced molecular stabilization and trapping and chemical bond hardening in intense laser fields. Chem. Phys. Lett. 197, 413–418 (1992). doi:10.1016/0009-2614(92)85793-A
- A. Zavriyev et al., Ionization and dissociation of H₂ in intense laser fields at 1.064μm, 532 nm, and 355 nm. Phys. Rev. A: At. Mol. Opt. Phys. 42, 5500 (1990). doi:10.1103/PhysRevA. 42.5500
- 94. A. Zavriyev, P.H. Bucksbaum, H₂ in intense laser fields (Chap. 2), in *Molecules In Laser Fields*, ed. by A.D. Bandrauk (Macel Dekker Inc., New York, 1994), pp. 71–108

Chapter 4 The Reaction Microscope

As discussed in Chap. 3, the interaction of strong laser fields with atoms or molecules often leads to ionization (and sometimes dissociation) and thus to the creation of charged particles. One suitable approach to investigate the underlying processes is the measurement of the momenta that these particles obtained during the ionization. Reaction microscopes (REMIs) are highly advanced momentum spectrometers which are perfectly suited for this task: They provide highly resolved, three-dimensional momentum distributions and can—despite the enormous mass difference—perform measurements for ions and electrons simultaneously. Thus, the particles can be observed in coincidence which is a key feature of the detector and which is necessary for detailed studies of multi-particle processes like e.g. double ionization. Extensive information about REMIs—or the COLTRIMS¹ technique, as also often referred to—can be found e.g. in [7, 8, 14–16, 23, 24]. The following chapter briefly outlines the basic working principle of REMIs starting with a description of the typical setup as used in this work. The second part, Sect. 4.2, treats the data processing procedures used to calibrate the system and reconstruct the particles' momenta.

4.1 Setup

REMIs are utilized in very different research areas, e.g. in the investigation of electron and ion collisions [6, 14] or the interaction of light from femtosecond laser sources [25], high harmonic radiation [9] or free-electron lasers [20] with single particles. The REMI used in this work was employed in several experiments over the last years, see e.g. [4, 10, 12]. In a typical strong-field experiment utilizing a REMI,

¹Cold target recoil ion momentum spectroscopy.

a dilute supersonic gas jet-originating from a nozzle, passing skimmers and attenuation slits, see Sect. 4.1.2—is crossed with the focussed laser beam. Figure 4.1 gives a schematic overview. The volume of intersection, the *reaction volume*, is the origin for all particles created in the interaction process. Important properties of the focus as the shape of the focal volume are derived in Sect. 2.1.3. The charged particles, ions and electrons, are accelerated and guided onto two time- and position-sensitive detectors by homogenous electric and magnetic fields aligned along the spectrometer axis. The fields are created by the spectrometer electrodes and large Helmholtz coils outside the vacuum, respectively. The spectrometer comprises cylindrical symmetry which is often also the case for the ionization process, e.g. for photoionization by light with linear polarization aligned along the spectrometer axis.

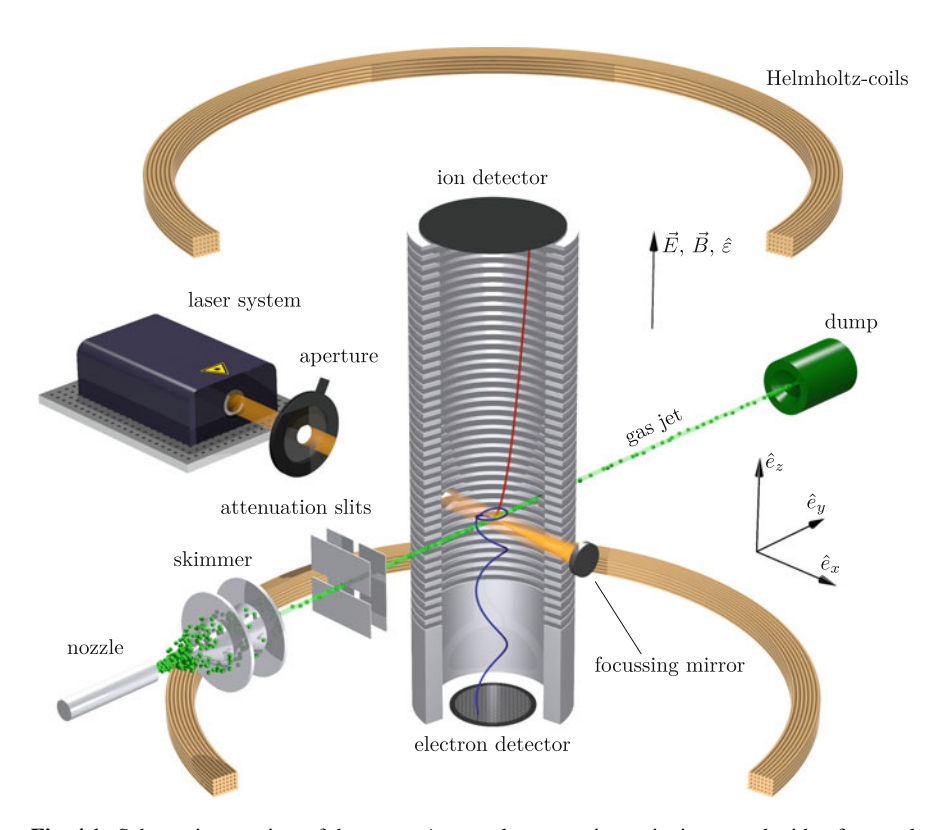


Fig. 4.1 Schematic overview of the setup. A neutral supersonic gas jet is crossed with a focussed laser beam inside the REMI. The latter first traverses the chamber and is afterwards reflected by a spherical mirror and thus focussed onto the atoms in the jet. Charged particles (*red* ion, *blue* electron) originating from the interaction volume are guided onto two time- and position-sensitive detectors by electric and magnetic fields, see text for details

4.1 Setup 55

4.1.1 The Spectrometer and Detectors

Figure 4.2 schematically shows the spectrometer used in this work in more detail. Atoms or molecules in the supersonic gas jet, entering from the bottom in this picture, are exposed to the laser in the center of the arrangement. Ions produced are accelerated onto the ion detector (left) by the electric extraction field. Due to the large directed initial momentum in the gas jet along \hat{e}_y , the resulting trajectories are given by mass-specific parabolas. At the two ends of the spectrometer, and as separation between the acceleration and drift region, three grids are placed and—in normal operation of the REMI—set to the voltage given by the electrode at the specific position. However, in the case of the two grids at the spectrometer ends, a free adjustment is possible. The grids suppress the formation of electrostatic lenses and field penetrations from outside and hence ensure the homogeneity of the field inside the spectrometer.

Depending on the geometry, the extraction field has to be chosen strong enough to project all ions of interest onto the detector, see Table 4.1 for dimensions and parameters used in the setup for this work. An increase of the electric field strength may seem beneficial in this context but the resulting shorter absolute flight times and smaller spatial distributions reduce the momentum resolution since experimental uncertainties typically stay constant, see Sect. 4.3 for details. The detection requires a strong post-acceleration of the particles onto the detector plates, hence a large electric field is pointing towards their surface. An additional grid directly in front

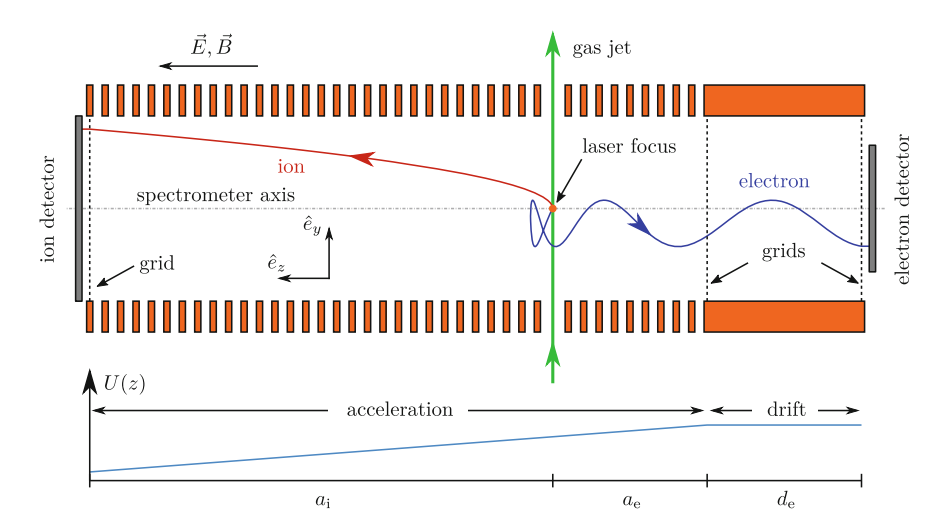


Fig. 4.2 Schematic illustration of the REMI spectrometer used in this work and particle trajectories arising from a single ionization event $A \to A^+ + e^-$. Ion and electron are created in the reaction volume and guided onto the ion detector (*left*) and electron detector (*right*), respectively, by the electric and magnetic fields applied. The lower part of the image shows the characteristic dependence of the electric potential U on the \hat{e}_z coordinate along the spectrometer axis: A linear trend in the acceleration regions and a constant value over the drift region

Property	Ions	Electrons
Acceleration length a (cm)	30	10
Drift length d (cm)	_	10
Ø _{active} MCP (mm)	120	75
Ø _{inner} electrodes (mm)	120	
Electric field E (typical) (V/cm)	2	
Magnetic field <i>B</i> (typical) (μT)	600	
Flight time t (typical) (ns)	$\mathcal{O}\left(10^4\right)$	$\mathcal{O}\left(10^2\right)$
Cyclotron period t_C (typical) (ns)	$\mathcal{O}\left(10^6\right)$	70

Table 4.1 Approximate basic geometry, typical field strengths and resulting characteristic times, see Sect. 4.2.1, for the REMI used in this work

of the detector, not shown in Fig. 4.2, may be used to encase this field. In the setup used, this is done in the case of the ion detector.

The flight time and impact position on the detectors of a particle of known mass and charge is well defined, provided it does not gain any additional momentum from the interaction with the laser. In the setup used in this work, the ions are accelerated over the full spectrometer until they pass the grid in front of the detector. In contrast to this, the electrons traverse a field-free drift region after their acceleration. The general case, namely the presence of a drift region also for the ions, will be discussed in the mathematical treatment in Sect. 4.2.1.

The electrons created in the ionization process are accelerated by the same electric field towards the electron detector. However, momentum conservation and the enormous mass difference between ions and electrons, see Table A.2, typically result in very different energies and velocities of the electrons compared to the ions. The projection of the fast electrons onto the electron detector by pure electric fields is possible only if much stronger fields are used like e.g. done in velocity-map imaging (VMI) experiments [2]. In order to retain a weak extraction field and benefit from the associated higher resolution, REMIs instead utilize a magnetic field to force the electrons on spiral trajectories and confine them close to the spectrometer axis [14]. Despite the more complex trajectories, a reconstruction of the momentum obtained in the interaction with the laser is still possible, see Sect. 4.2. The simultaneous measurement of the momentum vectors of all particles originating from the interaction of the laser with a target is commonly referred to as a *kinematically complete* measurement or experiment.

After their flight through the spectrometer, the particles impact on the detectors. The task of these devices is to precisely measure both the impact time and the position of each particle. The detection scheme essentially contains two steps: In the first, a micro-channel plate (MCP) amplifies the signal by creation of an electron cloud in an avalanche process, triggered by the single particle to detect. The current caused thereby can be detected and reveals the time of impact. A photo-diode inside the laser system provides a reference time such that the flight time t can be derived as

4.1 Setup 57

the difference. In the second step of the detection scheme, the impact position of the particle is determined by a measurement of the center of gravity of the electron cloud that is produced by the MCP detector with a delay line anode. A scheme of the full detector system is shown in Fig. 4.3. In the following, the two detection steps are explained in more detail.

Signal amplification and determination of the impact time After passing the grid at the end of the spectrometer, the particles hit a micro-channel plate, a thin disc homogeneously pervaded by fine channels coated with suitable semiconducting material. These are slightly tilted with respect to the normal vector of the disc, have a typical inner diameter of $25 \,\mu m$ and are separated from each other by roughly $30 \,\mu m$, see Fig. 4.3b. These and the typical values following in this paragraph were derived

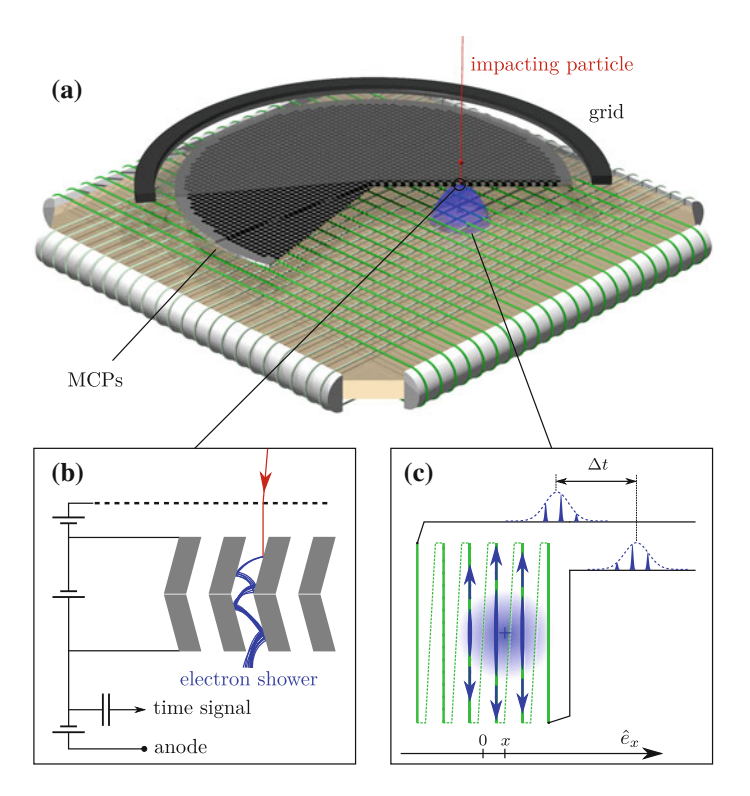


Fig. 4.3 Time and position sensitive single particle detection using a stack of MCPs and a delay-line anode. **a** A particle impacting in one of the channels of the MCP creates an electron cloud which is projected onto the delay line anode. **b** Creation of the electron cloud within single channels of the MCPs. The impacting particle creates secondary electrons and starts an avalanche amplification process. An electron shower leaves the second MCP at its back side. **c** Principle of position determination with the delay line anode, reduced to one coordinate for simplification. The centroid of the electron cloud has an offset of x in \hat{e}_x direction with respect to the center of the detector. Signals travel along the wire in both directions and are detected at its ends. The measured time difference Δt is proportional to the initial spatial offset x

from [18]. Typically, the resulting ratio of length to diameter for the channels is in the order of 40 to 80. Between the front and the back surface of the MCP a high voltage of typically 1200 V is applied. A particle impinging the detector may enter one of the channels and—in this case—will hit the inner surface. As a consequence, secondary electrons are produced, accelerated by the strong electric field and thus gain enough energy to create more secondary electrons on their next impact on the channel surface. This secondary impacts are forced by the slight angle between the channel direction and the electric field, see Fig. 4.3b. The process is repeated many times resulting in an avalanche-like amplification of the signal. Finally, a cloud of electrons leaves the MCP at its back side and consequently a (small) current can be detected by capacitive coupling of the MCPs' voltage supply to an acquisition system. A fraction of typically 50% of the incident particles do not create secondary electrons or simply hit the MCP directly on the front surface and thus are not detected. Two or three MCPs may be used subsequently forming a stack and enhance the amplification factor up to about 10⁷ and higher, commonly known as *Chevron MCP* and *Z-stack MCP*, respectively. In the experiments performed in this work, a stack of two MCPs is used for the detection of ions while three plates form the electron detector. Subsequent MCPs are turned by 180° with respect to each other, see Fig. 4.3b. As already mentioned, in the case of the ion detector, an additional grid is placed in between the end of the spectrometer and the MCP stack. This ensures a more homogenous field despite a high voltage difference in the order of 2000V between the last electrode and the front side of the first MCP.

Position detection The electron cloud emerging from the back side of the MCP stack can be used to determine the impact position of the particle. For this purpose the cloud is accelerated onto a delay-line anode [22] while expanding due to the repulsive Coulomb force between the electrons. For each of the two coordinates to determine, a long copper wire² is wrapped around the base plate such that for the side facing the MCP stack an equal spacing of the parallel wires is achieved. The electron cloud hits simultaneously several windings resulting in enhanced electron densities in the respective sections of the wire. Subsequently, the charges propagate along the wire in both directions until they are detected at the two ends. The measured time difference Δt depends on the initial spatial offset of the electron cloud with respect to the center of the windings and thus on the impact position of the particle, see Fig. 4.3c. The coordinate in the direction perpendicular to the wires is given by $c_{\rm w}\Delta t$ where $c_{\rm w}={\rm const}$ is the effective signal velocity in this direction. It has to be mentioned that Δt also slightly depends on the second coordinate of the impact position (along the wires). However, this leads only to a small effective rotation of the detector which are anyway aligned arbitrarily with respect to each other and the laboratory frame. An appropriate rotation of the detectors is performed after the data acquisition, during the calibration procedure, see Sect. 4.2.3. The delay-line anode is capable of detecting the position of several particles originating from the same ionization event and thus arriving in a very short time window. However, with

²In fact, two wires are utilized, one delivering the signal and one a reference. For simplicity of the discussion, this technical detail is omitted.

4.1 Setup 59

shrinking difference between impact time and position, the discrimination between the particles becomes more and more difficult until the position detection simply fails. For typical measurements performed with the REMI used in this work this is usually no restriction. However it should be mentioned for completeness that special *hexanode detectors* with three layers of wires have been developed to overcome this limitation [11].

4.1.2 Preparation of the Gas Jet

As already mentioned in the last section, both the flight time *t* and the impact position of a certain particle on the detector depend not only on the momentum gained in the interaction with the laser but also on the initial momentum, before the interaction takes place. Therefore, although this initial momentum is usually not of primary interest, it has to be considered. Any ensemble of atoms delivered to the interaction volume has a certain intrinsic momentum distribution or—in other words—a finite temperature. If the momentum gained from the interaction with the laser is small compared to this intrinsic spread, no meaningful information can be extracted from the measurements. A typical momentum for the ion or electron expected in strong-field ionization is in the order of 1 a.u. Close to threshold ionization may produce charged particles with even much smaller momenta.

The particle velocities which can be found in an ensemble of atoms with mass m and temperature T (in thermal equilibrium) are given by the Maxwell–Boltzmann distribution, see e.g. [5, Sect. 7.3.5]. However, if only the velocity component along a certain coordinate is considered instead of the absolute value of the velocity vector the particle velocities are described by a Gaussian distribution with a FWHM of $2\sqrt{2\ln(2)}\sqrt{k_{\rm B}T/m}$, [5, Sect. 7.3.5], where m is the particle mass and $k_{\rm B}$ is the Boltzmann constant. Under room temperature conditions ($T=300~{\rm K}$) the spread in the particles' momenta $\Delta p^{300~{\rm K}}$ is much larger than the momentum change expected to be caused by the interaction.

Supersonic expansion of a gas into the vacuum-chamber and the formation of a gas jet exhibits a very efficient way to convert the intrinsic thermal momentum distribution of the atoms into a directed, collective motion with a much smaller momentum spread. Even without additional cooling, very low temperatures can be reached in the reaction volume with moderate technical effort, see Table 4.2. The supersonic expansion starts at a nozzle through which the gas enters the vacuum chamber. In the experiments presented in this thesis, the gas is supplied with room temperature ($\approx 300\,\mathrm{K}$) and a pressure of around 3 bar to a nozzle with a diameter of 30 μ m. The mechanism of the expansion is complex, see e.g. [13], and not discussed in detail here. Briefly, the central part of the expanding atom cloud, the "zone of

 $^{^3}$ Consider e.g. a single ionization event Ar \rightarrow Ar $^+$ + e $^-$ and a total kinetic energy (excess energy) of 1eV. Using particle masses from Table A.2, energy and momentum conservation yield momenta of less then 0.3 a.u.

Species	$\Delta p^{300 \mathrm{K}}$ (a.u.)	$v_{\rm jet}({\rm m/s})$	$\overline{p}_{ }$ (a.u.)	$\Delta p_{ }$ (a.u.)	$T_{ }$ (K)	$p_{\perp,\max}$ (a.u.)
Ne	13.9	1320	21.9	1.14	2.0	$\lesssim 5 \times 10^{-3}$
Ar	19.6	930	31.0	1.06	0.9	
Kr	28.4	642	44.9	1.34	0.7	
H ₂	4.40	4900	8.23	1.04	17	
N ₂	16.4	1310	30.7	2.99	10	

Table 4.2 Characteristic properties of supersonic jets produced from different gases, calculated with [13, Eq. (2.18), Tables 2.3 and 2.5]

All widths denoted with a leading Δ refer to the FWHM. The value for $p_{\perp, max}$ is estimated from basic geometric properties of the experiment, see text for details

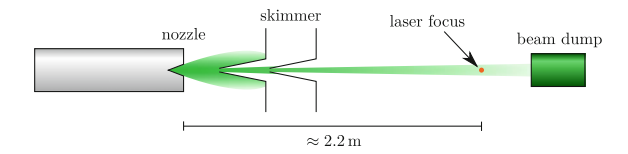


Fig. 4.4 Creation of the supersonic gas jet. The gas expands through the nozzle inside the vacuum chamber. Two skimmers with openings of 200 and 400 μ m in diameter, respectively, form a stable jet which is hit by the laser approximately after a flight distance of about 2.2 m. Gas atoms not ionized by the laser are captured by a beam dump

silence" is extracted using skimmers, specifically designed conical apertures, forming a jet and preventing its destruction by shock waves. In the machine used in this work, two skimmers are used with diameters of 200 and 400 μ m, respectively, see Fig. 4.4. The extracted atoms have—in jet-direction—a very sharp momentum distribution centered around a relatively large mean value representing their collective motion, see Table 4.2. The transverse momentum spread, perpendicular to the jet direction, is even smaller and limited by geometrical restrictions: Only atoms with a very low transverse momentum are interacting with the laser in the interaction volume. As estimated in Sect. 2.1.3, the latter has a size of $\approx\!500\,\mu\text{m}$ or less, depending on the direction and the wavelength and is reached by the gas jet after about 2.2 m flight distance. Gas atoms in the jet which are not ionized by the laser are captured by a beam dump to preserve the good vacuum conditions in the chamber.

4.2 Data Processing

The electronic signals delivered by the detectors are processed in a commercial *RoentDek* "fADC8/10-2" unit containing several fast 10bit analog-to-digital converters [19] (ADCs), sampling the trace before and after each peak. The raw data is further processed by *RoentDek's* software package "CoboldPC" which also may be used to reconstruct the particles' momenta. However, within this work, the software

4.2 Data Processing 61

is only used to record the data and to export flight times of particles and corresponding time differences measured with the delay-line detectors, see Sect. 4.1.1. The export can be restricted to particles fulfilling simple conditions, e.g. having a flight time in a certain range etc. Further data selection, calibration, momentum reconstruction and compilation of the final data is performed with scripts written and developed for *MathWorks* "Matlab". In contrast to CoboldPC, the scripts are able to perform operations on all events within a data file simultaneously rather than requiring the complete re-reading of the (large) raw data, the ADC-sampled electronic signals. For the reconstruction of the particles' momenta, the equations presented in the following section were implemented.

4.2.1 Momentum Reconstruction

The measurement of the flight time and the impact position of a particle allows the reconstruction of its momentum after the interaction with the laser. With regard to the reconstruction procedure it is appropriate to distinguish between two different classes of momentum components: The component in direction of \hat{e}_z , along the spectrometer axis, see Fig. 4.1, is usually named *longitudinal momentum component* p_1 and—as will be shown in this section—can be reconstructed from the measured flight time alone without any information about the impact position. In contrast, the reconstruction of the remaining *transverse momentum components* p_x and p_y perpendicular to the spectrometer axis relies on this additional information. Photoionization experiments often feature cylindrical symmetry with respect to the spectrometer axis, namely if linearly polarized light is used and its polarization $\hat{\varepsilon}$ is aligned with \hat{e}_z . In this case it is reasonable to combine the two transverse components and to define $\vec{p}_{tr} = \sqrt{p_x^2 + p_y^2} \cdot \hat{e}_{tr}$ where \hat{e}_{tr} is the direction in the transverse plane. This direction can alternatively be defined by an angle φ :

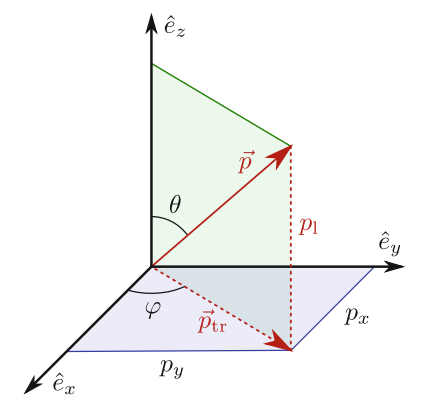
$$\vec{p} = \begin{pmatrix} p_1 \\ p_x \\ p_y \end{pmatrix} = \begin{pmatrix} p_1 \\ \vec{p}_{tr} \end{pmatrix} = p \cdot \begin{pmatrix} \cos(\theta) \\ \sin(\theta)\cos(\varphi) \\ \sin(\theta)\sin(\varphi) \end{pmatrix}. \tag{4.1}$$

Figure 4.5 summarizes the conventions of vectors and angles used throughout this work. It is important to note that the magnetic field—also aligned along the spectrometer axis—does only influence the transverse components of the momentum vector. As a consequence, the flight times of the particles and thus the momentum reconstruction of p_1 are independent of the magnetic field.

Longitudinal Momentum Component

The charged particles created in the interaction volume are first accelerated by the extraction field over a certain distance a and—in the general case—afterwards travel with constant velocity through a field-free drift region d. The latter is optional and

Fig. 4.5 Convention of momentum components and angles as used throughout this work. The direction \hat{e}_z is aligned along the spectrometer axis, cf. Fig. 4.1



may be omitted (d = 0) as it is done in the case of the ions in the setup used for this work, see Sect. 4.1.1. Solving the classical one-dimensional equation of motion for the \hat{e}_z component yields a flight time of

$$t_{m,q}(p_{1}) = \underbrace{a\left(-\frac{p_{1}}{q\Delta U} + \sqrt{\left(\frac{p_{1}}{q\Delta U}\right)^{2} + \frac{2m}{q\Delta U}}\right)}_{\text{flight time in acceleration region}} + \underbrace{d\left(\frac{p_{1}^{2}}{m^{2}} + \frac{2q\Delta U}{m}\right)^{-1/2}}_{\text{flight time in drift region}}.$$

$$(4.2)$$

Apart from spectrometer-geometry and the voltage difference across the acceleration region ΔU the flight time is a function of the particle's initial longitudinal momentum p_1 and its mass m and charge q. In general, the dependence on three particle-related quantities may be an issue for the momentum reconstruction, since different combinations result in identical flight times. Fortunately, the initial momentum gained in typical photoionization experiments leads to a shift in the flight time, which is much smaller than shifts caused due to different mass or charge. Thus, the different ion species usually form distinct peaks in the time-of-flight spectra, making it possible to distinguish them, see Fig. 4.9. The shape and width of the peaks reflect the initial momentum distribution: Ions initially moving towards the detector will arrive earlier, particles initially moving in the opposite direction later. In case of symmetric momentum distributions as typically produced e.g. with a linearly polarized laser, the maximum of each peak represents the flight time for vanishing longitudinal momentum. However, one restriction remains: Since this value, $t_{m,q}(p_1 = 0)$, exclusively depends on the ratio m/q, certain different species e.g. N_2^{++} and N^+ have identical flight times and the respective peak resembles a superposition of both. This is a problem the REMI shares with other mass-spectrometers. Often, one of the species clearly dominates the peak and the contribution of the other can be neglected. To prevent confusion it should be mentioned that in many references, e.g. [17], instead of Eq. (4.2) a mathematically identical equation can be found:

4.2 Data Processing 63

$$t_{m,q}(p_1) = m \left(\frac{2a}{\sqrt{p_1^2 + 2mq\Delta U} \pm p_1} + \frac{d}{\sqrt{p_1^2 + 2mq\Delta U}} \right). \tag{4.3}$$

The meaning of the \pm in the denominator is explained later.

In the following, m and q are assumed to be known. In order to reconstruct the initial momentum, the inverse function of Eq. (4.2), $p_1(t)$, has to be evaluated. If no drift region is present (d = 0), the analytical solution is given by

$$p_{1}(t) \stackrel{d=0}{=} \frac{ma}{t} - \frac{q \Delta U}{2a} t. \tag{4.4}$$

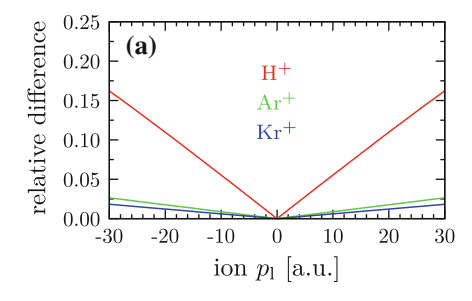
However, for the general case, $d \neq 0$, no such analytical solution can be found. Different methods may be applied in order to extract the longitudinal momentum, some are discussed in the following.

Approximation for small momenta This method has the advantage that it does provide an analytic equation which is an approximation to the exact solution, valid for initial momenta small compared to the momentum gained in the extraction field, $p_1 \ll \sqrt{2mq \Delta U}$. Expanding Eq. (4.2) in a Taylor-series around $p_1 = 0$ and isolating p_1 in the result yields [24, Eq. (10) without the prefactor for unit conversion]

$$p_{1}(t) \approx \frac{q\Delta U}{a} (t_{0} - t) + \mathcal{O}[(t_{0} - t)^{2}]$$

$$t_{0} = \sqrt{\frac{m}{q\Delta U}} \left(\sqrt{2}a + \frac{d}{\sqrt{2}}\right).$$
(4.5)

Here, t_0 is the flight time of a particle with vanishing initial momentum. Figure 4.6 shows—for selected ion species (a) and electrons (b)—the relative difference $|\Delta p_1/p_1|$ between an exact numerical solution of Eqs. (4.2) and (4.5) for a geometry as used in the experiment, see Table 4.1. The approximation is in particular good for heavy ions with small momenta, typically produced in photoionization processes. However, for



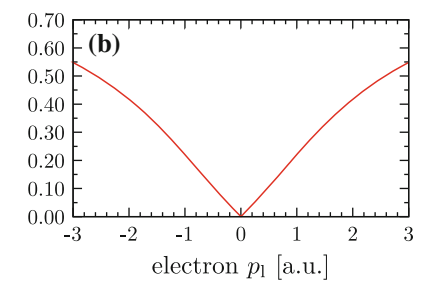


Fig. 4.6 Comparison of different reconstruction methods. Relative difference $|^{\Delta p_l}/p_l|$ between approximation for small momenta, Eq. (4.5), and numerical solution of Eq. (4.2) for the spectrometer properties given in Table 4.1. **a** Singly charged ions of different mass. **b** Electrons

light and fast particles like atomic hydrogen-ions as they appear e.g. from dissociation of an H_2 -molecule (about 20 a.u. and larger, see Sect. 7.1), the approximation is poor and even worse for electrons. Here the deviation is striking already for small momenta.

Numerical solution For every particle and its measured flight time, Eq. (4.2) can be solved numerically. This requires some computational effort but can nowadays be performed in real-time already during the data acquisition on a standard computer or workstation if an efficient algorithm is used. One example for such an algorithm is the *Newton's Method* which usually converges after few iterations [21, Appendix B].

Lookup table Also very fast and very convenient is the utilization of a *Lookup table*: The first column of the table is filled with equidistant momentum values in a suitable (large) range. The resulting flight time *t* for each of the entries can simply be calculated with Eq. (4.2) and stored in the second column. The difference of adjacent flight times obtained should be small compared to the time resolution of the ADC, which can be achieved by an appropriate choice of the momentum steps for creation of the first column. After having calculated the table at the beginning of the analysis, a sufficiently close value can be found for every measured flight time in the second column of the table together with the associated momentum in the first. The results of this method can easily be refined by linear interpolation between the rows.

In this work, look-up tables with a momentum step size of 10^{-4} a.u., resulting in typical flight time steps of about 10^{-2} ns for both ions and electrons, and additional linear interpolation are used for the reconstruction of both—the ions' and the electrons' longitudinal momenta. This keeps the code fast and flexible and allows e.g. an easy future implementation of a drift-region for the ions or—in combination with particle trajectory simulations—a reconstruction if the fields are switched or ramped while the particles are still flying.

If the longitudinal momenta of the particles are calculated essentially based on Eq. (4.2), larger flight times always result in larger values for the momentum. In other words, the coordinate system is chosen such that a positive (negative) momentum is assigned for a particle initially moving away (towards) the respective detector. In the simultaneous detection of ions and electrons on two opposing detectors consequently two coordinate systems are defined. In order to obtain a momentum conservation-induced anticorrelation between the particles, one of the coordinate systems has to be inverted. The coordinate system in this work is chosen such that positive momenta are assigned to ions with larger flight times according to Eq. (4.2). For electrons, a + has to be replaced by - in the denominator of Eq. (4.2) as already considered in Eq. (4.3).

Transverse Momentum Components

For the reconstruction of the transverse momentum components from the flight time and the impact position of the particles, the influence of the magnetic field has to be considered as well as the directed (mean) velocity of the atoms in the jet. The latter leads to a spatial shift of the particles' impact positions: A particle which does not gain momentum from the laser will hit the detector not at the center but at a

4.2 Data Processing 65

position $\Delta y = v_{\rm jet}t$ apart. With typical values from Tables 4.1 and 4.2 the effect can be estimated to be in the order of a few cm for ions and $100 \times$ smaller for the electrons.

The magnetic field does not affect the absolute value of the particle's momentum but continuously changes its direction. This leads to a cyclotron motion of the particle while it is accelerated in the electric field along the spectrometer axis. The cyclotron frequency ω_C and the radius R of the trajectory are given by [24]

$$\omega_{\rm C} = \frac{2\pi}{t_{\rm C}} = \frac{qB}{m} \tag{4.6}$$

$$R = p_{\rm tr}/q_B, \tag{4.7}$$

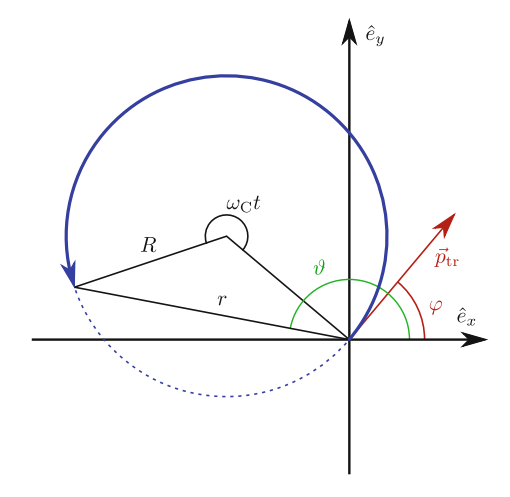
where q and m denote charge and mass of the particle, B is the strength of the magnetic field and t_C is called the *cyclotron period*. Thus, if the charge and the magnetic field strength are known, a measurement of R allows directly the determination of p_{tr} . Figure 4.7 shows a projection of a typical cyclotron trajectory on the detector. Since the trajectory starts at the interaction volume, the particle revisits the spectrometer axis after every integer multiple of the cyclotron period $t = n \cdot t_C$. The cyclotron trajectory itself is *not* centered around this axis. In fact, the central axis is unique for every particle and depends on both the absolute value and the direction of its initial momentum.

From Fig. 4.7 the relation $R = r/2|\sin(\omega_C t/2)|$ can be obtained with fundamental geometrical considerations. Together with Eqs. (4.6) and (4.7) this yields [24]

$$p_{\rm tr} = \frac{m\omega_{\rm C}}{2|\sin(\omega_{\rm C}t/2)|}r. \tag{4.8}$$

The emission angle φ of the particle can be obtained from the measured angle ϑ by [24]

Fig. 4.7 Projection of electron trajectory on the detector plane, adapted from [24]



$$\varphi = \vartheta - \frac{\omega_{\rm C}t - 2\pi N}{2},\tag{4.9}$$

where $N = \lfloor t/t_C \rfloor = \text{floor}(t/t_C)$ is the number of complete turns performed by the particle.

Typical values for the cyclotron period t_C and the flight times t of electrons and ions are given in Table 4.1. For the electrons, $N \gtrsim 1$ while for the ions the cyclotron period is very large compared to their flight times and thus $\omega_C t \approx 0$. In this case, the sine-function in Eq. (4.8) can be well approximated by its argument which results in

$$p_{\rm tr}^{\rm ions} = \lim_{\omega_r t \to 0} p_{\rm tr} = {}^{mr}/_t. \tag{4.10}$$

The effect of the magnetic field can thus be compensated sufficiently by a rotation of the ion detector in the calibration procedure described in Sect. 4.2.3.

4.2.2 Solid-Angle Correction

After the reconstruction of the transverse momentum component $p_{\rm tr}$, the distribution of the particles $W(p_{\rm tr})$ may be investigated. It is important to note that $W(p_{\rm tr})$ does *not* resemble a "cut" through the respective two-dimensional momentum distribution. However, such a "cut" may, if desired, be calculated from $W(p_{\rm tr})$ by performing an adequate solid-angle correction. This is in particular important if the experimental results are to be compared with theoretical predictions, which often refer to this.

In the following, the different distributions and the solid-angle correction are explained by means of a simple example, namely a two-dimensional Gaussian distribution $W(p_x, p_y)$, visualized in Fig. 4.8a. The distribution $W(p_{tr})$, which can be derived using the definition of p_{tr} given in the beginning of Sect. 4.2.1, is shown

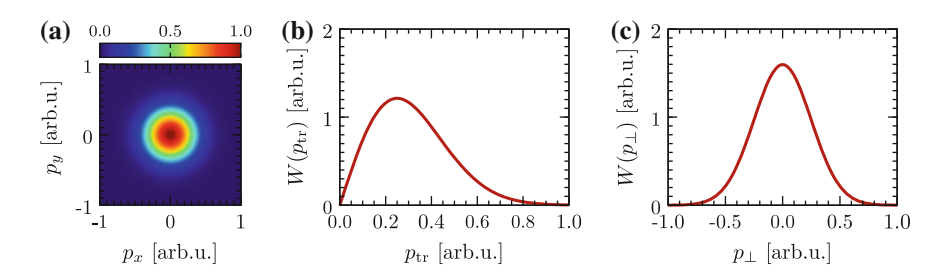


Fig. 4.8 Visualization of the difference between the coordinates p_{tr} and p_{\perp} . **a** A perfect two-dimensional Gaussian distribution as an example of a rotational symmetric transverse momentum distribution. **b** $W(p_{tr})$ (normalized) as directly accessible in an experiment with a REMI, see Sect. 4.2.1. **c** Distribution $W(p_{\perp})$ (normalized) as obtainable by a cut along an arbitrary axis through the origin of the distribution shown in (a). The distributions in (b) and (c) are connected by simple division and multiplication, respectively, see text for details

4.2 Data Processing 67

in (b). $W(p_{\rm tr})$ vanishes for zero momentum rather than resembling the maximum of the two-dimensional distribution. This can be explained by the implicit integration of the two-dimensional distribution along φ , see Fig. 4.5. For a fixed value of $p_{\rm tr}$, the length of the path along which the distribution is integrated is given by $2\pi p_{\rm tr}$, thus by zero for vanishing momentum. Without correcting for the solid angle, large momenta are enhanced in the resulting distribution $W(p_{\rm tr})$ while the region around zero is suppressed.

In order to obtain a distribution which resembles a "cut" through $W(p_x, p_y)$, $W(p_{tr})$ obviously has to be divided by $2\pi p_{tr}$ or—subsequent renormalization assumed—simply by its argument p_{tr} . This is nothing else than the Jacobian determinant associated with the transition from the Cartesian coordinates (p_x, p_y) to the polar coordinates (p_{tr}, φ) , see e.g. [3] Sect. 8.4.2. The resulting distribution is shown in Fig. 4.8c. In order to avoid confusion, in this work, the transverse component of solid-angle corrected distributions is denoted p_{\perp} rather than p_{tr} .

In the same way, solid-angle correction may be performed in the case of experimental data. Here, due to the finite bin size $\Delta p_{\rm tr}$, the distribution has to be divided by the respective area in the p_x - p_y -plane, $2\pi p_{\rm tr}\Delta p_{\rm tr}+\pi p_{\rm tr}^2$ rather than by the length of the integration path. However, satisfying results require a high level of statistics in particular in the region of low transverse momenta, where $W(p_{\rm tr})$ is divided by very small numbers and the absolute uncertainties are massively increased. In contrast, a theoretical distribution $W^{\rm t}(p_\perp)$ can always be converted into $W^{\rm t}(p_{\rm tr})$ without any problems. In case of a low level of statistics in the experiment, this approach may be beneficial in order to compare the results to theory.

4.2.3 Calibration of the REMI

The momentum reconstruction procedure as described in the previous section requires an exact knowledge of all experimental parameters, from the position of the gas jet and the precise spectrometer geometry to the voltages applied and more, e.g. the gas jet velocity. Those parameters can not be determined with a sufficient precision and partly may change inevitably over time or from measurement to measurement. For example, a change of the wavelength using the OPA as described in Sect. 2.2.5 leads to a slight spatial offset of the laser beam and thus to a small shift of the interaction volume inside the REMI. As a consequence, the distances over which the ions and electrons are accelerated, a_i and a_e in Fig. 4.2, are altered. Even very small shifts lead to evident deviations in the momentum spectra if the change of the parameters is not considered. This is done within a suitable calibration procedure performed for every individual set of data. The procedure yields consistency within the single data-sets, e.g. between ion and electron momenta, and ensures comparability of the different data sets. In the following, the most relevant steps are described.

Figure 4.9 exemplarily shows flight time distributions obtained in the experiment with a krypton gas jet and a wavelength of 470 nm. The distributions for ions in (a) and (b) bear resemblance with results obtained with a conventional time-of-flight

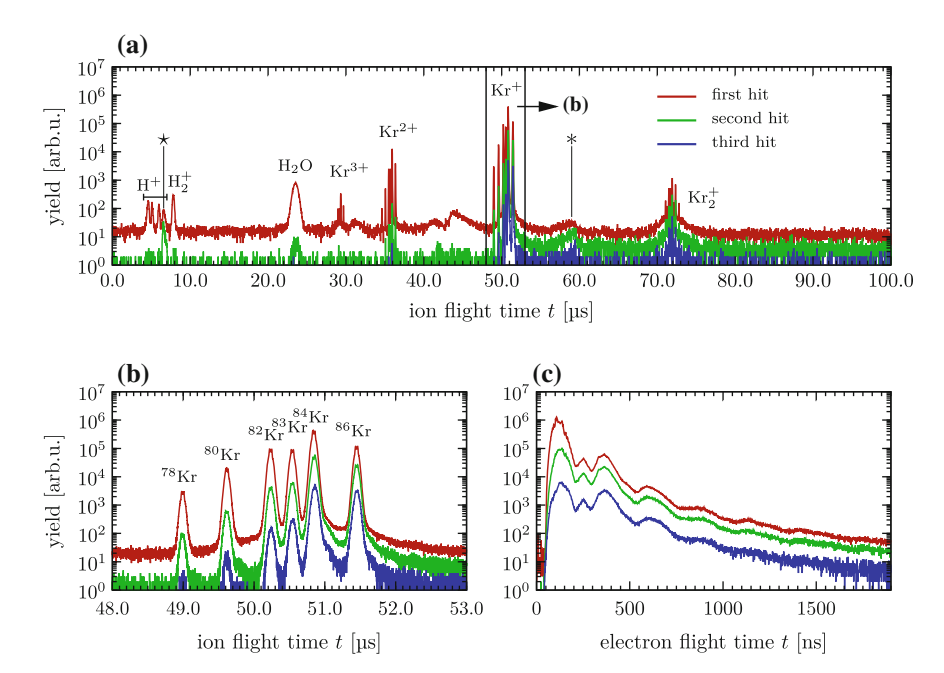


Fig. 4.9 Particle flight time distributions measured with the REMI. **a** Ion flight time distribution using a krypton gas jet and laser radiation at 470 nm. **b** Closer look on the Kr⁺ peaks visible in (**a**). **c** Electron flight time distribution

mass spectrometer: The maximum of each peak corresponds to the flight time of a specific ion with vanishing momentum component p_z while its shape resembles the momentum spread in the ensemble, here (mainly) caused by the interaction with the laser. Different species are visible, from light H⁺ ions originating from dissociation of H₂ molecules to Kr₂⁺ dimers formed during the creation of the jet. With a flight time of about 23.5 µs, water molecules from the residual gas in the chamber are detected. In contrast to the species carried by the cold gas jet, they form a much broader peak due to the higher temperature of about 300 K. In (b), all krypton isotopes with noteworthy natural abundance [1] are clearly resolved. Due to the multi-hit-capability of the detector systems, several (here up to three) ions per laser shot can be recorded. Regarding the four visible H⁺ peaks, this feature of the spectrometer already reveals an interesting fact in the raw time-of-flight spectra: One of the peaks, marked with (*) in Fig. 4.9a, has an increased contribution from the particles detected as second hit. This can be utilized later to identify the underlying process as Coulomb explosion $H_2 \longrightarrow 2H^+ + 2e^-$ releasing two correlated ions within the same laser pulse, see Sect. 3.5.1. In the same manner, also the presence of dissociating krypton dimers can be proven, marked with (*) in Fig. 4.9a. The electron spectra shown in Fig. 4.9c show less intuitive structure.

Many parameters are used in the momentum reconstruction of the particles such that the system is clearly overdetermined. If any of the parameters is varied, the 4.2 Data Processing 69

resulting effect on the reconstructed momenta can approximately be compensated by an appropriate adaption of others. Thus, a distinct set of parameters has to be chosen and adapted during the calibration procedure while the remaining are fixed initially to reasonable values. In this work, the latter is done for the spectrometer geometry, see Table 4.1, while e.g. the exact value for the voltage applied is one of the varied parameters.

Figure 4.10 displays some of the important graphs obtained in the calibration procedure. From the measured flight times the longitudinal momentum is reconstructed for singly and doubly ionized atoms. By adapting the spectrometer voltage and subtracting a time-offset from the flight times, both momentum distributions can be simultaneously centered around zero, see Fig. 4.10a. The spatial distributions delivered by the detectors are scaled to circular symmetry. The detector sizes are adjusted during the scaling of $p_{\rm tr}$ described later.

The electrons move along their spiral trajectories and—independent of their momentum—revisit the spectrometer axis at every integer multiple of the cyclotron period. However, this is only true if the laser focus is actually situated perfectly on this axis. Small deviations can—as inhomogeneities in the fields—be compensated as follows: If the impact position of the electrons is plotted over their flight time, a periodic structure can be observed as expected. At every multiple of the

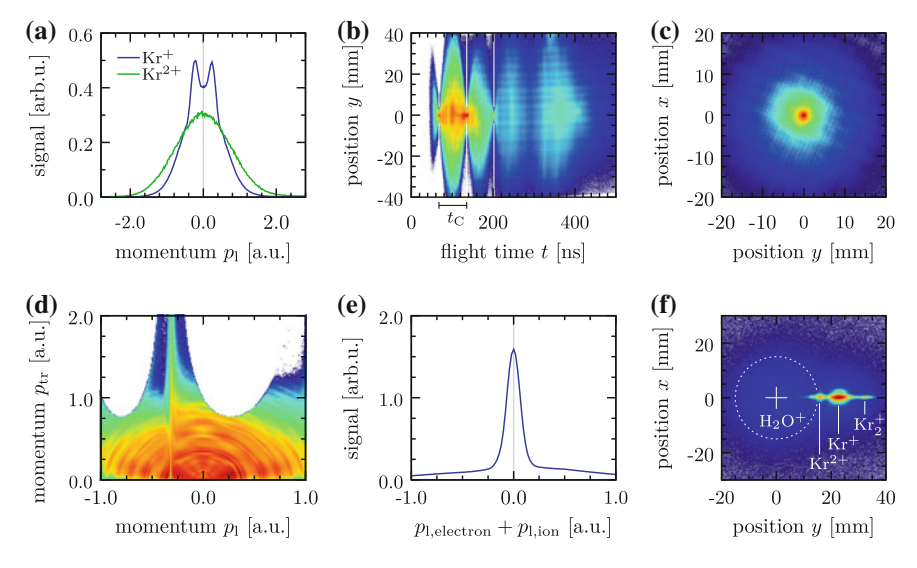


Fig. 4.10 Pictures obtained during important steps of the calibration procedure, see text for details. A krypton gas jet is ionized with radiation of 470 nm. **a** Longitudinal ion momentum p_1 for singly and doubly charged ions. **b** Cyclotron motion of the electrons. **c** Spatial distribution obtained on the electron detector. **d** Two-dimensional electron momentum distribution. **e** Sum of longitudinal momenta for ions and electrons recorded in coincidence for single ionization. **f** Spatial distribution obtained on the ion detector. The color scale used is a logarithmic version of the one displayed in Fig. A.1a

cyclotron period, the electrons' impact positions are concentrated onto one single spot, which allows a direct determination of $t_{\rm C}$. However, initially, the coordinate of this spot depends on the flight time rather than representing the center of the detector. Electrons with large flight times experience the magnetic field in other parts of the spectrometer and—due to the inhomogeneities mentioned before—are slightly deflected from their spiral trajectory. Quadratic polynomials $at^2 + bt + c$ are fitted through the impact positions observed with respect to x and y at multiples of $t_{\rm C}$ and subsequently used to correct the electron impact positions. After this procedure, the impact positions at multiples of the cyclotron period are aligned on the horizontal axis, see Fig. 4.10b, and the corresponding two-dimensional time-integrated spatial distribution, Fig. 4.10c, is centered around the origin.

The changeable parameters were chosen such that the overall result for the *ion* longitudinal momenta were optimized. It is not surprising that such setting does not perfectly work for the electrons. For example, the axis of symmetry in the two-dimensional momentum distribution in Fig. 4.10d, at first is not located exactly at $p_1 = 0$. Its position can be optimized by a linear scaling of the electron flight times t according to t' = at with $a \sim 1$. The sum of the longitudinal momenta obtained for coincident ions and electrons, see Fig. 4.10e, then features a sharp peak centered around zero resembling momentum conservation. Since certain processes selectively produce electrons with sharp energies, see Sect. 3.4, corresponding ring-like structures are usually visible which are used to linearly scale the transverse momentum component p_{tr} . If the underlying physical process forming the structures and thus their energy is known, a linear scaling of the full picture p' = bp with $b \sim 1$ finally can yield an *absolute calibration*. The approach of a direct, linear scaling of the measured flight times and the momenta within the calibration procedure has already been used e.g. in [17].

In contrast to the case of the electrons, the center of the ion detector, the position centered above the interaction volume, is not simply emphasized by the particles' impact positions. In fact—regarding exclusively ions originating from the jet—the center is expected to be hit rarely. Therefore, the water ions originating from the residual gas are used to determine the central position on the detector. After compensation of the initial offset, the detector can be turned such that the gas jet appears aligned horizontally along the \hat{e}_y axis of the coordinate system, see Fig. 4.10f. As discussed in Sect. 4.2.3, this simple rotation sufficiently compensates the influence of the magnetic field on the ions' trajectories. The relative rotation of the electron detector and the scaling of the transverse momentum components of the ions can be adjusted again by utilization of the correlation between the particles when originating from the same ionization event.

At the end of the calibration procedure, the reconstructed momentum components of the ions and electrons are consistent in direction and magnitude. This means for example that the electron and the ion created in a single ionization process have momenta with opposite direction and the same magnitude. The (very small) momentum carried by the photons is neglected in this respect. Figure 4.11 summaries the relations between the different momentum components provided by steps of the calibration procedure.

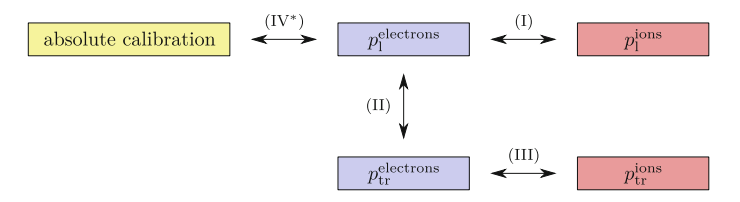


Fig. 4.11 Methods used in the calibration procedure to relate the different momentum components to each other, see also text: (I) Longitudinal momenta sum of electrons and ions, see Fig. 4.10e. (II) Shape of the rings formed in two-dimensional electron momentum spectra by electrons with the same energy, see Fig. 4.10d. (III) Same as for (I) but for the transverse momentum components of the electrons and ions. (IV*) Identified structures of known momentum (if available)

4.3 Performance of the System

The most important features characterizing the performance of a spectrometer are the acceptance and the resolution for the different particles of interest. These quantities will briefly be discussed in the following.

4.3.1 Acceptance

As discussed earlier, photoionization experiments usually produce electrons much faster than the corresponding ions. Detection of the latter is therefore typically less complicated. Even (small) clusters are safely projected onto the detector, see Fig. 4.10f. However, dissociation processes may result in fast ions which might partly miss the detector. In the experiments presented within this work this is relevant for the results obtained e.g. in $H_2 \longrightarrow 2H^+ + 2e^-$ processes, see Sect. 7.1. The transverse acceptance for these very light ions can be estimated roughly from the distance of the center of gravity of the spot observed to the edge of the ion detector and Eq. (4.10) to a momentum of about 5 a.u. or an energy of about 14 a.u. The longitudinal acceptance is limited by the potential difference of the interaction region and the electron detector since fast ions initially directed towards the latter have to return before reaching the end of the spectrometer. For the typical parameters given in Table 4.1 and a singly charged particle this limit is at an energy of about 20 eV or 0.7 a.u. Depending on the mass of the ion this calculates for example to momenta of about 52 (H⁺) or 470 a.u. (Kr⁺).

In case of the longitudinal momentum, the same arguments can be used for a rough estimation on the acceptance in the case of the electrons which then typically yields $60\,\mathrm{eV}$ or $2.2\,\mathrm{a.u.}$ of energy corresponding to a momentum of $2.1\,\mathrm{a.u.}$ However, the determination of the transverse acceptance for electrons is much more complex and depends on the flight times. This is a consequence of the magnetic field which confines the electrons on spiral trajectories. Figure $4.12\mathrm{a}$ displays the radius r against the flight time t for the same data-set as shown in Fig. 4.10. At integer multiples of the cyclotron

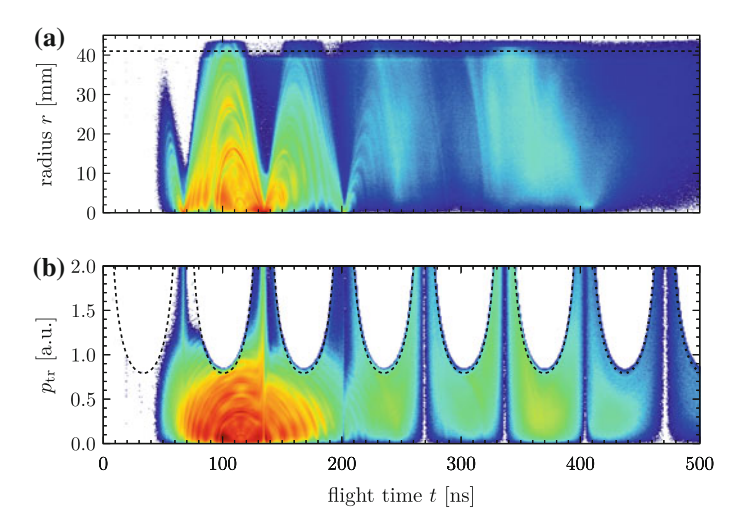


Fig. 4.12 Electron acceptance of the spectrometer. **a** Measured radius r over the flight time t of the electrons. A "node" is appearing after each integer number of cyclotron periods $t_{\rm C}$. Electrons having this flight times are projected onto the center of the electron detector regardless of their transverse momentum. The radius of the detector is shown as *black dashed line*. Counts above appear due to a not perfectly centered electron distribution. **b** Reconstructed transverse momentum $p_{\rm tr}$. At flight times where nods appeared in (**a**), the reconstruction only gives arbitrary values. The *white line* resembles the acceptance, the highest transverse momentum $p_{\rm tr}^{\rm max}$ an electron may own and still be detected. The color scale used is a logarithmic version of the one displayed in Fig. A.1a

period t_C all electrons regardless of their initial transverse momentum $p_{\rm tr}$, hit the detector at the same central position and consequently the acceptance is infinite (as long as the particles do not hit e.g. the spectrometer electrodes on their trajectories). At the same time, for these electrons any information about $p_{\rm tr}$ is lost. Mathematically, a division by zero occurs in Eq. (4.8). Due to the finite accuracy in time and position determination in the experiment the reconstruction already fails in the closer vicinity of this singularities. In contrast to this, right in the middle between these flight times, the acceptance reaches its minimum and the resolution its maximum: The electrons are detected in the moment when they have the largest distance to the center and R = r/2, cf. Fig. 4.7. As can be seen from Fig. 4.12b, electrons with a transverse momentum component smaller than about 0.8 a.u. corresponding to an energy of about 0.32 a.u. or 8.7 eV are detected independent of their flight time. It is reasonable to regard this as the "overall" transverse acceptance of the spectrometer for electrons.

4.3.2 Resolution

The momentum resolution which can be achieved with a REMI depends—beside the geometry and field strengths—on the momentum component considered, the particle

type and—in the case of the ions—on their mass and the temperature of the gas jet. If the uncertainty Δp is calculated by Gaussian error propagation of Δt and Δr in Eqs. (4.2) and (4.8), a general decrease of the resolution can be expected with increasing mass of the particles [17]. A quantity often used as indicator of the overall spectrometer performance is the width of the peak formed in the momentum sum distribution of correlated particles arising from single ionization events, see e.g. [14]. In Fig. 4.13, this is shown for single ionization of two different species, krypton and molecular hydrogen, at a wavelength of 470 nm.

The difference in width amounts to almost one order of magnitude. For the hydrogen measurement, a width of less than $\Delta p_1 = 0.018$ a.u. is observed. Since both, an electron and an ion are involved in forming the peak, its width is a measure of the "overall" spectrometer resolution. As the electron resolution can be expected to be constant, the difference in widths can be attributed to the different resolutions for the ions. However, the focus of this work lies on electron momentum distributions. The largest value for $p/\Delta p$ observed in the measurements is about 100 and 85 for p_1 and $p_{\rm tr}$, respectively, see Fig. 6.5a.

4.3.3 General Limitations and the Importance of Excellent Vacuum Conditions

Although REMIs offer many advantages such as kinematically complete data and excellent resolution, they also have general limitations. The most striking drawback of the technique, compared with e.g. VMI and others, is the restriction to essentially one ionization event per laser shot. Even though the detection of several particles is possible and the particles stemming from a certain ionization event can in principle be identified by their vanishing momentum sum, technical limitations often prevent a successful measurement if more than one particle is ionized. These are, for example,

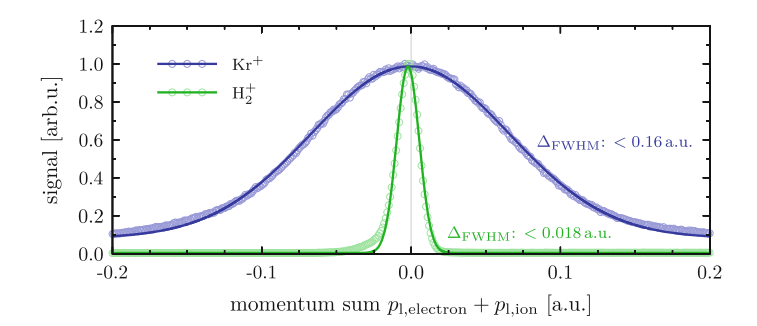


Fig. 4.13 Sum of longitudinal momentum components of ion and associated electron from single ionization of krypton and molecular hydrogen at a wavelength of 470 nm (*circles*). The FWHM values are obtained from (unweighted) Gaussian fits shown as *solid lines*

the finite dead time of the detectors and the maximum number of particles detected for every laser shot. Due to the fixed repetition rate of about $3\,\mathrm{kHz}$ in the measurements performed in this work, see Sect. 2.2.1, statistics may be an issue and long acquisition times result. Since every laser shot ionizing residual gas in the chamber is "lost" for the data analysis in this respect, special care has to be taken to minimize those events. Therefore, carefully selected materials, differential pump sections along the gas jet, adequate baking of the main chamber and an efficient beam dump are used to achieve excellent vacuum conditions. The operating pressure in the main chamber of the REMI used in this work is well in the 10^{-11} mbar regime.

References

- J.K. Böhlke et al., Isotopic compositions of the elements, 2001. J. Phys. Chem. Ref. Data 34, 57–67 (2005). doi:10.1063/1.1836764
- C. Bordas et al., Photoelectron imaging spectrometry: principle and inversion method. Rev. Sci. Instrum. 67, 2257–2268 (1996). doi:10.1063/1.1147044
- 3. I.N. Bronstein et al., Taschenbuch der Mathematik. Europa-Lehrmittel (2005)
- N. Camus et al., Attosecond correlated dynamics of two electrons passing through a transition state. Phys. Rev. Lett. 108, 073003 (2012). doi:10.1103/PhysRevLett.108.073003
- 5. Wolfgang Demtröder, Experimentalphysik 1: Mechanik und Wärme (Springer, Berlin, 2006)
- A. Dorn et al., Double ionization of helium by fast electron impact. Phys. Rev. Lett. 82, 2496–2499 (1999). doi:10.1103/PhysRevLett.82.2496
- R. Dörner et al., Cold target recoil ion momentum spectroscopy: a 'momentum microscope' to view atomic collision dynamics. Phys. Rep. 330, 95–192 (2000). doi:10.1016/S0370-1573(99)00109-X
- 8. R. Dörner et al., Multiple ionization in strong laser fields, in *Advances in Atomic, Molecular, and Optical Physics*, vol. 48, ed. by B. Bederson, H. Walther (Academic Press, New York, 2002), pp. 1–34
- A. Fischer et al., Electron localization involving doubly excited states in broadband extreme ultraviolet ionization of H₂. Phys. Rev. Lett. 110, 213002 (2013). doi:10.1103/PhysRevLett. 110.213002
- B. Fischer, Time resolved studies of H₂⁺ dissociation with phase-stabilized laser pulses. Ph.D. thesis. Ruperto-Carola University of Heidelberg, Germany. URN: urn:nbn:de:bsz:16-heidok-107569 (2010)
- O. Jagutzki et al., Multiple hit readout of a microchannel plate detector with a three-layer delayline anode. IEEE Trans. Nucl. Sci. 49, 2477–2483 (2002). doi:10.1109/TNS.2002.803889
- 12. M. Kremer, Einfluß der Träger-Einhüllenden-Phase auf die Wechselwirkung ultrakurzer Laserpulse mit Molekülen. Ph.D. thesis. Ruperto-Carola University of Heidelberg, Germany. URN: urn:nbn:de:bsz:16-heidok-100544 (2009)
- D.R. Miller, Free jet sources, in *Atomic and Molecular Beam Methods, Chap.* 2, vol. 1, ed. by G. Scoles (Oxford University Press, New York, 1988), pp. 14–53
- R. Moshammer et al., Low-energy electrons and their dynamical correlation with recoil ions for single ionization of helium by fast, heavy-ion impact. Phys. Rev. Lett. 73, 3371–3374 (1994). doi:10.1103/PhysRevLett.73.3371
- 15. R. Moshammer et al., A 4π recoil-ion electron momentum analyzer: a high-resolution "microscope" for the investigation of the dynamics of atomic, molecular and nuclear reactions. Nucl. Instrum. Methods Phys. Res. Sect. B: Beam Interact. Mater. Atoms **108**, 425–445 (1996). doi:10.1016/0168-583X(95)01259-1

References 75

16. R. Moshammer et al., Recoil-ion momentum spectroscopy and "reaction microscopes", in *Many-Particle Quantum Dynamics in Atomic and Molecular Fragmentation, Chap.* 2, ed. by J. Ullrich, V. Shevelko (Springer, Berlin, 2003), pp. 33–58

- 17. T. Pflüger, Electron impact ionization studies of small rare gas clusters. Ph.D. thesis. Ruperto-Carola University of Heidelberg, Germany. URN: urn:nbn:de:bsz:16-opus-133254 (2012)
- RoentDek. MCP Detector with Delay-Line Anode (Version 11.0.1403.1) (2014). http://www.roentdek.com/manuals/MCP%20Delay%20Line%20manual%20(11.0.1403.1).pdf. Accessed 30 July 2014. RoentDek Handels GmbH
- RoentDek fADC8. fADC8 description (2014). http://www.roentdek.com/products/ electronics_description/fADC8description.pdf. Accessed 1 Aug 2014
- A. Rudenko et al., Exploring few-photon, few-electron reactions at FLASH: from ion yield and momentum measurements to time-resolved and kinematically complete experiments. J. Phys. B: At. Mol. Opt. Phys. 43, 194004 (2010). doi:10.1088/0953-4075/43/19/194004
- A. Senftleben, Kinematically complete study on electron impact ionization of aligned hydrogen molecules. Ph.D. thesis. Ruperto-Carola University of Heidelberg, Germany. URN: urn:nbn:de:bsz:16-heidok-100153 (2009)
- 22. Stanley E. Sobottka, Mark B. Williams, Delay line readout of microchannel plates. IEEE Trans. Nucl. Sci. 35, 348–351 (1988). doi:10.1109/23.12740
- 23. J. Ullrich et al., Recoil-ion momentum spectroscopy. J. Phys. B: At. Mol. Opt. Phys. **30**, 2917–2974 (1997). doi:10.1088/0953-4075/30/13/006
- Joachim Ullrich et al., Recoil-ion and electron momentum spectroscopy: reaction-microscopes.
 Rep. Prog. Phys. 66, 1463–1545 (2003). doi:10.1088/0034-4885/66/9/203
- Th Weber et al., Recoil-ion momentum distributions for single and double ionization of helium in strong laser fields. Phys. Rev. Lett. 84, 443–446 (2000). doi:10.1103/PhysRevLett.84.443

Chapter 5 Tunnel Ionization from a Coherent Superposition in Ar⁺

This chapter presents the results obtained in measurements where a coherent superposition of electronic states, a spin-orbit wave packet (SOWP), in singly charged argon ions is utilized as an initial state for further tunnel ionization. The dynamic target enables state-selective investigation of the tunneling process and thus the testing of fundamental predictions about the electron momenta directly after tunneling. Although modern streaking-experiments including the attoclock rely on a well known initial momentum distribution, many aspects are not yet studied in detail. Equation (5.6), relating the transverse momentum distribution after tunneling to the respective situation in the bound orbital, is one prominent example. By utilizing the SOWP as dynamical target, the product form of the relation is tested—to the best of our knowledge—for the first time in an experiment. The main results and hence large parts of this chapter have already been published in [10]. First, in Sect. 5.1, SOWPs are introduced in a general fashion by a summary of the theoretical and experimental work carried out in the past, with particular regard on the possibility of SOWP creation via ionization with a strong laser field. Section 5.2 presents the experimental results obtained within this work and explains the model used to interpret the data. Both will follow [10], moreover provide supplementary information.

5.1 Spin-Orbit Wave Packets in Noble Gas Ions

If the coupling between the orbital angular momentum l and the spin s, the *spin-orbit coupling*, for the single electrons in an atomic shell is small, the system may be described best in terms of LS- or Russell-Saunders-coupling [18, §72]: The angular momenta and spins of the electrons couple first among themselves according to $\vec{L} = \sum_i \vec{l}_i$ and $\vec{S} = \sum_i \vec{s}_i$ followed by a coupling of the total angular momentum with the total spin according to $\vec{J} = \vec{L} + \vec{S}$. Although this scheme is most successful for the light atomic species, it allows a qualitative description also for heavier species, in particular in their ground state [18, §72].

The situation in a ground state atom has to be described in the *coupled basis*, using the eigenstates of the systems' extended atomic Hamiltonian, see e.g. [18, §72]. However, if the atom is exposed to a sufficiently strong external electric (laser) field, the situation changes substantially: Since the (non-relativistic) field exclusively interacts with the spatial part of the wave functions but not with the spin, the states become "uncoupled", see e.g. [30]. The interaction between laser and atom can then be treated in the *uncoupled basis*. This was already implied in Sect. 3.2, where all the equations for tunnel ionization depend on l and l rather than on l and l and l rather than on l and l and l and l rather than on l and l and l rather than on l rather than on l rather than on l rather than l rather than on l rather than l ra

These aspects gives rise to the following scenario [30, 32]: A laser pulse interacts with an atom and induces an electronic transition to a certain excited state, described in the uncoupled basis. Later, when the system approaches the field-free situation, this state has to be evaluated in the coupled basis. The respective expansion coefficients are given by the well-known *Clebsch–Gordan coefficients*, see e.g. [5, Fig. 40.1]. As a consequence, the population of one certain state in the transient uncoupled basis translates into a coherent superposition of states in the coupled basis. In the most simple case, namely a superposition of two states, this results in an electronic wave packet with a characteristic period of [30]

$$T_{\rm S} = 2\pi/\Delta\omega,\tag{5.1}$$

where $\Delta\omega$ is the energy difference of the two coupled states involved.

The timescale of the induced dynamics crucially depends on the system and is in the order of 70 ps for Rydberg states in cesium [30]. In the following, the mathematical description of a SOWP formed by the coherent superposition of a ${}^2P_{1/2}$ and a ${}^2P_{3/2}$ state is given, as it was carried out for the special case of alkali atoms in [30]. As shown in [32] and discussed later, the equations obtained can also be used to describe a SOWP in noble gas ions, involving the collective motion of five valence electrons.

Consider a single electron of spin projection $m_s = \pm 1/2$ to be excited during a laser pulse to a (uncoupled) state Ψ_{l,m,m_s} , here the selected state $\Psi_{1,0,\pm 1/2}(t=0)$. Using the Clebsch–Gordan coefficients, see e.g. [5, Fig. 40.1], this state can be evaluated in the coupled basis Φ_{J,J_m} to describe the situation after the laser pulse is over [30]

$$\Psi_{1,0,\pm^{1/2}}(t=0) = \sqrt{\frac{2}{3}}\Phi_{3/2,\pm^{1/2}} \mp \sqrt{\frac{1}{3}}\Phi_{1/2,\pm^{1/2}}.$$
 (5.2)

This is the superposition of states forming the SOWP. The subsequent dynamics of the system can be calculated by applying the time evolution operator $\hat{T} = \exp\left(-i\hat{H}t\right)$, see e.g. [7, complement F_{III}]. Since the states $\Phi_{1/2,\pm 1/2}$ and $\Phi_{3/2,\pm 1/2}$ are eigenstates of the field-free system with energy $\omega_{1/2}$ and $\omega_{3/2}$, respectively, it follows for $t \geq 0$ [30]

$$\Psi_{1,0,\pm^{1/2}}(t) = \sqrt{\frac{2}{3}} \exp(-i\omega_{3/2}t) \Phi_{3/2,\pm^{1/2}} \mp \sqrt{\frac{1}{3}} \exp(-i\omega_{1/2}t) \Phi_{1/2,\pm^{1/2}}.$$
 (5.3)

This expression describes the evolution of the SOWP in the field-free environment. A common way to investigate such dynamics is the probing of the system with a second laser pulse arriving at a later time. The situation which is found by this pulse depends on the time delay t with respect to the first. The coupled states in Eq. (5.3) again have to be evaluated in the decoupled basis which yields [30]

$$\Psi_{1,0,\pm^{1/2}}(t) = \frac{\sqrt{2}}{3} \left(e^{-i\omega_{3/2}t} - e^{-i\omega_{1/2}t} \right) \Psi_{1,\pm 1,\mp^{1/2}} + \left(\frac{2}{3} e^{-i\omega_{3/2}t} + \frac{1}{3} e^{-i\omega_{1/2}t} \right) \Psi_{1,0,\pm^{1/2}}.$$
 (5.4)

Independent of the spin projection of the initially excited electron, the probability to "find" the system in a certain state is given by the absolute square of the respective prefactors in Eq. (5.4) and depends on the quantum number m as [30]

$$P_{m=0}(t) = \frac{5}{9} + \frac{4}{9}\cos(\Delta\omega t)$$

$$P_{|m|=1}(t) = \frac{4}{9} [1 - \cos(\Delta\omega t)], \qquad (5.5)$$

where $\Delta \omega = |\omega_{3/2} - \omega_{1/2}|$ is the spin-orbit splitting. The oscillation of a large fraction of the population between the different orbitals causes a unique fingerprint in the time-resolved ionization yield [30].

Now, the focus will return to noble gas atoms exposed to strong fields. As seen in Sect. 3.2, the ADK rate Eq. (3.4) describing the tunneling process in linearly polarized light is highly sensitive on the quantum number m, cf. (3.5), and favors ionization from the m=0 orbital over orbitals with |m|=1. For typical laser intensities between 10^{14} and 10^{15} W/cm², the ratio $\frac{w_{m=0}}{w_{|m|=1}}$ given by (3.5) calculates to about 15 to 47 for Ar and 34 to 108 for Ar⁺, respectively. In both cases it decreases with increasing intensity. Consequently, single ionization of the noble gas atom most likely removes an electron from the m=0 orbital of the valence shell.

As shown theoretically in [24, 32], this fact can be used to ignite a SOWP in the valence shell of noble gases, where—after tunnel ionization of one electron—the remaining five valence electrons in the singly charged ion are collectively oscillating. A treatment of the missing electron as a "hole" in the valence shell allows the use of the single-particle equations (5.2)–(5.5) in order to describe the system [24, 32]. However, the time-scale of the process is still determined by the spin-orbit splitting in the system. The creation of such a SOWP in ultrashort strong laser pulses could experimentally be observed in Ne⁺ and Ar⁺ [11] as well as in Kr⁺ [12, 31]. Once created, the wave packet is stable since no decay channels are present and the dynamics lasts at least for nanoseconds [11], presumably even much longer.

Two aspects have to be considered in order to select the perfect species for measurements with a REMI: First, since statistics is always important, the atoms (and the respective singly charged ions) should be relatively easy to ionize with the laser system available, which favors heavier species, see Table A.2. Second, in the optimal case, the laser pulses used are much shorter than the period of the SOWP.

The pulse duration of about 7 fs provided by the laser system, see Sect. 2.2.2, rules out the usage of Kr^+ and Xe^+ . Therefore, argon is the optimal candidate for the measurements.

5.2 A SOWP in Ar⁺ as Initial State for Further Tunnel Ionization

The dynamics of the multielectron SOWP launched by a strong laser pulse and the consequences for the electron momentum distributions arising from further ionization was studied theoretically in [32]. The authors implicitly propose an experiment, involving two ultrashort, linearly polarized laser pulses in a pump-probe scheme: The first pulse is utilized to remove an electron from the atomic p-shell, most likely from the m=0 orbital aligned along the laser pulse. Thus, as discussed in the previous section, a coherent superposition of the two electronic eigenstates $^2P_{1/2}$ and $^2P_{3/2}$ is created in the Ar^+ ion, which can be used as an initial state for further tunnel ionization in the second laser pulse. Due to the dynamics of the wave packet, the relative contributions from the two states to this second ionization process vary with the time delay between the two pulses or—in other words—can be controlled by controlling the delay. Two of the consequences predicted in [32] are a delay-dependent ion yield and the possibility to find the imprint of the SOWP in the transverse momentum distribution $W(p_\perp)$ (perpendicular with respect to the laser polarization) of the electrons freed in the second ionization step.

In particular the latter topic is extremely interesting: Since the transverse momentum of the freed electron is not affected by the (non-relativistic) laser field, the measured momentum distribution reflects the actual situation right after the tunneling process. However, this is only true as long as the Coulomb interaction between the electron and its parent ion is neglected. In fact, as will be discussed later, the transverse momentum distribution is altered by this interaction. Nevertheless, it is possible to obtain information about the tunneling process and the relation between the measured momentum distribution and the bound-state momentum. This will be shown in Sect. 5.2.4.

In recent work and as an extension to Eq. (3.6), the transverse momentum distribution is—if the Coulomb interaction with the nucleus is completely neglected—supposed to almost directly represent the bound-state momentum distribution in the respective orbital [3, 8, 14, 29, 32]. The tunneling process is understood as a "filter" of Gaussian shape, projecting the respective absolute square of the wave function in momentum space $\tilde{\Psi}_{(n,l,)m}$ onto the plane perpendicular to the laser polarization, into the continuum [3]

$$W_{\perp}^{m}(p_{\perp}) = |\tilde{\Psi}_{m}(p_{\perp})|^{2} \exp\left(-\frac{\sqrt{2E_{i}}}{F}p_{\perp}^{2}\right). \tag{5.6}$$

It is noteworthy that the exponential term also occurs in the original expression of the ADK model, cf. Eq. (3.6). Since the Gaussian filter term is identical for orbitals with the same ionization potential, the product form of Eq. (5.6) may in principal be tested by comparing the distributions arising in selective tunnel ionization starting from different orbitals. However, in typical strong-field experiments, state-selectivity for energetically close states is hard to achieve and the observed signal always contains contributions from several orbitals. In the following it is shown, how the utilization of a SOWP as an initial state for further tunnel ionization can overcome these problems, offer state-selective information about the tunneling process and thus allows to test the product form of Eq. (5.6).

In the experiment a pair of ultrashort laser pulses with linear polarization is created from the output of a femtosecond laser system by spectral broadening in a neon-filled hollow-core fiber and subsequent chirped-mirror compression followed by a Mach–Zehnder interferometer as described in Sects. 2.2.2 and 2.2.3, respectively. As described in the latter, the pulse duration is optimized beforehand by utilizing the output signals of a Stereo-ATI spectrometer and can thus be estimated to be 7 fs or less. The laser intensity can be determined to be about $5 \times 10^{14} \,\mathrm{W/cm^2}$, see Sect. 5.2.1. In order to avoid the nonlinear autocorrelation signal arising in the temporal pulse overlap, the time delay t is chosen with an offset of some periods. The argon gas jet is created with a prepressure of about 3 bar and truncated by the attenuation slits in front of the REMI, see Sect. 4.1, in order to limit the ion count-rate detected by the REMI to about 800 events/s.

Figure 5.1 shows the characteristic fingerprint the SOWP leaves in the timeresolved Ar⁺⁺ ion yield as predicted [32] and measured [11] before. As shown in Table 5.1, the oscillation period for Ar⁺ is about 23.3 fs. The periodicity obtained from the oscillation and the position readout of the Mach–Zehnder interferometer

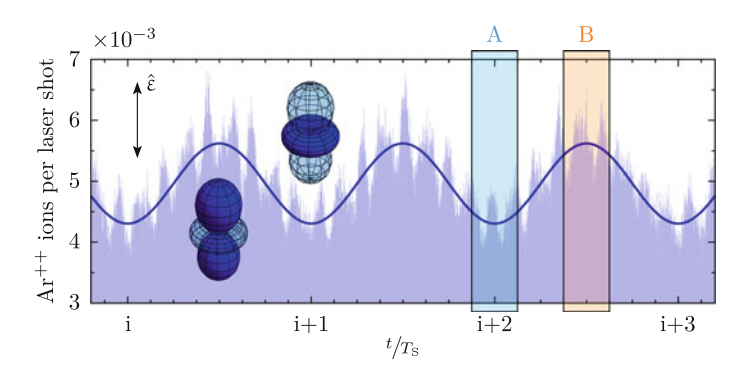


Fig. 5.1 Fingerprint of a SOWP in Ar^+ in the experimental ion yield (*light blue bars*). The *solid line* represents a sinusoidal fit to the data. Due to a higher ionization rate for the m=0 orbital in Ar^+ , the yield maximizes for phases of the SOWP, where the electron density in this orbital is highest as indicated by the inset orbitals. The fast oscillation arises from interference between the pulse pedestals of pump and probe pulse. Picture taken from [10] and slightly adapted, © 2014 American Physical Society.

Species	Spin-orbit splitting $\Delta\omega$ (meV) Period T_S of SOWP (fs)
Ne ⁺	96.8	42.7
Ar ⁺	177.5	23.3
Kr ⁺	665.8	6.2
Xe ⁺	1306.4	3.2

Table 5.1 Energy differences $\Delta\omega$ from [16] and resulting SOWP periods according to Eq. (5.1) for different noble gas ions

together with (2.27) is in good agreement with this value. Nevertheless, a final linear calibration of the time-axis t'=at with $a\sim 1$ is performed in order to find optimal agreement with the sinusoidal fit on the data shown additionally as solid line in Fig. 5.1.

At integer multiples of the period of the wave packet, $t = iT_{\rm S}$, the situation in the ion is exactly the same as directly after the preparation with the first laser pulse, the "pump" pulse: The electron density in the m=0 orbital is decreased due to the presence of the hole, cf. Eq. (5.5), and such is the total ionization rate since ionization from this orbital represents the main ionization channel for the ion. In contrast to this, at half periods $t=(i+1/2)T_{\rm S}$ the electron density maximizes hence the system is ionized more easily to ${\rm Ar}^{++}$. Interference spikes arise from temporal overlap of the pulses' pedestals.

An "event" recorded by the REMI consists of an ion of a certain species and—in the case of single and double ionization—of one or two associated electrons. In this two- or three- particle coincidence measurements, special care has to be taken according to the selection of the events to be further considered and processed in the data analysis. As it turns out, particles detected in coincidence do not always stem from the same ionization event. The correlation between the obtained momenta caused by momentum conservation can be utilized for event selection. In general, exclusively those events, in which exactly one ion (and no second) of the desired species is detected, are considered. In case of Ar⁺⁺, in addition only events are processed, where exactly two electrons are detected. The particles are then checked in terms of momentum conservation and only accepted if they stem from the same ionization event.

Figure 5.2a shows the correlation plot obtained for the longitudinal momenta of Ar^+ and the associated electrons in logarithmic scale. Pairs of particles originating from the same ionization event are found on the diagonal with negative slope. Only events between the two solid lines additionally shown are selected and further processed. The same can be done in the case of Ar^{++} , if the sum of the electron momenta is considered for the respective axis, see Fig. 5.2b. In (c) the photoelectron momentum spectrum of the selected electrons from (b) is shown. As discussed in Sect. 4.3, the cyclotron motion of the electrons leads to longitudinal momenta p_1 for which no information can be extracted along p_{tr} since all electrons hit the detector in one spot. These events are sorted out as well and hence not displayed in the picture.

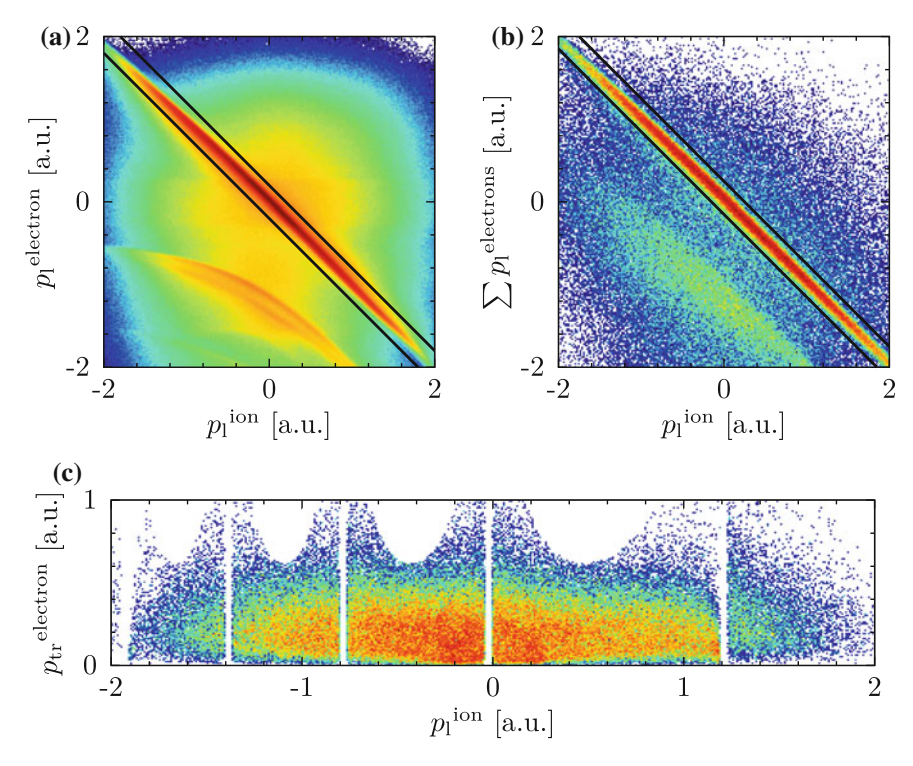


Fig. 5.2 Selection of associated ions and electrons from coincident data. In general only events are considered where exclusively one ion of the desired species is detected. **a** Longitudinal momenta of Ar⁺ ions and electrons measured in coincidence. Particles originating from the same reaction comprise anticorrelated momenta due to momentum conservation. These events form the diagonal structure from the *top left* to the *bottom right* in the figure. *Black solid lines* show the condition which is applied: Only events found between the lines are considered in the further data analysis. **b** Same as (**a**) but for a three-particle coincidence between Ar⁺⁺ and the two electrons associated. Here, it is the sum of the electron momenta which is anticorrelated to the ion momentum. **c** Electron momentum spectrum for the electrons selected in (**b**). Events with flight times close to integer multiples of the cyclotron period are sorted out due to the insufficient information about their transverse momenta obtainable. These events are also not considered in the further analysis. The color scale used is a logarithmic version of the one displayed in Fig. A.1a

It is reasonable to first examine the overall, time-integrated electron transverse momentum distributions, shown in Fig. 5.3 for the two individual steps of the sequential ionization, $Ar \rightarrow Ar^+$ and $Ar^+ \rightarrow Ar^{++}$, respectively. While the first distribution is directly accessible in coincidence with Ar^+ , the second one has to be reconstructed: From the (normalized) two-electron momentum distribution obtained in coincidence with Ar^{++} the (normalized) one for Ar^+ is subtracted and the second process thus approximately isolated. At first glance, the two distributions look surprisingly sim-

 $^{^{1}}$ Deviations could occur e.g. if the Ar $^{+}$ ions detected are preferentially in a different state than the Ar $^{+}$ ions serving as precursor for the second ionization step to Ar $^{++}$.

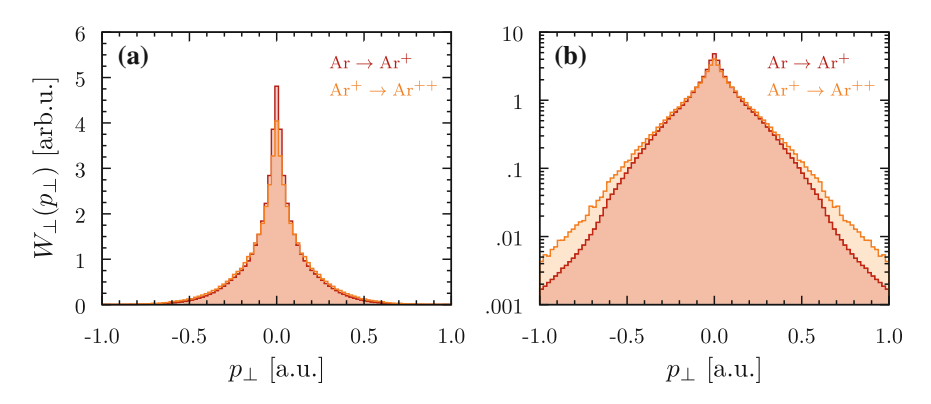


Fig. 5.3 Symmetrized, time-integrated, transverse momentum distributions for the two ionization steps $Ar \to Ar^+$ and $Ar^+ \to Ar^{++}$ obtained in the experiment in **a** linear scale and **b** logarithmic scale. The distributions only slightly differ in width. In both distributions, a sharp, cusp-like structure at zero momentum appears. The distribution for the second step has to be reconstructed, see text for details

ilar and only slightly differ in width although the shape of the Gaussian filter in Eq. (5.6) is clearly different. The overall shape of the distributions observed is not at all resembling what one would expect based on this expression. In particular the sharp cusp-like structures arising at zero momentum seem peculiar. However, this structure, commonly known as "Coulomb Singularity", has already been observed in other measurements with strong linearly polarized laser pulses for different noble gas atoms and can be related to the Coulomb interaction between the outgoing electron(s) and the parent ion [25].

The massive modification of the electron momentum distributions caused thereby raises the question, whether an imprint of the initial state, as predicted by Eq. (5.6), is preserved and detectable at all. More than a decade ago, in investigations of ionization processes in highly-energetic ion-atom collisions, the same question was asked: In different experiments, similar cusp-like structures caused by the Coulomb interaction were visible [20, 26]. However, as could be shown in [9, 21], the information about the underlying atomic structure indeed is preserved to some extent. Later it will be shown that this is also true for strong-field ionization.

5.2.1 Estimation of the Laser Intensity

Since the ionization process strongly depends on the field strength, the knowledge about the laser intensity present in the experiment is crucial in order to obtain realistic results from the model, which will be discussed in Sect. 5.2.2. The laser intensity is extracted from a Gaussian fit to the measured longitudinal momentum distribution $W(p_{\parallel})$ of the singly charged Ar⁺ ions. According to (3.6), the field strength

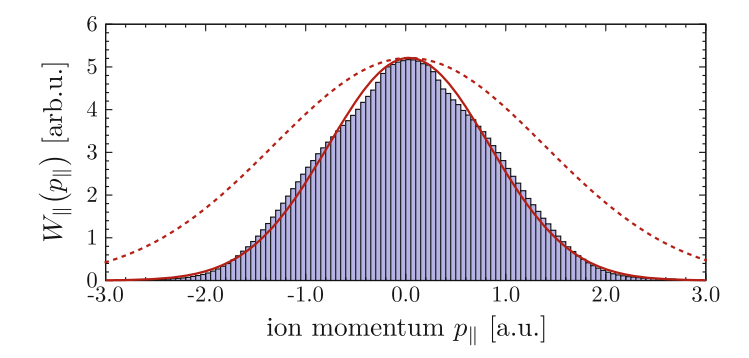


Fig. 5.4 Estimation of the laser intensity from the experimental data. Data (*bars*) together with best fit to the data (*solid line*) from which the intensity is derived. The *dashed line* visualizes the expected distribution for an intensity twice as high

(and thus the intensity) can directly be determined from the width of the distribution. For the fit, a wavelength of 790 nm is assumed. The experimental distribution and the best fit to the data is shown in Fig. 5.4, resulting with Eq. 3.6 in an intensity of $5.1871 \times 10^{14} \, \text{W/cm}^2$. Please note that the number of digits given by far overestimates the accuracy of the method. However, since the fit parameter is used in the model, it is given here with this accuracy. For later argumentation and in order to visualize the magnitude of change in the width of the distribution for a different intensity, the respective curve is shown for the doubled intensity value as dashed curve.

The laser intensity is ideally matching the requirements of the experiment: On one hand, it is high enough to avoid NSDI as the main double ionization process [4, 19]. On the other hand the intensity is not too high such that only a small fraction of atoms is directly doubly ionized in one of the two laser pulses. Furthermore, the Keldysh parameter, see Sect. 3.1, for the second ionization step $Ar^+ \to Ar^{++}$ calculates with atomic data from Table A.2 to $\gamma \approx$ 0.7. Hence, the ionization clearly takes place in the tunneling regime.

In this context it is also important to remind the properties of the laser focus discussed in Sect. 2.1.3 and the intrinsic averaging of different intensities in the experiment caused thereby. The extracted intensity value should be seen as the best "effective" value optimizing the agreement between experiment and the ADK model. Nevertheless, intensity estimations based on measured momentum distributions are widely-used, often for experiments with circularly polarized light, see e.g. [1, 28]. A more precise method has been developed only for the ionization of atomic hydrogen up to now [23].

5.2.2 The "Scaled Hydrogen" Model

The aim of the model presented in this section is—based on Eq. (5.6)—the prediction of electron transverse momentum distributions obtainable at different phases of the SOWP and thus at different electronic configurations of the dynamical target. This requires knowledge about the wave functions in momentum space $\tilde{\Psi}_m(p_\perp)$. Since argon with its 18 electrons is a fairly complicated atom, a high level of simplification has to be accepted in order to build a model that is able to deliver results with reasonable effort and computational time.

If instead of an argon atom a hydrogen atom is considered, the situation dramatically simplifies since appropriate analytic solutions are available. The model, used in [10] and described in the following is based on this hydrogenic situation. The adaption to the actual situation in Ar^+ is performed by an appropriate "scaling" of the wave functions, an approach also used e.g. in [8, 32]. The model resembles the one used in [32], however differences exist in details concerning the scaling and the calculation of the ionization rates to Ar^{++} .

Ionization Rates and Individual Contributions of the Orbitals

The first step in the experimental scheme is the preparation of the wave packet by single ionization of Ar in the pump pulse. The model in general only considers the electrons in the valence shell, in the case of neutral Ar six 3p electrons. Using the intensity value extracted in the last section, Eq. (3.5) yields—with the ionization potential from Table A.2— $w_{m=0}/w_{|m|=1}\approx 20.5$ for a single electron and thus—considering the number of electrons in each of the orbitals—an overall relative contribution of the |m|=1 orbitals to the ionization to Ar⁺ of less than 9%. In the following, this minor channel is neglected, hence the first ionization is assumed to always take place from the m=0 orbital. This assumption may lead to a slightly overestimated contrast in comparison to the experiment but, apart from that, does not have any further influence. In the model, the hole is thus defined to be created in the m=0 orbital by the pump pulse.

Further, the transitions to the field-free situation and back are assumed to happen instantaneously, such that the wave function can simply be evaluated in the new basis as discussed in Sect. 5.1. In this respect, the pulses are treated as of infinitely short duration. The SOWP is starting its dynamics in the Ar⁺ ion as discussed in Sect. 5.1.

The interaction with the probe pulse after a certain time delay t is treated as follows: The hole density in the orbitals is given by Eq. (5.5) and thus the electron density in the orbitals can simply be calculated as $2 - P_{m=0}(t)$ respectively $4 - P_{|m|=1}(t)$. The relative contribution of the orbitals is again calculated with (3.5) now using the ionization potential of the singly charged ion, see Table A.2. The (small) change of the ionization potential due to the excitation of the ion is neglected here.

Due to the increased ionization potential compared to the neutral atom, the contribution of the |m| = 1 orbitals is further suppressed and now varies for the given intensity between about 7.8% (at t = 0 and integer multiples of T_S) and 3.3% (at half periods) of the total signal. Figure 5.5 gives an overview about the configuration

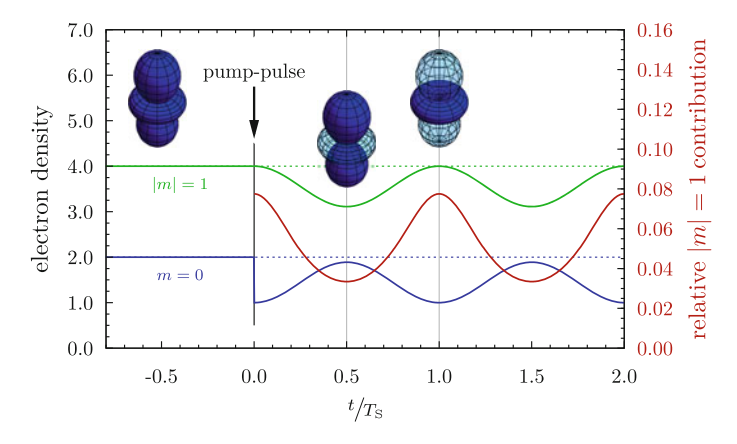


Fig. 5.5 Situation in the Ar atom and ion as treated in the model. The *blue* and the *green line* show the total number of electrons in the m=0 and |m|=1 orbitals, respectively. At t=0, the pump pulse instantaneously removes one of the electrons in the m=0 orbital and ignites the SOWP and thus a periodic redistribution of the remaining electrons. The *red curve* shows the varying relative contribution of the |m|=1 orbital to the subsequent second ionization to Ar⁺⁺ as calculated by the model, see text for details

of the electronic shell as assumed in this model and the varying relative contribution of the |m| = 1 orbitals induced by the SOWP.

Momentum Distributions for Ionization from the Individual Orbitals

Due to the laser field present during the ionization, the decoupled basis has to be considered as discussed in Sect. 5.1. The calculation of the momentum distributions resulting from ionization of the different orbitals using Eq. (5.6) requires knowledge of the respective wave functions in momentum space. For hydrogen-like systems, these can be derived analytically [22] and—as a direct consequence of the radial symmetry of the Hamiltonian—are given by a product of a radial and angular part like in the spatial domain, see e.g. [18, § 32]. The latter is given by the spherical harmonic functions Y_{lm} in both domains, see e.g. [5, Fig. 40.1]. In momentum domain it is [13, Sect. 9.1.3]

$$\tilde{\Psi}_{(n,l,)m}(p,\theta_p,\varphi_p) = \tilde{F}_{n,l}(p) \cdot Y_{lm}(\theta_p,\varphi_p), \tag{5.7}$$

with the radial part

$$\tilde{F}_{n,l}(p) = 2^{2l+2} n^2 l! \sqrt{\frac{2(n-l-1)!}{\pi Z^3(n+l)!}} \left(\frac{np}{Z}\right)^l \frac{Z^{2l+4}}{\left(n^2 p^2 + Z^2\right)^{l+2}} C_{n-l-1}^{l+1} \left(\frac{n^2 p^2 - Z^2}{n^2 p^2 + Z^2}\right)$$
(5.8)

and the Gegenbauer polynomials C_{n-l-1}^{l+1} , see e.g. [13, Sect. 9.4.3]. With n=3 and l=1 for the valence electrons in argon and $C_1^2(x)=4x$, Eq. (5.7) reads

$$\tilde{\Psi}_{m}(p,\theta_{p},\varphi_{p}) = \frac{216\sqrt{2}}{\pi} Z^{7/2} \frac{p(9p^{2} - Z^{2})}{(9p^{2} + Z^{2})^{4}} \cdot \begin{cases} \sqrt{2}\cos(\theta_{p}) & m = 0\\ \mp \sin(\theta_{p}) e^{\pm i\varphi_{p}} & m = \pm 1. \end{cases}$$
(5.9)

The square of this analytic expression can now be projected onto the plane transverse to the laser polarization defined by $\theta_p = \pi/2$, or—if appropriate Cartesian coordinates are used—the \hat{e}_x - \hat{e}_y -plane by numerical integration along \hat{e}_z . This procedure yields (numerically) the functions $|\tilde{\Psi}_m(p_\perp)|^2$. However, up to now, the result is only valid in the case of atomic hydrogen (Z=1) or any hydrogen-like ion $I^{(Z-1)+}$ with (Z>1). The situation in argon is substantially different. Due to the large amount of electrons, in particular in the inner shells, the nuclear charge Z is screened to some extent such that a particular valence electron effectively interacts with an *effective charge* $Z^* < Z$. Since also the valence electrons, in particular those with low angular momentum l, have a finite probability distribution close to the nucleus, the calculation of Z^* involves the full knowledge of the full spatial electron densities and thus the knowledge of the wave functions themselves.

The simplest approach, which is also used in this work, is the determination of Z^* such that the ionization potential is correctly reproduced. From the commonly known equation for the binding energy of the hydrogen atom $E_i^H = Z^2/2n^2$, see e.g. [13, Sect. 9.1.1], it follows

$$Z^* = \sqrt{2E_i}n. \tag{5.10}$$

Together with the atomic data from Table A.2 this yields $Z^* = 3.23$ a.u. and $Z^* = 4.28$ a.u. for the valence electrons of Ar and Ar⁺, respectively.

Alternatively, an effective quantum number n^* can be defined likewise, $n^* = \frac{Z}{\sqrt{2E_i}}$ as e.g. done (in a different context) in [2]. The definition of this effective quantum number was implied already in Eq. (3.5). However, in the context of atomic wave functions, non-integer quantum numbers are not convenient. The utilization of an effective charge in Eq. (5.7) or Eq. (5.9) can be interpreted as a scaling of the hydrogenic wave function both in momentum and spatial domain.

For completeness, it should be mentioned here that other scaling approaches exist and are used for similar calculations. For example, the effective charges may be estimated using Slater's rules for the atomic screening constants [27]. These rules were later refined by comparison with numerically calculated values using self-consistent-field methods [6]. The latter yields e.g. $Z^* \approx 2.25$ a.u. in the case of Ar^+ . Such values were used for example in [8] to calculate the electron transverse momentum distributions. However, violating Eq. (5.10) and hence predicting a completely wrong ionization potential, these values contradict the hydrogenic approach of the model. Therefore the values directly obtained from Eq. (5.10) are used.

5.2.3 Transverse Momentum Distributions

The electron transverse momentum distributions obtained in the experiment were already shown in Fig. 5.3. Now, the respective predictions can be calculated using the model discussed in the previous section. Figure 5.6a shows both the Gaussian filter $\hat{F}(p_{\perp})$ and the projected wave functions (solid curves) for the first ionization step, $Ar \to Ar^+$. The insets display the angular distribution of the orbitals in the same color code. The experimental data for this first ionization step is shown in (b) together with the distribution calculated with the model (red dashed curve). In addition, the individual distributions arising from the different orbitals weighted by their relative contribution are shown. The curve for |m|=1 is multiplied by a factor of 10 for improved visibility. Figure 5.6c displays the same as (b) but for the second ionization step, $Ar^+ \to Ar^{++}$. Due to the SOWP, the electron density and hence the relative contribution of the orbitals is time dependent in this case. The cycle-averaged distributions are shown as solid curves while semi-transparent areas display the expected variation. For the blue and the red curve, the variation is too small to be clearly visible.

Along the SOWPs' evolution, the electron transverse momentum distribution is expected to change slightly its width, see [32]. However, as the model used does not account for the Coulomb interaction with the parent ion at all, the cusp arising at zero momentum in the experiment is not reproduced. In return to [10], a more elaborated theoretical investigation has been performed beyond the simple model described here, namely solving the TDSE in SAE approximation with consideration of the Coulomb interaction [15]. The resulting momentum distributions from these calculations resemble the cusp-structure, however they are more narrow than the ones experimentally obtained.

Although the difference between experimental results and the model prediction is striking due to the Coulomb interaction, the similar widths of the two distributions obtained for the single ionization steps are reproduced by the model. This can now be understood as the result of the mutual compensation of three different effects [10]:

- 1. The shape of the bound-state wave function (in momentum space) is—according to Eq. (5.6)—expected to directly influence the width of the distribution. For Ar⁺ compared to Ar, the wave functions are spatially confined to a smaller volume due to the higher effective charge Z*. This results in broader distributions in momentum space which translates to a likewise *broader* distribution expected for the second ionization step.
- 2. The width of the Gaussian filter is the second term which—according to Eq. (5.6)—directly influences the observed width. Due to the higher ionization potential of Ar⁺ compared to Ar, the filter is more narrow for the second step. Therefore, this aspect speaks for a *more narrow* momentum distribution for the second ionization step.
- 3. The relative contribution of the different orbitals also has to be considered. Due to the higher ionization potential of Ar^+ compared to Ar, the ionization from the m=0 orbital is even more dominant than in Ar, cf. Eq. (3.5). This also

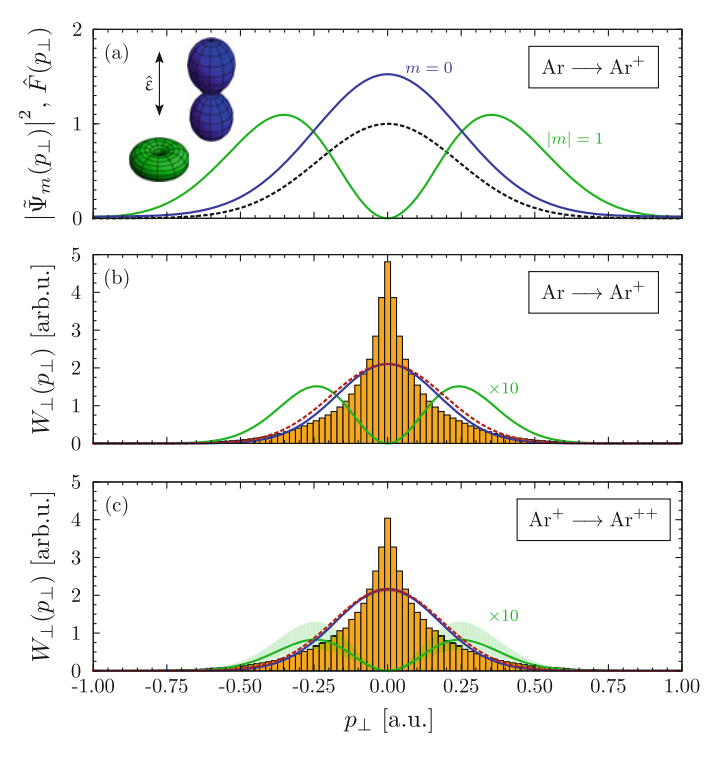


Fig. 5.6 Measured transverse momentum distributions and predictions from the model. a The Gaussian filter $\hat{F}(p_\perp)$ (dashed black line) together with projections of the squared wave functions onto the transverse momentum axis (blue and green solid line) for the ionization step $Ar \to Ar^+$. b Symmetrized, time-integrated, experimental data (bars) together with calculated total momentum distribution (red dashed line) and individual distributions arising from the different orbitals weighted by their relative contribution (color code from a), see text for details. The curve for |m|=1 is multiplied by a factor of 10 for improved visibility. c Same as b for the ionization step $Ar^+ \to Ar^{++}$, starting from a coherent superposition of states. The lines represent the cycle-averaged result while the range of variation is indicated by transparent areas. Picture taken from [10] and slightly adapted, © 2014 American Physical Society.

holds if the electron densities are considered as done in the model. Since the ionization of this orbital produces a fairly narrow distribution peaked around zero momentum, this aspect also *narrows* the momentum distribution observed for the second ionization step.

In summary, the first aspect broadens the distribution expected from the second ionization step while the latter two cause the opposite behavior and compensate for this effect.

5.2.4 Time-Resolved Momentum Distributions

In order to examine the dependence of the electron momentum distributions on the phase of the SOWP it is useful to define the difference between the momentum distribution obtained at a certain phase and the average distribution (integrated over all phases) as [10]

$$D(p,t) = W(p,t) - \overline{W}(p). \tag{5.11}$$

This expression, applicable to both longitudinal and transverse momentum components, emphasizes time-dependent components in the total signal while any time-independent background is suppressed. However, the time-resolved investigation has large impact on the available statistics which is—for each time-step—much lower than in the respective, time-integrated distribution in Fig. 5.6. Since solidangle correction in this situation leads to a massive increase of noise especially in the regions of small momenta, see Sect. 4.2.2, it should be avoided. Instead, as discussed in Sect. 4.2.2, the theoretical distributions—which resemble solid-angle corrected distributions—can be appropriately transformed.

 $D(p_{\rm tr},t)$ and $D(p_{\rm l},t)$ may first be calculated for the two "extreme" phases of the SOWP, namely the situation at full and half periods. In the case of the experimental data, an integration over a finite range is necessary to obtain enough statistics. As indicated in Fig. 5.1, two time windows A and B are defined for this purpose, each with a with of $T_{\rm s}/4$. Figure 5.7 shows the result in the case of the transverse and the longitudinal momentum component in (a), (b) and (c), (d), respectively. In the case of the transverse distributions, the respective predictions calculated with the model described in Sect. 5.2.2 for $t = iT_{\rm S}$ and $t = (i + 1/2)T_{\rm S}$ are additionally shown as black solid curves.

The fingerprint of the SOWP can clearly be seen in the electron transverse momentum distributions. Within the errorbars the experiment agrees remarkably well with the simple model, although e.g. the Coulomb interaction is not considered at all. As predicted from Eq. (5.6), the width of the transverse momentum distribution directly reflects the situation in the bound orbital. The only noticeable difference between experiment and model is the overall width of the distributions which seems to be slightly underestimated by the latter. Since this deviation can in principle be explained with a different laser intensity, this parameter is adjusted to find a better qualitative agreement. This is achieved with a two times larger intensity (see dashed curves in Fig. 5.7a, b). However, this value for the intensity—within the ADK model clearly causes large deviations between the expected and measured ion longitudinal momentum distributions as visible in Fig. 5.4, where the prediction with the higher intensity is shown as dashed line. Therefore it can be concluded that the product form of Eq. (5.6) is—at least in first order—valid, but the overall predicted transverse momentum distributions are slightly too narrow. In this context it should be mentioned that this trend was already seen in an experiment using circularly polarized light in [3, 8], where a deviation of about 15% was found.

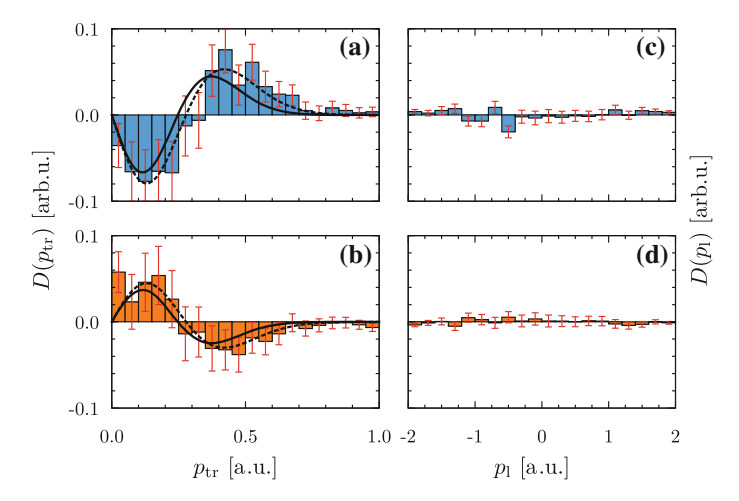


Fig. 5.7 Electron momentum distributions at different phases of the SOWP. **a** and **b** Difference between the transverse momentum distributions obtained in the time-windows A (**a**) and B (**b**) as defined in Fig. 5.6 and the average momentum distribution, cf. Eq. (5.11). The experimental data is shown as *bars*, the distribution predicted by the model from Sect. 5.2.2 as *black solid curve*. The *dashed lines* show the prediction of the model for an intensity twice as high as the vale extracted from the data, see text for details. **c** and **d** Same as **a** and **b** but for the longitudinal momentum component. Picture taken from [10] and slightly adapted, © 2014 American Physical Society.

Recently, TDSE calculations were carried out to investigate the momentum distributions beyond the "scaled hydrogen" model, including also the Coulomb interaction [15]. The resulting predictions for D(p,t) qualitatively reproduce the experimental results shown in Fig. 5.7a, b. However, as mentioned by the authors, deviations occur in particular in the situation of (a), where the simple model achieves clearly better agreement with the experimental data.

For the longitudinal component p_1 , no significant dependence on the phase can be seen, see Fig. 5.7c, d. This is in agreement with the common assumption that the electron is set free with zero momentum in the direction of the field polarization at the exit of the tunnel, see Sect. 3.2. However, any other distribution independent of m is likewise in agreement. In addition, as shown in [17], soft recollisions of the freed electron with its parent ion may lead to a "bunching" of the electron energies and thus could conceal any difference in the initial distributions.

The complete dynamics of the SOWP and its influence on the transverse momentum distribution is accessible using a "sliding-window" approach, where the center of window A from Fig. 5.1 is slid in tiny steps across the full period, resulting in a time-resolved momentum distribution, see Fig. 5.8a. Again, the model is evaluated at the central points of the windows without any averaging and the respective distribution shown in (b).

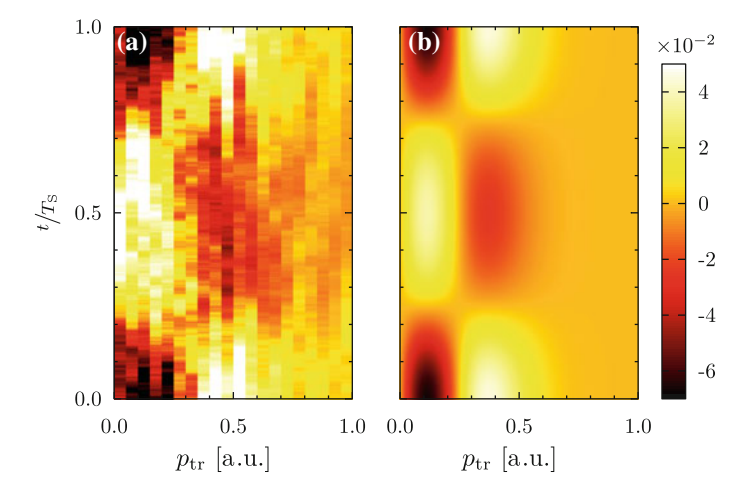


Fig. 5.8 Full dynamics of the SOWP in the transverse momentum distribution. **a** Same as Fig. 5.7a, b but for a scanned time delay using a sliding-window approach. **b** Shows the related prediction of the model. Outlines at $t/T_S = 0$ and 1/2 result in Fig. 5.7a, b. Picture taken from [10] and slightly adapted, © 2014 American Physical Society.

In conclusion, electron transverse momentum distributions were shown for the isolated steps of the sequential strong-field double ionization $Ar \longrightarrow Ar^+ \longrightarrow Ar^{++}$ induced by linearly polarized light. The Coulomb interaction between the electrons and the parent ion clearly influences these distributions, as already observed in [25]. A spin-orbit wave packet in the argon ion was used as initial state for further tunnel ionization. It was shown that—despite the Coulomb interaction—information about the momentum distribution in the bound state of the ion is preserved. The SOWP thus leaves a characteristic fingerprint in the electron transverse momentum distribution, as predicted in [32]. Common assumptions about the tunneling process is strong laser fields were tested including the product form of Eq. (5.6). The results of this chapter have been published in [10], a comparison to TDSE calculations can be found in [15].

References

- A.S. Alnaser et al., Laser-peak-intensity calibration using recoil-ion momentum imaging. Phys. Rev. A: At., Mol., Opt. Phys. 70, 023413 (2004). doi:10.1103/PhysRevA.70.023413
- M.V. Ammosov et al., Tunnel ionization of complex atoms and of atomic ions in an alternating electromagnetic field. Sov. Phys. JETP 64, 1191–1194 (1986)
- L. Arissian et al., Direct test of laser tunneling with electron momentum imaging. Phys. Rev. Lett. 105, 133002 (2010). doi:10.1103/PhysRevLett.105.133002
- S. Augst et al., Laser ionization of noble gases by Coulomb-barrier suppression. J. Opt. Soc. Am. B: Opt. Phys. 8, 858–867 (1991). doi:10.1364/JOSAB.8.000858
- J. Beringer et al., Review of particle physics. Phys. Rev. D: Part. Fields 86, 010001 (2012). doi:10.1103/PhysRevD.86.010001

- E. Clementi, D.L. Raimondi, Atomic screening constants from SCF functions. J. Chem. Phys. 38, 2686–2689 (1963). doi:10.1063/1.1733573
- 7. C. Cohen-Tannoudji et al., Quantum Mechanics (Hermann and Wiley, New York, 1977)
- I. Dreissigacker, M. Lein, Quantitative theory for the lateral momentum distribution after strong-field ionization. Chem. Phys. 414, 69–72 (2013). doi:10.1016/j.chemphys.2012.01.028
- P.D. Fainstein et al., Target dependence of slow electrons emitted in swift ion-atom collisions. Phys. Rev. A: At., Mol., Opt. Phys. 63, 062720 (2001). doi:10.1103/PhysRevA.63.062720
- L. Fechner et al., Strong-field tunneling from a coherent superposition of electronic states. Phys. Rev. Lett. 112, 213001 (2014). doi:10.1103/PhysRevLett.112.213001
- A. Fleischer, Probing angular correlations in sequential double ionization. Phys. Rev. Lett. 107, 113003 (2011). doi:10.1103/PhysRevLett.107.113003
- 12. E. Goulielmakis et al., Real-time observation of valence electron motion. Nature **466**, 739–744 (2010). doi:10.1038/nature09212
- 13. R.N. Hill, Hydrogenic wave functions, Chap. 9, in *Springer Handbook of Atomic, Molecular, and Optical Physics [online]*, ed. by G.W.F. Drake (Springer Science+Buisiness Media Inc, New York, 2006), pp. 153–171. doi:10.1007/978-0-387-26308-3
- M. Yu Ivanov et al., Anatomy of strong field ionization. J. Mod. Opt. 52, 165–184 (2005). doi:10.1080/0950034042000275360
- A.S. Kheifets, I.A. Ivanov, Transverse-electron-momentum distribution in pump-probe sequential double ionization. Phys. Rev. A: At., Mol., Opt. Phys. 90, 033404 (2014). doi:10.1103/PhysRevA.90.033404
- A. Kramida et al., NIST Atomic Spectra Database (ver. 5.1) [online]. National Institute of Standards and Technology, Gaithersburg, MD (2013), http://physics.nist.gov/asd Accessed 5 Aug 2014
- A. Kästner et al., Energy bunching in soft recollisions revealed with long-wavelength fewcycle pulses. J. Phys. B: At., Mol. Opt. Phys. 45, 074011 (2012). doi:10.1088/0953-4075/45/ 7/074011
- 18. L.D. Landau, E.M. Lifschitz, *Lehrbuch der Theoretischen Physik*, Band III, Quantenmechanik (Akademie-Verlag, Berlin, 1965)
- S. Larochelle et al., Non-sequential multiple ionization of rare gas atoms in a Ti: sapphire laser field. J. Phys. B: At., Mol. Opt. Phys. 31, 1201–1214 (1998). doi:10.1088/0953-4075/31/6/ 008
- R. Moshammer et al., Ionization of helium in the attosecond equivalent light pulse of 1 GeV/Nucleon U⁹²⁺ projectiles. Phys. Rev. Lett. 79, 3621–3624 (1997). doi:10.1103/ PhysRevLett.79.3621
- 21. R. Moshammer et al., Initial state dependence of low-energy electron emission in fast ion atom collisions. Phys. Rev. Lett. **83**, 4721–4724 (1999). doi:10.1103/PhysRevLett.83.4721
- 22. B. Podolsky, L. Pauling, The momentum distribution in hydrogen-like atoms. Phys. Rev. 34, 109–116 (1929). doi:10.1103/PhysRev.34.109
- M. G. Pullen et al., Measurement of laser intensities approaching 10¹⁵ W/cm² with an accuracy of 1%. Phys. Rev. A: At., Mol., Opt. Phys. 87, 053411 (2013). doi:10.1103/PhysRevA.87. 053411
- N. Rohringer, R. Santra, Multichannel coherence in strong-field ionization. Phys. Rev. A: At., Mol., Opt. Phys. 79, 053402 (2009). doi:10.1103/PhysRevA.79.053402
- A. Rudenko et al., Coulomb singularity in the transverse momentum distribution for strongfield single ionization. J. Phys. B: At., Mol. Opt. Phys. 38, L191–L198 (2005). doi:10.1088/ 0953-4075/38/11/L01
- W. Schmitt et al., Ultralow-energy electrons from fast heavy-ion helium collisions: the "target cusp". Phys. Rev. Lett. 81, 4337–4340 (1998). doi:10.1103/PhysRevLett.81.4337
- J.C. Slater, Atomic shielding constants. Phys. Rev. 36, 57–64 (1930). doi:10.1103/PhysRev. 36.57
- C. Smeenk et al., Precise in-situ measurement of laser pulse intensity using strong field ionization. Opt. Exp. 19, 9336–9344 (2011). doi:10.1364/OE.19.009336

References 95

M. Spanner et al., Reading diffraction images in strong field ionization of diatomic molecules.
 J. Phys. B: At., Mol. Opt. Phys. 37, L243–L250 (2004). doi:10.1088/0953-4075/37/12/L02

- 30. H. Wen et al., Observing angular precession of a Rydberg wave packet due to spin-orbit coupling by orthogonally polarized weak half-cycle pulses. Phys. Rev. A: At., Mol., Opt. Phys. **73**, 052504 (2006). doi:10.1103/PhysRevA.73.052504
- 31. A. Wirth et al., Synthesized light transients. Science **334**, 195–200 (2011). doi:10.1126/science. 1210268
- 32. H.J. Wörner, P.B. Corkum, Imaging and controlling multielectron dynamics by laser-induced tunnel ionization. J. Phys. B: At., Mol. Opt. Phys. 44, 041001 (2011). doi:10.1088/0953-4075/44/4/041001

Chapter 6 Population of Doubly Excited States in Strong Laser Pulses

In the measurements presented in the previous chapter, a superposition of the electronic ground state ${}^2P_{3/2}$ and the spin-orbit excited state ${}^2P_{1/2}$ of Ar^+ was created in a strong laser pulse. In this situation, the difference in energy between the two states, the spin-orbit splitting, drives the dynamics of the system. In contrast, if the system is situated in only one of its eigenstates, no dynamics is induced in the electron cloud. The general possibility to excite the ground state ion and thus temporally store a well defined amount of energy has wide implications for the interaction with strong laser pulses. In neutral Rydberg atoms, the population of *doubly excited states* (DES) has been observed in experiments with short wavelengths, see e.g. [7, 14]. However, for longer wavelengths approaching the tunneling regime, where the excitation of Rydberg states was recently related to the three-step model and the frustrated tunneling ionization (FTI) process, see Sect. 3.4.3, to the best of our knowledge no indication of excitation of DES has been reported yet.

In this chapter, results obtained with different noble gas atoms and a large range of ionizing wavelengths, from the beginning of the ultraviolet at 395 nm to the infrared at 1600 nm, are presented. By variation of the wavelength, a transition is driven from the multiphoton to the tunneling regime. The efficient population of *doubly excited states* (DES) involving the Rydberg series in the species is proven for several wavelengths, including long wavelengths associated with the tunneling picture and the FTI process. As will be discussed, the population of DES by FTI observed might involve resonant recapturing of a slow electron and simultaneous excitation of the ion to the excited ${}^2P_{1/2}$ state, a process commonly known as *dielectronic recombination* and heavily investigated—for higher charged or lighter ions—for decades in a manifold of experiments.

Section 6.1 gives a brief overview about the Rydberg series in noble gas atoms, where one of the electrons is highly excited and orbiting the respective singly charged species. The possibility of the excitation of this "inner ion" or the *electronic core* is discussed followed by its implications, namely the formation of two different Rydberg series and the possibility of autoionization. The experimental results are presented in Sect. 6.2. The population of DES during the laser pulse is proven for different wavelengths up to 1300 nm and a possible involvement of dielectronic

recombination discussed. Further experimental data and different considerations about the autoionization dynamics of the systems are presented in Sect. 6.3, where a second laser pulse is used to manipulate the population in the autoionizing states. Finally, results obtained with other species, namely neon and molecular nitrogen, are briefly discussed in Sect. 6.4.

6.1 Noble Gas Rydberg Atoms

The Rydberg state of an atom is characterized by the high excitation of one of the electrons and the associated large mean distance of this particular electron to the nucleus compared with e.g. the diameter of the electronic shell in the ground state, see e.g. [9, Sect. 6.6.4]. The situation is depicted in Fig. 6.1b. The nucleus together with the remaining part of the electron cloud, the *electronic core*, as referred to in the following, forms the well-known singly charged ion of the respective species. For an electron far outside, the exact shape and composition of the attracting central object is of minor importance such that the situation can often be approximated well by a hydrogenic picture, see Fig. 6.1c. The energy levels then follow the famous Rydberg equation, see e.g. [9, Sect. 6.6.4]

$$E_n = E_i - \frac{Ry}{n^2},\tag{6.1}$$

where E_i is the ionization potential, Ry the Rydberg constant and n the main quantum number. This approximation is in particular good for electrons which have a low probability density in the inner regions of the atom. As can be seen from an analysis of the radial part of the hydrogen wave functions $R_{n,l}(r)$, see e.g. [17, Sect. 9.1.1], e.g. by plotting the radial probability densities given by $r^2 \cdot R_{n,l}(r)$, this is the case especially for states with large angular momenta l (and large principal quantum number n).

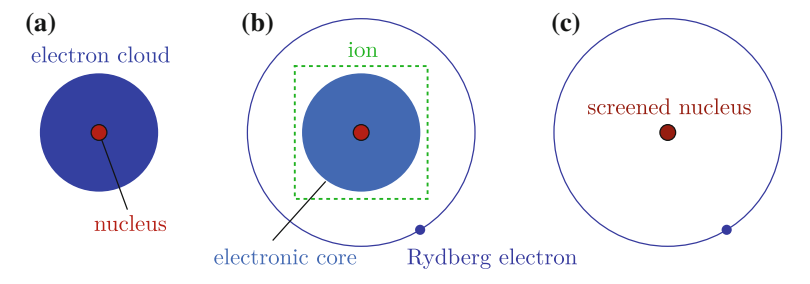


Fig. 6.1 Schematic representation of atomic ground and excited Rydberg states. a Neutral atom in its ground state. The nucleus is surrounded by the electron cloud. b The atom is excited to a Rydberg state where one electron is only loosely bound and has a large mean distance to the nucleus and the remaining part of the electron cloud, the *electronic core*. c Utilizing an effective charge for the partially screened nucleus, the system can approximately be treated as an hydrogen-like exited atom

However, for the other states with lower angular momenta, the finite probability density at smaller distances to the nucleus, particularly *inside* the electronic core, has to be considered. Here, due to the reduced shielding of the nuclear charge, the Rydberg electron experiences a more attractive potential, which shifts the energy of the states. Equation (6.1) thus is often generalized to, see e.g. [9, Sect. 6.6.4]

$$E_{n,l} = E_{i} - \frac{Ry}{(n - \delta_{n,l})^{2}},$$
 (6.2)

where the states are not degenerated in l any longer due to the *quantum-defect* $\delta_{n,l}$. Surprisingly few spectroscopic measurements have been performed for the lowest Rydberg states and only data for certain (small) values of l is available [20]. Nevertheless, the available experimental values can be compared with the respective calculation performed with Eq. (6.1), which is done in Fig. 6.2a, b for a part of the krypton and argon ${}^2P_{1/2}$ series, respectively. For both species, the increasing agreement of the experimental data with increasing angular momentum is clearly visible. Already for $l \approx 3$, the deviations are far smaller than the distance to the neighboring states. Furthermore, it is important that all states with higher values of l are expected to have approximately the same energy.

The Rydberg series investigated is approaching the ${}^2P_{1/2}$ ionic state which is *not* the ground state of the ion. In fact, the Rydberg states shown in Fig. 6.2 are valid for an excited electronic core, a situation discussed in the following section.

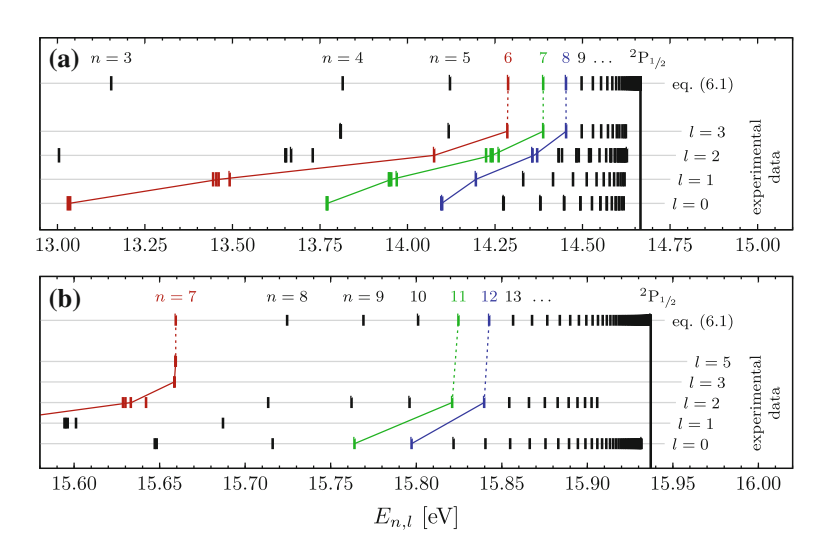


Fig. 6.2 Comparison of spectroscopic data from [20] with the Rydberg equation, Eq. (6.2), for a part of the ${}^{2}P_{1/2}$ series of **a** krypton and **b** argon. Selected states are colored according to the main quantum number *n* and connected by lines to guide the eye

6.1.1 Doubly Excited States and Autoionization

The electronic core of a Rydberg atom comprises the electronic structure of a singly charged ion, in the case of argon and krypton a complicated multielectron system. Most importantly for this work, it contains—due to the spin-orbit interaction as seen in the beginning of Sect. 5.1—the excited ${}^2P_{1/2}$ state beside the ${}^2P_{3/2}$ ground state. Since the ionization potentials of the two states differ by the spin-orbit splitting $\Delta \omega$, two different Rydberg series exist, depending on the state of the electronic core, see e.g. [32]. Figure 6.3 displays the situation for krypton, argon and neon in a simplified scheme using Eq. (6.1) and atomic data from [20]. The states approaching the ${}^2P_{1/2}$ continuum for $n \to \infty$ are commonly known as autoionizing Rydberg states (ARS), see e.g. [32]. Due to the simultaneous presence of two excitations, namely the Rydberg excitation of the electron and the spin-orbit excitation of the ionic core, these states are referred to as *doubly excited states* (DES) in the following.

Above a certain minimum value for n, which depends on the species considered, the DES energetically exceed the lower lying ${}^2P_{3/2}$ ionization limit, displayed in red in Fig. 6.3. In these states, the system already contains enough energy for an ionization process and may in principle ionize without an external energy source. In this process, the energy "stored" in the excitation of the electronic core is given to the Rydberg electron, which escapes and leaves back the ion in its ground state. Indeed, such processes, commonly known as *autoionization*, have been observed in a manifold of experiments, see e.g. [32] and references therein. In the context of this work, the autoionization process is important mainly due to its characteristic ability, to "convert" a doubly excited neutral atom into two charged particles, namely an ion and an electron, which can be detected with the REMI. As will be discussed in the following, this provides insight in the population of DES in strong laser fields.

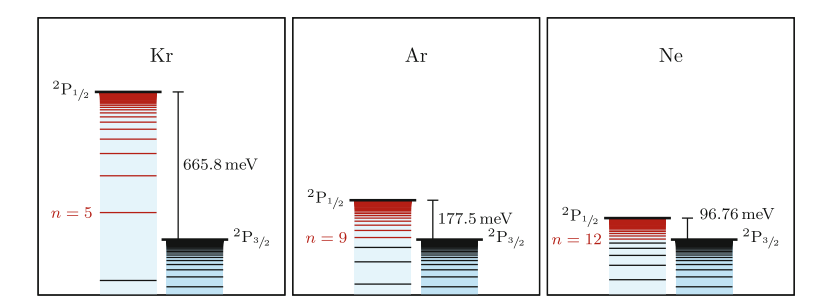


Fig. 6.3 Doubly excited Rydberg states in the noble gases krypton, argon and neon. Above a certain minimum value for the main quantum number n, the Rydberg states approaching the ${}^2P_{1/2}$ ionization limit, associated with an excited electronic core, exceed the first ionization potential ${}^2P_{3/2}$. These states are shown in *red* together with the respective minimum value for the main quantum number

6.2 Population of DES at Different Wavelengths

The experiment is carried out as follows. Using a BBO and the OPA, see Sects. 2.2.4 and 2.2.5, respectively, laser pulses of different wavelength are produced and guided into the REMI, where they interact with an argon or krypton gas jet produced with a backing pressure around 3 bar. Measurements at 790 and 395 nm are carried out with the direct output of the laser system and with the second harmonic of this radiation produced in a BBO crystal (see Sect. 2.2.4), respectively. For time-resolved measurements, the 790 nm radiation is used together with the Mach–Zehnder interferometer, see Sect. 2.2.3.

The laser intensity is difficult to estimate. In Sect. 5.2.1, it was derived from the observed momentum spread of singly charged ions. The formula used, Eq. (3.6), is valid only in the tunneling regime and therefore not applicable to the full range of wavelengths used here. In order to give an estimation of the laser intensities, the measurements taken at 1300 and 1600 nm are analyzed, yielding intensities of about 3 to $6 \times 10^{14} \,\mathrm{W/cm^2}$. However, at other wavelengths the situation may be different. Many parameters, from the reflectivity of the mirrors used to guide the beam over the efficiency of the OPA and the duration of the pulses produced, to the focal volume described by Eqs. (2.20) and (2.19) depend on the wavelength. The given range of the intensity has therefore be seen more as indication of the correct order of magnitude. If an intensity of $6 \times 10^{14} \,\mathrm{W/cm^2}$ is assumed, the Keldysh parameter, calculated with Eq. (3.1) and the ionization potentials in Table A.2, in the measurements range from $\gamma_{\rm Kr} \approx 0.82$ and $\gamma_{\rm Ar} \approx 0.87$ (at 470 nm) to about $\gamma_{\rm Kr} \approx$ 0.24 and $\gamma_{Ar} \approx 0.26$ (at 1600 nm) for krypton and argon, respectively. For krypton, an additional measurement was performed at a wavelength of 395 nm corresponding to $\gamma_{\rm Kr} \approx 0.98$.

Figure 6.4a displays exemplarily the distribution of ion flight times recorded in the measurement with argon carried out at $470 \, \mathrm{nm}$. The peak corresponding to $\mathrm{Ar}^+\mathrm{is}$ clearly dominating such that the other peaks are visible only if a logarithmic scaling is used for the *y*-axis. In total, more than 90% of the detected ions have a flight time associated with Ar^+ . As already done in Sect. 5.2, an appropriate condition on the flight time in combination with a subsequent consideration of the particles momentum sum can be used in order to select the events for further processing. The condition for the flight time is visualized in Fig. 6.4b.

However, in the situation where the signal is clearly dominating over background and noise, this procedure will worsen the statistics rather than improving the results. Since the efficiency of the ion detector is only about 50%, see Sect. 4.1.1, about half of the "clean" events, in which only one atom is ionized and at least the associated electron is successfully measured, will be sorted out. To avoid this, an alternative procedure is applied: Only those events are rejected, in which a background ion is detected. If this is not the case, and the event thus comprises either exclusively singly charged ions of the desired species or no ion at all, it is further processed. Figure 6.4c, d show the electron momentum distributions obtained in true

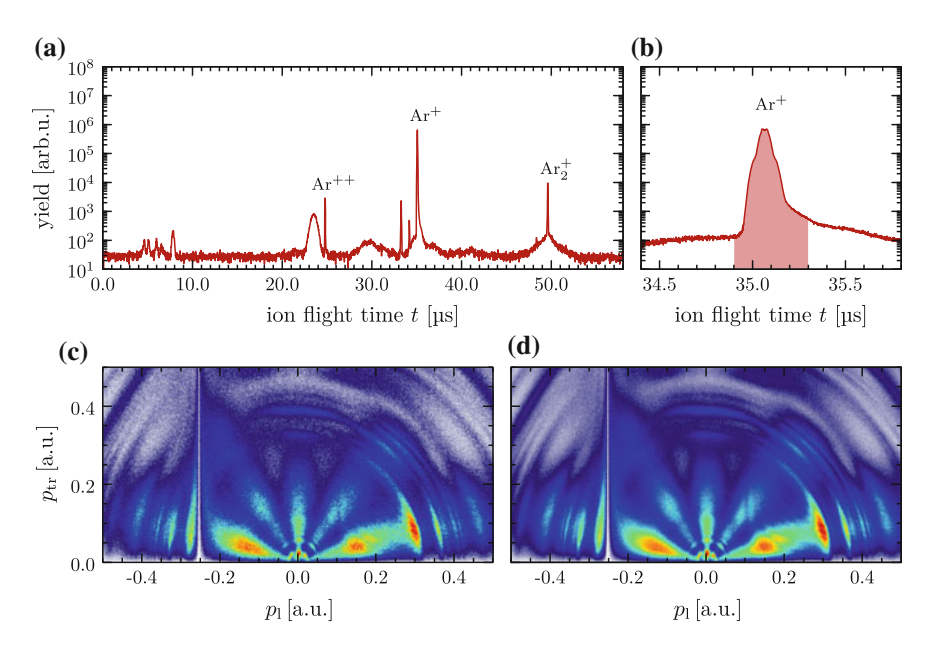


Fig. 6.4 Spectrum of ion flight times and different approaches for the data selection. **a** Typical ion flight time spectrum obtained in the experiment, here for argon at a wavelength of 470 nm. Single ionization clearly dominates. **b** Selection of the Ar⁺ions with a suitable condition on the flight times (*light red area*). **c** and **d** Electron momentum distributions obtained with different conditions applied in the data selection process, see text for details. The linear color scale used is displayed in Fig. A.1a

coincidence with Ar⁺, also considering the momentum sum, and the one obtained with the alternative method, respectively.

Although the distributions look very similar, the statistics is clearly better in (d). Most important, all structures visible in (d) are also visible in (c) and thus can be clearly assigned to arise from single ionization of argon. Therefore, in the following, all distributions shown are acquired as done in the case of Fig. 6.4d. However, although not shown, all structures discussed are proven to be present likewise in the distributions obtained with the stricter conditions for the selection of the data, thus they can safely be assigned to single ionization of the respective species.

Figure 6.5 shows the electron momentum distributions obtained for krypton in increasing order with respect to the wavelength. The wavelength actually produced from the OPA system may slightly differ from the values given here, which resemble the selected wavelength using the OPA control software. Measurements performed with an optical spectrometer during the experiments presented in Chap. 7 prove the mean deviation to be less than 5 nm, see Fig. 7.3 and Table 7.1.

At first glance, without considering any details in the pictures, a qualitative change is visible along increasing wavelength: While the measurements on the lower end, e.g. with 395 and 470 nm, produce distributions with a manifold of narrow and

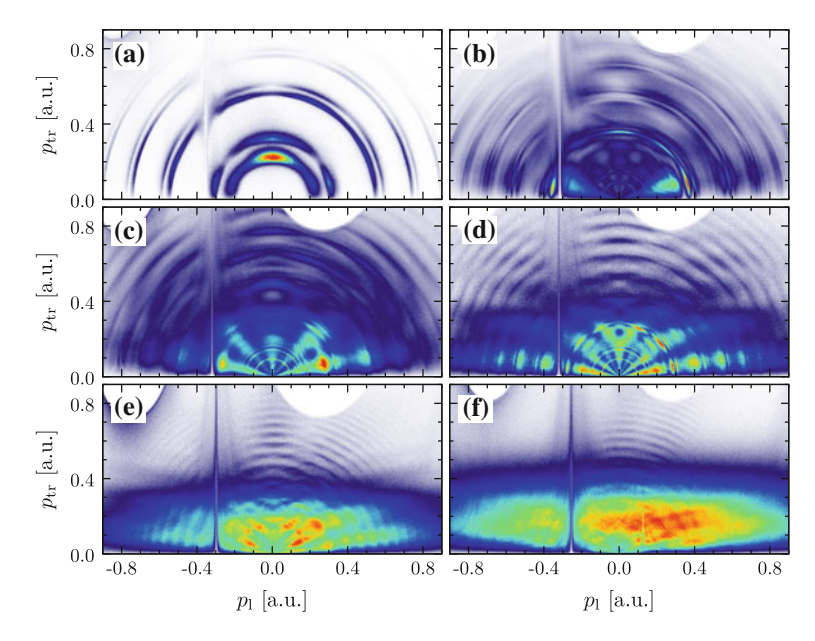


Fig. 6.5 Electron momentum distributions obtained with Kr at different wavelengths: **a** 395 nm, **b** 470 nm, **c** 530 nm, **d** 790 nm, **e** 1300 nm, **f** 1600 nm. The linear color scale used is displayed in Fig. A.1a

separated structures, Fig. 6.5a, b, the ones obtained at 1300 and 1600 nm comprise only one single, broad and almost homogeneously filled peak. This can be interpreted as a transition from the multiphoton to the tunneling regime, driven by the change in the wavelength of the ionizing laser, see Sect. 3.1. Due to a very high ionization rate in the measurement at 1600 nm, Fig. 6.5f shows a clear asymmetry, namely significantly more electrons detected for positive p_1 . The ionization of two ions in the same laser pulse and hence the production of two electrons suppresses events with negative p_1 associated to long flight times since only the electron which is detected first is considered. In addition, an artifact is visible, presenting itself as vertical structure at $p_1 \approx 0.1$ a.u. This is, though less pronounced, also the case in some of the other measurements. The origin of the structure can not be clarified unambiguously, however it is likely caused by reflexions in the signal wires.

The electron energy spectra, which can be calculated from the momentum distributions, are shown in Fig. 6.6. Also here, the qualitative change between ionization at short and long wavelengths is clearly visible. At the energies related to the artifact mentioned above and the vertical structure arising at $p_1 \approx -0.3$ a.u., explained in Sect. 4.3, no indication of any influence is visible in any spectrum. The distribution obtained with 395 nm differs clearly from the others. The spectrum contains *exclusively* a sequence of distinct peaks, grouped in pairs and approximately equally spaced. Similar observation has been reported recently in [14] for the multiphoton ionization of xenon with 388 nm at moderate intensities. Following the

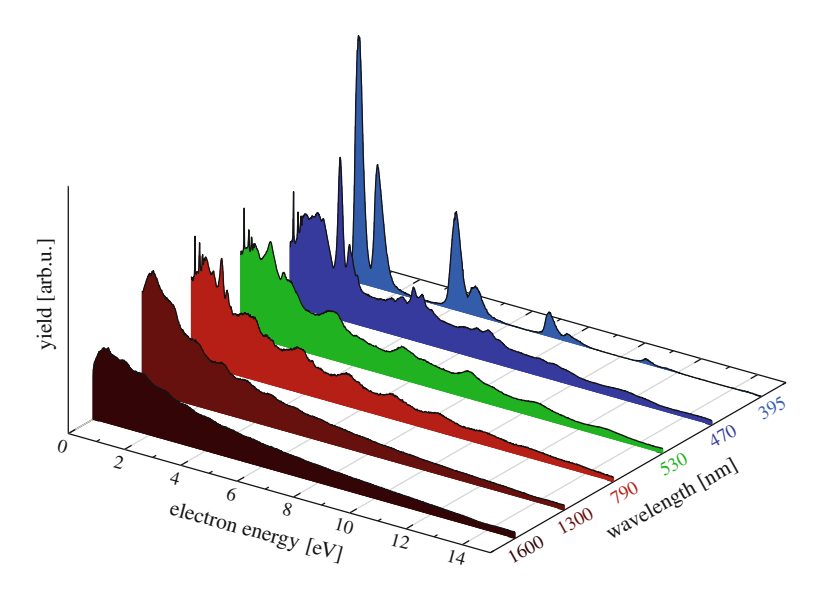


Fig. 6.6 Photoelectron energy spectra observed for krypton at different wavelengths. The curves are normalized with respect to the their total area. The curve for 395 nm is additionally divided by a factor of 2 for better visibility

argumentation in this reference, the two peaks of lowest energy observed here can be assigned to resonant (4+1) photon processes into the ${}^2P_{3/2}$ and ${}^2P_{1/2}$ ionization limit.

The sharp characteristics of the peaks suggest a resonant process in the krypton atom whose electronic structure can be found e.g. in [20]. In contrast, non-resonant processes are related to broad distributions, strongly aligned with the laser polarization, see e.g. [14]. The ponderomotive shift of the ionization potentials and excited states as discussed in Sects. 3.1 and 3.4, respectively, is expected to be relatively small due to the short wavelength and can be neglected for the moment. The first excited state of krypton is found almost 10 eV above the ground state such that any transition driven by three or less 395 nm photons (containing an energy of about 3.1 eV each) can be excluded. On the other hand, the energy of five photons (in total about 15.7 eV) already exceeds both ionization potentials $E_i^{3/2}$ and $E_i^{1/2}$ associated with a ${}^2P_{3/2}$ and $^2P_{1/_2}$ state of the electronic core, respectively. A four photon transition starting from the p-like ground state is in electric dipole approximation only possible into $p(\Delta L = 0)$, $f(\Delta L = 2)$ and $h(\Delta L = 4)$ states, see e.g. [9, Sect. 7.2.4]. Indeed, the $(^{2}P_{1/2})5p$ states are located at about 12.2 eV, just below the four-photon resonance at about 12.6 eV. Due to the fairly large spectral width of the laser and the ponderomotive shift of the level in the laser pulse, see Sect. 3.4, the state may be populated. By absorbing a fifth photon, the system can subsequently be ionized to the ${}^2P_{3/2}$ or $^{2}P_{1/2}$ continuum.

The kinetic energy of the electron depends on the final state of the parent ion and is—if ponderomotive shifts are neglected—given by the difference of the total energy carried by five photons and the respective ionization potential. Since the latter is different for the two continua and differs by the spin-orbit splitting of the system, see Table A.2, this splitting is expected to be reflected in the energy spectrum as observed in [14]. This information can be used in the final step of the procedure described in Sect. 4.2.3 to calibrate the momentum spectrum as it is done for the respective distributions shown in Figs. 6.5a and 6.6. However, not only the distance between the two smallest rings observed in Fig. 6.5a, but also the energetically very similar spacings between the rings in the other pairs (the third and fourth ring etc.) are utilized in this respect. These pairs are attributed to ATI of different order, involving the absorption of one or more additional photons, see Eq. (3.10).

After the calibration, which consist of a linear scaling in momentum space according to p' = bp with $b \sim 1$, both the distances between neighboring rings as well as the large splitting associated with ATI are almost constant over the full energy range shown in Fig. 6.6. However, the photon energy of 395 nm assumed does not fit to the distances observed between the pairs of peaks. From the value obtained, the wavelength of the ionizing radiation can be calculated to 373(17) nm. The error on this value is calculated from the mean deviation of the eight and four values extractable from the structures shown in Fig. 6.5 for the photon energy and the spin-orbit splitting, respectively. For example a small misalignment of the BBO crystal may explain this results since it leads to phase matching for frequencies close to the central wavelength of the spectrally broad output of the Ti:sapphire laser.

If comparing the angular distribution of the electrons forming two adjacent rings, clear deviations can be obtained despite identical initial states and the same number of photons absorbed. The reason for this is not yet clear. However, the angular distributions obtained in strong-field experiments are known to depend also on ponderomotive effects [11].

Apart from the measurement at 395 nm, ATI structures appear in all other distributions shown in Fig. 6.5. Even at 1600 nm they are clearly visible in direction of transverse momenta, where other processes are not strongly dominating. However, with increasing wavelength, the structures become less and less pronounced and the distance between neighboring rings decreases—as expected—with the photon energy, see Fig. 6.6.

If the angular distribution of the observed structures is to be investigated, a "cut" through the three-dimensional distribution has to be considered. As discussed in Sect. 4.2.2, the respective solid-angle corrected distribution $W(p_{\perp})$ has to be considered rather than $W(p_{\rm tr})$, shown in Fig. 6.5. This distribution is displayed in Fig. 6.7. Due to additional angular momentum transferred to the system with every photon absorbed, the angular distribution of the photoelectrons changes with every additional photon from one pair of rings to the next. For example, the rings in the first pair in (b) comprise four maxima each while the ones in the second pair contain six. The number of rings observed support the assumption of an initial population

 $^{^1}$ This statement refers to the complete rings, considering also the identical second half with $p_{\perp} < 0$.

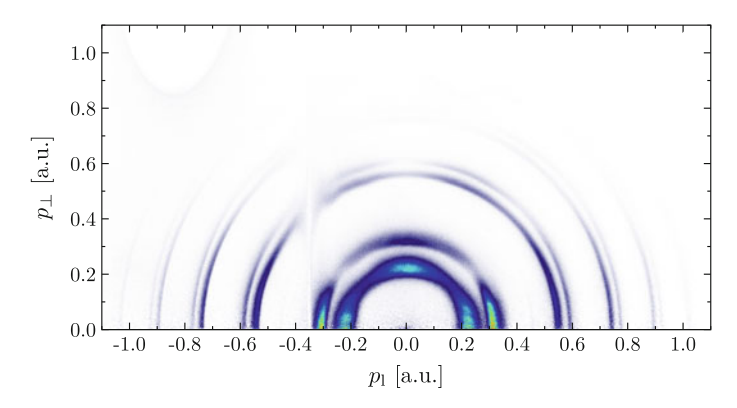


Fig. 6.7 Solid-angle corrected electron momentum distribution obtained with krypton at a wavelength of 395 nm. The linear color scale used is displayed in Fig. A.1a

of the $\binom{2}{P_{1/2}}5p$ states. The absorption an additional photon and the thereby caused change in angular momentum gives access to both s and d-like continuum states. Due to the selection rules in linearly polarized light, see e.g. [9, Sect. 7.2], only the $m=0,\pm 1$ states are accessible. The angular distribution is then given by a coherent sum of the associated spherical harmonics which can be found e.g. in [6, Fig. 40.1]. The additional quanta of angular momentum transferred with even more photons give access to more continuum states with higher angular momenta and thus explain the increasing number of peaks obtained along the increasing orders of ATI.

The distributions obtained with "intermediate" wavelengths comprise other structures. In the following, the distribution obtained with 790 nm, Fig. 6.5d, is discussed exemplarily. As already mentioned above, ATI structures are visible also in this case. Their appearance may also be understood in a field picture as arising from trajectory interferences within the laser pulse as shown in Fig. 3.4. However, if all interferences are considered, the structures are expected to be more complex, cf. Fig. 3.4. Indeed, in radial direction, "fan"-like structures can be observed, pointing at zero momentum, see also Fig. 6.8. These structures have been observed before, see e.g. [22, 23]. However, if comparing the obtained distribution to the simulation shown in Fig. 3.4a or c, qualitative deviations are obviously existing. In the simulation, the structures do not point at the origin and the characteristic "fan"-shape is not reproduced at all. More sophisticated calculations, e.g. [8] or the CVA and TDSE calculations carried out in [2], show that the long-range Coulomb interaction with the parent ion—neglected in the simple model producing Fig. 3.4—gives rise to these structures. Close to 0.3 a.u., very sharp resonances appear comprising several maxima along θ , the angle between the directions of p_1 and p_{tr} , see Fig. 4.5.

If a measurement is performed at the same wavelength but with a different intensity, the change in the ponderomotive energy is expected to cause a certain shift in the kinetic energies of the electrons, see Sect. 3.3.1. In Fig. 6.9 two electron energy spectra obtained for krypton at a wavelength of 790 nm with different intensities are

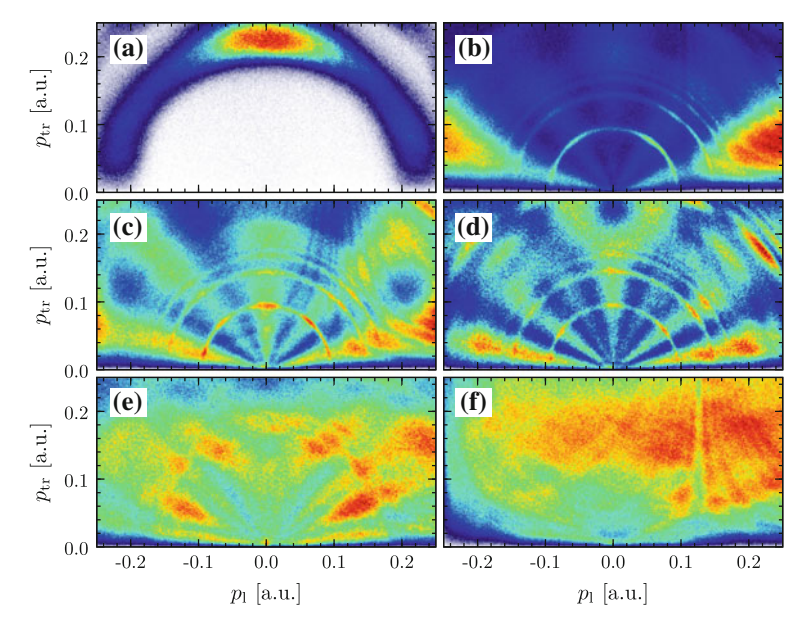


Fig. 6.8 Magnification of the regions of small momenta in the electron momentum distributions obtained with Kr at different wavelengths, shown in Fig. 6.5: **a** 395 nm, **b** 470 nm, **c** 530 nm, **d** 790 nm, **e** 1300 nm, **f** 1600 nm. The linear color scale used is displayed in Fig. A.1a

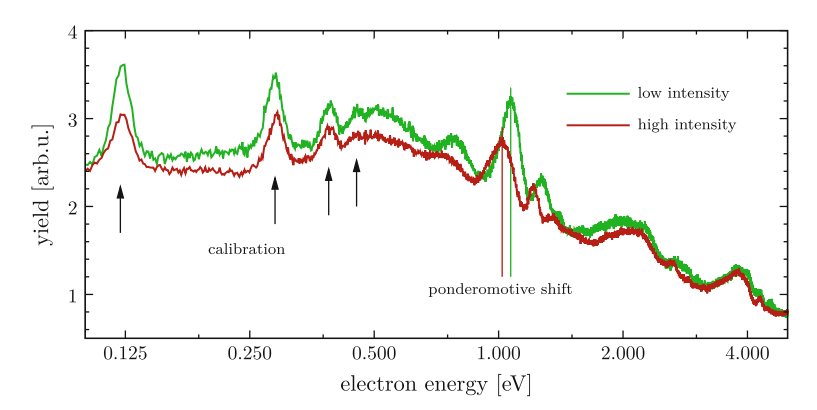


Fig. 6.9 Photoelectron energy spectra for krypton obtained at 790 nm with different laser intensities. *Arrows* mark the peaks used for calibration whose positions are—as explained later—independent of the intensity. The structures visible in the measurement with higher intensity are clearly shifted towards lower kinetic energies by about 50 meV, see text for details

compared. The spectra are calibrated using the sharp peaks at very low energies, whose positions are—as explained later—known on an absolute scale and independent of the intensity and wavelength. Indeed, a shift of the structures—attributed to Freeman resonances—observed in the measurement with higher intensity by about 50 meV towards lower kinetic energies can clearly be determined.

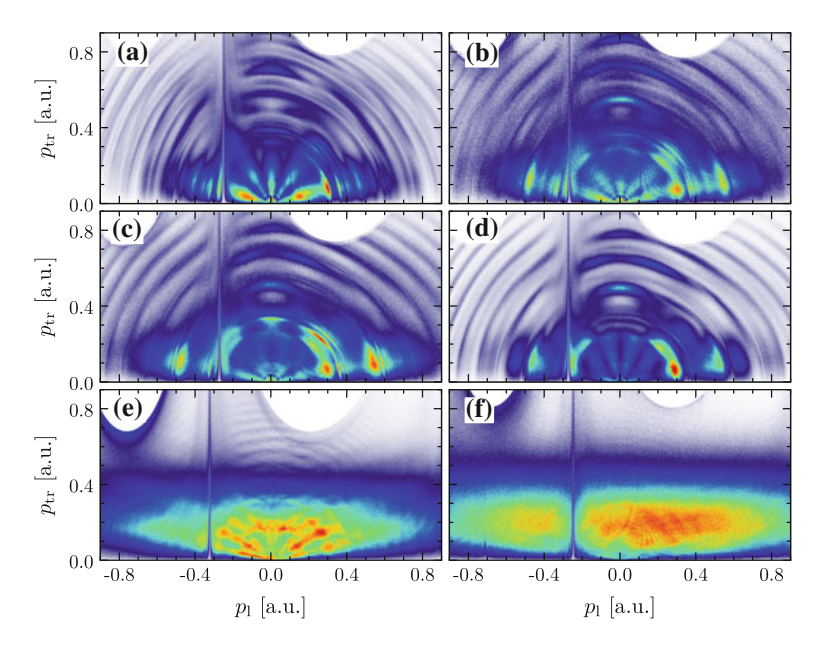


Fig. 6.10 Electron momentum distributions obtained with argon at different wavelengths: **a** 470 nm, **b** 488 nm, **c** 514 nm, **d** 530 nm, **e** 1300 nm, **f** 1600 nm. The linear color scale used is displayed in Fig. A.1a

The distribution observed for 1600 nm, shown in Fig. 6.5f, is in very good agreement to the expectations from Eq. (3.6), namely comprising only one single, broad and almost homogeneously filled peak.² Figure 6.10 displays a very similar set of measurements, now with argon as target. The same general trends and structures can be observed as in the measurements with krypton. However, details as e.g. the exact shape of the interference structures differ due to their dependence on the ionization potential and the inner structure of the species.

In the following, a closer look is taken on the small momentum region of the distributions, shown in Figs. 6.8 and 6.11 for krypton and argon, respectively. Apart from the fan-like structures already discussed above, sharp rings are visible in some of the spectra, representing electrons with very low but well defined kinetic energies. In the case of krypton, these rings are most prominent in the distribution obtained with 470 nm, Fig. 6.8b, were the intensity in the fan-like structures is concentrated along p_1 . With the bare eye, at least four almost homogeneous rings can be distinguished followed by a faint "plateau" at even higher momenta, around 0.2 a.u. This holds also for the measurements obtained with 530 and 790 nm, (c) and (d), where the same sequence of rings is visible. It has to be mentioned that the positions of the rings were in fact used for the absolute calibration of the spectrometer which will be discussed

²This statement refers to the solid-angle corrected distribution $W(p_{\perp})$.

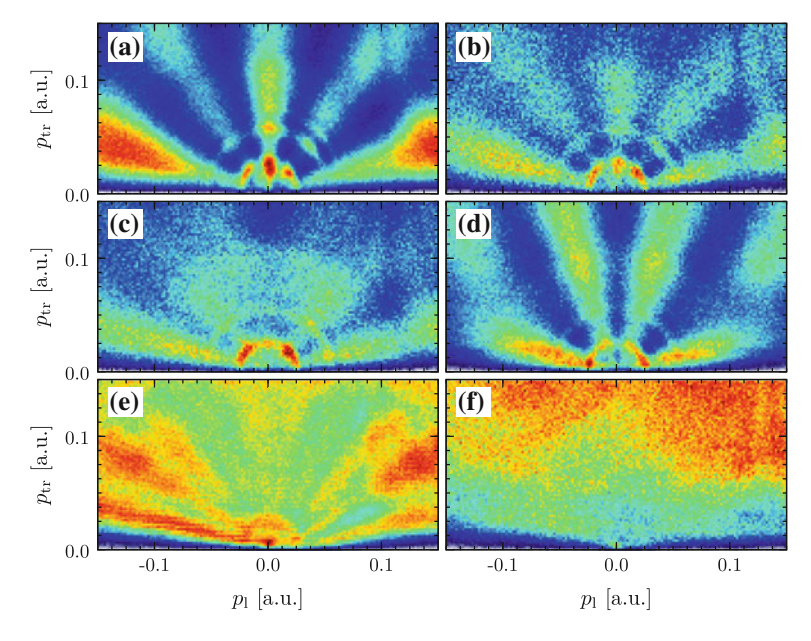


Fig. 6.11 Magnification of the regions of small momenta in the electron momentum distributions obtained with argon at different wavelengths, shown in Fig. 6.10: **a** 470 nm, **b** 488 nm, **c** 514 nm, **d** 530 nm, **e** 1300 nm, **f** 1600 nm. The linear color scale used is displayed in Fig. A.1a

later. In case of argon, rings are visible at smaller momenta in all measurements between 470 and 1300 nm, Fig. 6.11a–e.

Obviously, the observed momentum distributions resemble the inner structure of the species ionized. Moreover, the electron energies are extraordinary small which is not easily seen in the momentum domain. In fact, the rings observed for krypton and argon correspond to electron energies of less than 500 and 100 meV, respectively. The smallest ring observed, the most inner one for argon, has an energy of only about 10 meV and is separated to the next by approximately 30 meV. In general, the energetic difference between neighboring peaks decreases towards higher energies.

A sequence of states with relatively small and decreasing differences in energy can be found in the Rydberg series, see Sect. 6.1. If several states can be populated and subsequently ionized, the energy differences can be expected to be found in the photoelectron distributions. However, in this case, the energetic position of the structures observed depends directly on the laser wavelength. Moreover, due to the small binding energy of the higher Rydberg states, the absorption of an additional photon (with an energy of up to about 2.6 eV in the case of 470 nm radiation) is expected to lead to much higher absolute kinetic energies E_{γ} . The low energetic electrons observed thus can not be produced through the photoionization channel, schematically shown in Fig. 6.12 for krypton ("PI").

However, as discussed in Sect. 6.1, certain DES of the Rydberg series approaching the ${}^2P_{3/2}$ ionization limit, have the ability to autoionize which represents an alterna-

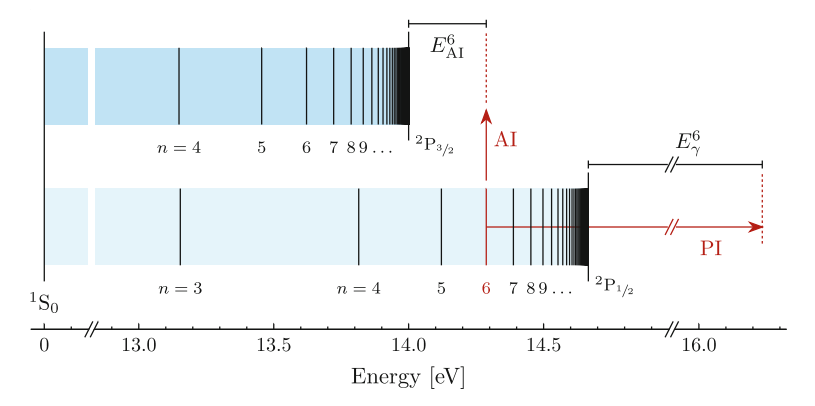


Fig. 6.12 Possible ionization channels for Rydberg states in krypton. The scheme can be easily adapted to other noble gas species, cf. Fig. 6.3. Both Rydberg series may be ionized by absorption of a photon in the photoionization channel (PI), shown exemplarily for the n=6 level of the ${}^2P_{1/2}$ series. In addition, the ${}^2P_{1/2}$ states with $n \ge 5$ may autoionize (AI)

tive ionization channel, "AI" in Fig. 6.12. The energy of the electrons E_{AI} produced through this channel is smaller than the spin-orbit splitting of the respective species, and thus in the correct range, see Fig. 6.3.

Figure 6.12 simplifies the situation in the real atom by neglecting the angular quantum number l such that the energy levels are given by Eq. (6.1). Excitation to one of the states and subsequent ionization by the laser thus leads to a final electron energy of

$$E_{\gamma}^{n} = E_{n} + \omega_{0} \stackrel{(6.2)}{=} E_{i} - \frac{Ry}{n^{2}} + \omega_{0},$$
 (6.3)

depending on both the initial state and the photon energy, but not on the state of the electronic core. The process is shown exemplarily for the n=6 state of the ${}^2P_{1/2}$ series in Fig. 6.12 but is likewise possible from the respective ${}^2P_{3/2}$ state. In case of the ionization from the ${}^2P_{1/2}$ series, the created ion is left behind in the excited state.

In contrast, autoionization is only possible for states belonging to the ${}^2P_{1/2}$ series energetically exceeding the ${}^2P_{3/2}$ ionization potential. For krypton, in the simplified picture³ this is true for all states with $n \ge 5$. The final electron energy of the autoionization channel is then given by

$$E_{\text{AI}}^{n} = E_{n} - E_{i}^{1/2} \stackrel{\text{(6.2)}}{=} E_{i}^{3/2} - \frac{Ry}{n^{2}} - E_{i}^{1/2}$$
$$= \Delta\omega - \frac{Ry}{n^{2}}, \tag{6.4}$$

 $^{^3}$ However, e.g. the actual $5p_{1/2}$ state is located below this threshold and may not autoionize as discussed earlier.

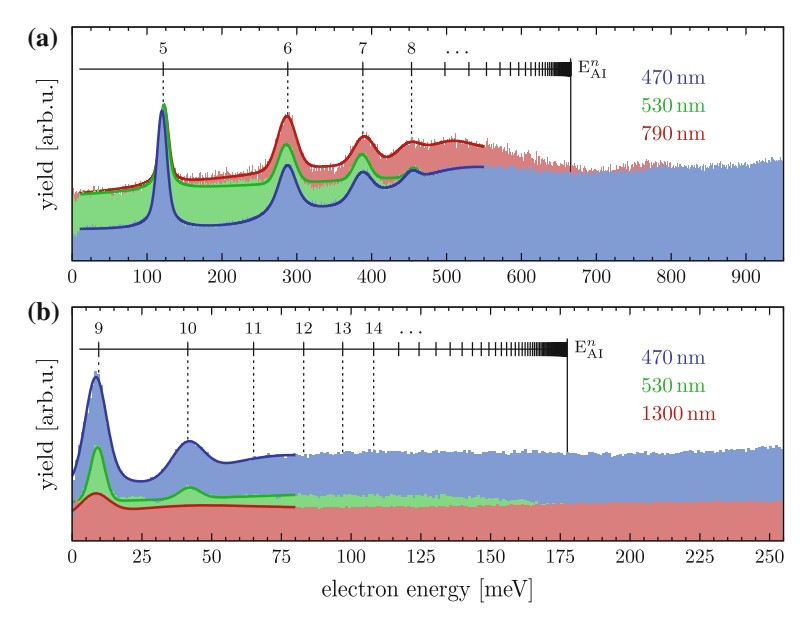


Fig. 6.13 Electron energy spectra in the very low energy region for selected measurements with krypton (a) and argon (b) with different wavelengths. The data is shown as *filled areas*, the *solid lines* represent fits to the data, see text for details. Additionally, theoretical electron energies for the autoionization channel $E_{\rm AI}^{\rm AI}$ are displayed as calculated with Eq. (6.4)

and—in contrast to the photoionization channel—depends only on the initial state and the spin-orbit splitting $\Delta\omega$ of the species but not on the laser wavelength.

In Fig. 6.13, the lower region of electron energy spectra for krypton and argon is displayed in comparison with the kinetic energies E_{AI}^n calculated with Eq. (6.4). The solid lines represent fits to the data consisting of a broad Gaussian distribution absorbing the background and up to four pseudo-Voigt peaks [36] for the single sharp peaks. After a linear scaling of the individual momentum spectra according to p' = bp with $b \sim 1$ as the last step of the calibration procedure described in Sect. 4.2.3, excellent agreement between the observed and the calculated energies is achieved. It is important to note that the overall agreement between the measured and calculated positions was used for the absolute calibration of the system and thus optimized. However, only one free scaling parameter is necessary to obtain excellent agreement for the full sequence of peaks. Moreover, the plateau-region, best visible in Fig. 6.13a for 470 and 790 nm, can be understood as the result of autoionization of the higher Rydberg states whose separation is not large enough to resolve individual peaks. Consequently, close to the upper ionization threshold $E_i^{1/2}$, the plateau-region ends and a drop in the signal can be observed. However, it has to be kept in mind that the manifold of interference structures visible in Fig. 6.5 provide a certain background.

As discussed already in Sect. 3.4.3, the population of Rydberg states in the multiphoton regime, is known for quite a while and also the population of DES has been reported, e.g. in [7, 14]. Recently, the excitation of Rydberg states has been observed also in experiments approaching the tunneling regime and was embedded into the common three-step model within the FTI picture, see Sect. 3.4.3. However, up to our best knowledge, no indication of the population of DES by FTI has been reported yet. The observation of the peaks associated to autoionization up to wavelengths of 1300 nm in Fig. 6.13 shows that DES indeed are populated in this regime.

Within the FTI mechanism, two scenarios are possible resulting in a population of DES, schematically depicted in Fig. 6.14. In the first scenario, (a), the electronic core is excited during the tunneling process at the very beginning of the sequence of the three steps associated with FTI. The electron is subsequently driven by the laser and—if the ionization took place at an appropriate phase of the laser field, see Sect. 3.3.1—recollides with very low energy, thus being recaptured. The tunneling excitation of a noble gas atom is indeed possible: For example, the creation of the spin-orbit wave packet in Chap. 5 relies on this process. In fact, it involves exactly the same states relevant here, namely ${}^2P_{1/2}$ and ${}^2P_{3/2}$ of the noble gas ions. It has been shown that even molecules can be found in excited states after tunnel ionization [24, 30, 34].

In the second possible scenario, depicted in Fig. 6.14b, the tunneling process takes place without the excitation of the parent ion. In contrast to the usual FTI process, the electron may gain a certain amount of kinetic energy E, which is—added to the binding energy $E_i^{1/2} - E_n$ of the Rydberg states it is captured into—just enough to drive the excitation of the electronic core to the ${}^2P_{1/2}$ state. Such resonant recapture processes, commonly known as *dielectronic recombination* (DR), have been heavily

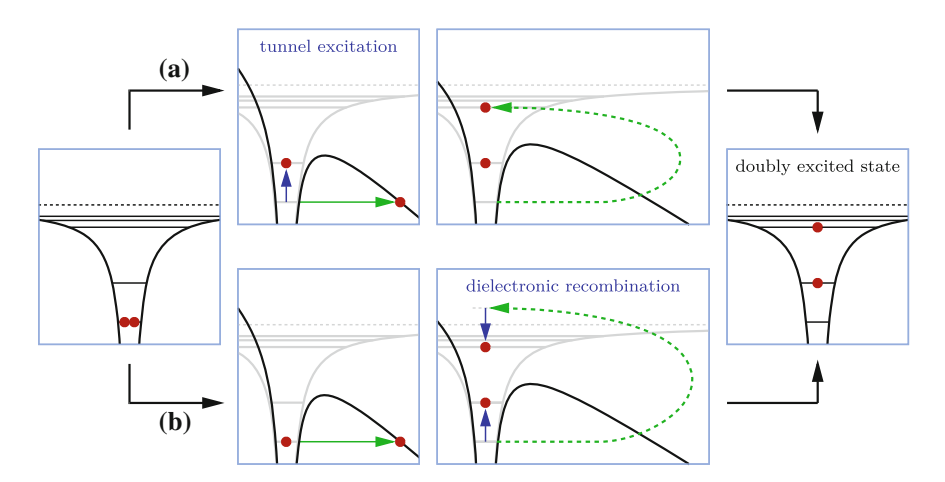


Fig. 6.14 Possible scenarios for population of DES by FTI. The electronic core may be excited either during the tunneling (a), or by dielectronic recombination in the recollision process (b), see text for details

investigated for decades in single-pass measurements, see e.g. [4, 16, 25], electron beam ion traps (EBITs), see e.g. [1, 3, 12], as well as in ion storage ring experiments, see e.g. [10, 19, 21, 27, 28].

However, to the best of our knowledge, the process has never been studied in any experiment neither for Kr⁺ nor for Ar⁺. EBITs are typically utilized for experiments with much higher electron energies while for storage rings the lifetimes of the singly charged species are far to short for a sufficient cooling of the ions [15]. Therefore, the double excitation of the noble gas atoms observed within this work could—if the second population scenario applies—represent the first realization of DR with singly charged argon and krypton ions. Of course it is possible that both pathways have to be considered in order to fully describe the population dynamics, either because both channels are simultaneously active or since already the strict differentiation of the two scenarios might represent a too excessive demand to the semi-classical model. Naturally, it would be interesting to clarify this in a suitable experiment. Though, the experimental discrimination between the two scenarios is difficult, since the subsequent autoionization process is independent of the excitation mechanism. The possible existence of two indistinguishable paths, leading from the same initial to the same final state, suggests the search for quantum interferences, which could arise in this scenario.

In the following, the results shown in Fig. 6.13 are further analyzed. The photoelectron energies calculated with Eq. (6.4) are in very good agreement with the observation. In particular, every peak observed can clearly be assigned to one of the calculated values although the angular momentum l is completely neglected. If the situation is compared to the manifold of Rydberg states actually present in the atoms, cf. Fig. 6.2, this is remarkable. As visible in this figure, the states with higher values for l are in very good agreement with the simple Rydberg equation, Eq. (6.1). It can be concluded that exclusively Rydberg states with higher angular momentum are observed whereas no clear indication is found for the other states. This could be explained by a selectivity in the population process, favoring the population of states with high angular momenta. By comparison to appropriate calculations, this information could in principle be used to argue for one or the other of the processes. For example, it has been shown theoretically that the FTI process for certain laser parameters favors the population of states with l < 8 in helium [26]. Unfortunately, the absence of certain peaks in Fig. 6.13 may also be caused by other factors:

1. In contrast to the almost degenerated states with higher angular momenta, the states with lower values for l are spread over a large energy range, cf. Fig. 6.2. While for example the ${}^2\mathrm{P}_{1/2}$ states in krypton with n=6 and l=3,4,5 all produce electrons of practically the same energy, autoionization of the state with l=2 leads to a significantly different energy. Therefore, it appears at least reasonable that states with higher angular momenta may be easier to observe. The other states may contribute to the background rather than produce distinct peaks.

- In order to autoionize, a state must not have decayed through a different channel, e.g. by radiative decay or ionization of the Rydberg electron by the laser field. The first mechanism is known to be highly selective regarding to the differences in angular momentum of the states involved, see e.g. [9, Sect. 7.2]. For high lying Rydberg states (with *l* ≪ *n*) it scales with *n*³*l*² [13]. However, the detailed dependence of the radiative lifetime on the angular momentum of a specific state is complex, the time often much longer than the typical time needed for autoionization [32]. Though, as shown in [18] for barium, the autoionization lifetime may be of the same order or even exceed the radiative one for certain states: a very steep rise of the autoionization lifetime with *l* was obtained. In the second case, for photoionization in strong fields, it is the efficiency of the stabilization mechanisms in strong laser fields, discussed in Sect. 3.4.3, which can be expected to introduce such a dependence on *l*. For example, in [5, 29] it is argued that states with higher angular momenta are stabilized more efficiently.
 If the outoionization lifetimes are extremely short for the states with low *l* and
- 3. If the autoionization lifetimes are extremely short for the states with low *l* and hence the energetic width of the associated peaks very large, they might be absorbed in the background rather than being distinguishable.

6.2.1 Angular Distributions

In [14], a strong suppression of the rings associated with autoionization was observed in direction of p_1 , which was explained by the domination of the non-resonant ionization of the system along the laser polarization. A precise investigation of the angular distributions of the electrons is difficult since the rings are superimposed with the fan-like structures. Figure 6.15 shows the central region of the photoelec-

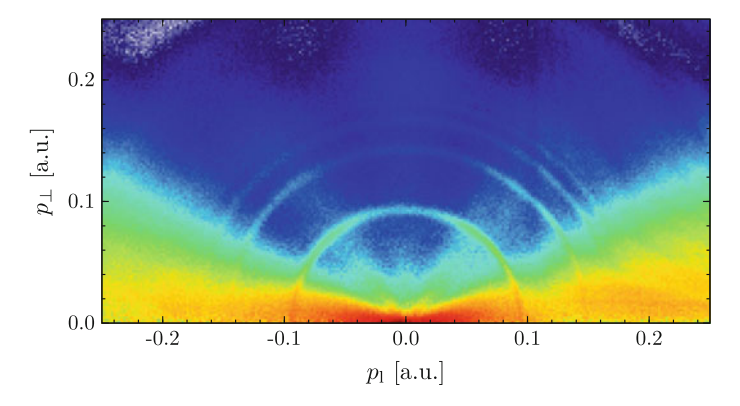


Fig. 6.15 Solid-angle corrected electron momentum distribution obtained in the region of small momenta with krypton at a wavelength of 470 nm. The color scale used is a logarithmic version of the one displayed in Fig. A.1a

tron momentum distribution obtained for krypton at a wavelength of 470 nm after solid-angle correction. Autoionization can clearly be observed for small angles of θ , close to the direction of p_1 , however the signal is much better distinguishable in perpendicular direction due to the lower level of background.

6.3 Considerations About Lifetimes and Pump-Probe Measurements

Before the results of a pump-probe measurement are presented, some information about the dynamics of the autoionization process will be derived from the electron momentum distributions and the electron energy spectra presented in the last section.

The observation of distinct rings in the momentum spectra itself gives a first indication about the lifetime of the autoionizing states involved. As discussed in Sect. 4.2.3, the momentum reconstruction process for both p_1 and p_{tr} makes use of the flight time t, measured for each individual particle. The time measurement is triggered by the laser pulse via a photodiode and within the calibration procedure, see Sect. 4.2.3, it is ensured that t=0 is exactly assigned to the point in time when the laser ionizes particles from the gas jet. However, if a small fraction of ionization processes actually takes place *after* this interaction, the flight times will slightly differ from the actual values.

One may now ask the question, how large the delay in ionization has to be in order to significantly alter the reconstructed values for the momentum components. If, for example, electrons with a longitudinal momentum of $p_1 \approx \pm 0.1$ a.u. and vanishing transverse momentum are considered, as they appear on the smallest of the rings visible in Fig. 6.7, the associated difference in flight times of these particles in comparison to an electron with vanishing initial momentum is about ∓ 6 ns. The influence of the delayed ionization can be expected to become significant, if it gets comparable with this time. In order to extend this considerations on the full momentum space, including also the reconstructed values of p_{tr} , an appropriate simulation is performed. The starting point is the generation of a set of particles with a momentum distribution approximately corresponding to the ring structures observed in the experiment, see Fig. 6.16a. The radial profile of each ring is chosen Gaussian with parameters for position and width similar to those obtained experimentally. The number of events in the rings scales with their radius in order to achieve identical particle densities. In total, more than 6×10^8 particles are simulated for each figure.

Equations (4.2) and (4.7) can be employed together with the spectrometer parameters found in the calibration process for the krypton measurement at 470 nm to calculate a flight time and a radius on the detector for each of the events. If the reconstruction procedures, as described in Sect. 4.2.1, are directly applied afterwards, the initial distribution from Fig. 6.16a—quite trivially—results. However, the flight times may be manipulated before. In particular, the time delay between the interaction with the laser and the actual autoionization can be added.

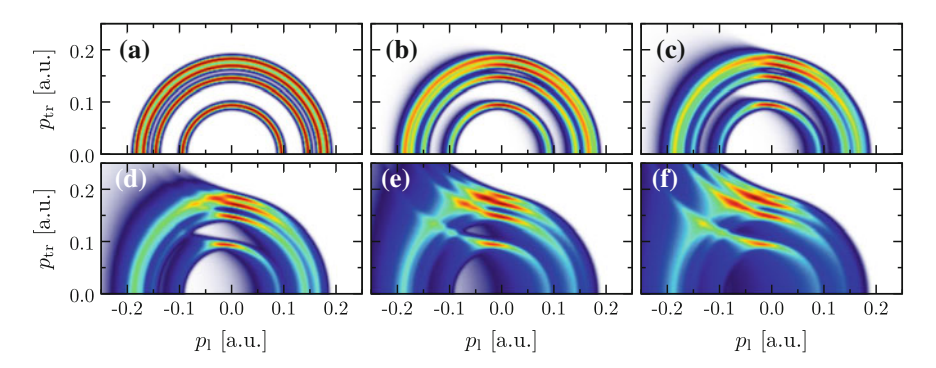


Fig. 6.16 Simulation of reconstructed momentum distributions for electrons freed by autoionization after the laser pulse. Starting from the actual distribution shown in (a), the results for exponential decay of the autoionizing states $\propto \exp(t/\tau)$ is shown for $\mathbf{b} \ \tau = 0.5 \, \mathrm{ns}$, $\mathbf{c} \ 1 \, \mathrm{ns}$, $\mathbf{d} \ 2 \, \mathrm{ns}$, $\mathbf{e} \ 5 \, \mathrm{ns}$ and $\mathbf{f} \ 10 \, \mathrm{ns}$. The linear color scale used is displayed in Fig. A.1a

Assuming an exponential decay of the autoionizing states $\propto \exp{(t/\tau)}$, the results shown in Fig. 6.16b–f are obtained for increasing values of τ . Already in (b), for $\tau=0.5$ ns, a significant modification is visible: The electrons are shifted towards negative momenta associated with longer flight times. Since they approach—for the parameters used—at the same time an integer multiple of the cyclotron period, the reconstructed value for $p_{\rm tr}$ also increases, cf. Fig. 4.12. With increasing values for τ along Fig. 6.16c–f the effect becomes more and more pronounced. In particular the isotropy of the rings is disturbed and many events are concentrated on a position close to zero longitudinal momentum. For larger τ , additionally bend "stripes", pointing towards the top left corner of the pictures can be observed. Since no indication of any "stripes" or at least a concentration of the signal on a certain point on the rings is observed in the experiment, it can directly be concluded that the time delay in ionization and thus the typical lifetime of the states is less then about 1 ns.

As described in the beginning of Sect. 6.2, no condition on the sum momentum of electrons and associated ions is utilized for event selection. Nevertheless, one can ask the general question whether such a condition could remove the events with a large ionization delay such that—due to selection of the almost instantaneous ionizing events—the rings observed appear sharp independent of the delay. Despite their much larger flight times, the reconstructed ion momenta are altered as well. In fact, for *very* small momenta, where Eq. (4.5) is a good approximation for ions *and* electrons, $\Delta p_1/\Delta t$ is independent of the particles' mass and thus equal for ions and electrons, such as the caused momentum shift. However—due to convention for the sign of the momenta discussed in Sect. 4.2.1—the sum of the momenta is constant. Therefore, a condition on the momentum sum of the particles is in general not suitable to remove those delayed ionization events from the distributions obtained.

The classical "spectroscopic" access to lifetimes is the measurement of the *natural* line width $\Delta\omega$, the energetic width of the peaks. This can be directly related to the respective lifetime τ , see e.g. [9, Sect. 7.4.1],

$$\tau = 1/\Delta\omega. \tag{6.5}$$

Since the rings represent the sharpest structures observed in the very low energy region, it can not be excluded that the width of the rings is partly or even mainly caused by the finite resolution of the REMI. However, the obtained width can be used as an upper limit hence a lower limit for the lifetime can be extracted. The results obtained with 470 nm are analyzed in this regard exemplarily. From the fits to the results shown in Fig. 6.13, the lower limits can be estimated to approximately 40, 20, 20 and 25 fs and to 50 and 45 fs for the four peaks in krypton and the two in argon (in increasing order of energy), respectively.

A more direct access to the dynamics of the autoionizing states is offered by time-resolved measurements, utilizing the pump-probe setup described in Sect. 2.2.3 together with the direct 790 nm output of the laser system. The first pulse is used to populate the DES in krypton atoms. Subsequently, the atom may autoionize or get ionized through the competing photoionization channel, see Fig. 6.12. The utilization of a second laser pulse offers the possibility to enhance the photoionization channel and at the same time frustrate autoionization. Of course, the probe pulse may only ionize the system, if the autoionization did not already take place. Therefore, if the time delay between the two pulses is varied on a timescale comparable to the autoionization lifetime of the states, the ratio between atoms that undergo photoionization and autoionization is expected to change.

The intensity of the probe pulse ideally is limited to a level which does not allow ionization or excitation of the system without a preceding pump pulse. For this reason—and in contrast to the measurements presented in Chap. 5—the intensity sharing between the pulses is chosen asymmetric by utilization of an appropriate beam splitter: 90% is used to create the pump and only 10% for the probe pulse. In this configuration, the REMI can not detect any ionization if the pump pulse is blocked. A weak probe pulse is also beneficial when considering the stabilization of Rydberg states in strong laser pulses discussed in Sect. 3.4.3.

Calibration of the time delay is performed by recording and analyzing the autocorrelation trace in the Kr^+ yield around the temporal overlap of the two pulses. The observed trace can be approximated very well by a product of a Gaussian envelope and a sinusoidal oscillation. Two parameters determined from an according fit to the data, namely the maximum of the envelope and the oscillation period of the sinusoidal, can be utilized in this respect: The first indicates the mirror-position for a vanishing time delay while the second gives—together with the known wavelength of 790 nm—the scaling of the time delay.

For reasons of statistics, distinct time delays are chosen rather than the time delay is continuously scanned. A reference measurement is performed at a negative time delay of $t \approx -82$ fs, where the weak probe pulse arrives first at the gas jet. In this configuration, its interaction with the atoms is assumed to be irrelevant for the state

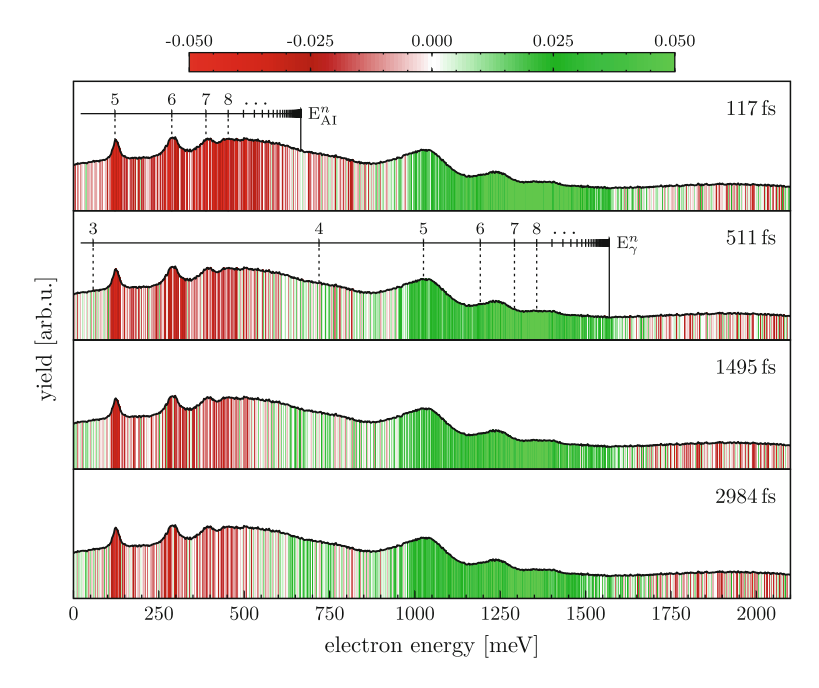


Fig. 6.17 Depletion of the autoionizing Rydberg states in krypton by a second laser pulse. The (identical) *black solid line* displays the reference electron energy spectrum observed for negative time-delay, the color code visualizes the relative change observed for different time delays, see text for details

of the atom. Thus, a momentum spectrum is obtained as it would be created from the pump pulse alone. From this distribution, the reference electron energy spectrum $E_{\rm ref}$ can be calculated, shown (multiple times) as black line in Fig. 6.17. Energy spectra obtained at positive time delays, E(t), where the pump pulse arrives first at the target, can be related to this reference in order to emphasize the effects caused by the probe pulse. To be more specific, the relative difference of the normalized electron energy spectra,

$$D(t) = \frac{E(t) - E_{\text{ref}}}{E_{\text{ref}}},$$
(6.6)

is calculated.

The results for different time delays is visualized in Fig. 6.17 as colored bars: Red color shades indicate a suppression of the signal caused by the probe pulse with respect to the reference spectrum while green shades indicate the opposite, namely a respective enhancement. In addition, the picture displays the energies for the autoionization and photoionization channels, $E_{\rm AI}^n$ and E_{γ}^n as calculated with Eqs. (6.4) and (6.3), respectively. Over all tested time delays, from about 110 fs up to almost 3 ps, a suppression of the peaks assigned to autoionization can be observed. At the same time, the photoionization channel is enhanced.

Moreover, a decrease of the contrast can clearly be distinguished with increasing time delay. Nevertheless, the probe pulse has a significant effect also with the maximum time delay of 3 ps. This holds specifically for the lowest autoionizing state with n=5, which appears similarly red-shaded for all time delays. In contrast to this, the higher states, in particular the ones with $n \geq 8$ seem to autoionize faster. It can be concluded that the typical lifetime for the autoionizing states lies in the order of the time delays tested and thus in the order of picoseconds. Further, although the DES obviously survive during the remaining part of the strong pump pulse, manipulation with a second, almost one order of magnitude weaker probe pulse is possible.

6.4 Other Targets: Neon and Molecular Nitrogen

Apart from measurements with krypton and argon, also neon and molecular nitrogen have been exposed to radiation created with the OPA during the measurement campaign. The momentum distributions obtained will be briefly shown and discussed here for completeness, in particular with regard to provide evidence of DES.

The situation in neon is quite similar to those in the other noble gases. As visible from Fig. 6.3, autoionizing states likewise exist, however the minimum main quantum number in this case is n = 12 and the associated electron energies are very limited due to the small spin-orbit splitting. In contrast, the absolute ionization potentials are larger than the ones in argon, see Table A.2. Therefore, in general, fairly high laser intensities are necessary in such measurements and statistics still may be an issue. In Fig. 6.18a the momentum distribution obtained for neon at a wavelength of 470 nm is displayed. The large saturated region appearing for negative p_1 is caused by electrons emerging most likely from the spectrometer plates as a consequence of stray light. The reason for this is the high laser intensity and the associated large beam diameter used in particular for this experiment. No distinct rings are visible in the small momentum region, however, a central diffuse spot appears at very small momenta, see magnification in (b). The lowest kinetic energies arising from autoionization of neon can be calculated with Eq. 6.4 to about 2.3, 16.3 and 27.3 meV. If these values are compared to the results for argon in Fig. 6.11, where the first peak is centered at about 10 meV, it seems very reasonable that the neon series can not be resolved.

Finally, Fig. 6.18c–f show the result of a similar experiment with a molecular N_2 target with 470 and 530 nm, respectively. Interestingly, one clear and several very faint and sharp rings are visible in the momentum range between 0.1 and 0.2 a.u., marked with arrows in (d) and (f). The smallest appears for both wavelengths with approximately the same radius although no absolute or relative calibration of the pictured is performed. The origin of these structures is not investigated in this work, however they could originate from autoionizing states, which also exist for molecules, see e.g. [31, 33]. More measurements at longer wavelengths have to be carried out in order to relate their population to the FTI mechanism. Interestingly, FTI has recently been observed in more complex systems than atoms, namely in noble gas dimers [35].

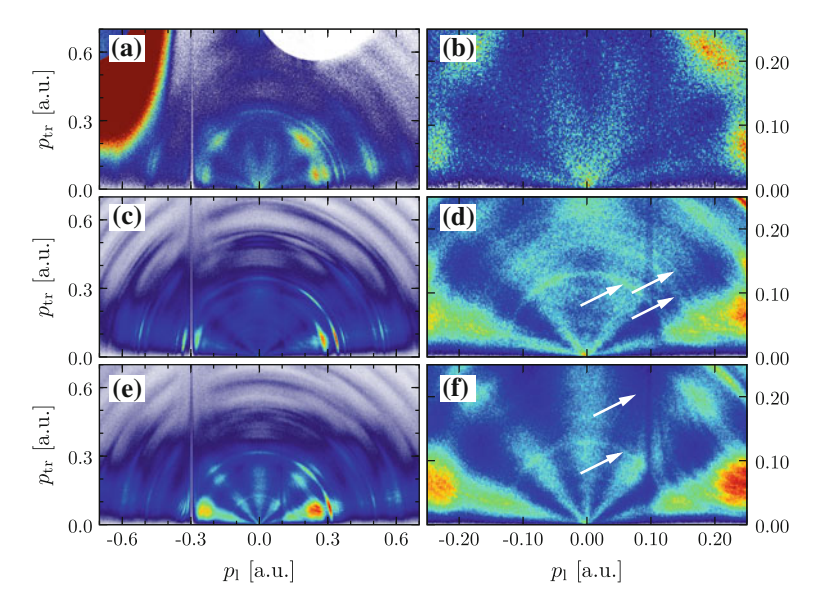


Fig. 6.18 Electron momentum distributions and magnifications of the regions of small momenta obtained with Ne and N₂ at different wavelengths: **a** and **b** Ne at 470 nm, **c** and **d** N₂ at 470 nm, **e** and **f** N₂ at 530 nm. The linear color scale used is displayed in Fig. A.1a

In conclusion, highly resolved electron momentum distributions were presented, obtained with krypton and argon at different wavelengths. The fundamental change of the distributions along increasing wavelengths, from the multiphoton to the tunneling regime, was observed and discussed. Unique fingerprints of autoionizing doubly excited states were identified. The population of these states in the laser field was proven up to 1300 nm in argon and related to the recently explored mechanism of frustrated tunneling ionization [26]. A possible connection to the well-known dielectronic recombination processes, see e.g. [19, 27], was discussed. Photoionization of the DES with a second laser pulse in a pump-probe experiment revealed lifetimes in the order of picoseconds.

References

- R. Ali et al., Dielectronic recombination on heliumlike argon. Phys. Rev. Lett. 64, 633–636 (1990). doi:10.1103/PhysRevLett.64.633
- D.G. Arbó et al., Doubly differential diffraction at a time grating in above-threshold ionization: intracycle and intercycle interferences. Nucl. Instrum. Methods Phys. Res. Sect. B: Beam Interact. Mater. At. 279, 24–30 (2012). doi:10.1016/j.nimb.2011.10.030
- 3. C. Beilmann et al., Prominent higher-order contributions to electronic recombination. Phys. Rev. Lett. 107, 143201 (2011). doi:10.1103/PhysRevLett.107.143201
- D.S. Belic et al., Dielectronic recombination: a crossed-beams observation and measurement of cross section. Phys. Rev. Lett. 50, 339–342 (1983). doi:10.1103/PhysRevLett.50.339

References 121

 F. Benvenuto et al., Stability of Rydberg atoms in a strong laser field. Phys. Rev. A: At. Mol. Opt. Phys. 45, R7670–R7673 (1992). doi:10.1103/PhysRevA.45.R7670

- J. Beringer et al., Review of particle physics. Phys. Rev. D: Part. Fields 86, 010001 (2012). doi:10.1103/PhysRevD.86.010001
- P.R. Blazewicz et al., Four-photon excitation of even-parity Rydberg states in krypton and xenon. Phys. Rev. A: At. Mol. Opt. Phys. 35, 1092–1098 (1987). doi:10.1103/PhysRevA.35. 1092
- 8. Z. Chen et al., Analysis of two-dimensional photoelectron momentum spectra and the effect of the long-range Coulomb potential in single ionization of atoms by intense lasers. Phys. Rev. A: At. Mol. Opt. Phys. **74**, 053405 (2006). doi:10.1103/PhysRevA.74.053405
- 9. W. Demtröder, Experimentalphysik 3: Atome, Moleküle und Festkörper (Springer, Berlin, 2005)
- P.F. Dittner, Dielectronic recombination measurements of multicharged ions. Phys. Scr. T22, 65–68 (1988). doi:10.1088/0031-8949/1988/T22/008
- 11. R.R. Freeman et al., Pondermotive effects on angular distributions of photoelectrons. Phys. Rev. Lett. **57**, 3156–3159 (1986). doi:10.1103/PhysRevLett.**57**.3156
- 12. A.J. González Martínez et al., State-selective quantum interference observed in the recombination of highly charged Hg^{75+..78+} mercury ions in an electron beam ion trap. Phys. Rev. Lett. **94**, 203201 (2005). doi:10.1103/PhysRevLett.94.203201
- 13. S.P. Goreslavskii et al., Probabilities of radiative transitions between highly excited atomic states. J. Exp. Theor. Phys. **55**, 1032–1036 (1982)
- M. Goto, K. Hansen, Branching ratio between resonant and non-resonant ionization of xenon evaluated from photoelectron angular distributions. Phys. Scr. 86, 035303 (2012). doi:10.1088/ 0031-8949/86/03/035303
- 15. M. Grieser, Private communication (2014)
- Y. Hahn, K.J. LaGattuta, Dielectronic recombination and related resonance processes. Phys. Rep. 166, 195–268 (1988). doi:10.1016/0370-1573(88)90021-X
- 17. R.N. Hill, Hydrogenic Wave Functions, in *Springer Handbook of Atomic, Molecular, and Optical Physics [online]*, ed. by G.W.F. Drake (Springer Science+Buisiness Media Inc., New York, 2006), Chap. 9, pp. 153–171. doi:10.1007/978-0-387-26308-3
- R.R. Jones, T.F. Gallagher, Autoionization of high-l Ba 6p_{1/2}nl states. Phys. Rev. A: At. Mol. Opt. Phys. 38, 2846–2853 (1988). doi:10.1103/PhysRevA.38.2846
- G. Kilgus et al., Dielectronic recombination of hydrogenlike oxygen in a heavy-ion storage ring. Phys. Rev. Lett. 64, 737–740 (1990). doi:10.1103/PhysRevLett.64.737
- A. Kramida et al., NIST Atomic Spectra Database (ver. 5.1) [Online]. National Institute of Standards and Technology, Gaithersburg, MD (2013). http://physics.nist.gov/asd. Accessed 5 Aug 2014
- M. Larsson, Atomic and molecular physics with ion storage rings. Rep. Prog. Phys. 58, 1267– 1319 (1995). doi:10.1088/0034-4885/58/10/003
- T. Marchenko et al., Electron angular distributions in near-threshold atomic ionization. J. Phys. B: At. Mol. Phys. 43, 095601 (2010). doi:10.1088/0953-4075/43/9/095601
- T. Marchenko et al., Wavelength dependence of photoelectron spectra in above-threshold ionization.
 J. Phys. B: At. Mol. Phys. 43, 185001 (2010). doi:10.1088/0953-4075/43/18/185001
- B.K. McFarland et al., High harmonic generation from multiple orbitals in N₂. Science 322, 1232–1235 (2008). doi:10.1126/science.1162780
- J.B.A. Mitchell et al., Dielectronic-recombination cross-section measurements for C⁺ ions. Phys. Rev. Lett. 50, 335–338 (1983). doi:10.1103/PhysRevLett.50.335
- T. Nubbemeyer et al., Strong-field tunneling without ionization. Phys. Rev. Lett. 101, 233001 (2008). doi:10.1103/PhysRevLett.101.233001
- S. Schippers, Astrophysical relevance of storage-ring electron-ion recombination experiments.
 J. Phys.: Conf. Ser. 163, 012001 (2009). doi:10.1088/1742-6596/163/1/012001
- S. Schippers, Relativistic, QED and nuclear effects in highly charged ions revealed by resonant electron-ion recombination in storage rings. Nucl. Instrum. Methods Phys. Res. Sect B: Beam Interact. Mater. At. 267, 192–195 (2009). doi:10.1016/j.nimb.2008.10.040

- A. Scrinzi et al., Stabilization of Rydberg atoms in superintense laser fields. Phys. Rev. A: At. Mol. Opt. Phys. 48, R2527–R2530 (1993). doi:10.1103/PhysRevA.48.R2527
- 30. O. Smirnova et al., High harmonic interferometry of multi-electron dynamics in molecules. Nature **460**, 972–977 (2009). doi:10.1038/nature08253
- I. Sánchez, F. Martin, The doubly excited states of the H₂ molecule. J. Chem. Phys. 106, 7720–7730 (1997). doi:10.1063/1.473773
- V.L. Sukhorukov et al., Photoionization dynamics of excited Ne, Ar, Kr and Xe atoms near threshold. J. Phys. B: At. Mol. Opt. Phys. 45, 092001 (2012). doi:10.1088/0953-4075/45/9/ 092001
- M. Ukai, Spectroscopy and dynamics of superexcited molecules as probed by fluorescence measurements. J. Electron Spectrosc. Relat. Phenom. 79, 423–428 (1996). doi:10.1016/0368-2048(96)02886-1
- X. Urbain et al., Intense-laser-field ionization of molecular hydrogen in the tunneling regime and its effect on the vibrational excitation of H₂⁺. Phys. Rev. Lett. 92, 163004 (2004). doi: 10.1103/PhysRevLett.92.163004
- A. von Veltheim et al., Frustrated tunnel ionization of noble gas dimers with Rydberg-electron shakeoff by electron charge oscillation. Phys. Rev. Lett. 110, 023001 (2013). doi:10.1103/ PhysRevLett.110.023001
- 36. G.K. Wertheim et al., Determination of the Gaussian and Lorentzian content of experimental line shapes. Rev. Sci. Instrum. 45, 1369–1371 (1974). doi:10.1063/1.1686503

Chapter 7 Channel-Selective Electron Spectra for H₂ at Different Wavelengths

In the previous chapter, an OPA was utilized to expose noble gas atoms to strong fields of different wavelengths. A change of the photoelectron momentum distributions could be observed while approaching the tunneling regime. In the following chapter, this investigation is extended to a more complex system, namely molecular hydrogen. As already discussed in Sect. 3.5, the exposure of H_2 to strong laser fields results in pure ionization to H_2^+ , as well as in single or double ionization and subsequent dissociation or Coulomb explosion of the molecule, respectively. By utilizing the ability of the REMI to record all products of a reaction in coincidence and to provide kinematically complete data, the different channels can be separated. Highly resolved electron momentum distributions are recorded for each of the channels at different wavelengths and compared to each other.

The chapter starts with the description of the ion—ion coincidence mapping technique utilized for the separation of the different reaction channels in Sect. 7.1. The experimental setup and the determination of the central wavelength delivered by the OPA are the subjects of Sect. 7.2. After this, the experimental results are presented. In Sect. 7.3, ion momentum distributions obtained are discussed and compared to results of a numerical solution of the TDSE. The electron momentum distributions measured for the different channels and wavelengths are shown and compared to each other in Sect. 7.4.

7.1 Separation of the Different Reaction Channels

Although molecular hydrogen contains only four particles—two nuclei and two electrons—it represents a fairly complicated target for experimental investigation. In contrast to the atomic targets investigated in Chaps. 5 and 6, the number of electrons removed from the neutral system is not encoded in the charge of the ions finally detected. In fact, H⁺ ions may be produced from single as well as from double ionization of the system. In addition, single ionization may also create a stable H₂⁺

molecular ion. Those different processes, namely dissociation, Coulomb explosion (CE) and ionization were already introduced in Sect. 3.5.1:

$$H_2 \longrightarrow H + H^+ + e^-$$
 (dissociation)
 $H_2 \longrightarrow 2H^+ + 2e^-$ (Coulomb explosion)
 $H_2 \longrightarrow H_2^+ + e^-$ (ionization)

The key to distinguish in particular between the dissociation and the CE channel lies—as will be shown in the following—in the coincident detection of the emerging ions. With its ability to detect additionally the freed electrons, the REMI represents an ideal tool for the investigation of hydrogen exposed to strong laser fields.

Figure 7.1a displays a typical spectrum of ion flight times obtained in the experiment. The black line, representing all ions detected, comprises five main peaks in total, from which two can be related to dissociation and two to CE, see Sect. 3.5.1. The peak on the very right is formed by the molecular H_2^+ ions. In Fig. 7.1b, the

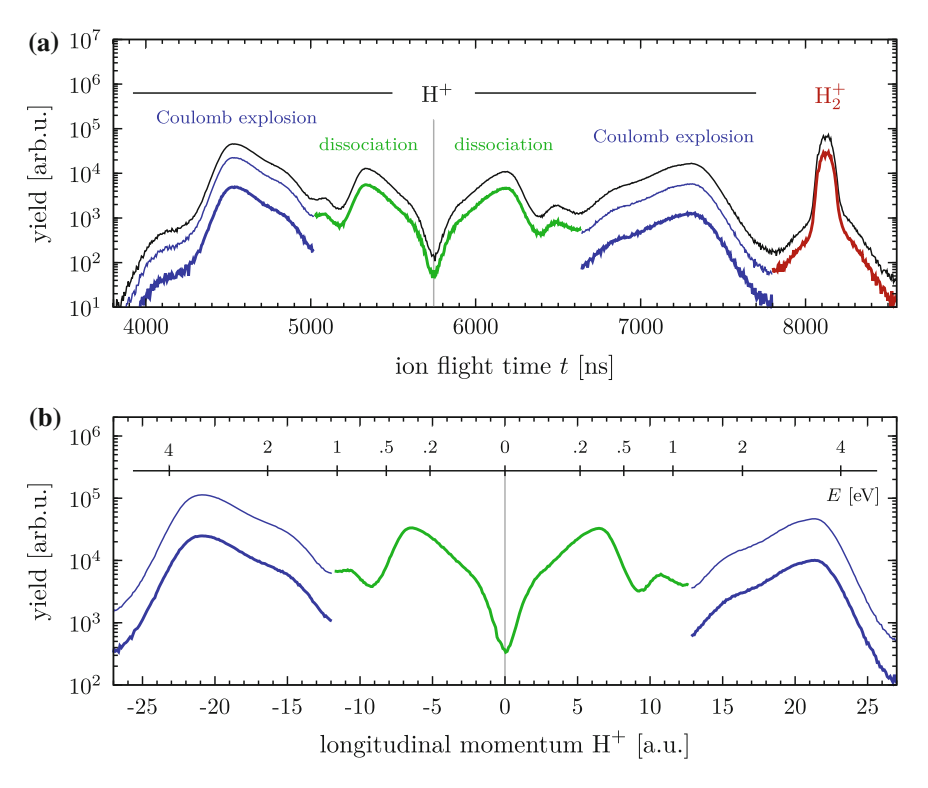


Fig. 7.1 a Ion flight times obtained with a wavelength of $570 \,\mathrm{nm}$. The *black curve* resembles all recorded ions while in the *colored curves* exclusively those events are considered, in which the associated electron(s) is (are) detected in coincidence with the ion(s), see text for details. **b** Reconstructed longitudinal momenta for the H⁺ ions, same color code as in (a)

reconstructed longitudinal momentum distribution of the H^+ ions is shown together with a scale for the kinetic energy of the particles. Due to the almost identical mass of the H atom and the H^+ ion, the total energy released, the *kinetic energy release* (KER), is shared symmetrically between the two particles in the dissociation as well as in the CE process. Therefore, the KER is given by twice the respective value shown on the scale. As discussed in Sect. 3.5.1, the fragmented H_2 molecules are strongly aligned along the polarization direction of the laser such that the transverse momentum components of the detected particles can be neglected. The same holds for the small amount of energy carried by the emerging electron(s).

In order to have a closer look into the processes and in particular to be able to separate the different channels from each other, an ion–ion coincidence mapping technique is used, where the momentum of the first ion detected is related to the one of the second, see e.g. [1]. Examples of the resulting coincidence maps for the longitudinal momenta of the ions are shown in Fig. 7.2. The maps contain exclusively those events, in which two ${\rm H}^+$ ions are detected in coincidence. In addition, the respective projections on the axes are shown as red lines. The black line on the horizontal axis depicts the spectrum obtained if in addition those events are included, in which only one ion is detected. The curves are scaled in height such that their global maxima coincide.

A strong correlation between the two peaks with the highest absolute momenta can be observed, thus identifying the CE channel. In contrast, the ions created by dissociation, forming the inner peaks, are not correlated to each other. Instead, each of these ions shares momentum with a neutral H atom that is not detected. Consequently, the selection of the events, in which two ions are detected in coincidence, already suppresses the dissociation channel as can be seen from comparison of the red and the black curve.

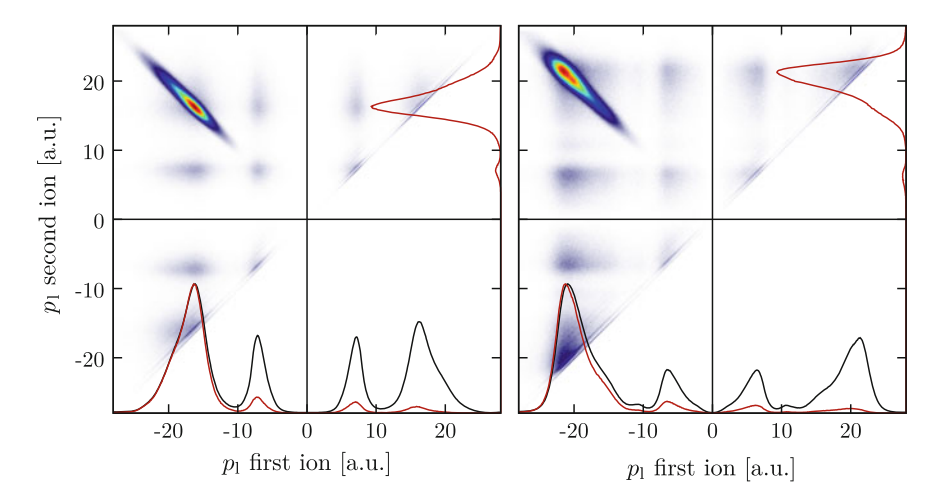


Fig. 7.2 Ion–ion coincidence maps for the longitudinal H^+ momenta obtained at 470 nm (*left*) and 570 nm (*right*), see text for details

The shapes of the peaks clearly change with the wavelength. Nevertheless, they can always be assigned to the different channels by exploiting the characteristic fingerprint the CE leaves in the coincidence maps. However, it can of course not be ruled out that the correlated peaks in the flight time spectra also comprise certain contribution from ions produced with similar energies in dissociation processes.

By utilizing appropriate conditions on the flight time of the ions, the events associated with the dissociation channel can be separated from the ones associated with CE in an early stage of the analysis. Only those events are processed, in which—depending on the process—exactly one (dissociation) or up to two ions (CE) are detected together with the photoelectrons. The respective ion time-of-flight spectra for those events are displayed in Fig. 7.1 as thick curves in green and blue, respectively. For the CE channel, the method represents a three-particle ($\mathrm{H^+} + 2\mathrm{e^-}$) or even four-particle ($\mathrm{2H^+} + 2\mathrm{e^-}$) coincidence measurement, which is in general fairly critical with regard to statistics. Compared to the events, in which at least one of the two electrons is detected—shown as the thin blue curve in Fig. 7.1—, the total number is decreased by about 80% due to the limited efficiency of the detector and its dead time after the detection of the first electron. Nevertheless, as will be shown in Sect. 7.4, the statistics achieved is still good enough for highly resolved electron momentum distributions.

The peak arising from CE at positive momenta in Fig. 7.1b has, compared to the respective one at negative momenta, a decreased magnitude. The initial momentum vectors of the respective ions point towards the electron detector which results in long flight times and in larger spatial coordinates for the impact position on the ion detector. A part of the ions therefore misses the detector. If the laser polarization is not perfectly aligned along the spectrometer axis, this effect is further enhanced. However, apart from decreasing the level of statistics, the decreased magnitude of the peak has no influence on the results presented in the following sections.

7.2 Experimental Setup and Measurement of the Wavelengths

The experimental setup used for the measurements presented in this chapter is essentially the same as used for the single pulse measurements in Chap. 6. Beside the direct output of the laser system at about 790 nm, see Sect. 2.2.1, the OPA is utilized for the creation of radiation from about 470 to 1300 nm as described in Sect. 2.2.5. Additionally, an optical spectrometer is used to measure the actual wavelength delivered to the REMI. The spectra obtained are shown in Fig. 7.3. By performing Gaussian fits—shown as solid lines—the central wavelengths are extracted, listed in Table 7.1. Considering only the wavelengths delivered by the OPA, the dependence of the measured output on the value selected in the software is linear with a slope of one within 1σ . The mean deviation between the selected and produced wavelength calculates to less than 5 nm and thus is much smaller than the typical spectral width of the pulses.

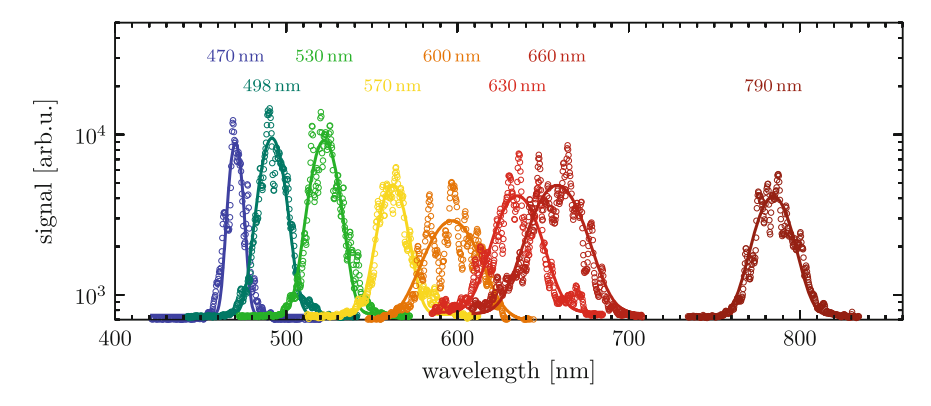


Fig. 7.3 Measured optical spectra of the output of the OPA and the direct output of the laser system. The labels represent the selected wavelengths, the central wavelengths obtained from fits to the spectra are given in Table 7.1. In some of the spectra, interference fringes can be observed. This is caused by the method used for the measurement, namely the coupling of stray light into the spectrometer via a fiber

Table 7.1 Comparison between the wavelength selected with the control software of the OPA and the measured output, obtained from the fits to the optical spectra shown in Fig. 7.3

	Wavelength (nm)								
Selected	470	498	530	570	600	630	660	1300	$(790)^{\alpha}$
Measured	470	492	522	562	597	635	658	^{\beta}	784
γ^* , Eq. (3.1)	0.86	0.83	0.78	0.72	0.68	0.64	0.62	0.31	0.52

 $^{^{\}alpha}$ Direct output of the laser system

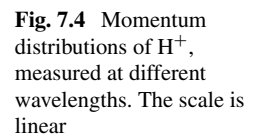
This proves the reliability of the OPA system with respect to the produced wavelengths. In all calculations and simulations presented in this chapter the measured wavelengths are used, if available. However, in order to keep consistency with the previous chapter, all spectra are still referred to according to the wavelength *selected*.

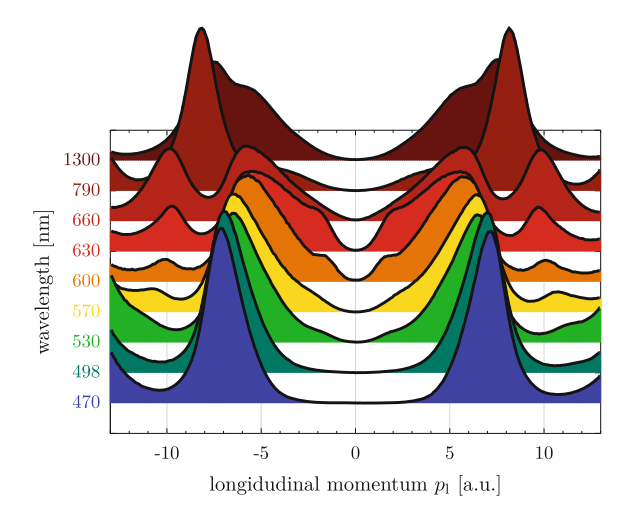
7.3 Changes in the Ion Momentum Distributions

First, the longitudinal momentum distributions obtained for the ions are investigated, in particular the distributions arising from dissociation of the molecule. Figure 7.4 displays the lower regions of the momentum distributions of H^+ obtained at different wavelengths. Every spectrum is normalized with respect to the area under the curve. Due to the almost perfect symmetry, the following discussion is restricted to the positive part with $p_1 \geq 0$.

^βWavelength exceeds specifications of the spectrometer

^{*}For single ionization of H_2 at a laser intensity of $5 \times 10^{14} \,\mathrm{W/cm^2}$





At a short wavelength of 470 nm, only one peak is visible at about 7.2 a.u. The rising of the signal at about 12 a.u. resembles the low-energetic tail of the peak assigned to CE of the molecule and may be ignored for the moment. For wavelengths of 530 nm and above, the formation of a second peak can be observed at a momentum of about 11 a.u., also shifting to lower values with increasing wavelengths. However, in the measurement carried out at 660 nm this trend does not continue. The distributions obtained at 790 and 1300 nm differ to a large extent from each other and the one at 660 nm, which can be explained by the large steps in wavelength. The first shows again only one large peak with an elongated pedestal towards zero momentum, while the latter comprises two peaks very close to each other and thus merged.

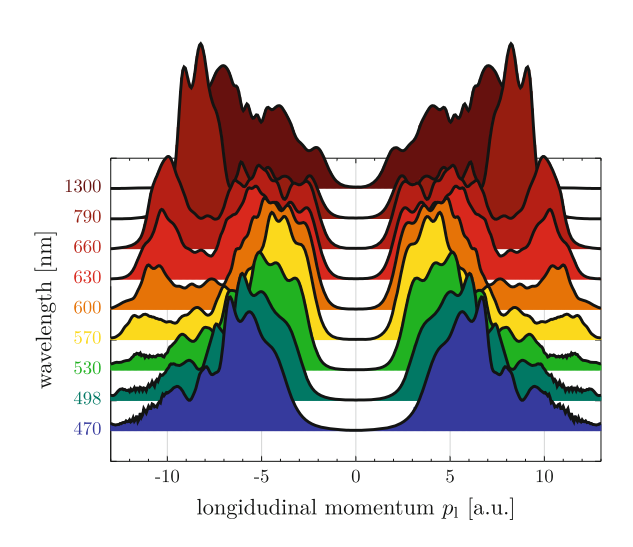
The presence of two peaks in the KER spectrum of the dissociation channel has been observed also in other experiments and was related to the different number of photons involved in the transition from the bound H_2^+ system to the dissociative potential curve [5]: The peak representing slowly dissociating molecules is the result of the absorption of one photon, while the other is caused by a net-two-photon absorption, possible e.g. as a sequence of an initial three-photon absorption followed by the emission of one photon. As shown in [3]¹ for longer pulses, the latter is created in the rising edge of the pulse, while the first emerges in the trailing edge, where the intensity already decreases. The position of the peaks is—in contrast to their magnitude—independent from the laser intensity as shown experimentally in [5].

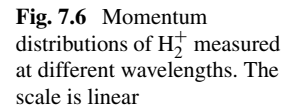
One suitable approach for the reproduction of the experimental distributions is a numerical solution of the TDSE for the dissociation process. However, this is difficult since the results crucially depend on the laser intensity, which is hard to quantify and known to vary in the laser focus, see Sect. 2.1.3. If only the dissociation of the molecule is subject of the calculation, rather than including also the preceding ionization of the molecule, additionally assumptions about the initial state are required.

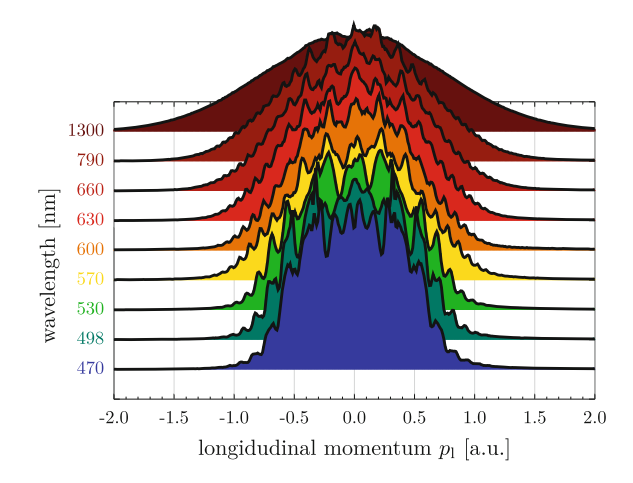
¹See also [4] for original figure in higher quality and a detailed discussion.

Despite this problems, a set of simulation has been carried out by [2], using a split-operator formalism to approximate the time-evolution operator of the system. A set of reasonable parameters for laser intensity and pulse duration was tested. The contribution from each of the vibrational states of H₂⁺ was calculated separately and the respective distributions were added incoherently afterwards. An initial population of the vibrational states proportional to the respective Franck-Condon overlap with the ground state of the neutral hydrogen molecule was assumed. The photon energies resemble the measured values for the wavelengths given in Table 7.1. Excellent overall agreement was found for a rather low, but still reasonable laser intensity of about $1.3 \times 10^{14} \,\mathrm{W/cm^2}$ and a pulse duration of 30 fs. The momentum distributions obtained are displayed in Fig. 7.5. The main features observed in the experiment, namely the appearance of two peaks in the momentum spectra as approaching longer wavelengths and their characteristic shifts are nicely reproduced. Since CE is not considered in the simulation, the distributions approach zero, rather than showing a plateau or already an increase at a momentum of about 12 a.u. The remaining deviations to the experimental results can be assigned to different initial population of the states in H₂⁺ and the finite intensity distribution in the laser focus, see Sect. 2.1.3, which is also not considered. In addition, the experimental intensity varies from measurement to measurement, for example due to differing conversion efficiencies in the OPA and changing dimensions of the laser focus. Since the calculated distributions are fairly sensitive to these parameters, it is reasonable to assume that even better results could be obtained by an individual optimization of the parameters for each measurement. For example, the width of the peaks in particular in the measurement at 470 nm is nicely reproduced with an assumed intensity of about $8.8 \times 10^{13} \,\mathrm{W/cm^2}$, for which the results of the simulation are shown in Fig. A.2. However, the rise of the second peak for wavelengths larger than 570 nm is much better visible in Fig. 7.5, at $1.3 \times 10^{14} \,\mathrm{W/cm^2}$. Since the main results are already

Fig. 7.5 Simulated momentum distributions of dissociating H⁺ [2] at about 1.3×10^{14} W/cm², see text for details. The scale is linear







reproduced with global parameters, and a further optimization is barely expected to yield new information, this was not carried out.

Apart from the dissociation channel, stable H_2^+ is formed by simple ionization of the molecule. The momentum distributions obtained are shown in Fig. 7.6. Substructures in the broad distributions are clearly visible in particular in the measurements at short wavelengths. The peaks of these structures are separated by momenta, which correspond to the small fraction of the photon energy, the ionic molecule gains in the ionization process. This energy is in good approximation given by $\frac{m_e}{m} \times \omega_0 \approx 2.7 \times 10^{-4} \times \omega_0$, see Table A.2. Each of the peaks can thus be related to an ATI process of particular order. Consequently, with increasing wavelength, the separation of the peaks decreases. At the same time, their magnitude becomes smaller and smaller, such that they finally—at 1300 nm—are not visible any more.

With regard to the overall distributions, a continuous increase in width can be noticed with increasing wavelength as—for long wavelengths and the tunneling regime—predicted by the ADK theory in Eq. (3.6). However, the trend is likewise reasonable in the multiphoton picture for short wavelengths: With decreasing photon energy, the number of photons needed for the ionization of the molecule increases. Since the uncertainty in the photon energy in an ultrashort laser pulse—see Sect. 2.1—adds up, the energy range accessible and thus the final momentum spread of the created particles becomes larger and larger.

7.4 Electron Momentum Distributions

After the different channels are identified and separated from each other, respective electron momentum distributions can be obtained in coincidence with the respective ionic fragments. In general, in addition to the event selection described in Sect. 7.1,

a condition on the momentum sum of the particles can be used in order to remove false coincidences from the data, as done in Sect. 5.2. However, this is not done here due to different reasons given in the following.

Dissociation channel: One of the particles, namely the neutral H atom emerging, is not detected and its momentum thus always missing in the total momentum sum.

CE channel: For this channel, the main difficulty lies in the number of particles to consider in the momentum sum. The detection of four particles in coincidence is possible, but a strong constraint with regard to statistics. For this reason, all those events are considered, in which both electrons and *at least* one of the ions is detected. In a significant part of these events the situation is therefore similar to the case of the dissociation channel.

Ionization channel: The simple single ionization to H_2^+ and the creation of only two particles in fact is an ideal situation to apply an additional condition on the momentum sum. However, since the momentum distributions are to be compared to the ones arising from the other channels, for which this is not possible, it is reasonable to abstain from this here as well.

Figure 7.7 shows the electron momentum distributions obtained in coincidence with H_2^+ at different wavelengths. At 470 nm, shown in (a), the distribution features a manifold of distinct broader formations of peaks along with sharp Freeman resonances and four "fan-like" structures, pointing towards the origin. Signatures of ATI dominate the regions of large momenta, visible also in the respective ion longitudinal momentum distributions shown in Fig. 7.6. The measurement at 498 nm, (b), already provides a distribution fairly different. The sharp Freeman resonances now dominate the spectrum and at the position of the broader distinct peaks in (a), only faint indication of signal remains. In addition, the four fan-like structures in the central region are more aligned along the p_1 axis and a fifth vertical stripe arises.

With increasing wavelength from 530 to 660 nm, along the distributions shown in Fig. 7.7c-g, more and more of the formally distinct formations become "connected" in radial direction thus forming elongated stripes, pointing from regions of large momenta towards the origin and absorbing the fan-like structures. The region below a transverse and longitudinal momentum of about 0.3 and 0.8 a.u., respectively, becomes more and more homogeneously filled. In the outer regions of the distributions, ATI structures are still present, however less separated due to the decreasing photon energy. It has to be mentioned that the intensity in the measurement at 600 nm was lower compared to the other measurements, which will be derived later from the signal in the CE channel. Finally, at 1300 nm, (i), a distribution is obtained that fills the full area specified above almost uniformly. Faint indications of ATI structures are still visible in transverse direction, at about 0.4 a.u. The transition of the electron momentum distributions observed for H₂⁺ from short to long wavelengths shows qualitatively the same trends as the respective transition observed for the noble gas atoms: Broad, uniform and homogeneous distributions at long wavelengths, and distributions with distinct structures and Freeman resonances at short wavelengths. The sensitivity on the ionized species clearly decreases with increasing wavelength.

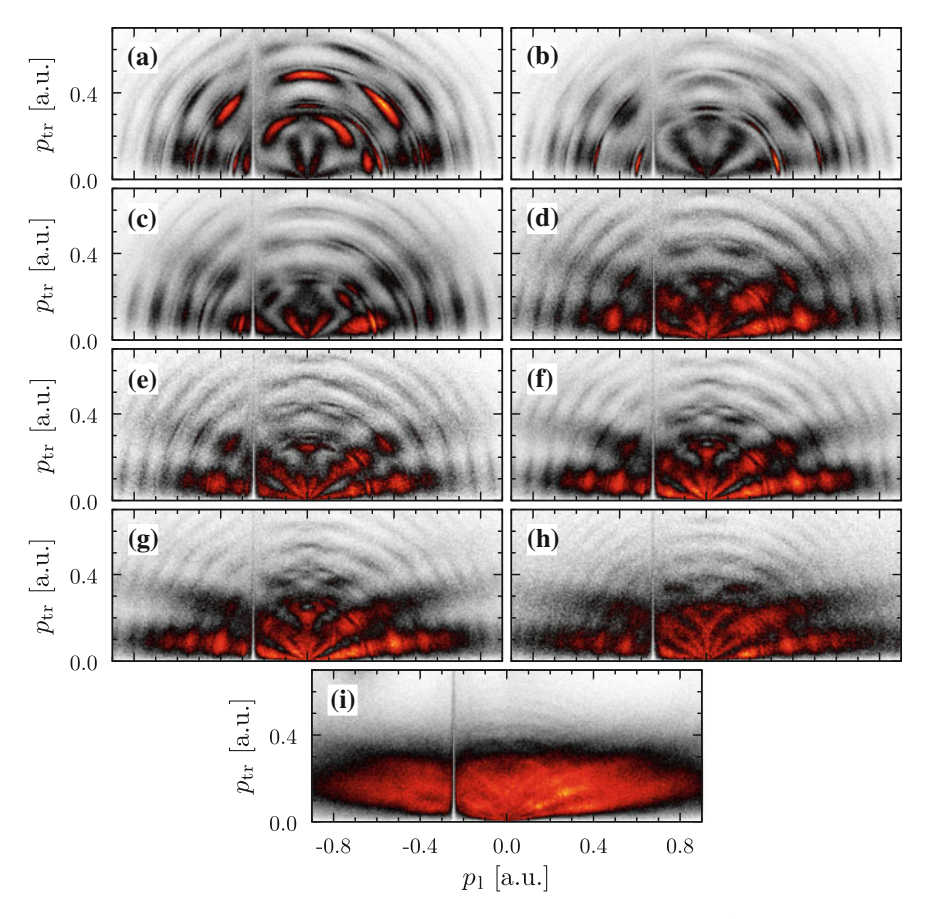


Fig. 7.7 Electron momentum distributions obtained in coincidence with H₂⁺ at different wavelengths: **a** 470 nm, **b** 498 nm, **c** 530 nm, **d** 570 nm, **e** 600 nm, **f** 630 nm, **g** 660 nm, **h** 790 nm, **i** 1300 nm. The linear color scale used is displayed in Fig. A.1b

Already for 790 nm, where still a manifold of distinct structures are visible, the distributions for H_2 and Kr show many similarities, compare Fig. 7.7h to Fig. 6.5d: In both cases, seven fan-like structures are visible and the structure emerging in direction of p_{tr} splits at about 0.2 a.u. In contrast, the momentum distributions obtained for short wavelengths crucially depend on the species ionized.

Can these observations be transferred to the comparison of momentum distributions obtained for a different reaction channel of the molecule? In particular interesting is the dissociation channel, since it is expected to contain in principle the same initial ionization from H_2 to H_2^+ . If this ionization and the subsequent dissociation are treated as completely independent processes, the electron momentum distribution of this channel, shown in Fig. 7.8, should be identical to those obtained in coincidence

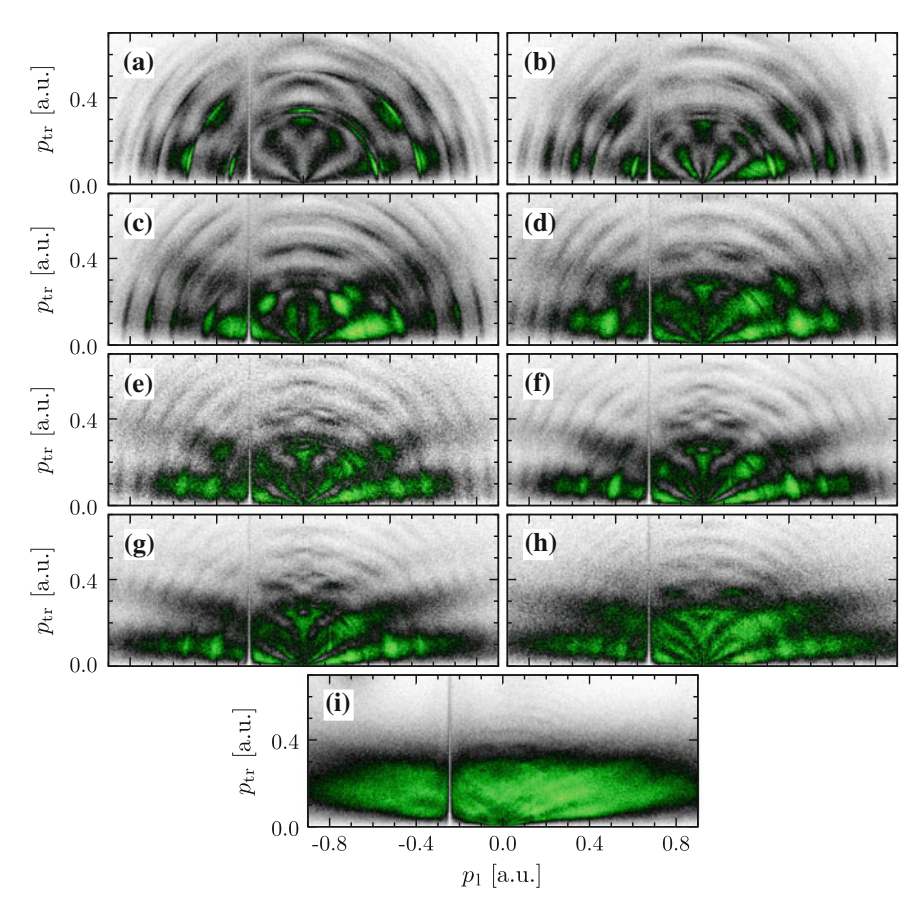


Fig. 7.8 Electron momentum distributions associated with dissociation of the molecule at different wavelengths: **a** 470 nm, **b** 498 nm, **c** 530 nm, **d** 570 nm, **e** 600 nm, **f** 630 nm, **g** 660 nm, **h** 790 nm, **i** 1300 nm. The linear color scale used is displayed in Fig. A.1c

with H_2^+ . However, already in this representation, striking differences are visible compared to the sequence shown in Fig. 7.7.

In order to visualize the discrepancies between the distributions more clearly, the straight-forward approach would certainly be, to simply calculate the difference of the respective spectra. However, in this process, information is lost. For example, for both an equally strong or a likewise vanishing signal in the distributions, the difference always calculates to zero. The full information about the two distributions can therefore—still—only be obtained if two pictures are considered, namely the calculated difference and one of the original distributions. In order to encode all information in one single picture, a different approach is used, described in the following.

Starting from the two binned momentum distributions to be compared to each other (normalized to their respective maximum), a constant value of 0.1 is subtracted in order to suppress background. Negative values are afterwards set to zero and the distributions are again normalized. Depending on the channel, one of the color scales shown in Fig. A.1e–g is applied. The scales are chosen according to the assignment to the channels made in Fig. 7.1, and designed such that each contains only shades of pure red, green or blue. Besides pure black, associated with vanishing signal, none of the colors present in one particular scale can be produced by additive color mixing between the others. As a final step, the two distributions are added by means of additive color mixing. If this is done e.g. for the distributions arising in the ionization channel (red) and the dissociation channel (green), the resulting distribution contains these colors and—in regions where both of the former distributions showed signal—shades of yellow. Figure 7.9 visualizes the approach.

Figure $7.10a_1$ – a_3 displays the resulting graphs for the comparison of the ionization and the dissociation channel for three selected wavelengths. The full series of graphs for all wavelengths can be found in Fig. A.3. While the differences in the distributions obtained is clearly visible in measurements at short wavelengths, shown in (a_1) and (a_2) , for long wavelengths, (a_3) , the distributions are almost identical. If approaching the regime of tunnel ionization, the resulting electron momentum distributions thus become insensitive not only to the species, but also to the channel.

The differing distributions obtained at short wavelengths prove the simple sequential picture, in which the dissociation of the molecule is treated as completely separated from the ionization process, to be wrong. In the simplest case, this can be explained by a post-selection effect: Molecules in lower vibrational levels resist dissociation to a larger extent. The electron momentum distribution associated to the dissociation channel thus may contain primarily events, in which the H_2 molecules are ionized to one of the higher lying levels in H_2^+ in the first step. The difference between the lower and the upper vibrational levels is comparable to the photon energies used, such that the separation of the channels may be equivalent to a selection of the number of photons involved in the ionization process. Due to the difference in total angular momentum that can be transferred, the associated electron momentum distributions are expected to differ from each other. For long wavelengths, were the photon energy becomes small against the energy difference of the upper and the lower levels, this effect is then expected to vanish. In this case, the number of photons

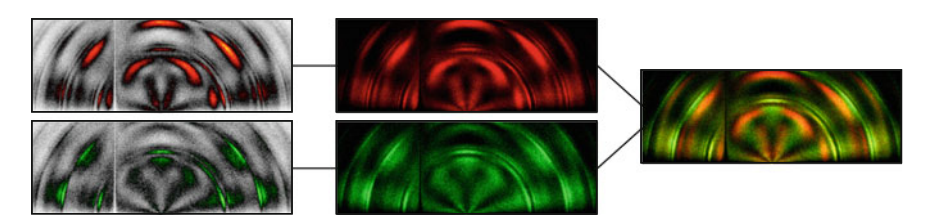


Fig. 7.9 Overlays of momentum distributions for comparison, see text for details

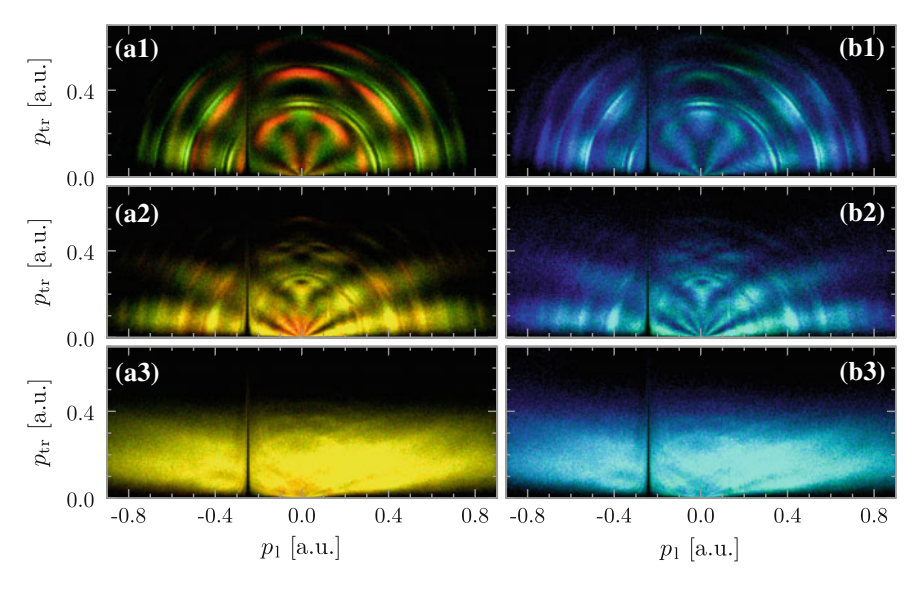


Fig. 7.10 Combined electron momentum distributions. **a** Ionization channel (*red*) and the dissociation channel (*green*) at (**a**₁) 470 nm, (**a**₂) 498 nm and (**a**₃) 1300 nm. **b** Same series as is (**a**) but comprising the dissociation channel (*green*) and CE channel (*blue*)

required to access a particular state in H_2^+ is not well-defined any more. Since all possible channels contribute to the total signal, broad distributions result.

Finally, the electron momentum distributions associated to the CE channel are displayed in Fig. 7.11. The level of statistics in the measurement at $600 \, \text{nm}$, e, is lower for this channel due to a lower laser intensity, favoring ionization and dissociation of the molecule. Since the ionization process is completely different, at least for one of the electrons, the resulting distributions can be expected to clearly differ from those obtained for the other channels. However, the difference to the dissociation channel, Fig. $7.10b_1$ – b_3 , appears actually less pronounced than the one between the other two channels. It has to be mentioned that the limited statistics in the CE channel lowers the visibility of the differences in this representation to some extent. At $1300 \, \text{nm}$, (b_3) , the distributions are again identical. The full series of graphs and the respective comparison between the dissociation and CE channel are shown in Figs. A.4 and A.5, respectively.

In conclusion, molecular hydrogen was exposed to strong laser pulses of different wavelengths. The utilization of the reaction microscope and the possibility of multicoincidence measurements in combination with an ion–ion coincidence mapping technique, see e.g. [1], gave access to channel-selective momentum distributions. Experimental results for the momentum distribution of the ions produced in the dissociation channel could be reproduced in TDSE calculations carried out by [2]. The change of the channel-selected electron momentum distributions with changing

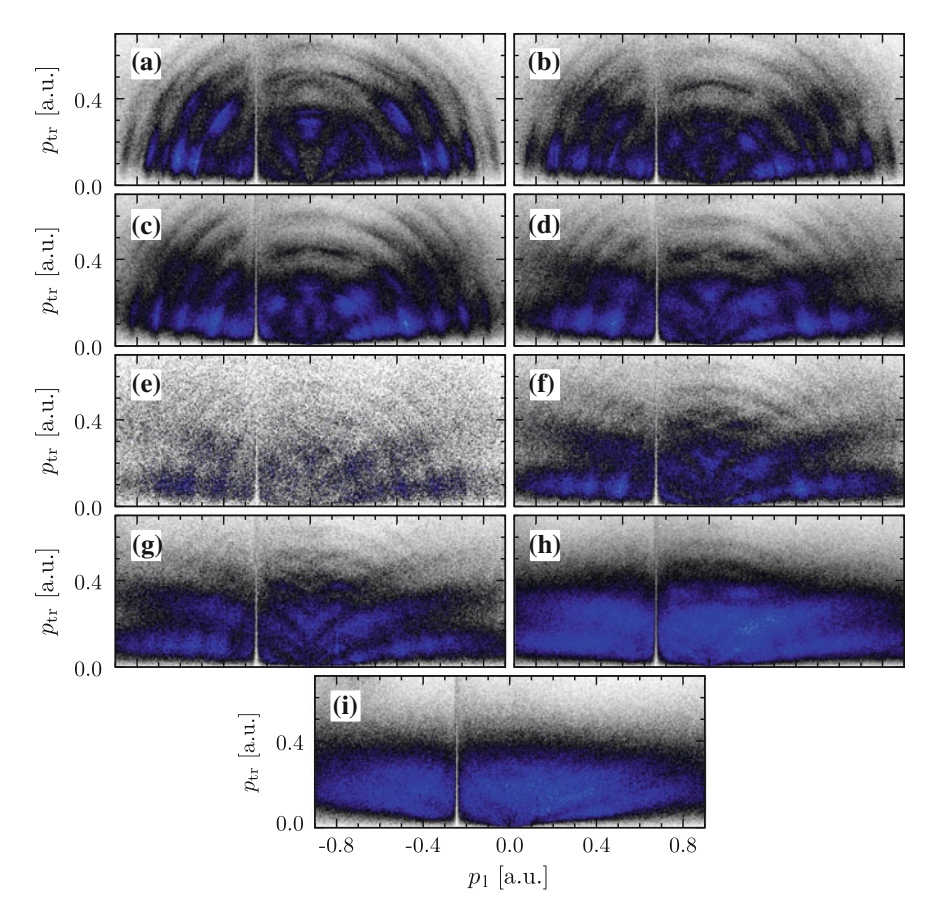


Fig. 7.11 Electron momentum distributions associated with CE of the molecule at different wavelengths: **a** 470 nm, **b** 498 nm, **c** 530 nm, **d** 570 nm, **e** 600 nm, **f** 630 nm, **g** 660 nm, **h** 790 nm, **i** 1300 nm. The linear color scale used is displayed in Fig. A.1d

wavelengths was discussed. Moreover, the distributions arising in different channels were compared to each other. With increasing wavelengths, more and more similar distributions could be obtained.

References

C. Cornaggia, Small polyatomic molecules in intense laser fields (Chap. 3), in *Molecules and Clusters in Intense Laser Fields*, ed. by J. Posthumus (Cambridge University Press, Cambridge, 2001), pp. 84–113

References 137

A. Fischer, Private communication (2014). Details about the methods used for the simulations
may be found in: A. Fischer, Dissociative photoionization of molecular hydrogen—a joint experimental and theoretical study of the electron-electron correlations induced by XUV photoionization and nuclear dynamics on IR-laser dressed transition states. Ph.D. thesis. Ruperto-Carola
University of Heidelberg, Germany. URN: urn:nbn:de:bsz:16-heidok-180165 (2015)

- A. Giusti-Suzor et al., Dynamics of H₂⁺ in intense laser fields. J. Phys. B: At. Mol. Opt. Phys. 28, 309–339 (1995). doi:10.1088/0953-4075/28/3/006
- J.H. Posthumus, The dynamics of small molecules in intense laser fields. Rep. Prog. Phys. 67, 623–665 (2004). doi:10.1088/0034-4885/67/5/R01
- M.R. Thompson et al., One and two-colour studies of the dissociative ionization and Coulomb explosion of H₂ with intense Ti:sapphire laser pulses. J. Phys. B: At. Mol. Opt. Phys. 30, 5755– 5771 (1997). doi:10.1088/0953-4075/30/24/014

Chapter 8 Conclusion and Outlook

Throughout this thesis, the interaction of strong laser fields with atoms and molecules has been investigated by utilizing a Ti:sapphire laser system and a reaction microscope (REMI). Before the laser pulses interacted with particles, different techniques allowed their manipulation. In detail, pulses of different wavelengths were created by making use of an optical parametric amplifier and nonlinear crystals for frequency mixing. Few-cycle pulses were produced by exploiting nonlinear effects in a neon-filled hollow-core fiber and subsequently the technique of chirped-mirror compression. The use of a piezo-driven Mach—Zehnder interferometer enabled time-resolved measurements. The ability of REMIs to detect all created ions and electrons in coincidence with very high resolution and a large acceptance is what makes these momentum spectrometers ideal tools for the investigation of ionization and dissociation processes.

The experimental investigations performed and the results obtained in the course of this thesis can be divided into three parts. In the first part, presented in Chap. 5, the fundamental strong-field tunneling process itself is the subject of investigation, exploiting a spin-orbit wave packet (SOWP) in the singly charged argon ion. In the second part, Chap. 6, the strong-field ionization of krypton and argon is investigated for different wavelengths. The subject of the third part, Chap. 7, is the extension of wavelength-dependent measurements to molecular hydrogen.

In the following, an individual, detailed summary for each of the parts is given together with future perspectives.

Tunnel Ionization from a Coherent Superposition in Ar⁺

Two identical few-cycle laser pulses were utilized in a pump-probe scheme to launch and probe a SOWP in singly charged argon ions. By removing an electron from a neutral argon atom, a coherent superposition of electronic states was created within the pump pulse. The second pulse was used to probe the system subsequently to Ar⁺⁺ by tunnel ionization.

Although the influence of the ions' long-range Coulomb field has striking implications on the transverse momentum distributions, perpendicular to the laser polarization, the dynamics of the SOWP was proven to be reflected in these distributions, as predicted in [21]. This has a close relationship to the observation made more than 15 years ago in highly-energetic ion-atom collisions, where—despite the Coulomb interaction—the underlying atomic structure was likewise preserved [10, 17].

Since the Coulomb interaction is similarly influencing the freed electrons, its effect cancels out to a large extent if the change in the observed electron momentum distributions with the time-delay is examined rather than the distribution itself. Thus, state-selective information about the momentum distribution directly after the tunneling process was extracted and common theoretical models were tested.

In the case of the transverse momentum component, a prediction by the models is given by Eq. (5.6): The distribution is assumed to be described by a product of the absolute squared, projected bound-state wave function and a Gaussian "filter" [2]. In the measurements presented in this part, the product form of this expression was, to the best of our knowledge, explicitly tested for the first time. The bound-state wave function indeed is reflected in the momentum distribution obtained and the Gaussian shape of the filter is reasonable. A simple model, based on scaled hydrogenic wave functions and ADK ionization rates, qualitatively reproduced the results. The remaining deviation, namely the too narrow momentum distributions, were likewise observed in experiments using circularly polarized light [2, 7]. A comparison of the results to calculations based on the numerical solution of the time-dependent Schödinger equation (TDSE) can be found in [15].

Along the laser polarization, where the electron is directly influenced by the laser field, no state-dependence could be observed. This is in agreement with the common assumption of a vanishing momentum component right after tunneling [5], although could possibly arise from "bunching" effects in the laser field [14].

Beside being interesting with respect to the understanding of the very fundamental process of strong-field tunneling, the results of this part are similarly important for state-of-the-art streaking techniques such as the attoclock [9]. The interpretation of data obtained with these techniques relies on a precise knowledge about the electron momenta right after the tunneling process. For this reason, providing information about the latter resembles an important step towards higher precision and towards answering fundamental questions such as whether a tunneling time exists or not [8].

The results described in this part of the thesis have been published in [11].

Population of Doubly Excited States in Strong Laser Pulses

In the experiments presented in Chap. 6, ionization of krypton and argon was initiated with strong laser pulses of different central wavelengths, ranging from 395 to 1600 nm. The fundamental change in the interaction between the laser field and the atoms, namely the transition from the multiphoton regime for short wavelengths to the tunneling regime at long wavelengths, was directly observed in the photoelectron momentum distributions.

In the multiphoton picture, Rydberg states in the noble gas atoms may be excited resonantly by absorption of an appropriate number of photons. In contrast, in the

tunneling regime, a different mechanism, known as *frustrated tunneling ionization* (FTI) [18], was recently identified and the process thus embedded into the successful three-step model [5]: After tunneling, the electron is driven by the laser field and recollides with its parent ion. For some of the electrons, ionized close to a field maximum, the kinetic energy is very low such that the electron may be recaptured into a Rydberg state, forming a neutral Rydberg atom.

Due to the excellent resolution and the high level of statistics obtained in this work, unique fingerprints of autoionizing *doubly excited states* (DES) could be identified in the electron momentum distributions up to a wavelength of 1300 nm, associated with the tunneling regime and thus the FTI process rather than resonant multiphoton excitation. In these states, not only the Rydberg electron is excited but also the electronic core close to the nucleus. To the best of our knowledge, this is the first report of the creation of DES within the FTI process. Furthermore, by utilizing a pump-probe scheme, the possibility of manipulating the states with a fairly weak second laser pulse was demonstrated.

However, the question remains whether the excitation of the electronic core takes place in the tunneling step or later, in the moment of recollision. Particularly interesting is the second scenario. The excitation of the electronic core by resonant recapturing of a slow electron is a process precisely investigated in a manifold of experiments and commonly known as *dielectronic recombination* (DR). Among others, storagering experiments and measurements in electron-beam ion traps have been performed, see e.g. [16, 19] and [1, 3], respectively. However, only higher charged or lighter ions have been investigated before. In this respect, the results presented in this thesis could be the first realization of a DR experiment for singly charged krypton and argon ions.

Future facilities might overcome the technical limitations inhibiting the measurement of DR in singly charged ions. The storage of Ar⁺, although not yet cooled, has been successfully demonstrated recently at the Cryogenic Storage Ring (CSR) [20], currently being built at the Max Planck Institute for Nuclear Physics in Heidelberg [4]. Once efficient cooling of the stored ions is achieved, experiments on DR in Ar⁺ may be possible with very high precision [13].

Channel-Selective Electron Spectra for H₂ at Different Wavelengths

In Chap. 7, the systematic investigation of momentum distributions created in the interaction with strong fields of different wavelengths was extended to molecules. Molecular hydrogen was chosen as a target because advanced calculations including the numerical solution of the TDSE are possible for this system. The molecule provides—in addition to pure ionization—more complex reaction channels, namely dissociation and Coulomb explosion. Exploiting ion—ion coincidence mapping, see e.g. [6], the different peaks appearing in the time-of-flight spectra of the ions could be identified and associated with the different mechanisms.

Concerning the dissociation channel, the momentum distributions of the emerging ions were investigated and compared with calculations based on the solution of the TDSE [12]. Excellent agreement could be obtained for reasonable laser parameters

although the initial ionization to H_2^+ was not included in the simulation and focal-volume averaging effects were not considered.

The ability of the reaction microscope to perform multi-coincidence measurements, including simultaneous detection of ions and electrons, allowed the extraction of channel-selected electron momentum distributions that were compared to each other. For short wavelengths, clear deviations between the distributions produced in different channels were observed, decreasing with increasing wavelength. At 1300 nm, almost identical distributions could be obtained. Since only a few particles have to be considered, calculations based on the TDSE are possible for the system and may be used for further investigation of the dissociation dynamics and to gain a deeper insight into the underlying mechanisms at different wavelengths.

References

- R. Ali et al., Dielectronic recombination on heliumlike argon. Phys. Rev. Lett. 64, 633–636 (1990). doi:10.1103/PhysRevLett.64.633
- L. Arissian et al., Direct test of laser tunneling with electron momentum imaging. Phys. Rev. Lett. 105, 133002 (2010). doi:10.1103/PhysRevLett.105.133002
- C. Beilmann et al., Prominent higher-order contributions to electronic recombination. Phys. Rev. Lett. 107, 143201 (2011). doi:10.1103/PhysRevLett.107.143201
- CSR, Status of the Cryogenic Storage Ring CSR (2014). http://www.mpi-hd.mpg.de/blaum/ storage-rings/csr/index.en.html. Accessed 16 Sept 2014
- P.B. Corkum, Plasma perspective on strong-field multiphoton ionization. Phys. Rev. Lett. 71, 1994–1997 (1993). doi:10.1103/PhysRevLett.71.1994
- C. Cornaggia, Small polyatomic molecules in intense laser fields, in *Molecules and Clusters in Intense Laser Fields*, chap. 3 ed. by J. Posthumus (Cambridge University Press, Cambridge, 2001), pp. 84–113
- I. Dreissigacker, M. Lein, Quantitative theory for the lateral momentum distribution after strong-field ionization. Chem. Phys. 414, 69–72 (2013). doi:10.1016/j.chemphys.2012.01.028
- 8. P. Eckle et al., Attosecond ionization and tunneling delay time measurements in helium. Science 322, 1525–1529 (2008). doi:10.1126/science.1163439
- P. Eckle et al., Attosecond angular streaking. Nat. Phys. 4, 565–570 (2008). doi:10.1038/ nphys982
- P. D. Fainstein et al., Target dependence of slow electrons emitted in swift ion-atom collisions. Phys. Rev. A: At. Mol. Opt. Phys. 63, 062720 (2001). doi:10.1103/PhysRevA.63.062720
- 11. L. Fechner et al., Strong-field tunneling from a coherent superposition of electronic states. Phys. Rev. Lett. 112, 213001 (2014). doi:10.1103/PhysRevLett.112.213001
- 12. A. Fischer, Private communication (2014). Details about the methods used for the simulations may be found in: A. Fischer, Dissociative photoionization of molecular hydrogen—a joint experimental and theoretical study of the electron-electron correlations induced by XUV photoionization and nuclear dynamics on IR-laser dressed transition states. Ph.D. thesis. Ruperto-Carola University of Heidelberg, Germany. URN: urn:nbn:de:bsz:16-heidok-180165 (2015)
- 13. M. Grieser, Private communication (2014)
- A. Kästner et al., Energy bunching in soft recollisions revealed with long-wavelength fewcycle pulses. J. Phys. B: At. Mol. Opt. Phys. 45, 074011 (2012). doi:10.1088/0953-4075/45/ 7/074011
- A.S. Kheifets, I.A. Ivanov, Transverse-electron-momentum distribution in pump-probe sequential double ionization. Phys. Rev. A: At. Mol. Opt. Phys. 90, 033404 (2014). doi:10.1103/PhysRevA.90.033404

References 143

 G. Kilgus et al., Dielectronic recombination of hydrogenlike oxygen in a heavy-ion storage ring. Phys. Rev. Lett. 64, 737–740 (1990). doi:10.1103/PhysRevLett.64.737

- 17. R. Moshammer et al., Initial state dependence of low-energy electron emission in fast ion atom collisions. Phys. Rev. Lett. 83, 4721–4724 (1999). doi:10.1103/PhysRevLett.83.4721
- T. Nubbemeyer et al., Strong-field tunneling without ionization. Phys. Rev. Lett. 101, 233001 (2008). doi:10.1103/PhysRevLett.101.233001
- S. Schippers. Astrophysical relevance of storage-ring electron-ion recombination experiments.
 J. Phys.: Conf. Ser. 163 (2009), 012001. doi:10.1088/1742-6596/163/1/012001
- R. von Hahn et al., The electrostatic cryogenic storage ring CSR mechanical concept and realization. Nucl. Instrum. Methods Phys. Res. Sect. B: Beam Interact. Mater. At. 269, 2871– 2874 (2011). doi:10.1016/j.nimb.2011.04.033
- H. J. Wörner, P. B. Corkum, Imaging and controlling multielectron dynamics by laser-induced tunnel ionization. J. Phys. B: At. Mol. Opt. Phys. 44, 041001 (2011). doi:10.1088/0953-4075/ 44/4/041001

A.1 Atomic Units and Physical Constants

In atomic physics it is often useful and convenient to relate quantities to the respective values in the hydrogen atom. This defines the system of *atomic units*, see e.g. [1, Sect. 1.2], which is used in this work unless otherwise stated. Table A.1 summarizes the basic quantities and relations to other unit systems.

A.2 Particle Data

See Table A.2.

A.3 Color Scales

See Fig. A.1.

A.4 Supplementary Graphs

See Figs. A.2, A.3, A.4 and A.5.

Quantity	Definition	1 a.u. corresponds to
Length	Bohr radius a ₀	$0.52917721092 \times 10^{-10} \mathrm{m}$
Mass	Electron mass m_e	$9.10938291 \times 10^{-31} \text{ kg}$ $1822.88848^{-1} \text{ u}$
Charge	Elementary charge e	$1.602176565 \times 10^{-19} \mathrm{C}$
Energy	Hartree energy E_h	$4.3597443 \times 10^{-18} \mathrm{J}$ 27.21138505 eV
Angular momentum	\hbar	$1.054571726 \times 10^{-34} \text{ Js}$ $6.58211928 \times 10^{-16} \text{ eV s}$
Time	$t = \hbar/E_h$	$2.41888433 \times 10^{-17} \mathrm{s}$
Momentum	$m_e a_0/_t$	$1.99285174 \times 10^{-24} \mathrm{kg}\mathrm{m/s}$
Electric field	$E_h/_{ea_0}$	$0.514220642 \times 10^{12} \text{ V/m}$
Intensity	$E_h^2/\hbar a_0^2$	$6.4364091 \times 10^{15} \mathrm{W/cm^2}$
Laser intensity ^a	$\varepsilon_0 c E^2/2$	$3.5094451 \times 10^{16} \mathrm{W/cm^2}$

Table A.1 Definition of the system of atomic units and relationship to other systems

All values are taken or derived from [6]

 Table A.2
 Masses and ionization potentials important for this work

	Ne	Ar	Kr	Xe	H ₂
E _i (eV)	21.564540	15.7596112	13.9996049	12.1298431	15.42593
mass (u)	20.1797	39.948	83.798	131.293	2.01588
	Ne ⁺	Ar ⁺	Kr ⁺	Xe ⁺	
E _i (eV)	40.96296	27.62967	24.3598	20.975	
$\Delta\omega$ (eV)	0.09676024	0.17749368	0.665808	1.306423	
	Electron	Н			
Mass	1 a.u.	1.00782503207 u			

The atomic ionization potentials E_i and spin-orbit splittings $\Delta \omega$ are taken from [4], the standard atomic weights for the atoms from [2], the electron mass from [6] and the H₂ data from [5]

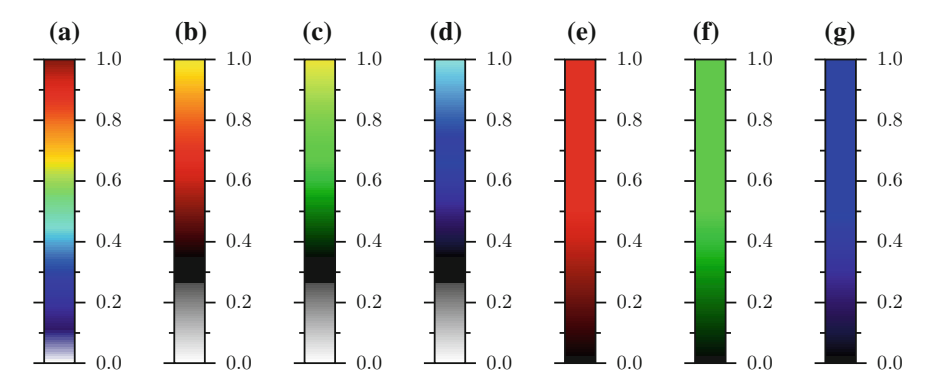


Fig. A.1 Color scales used for visualization of experimental and theoretical data

^aCommon convention in strong-field physics, see e.g. [7]

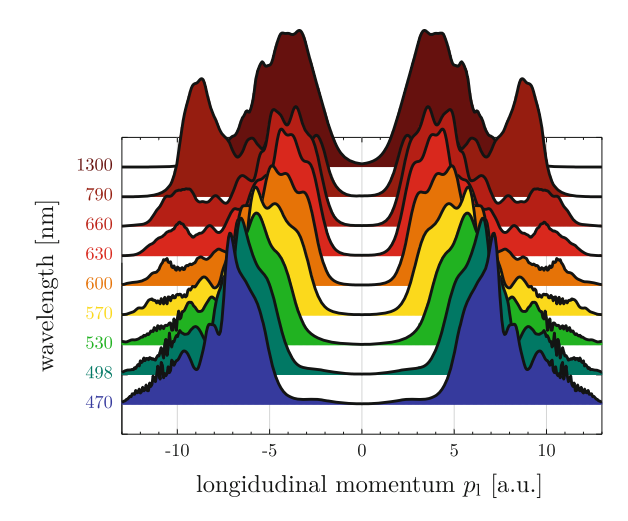


Fig. A.2 Simulated momentum distributions of dissociating H⁺ [3] at an intensity of about 8.8×10^{13} W/cm² and pulse duration of 30 fs. The scale is linear

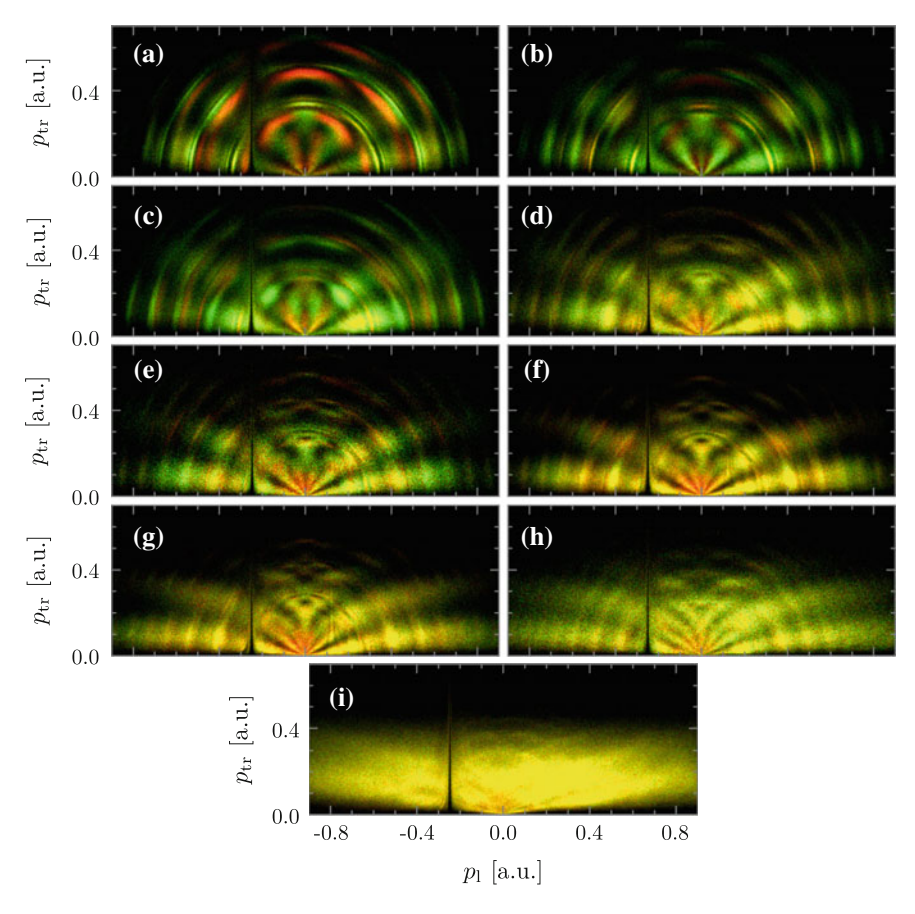


Fig. A.3 Combined electron momentum distributions obtained for the ionization channel (*red*) and the dissociation channel (*green*). **a** 470 nm, **b** 498 nm, **c** 530 nm, **d** 570 nm, **e** 600 nm, **f** 630 nm, **g** 660 nm, **h** 790 nm, **i** 1300 nm

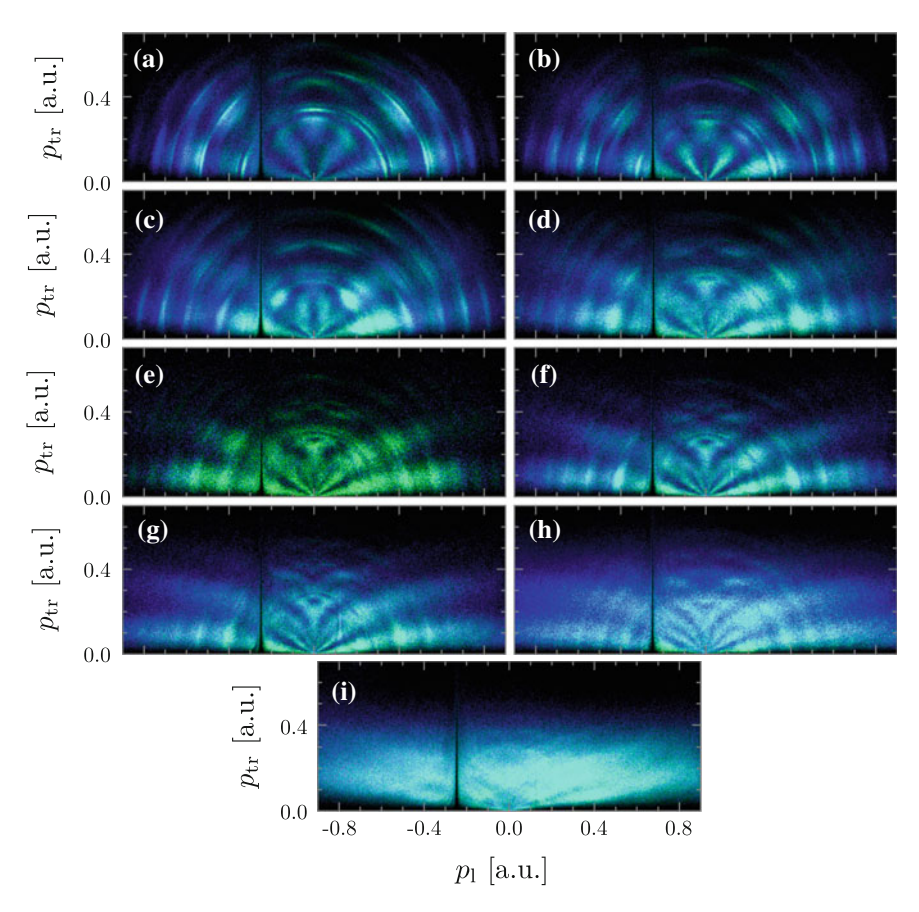


Fig. A.4 Combined electron momentum distributions obtained for the dissociation channel (*green*) and the Coulomb explosion channel (*blue*). **a** 470 nm, **b** 498 nm, **c** 530 nm, **d** 570 nm, **e** 600 nm, **f** 630 nm, **g** 660 nm, **h** 790 nm, **i** 1300 nm

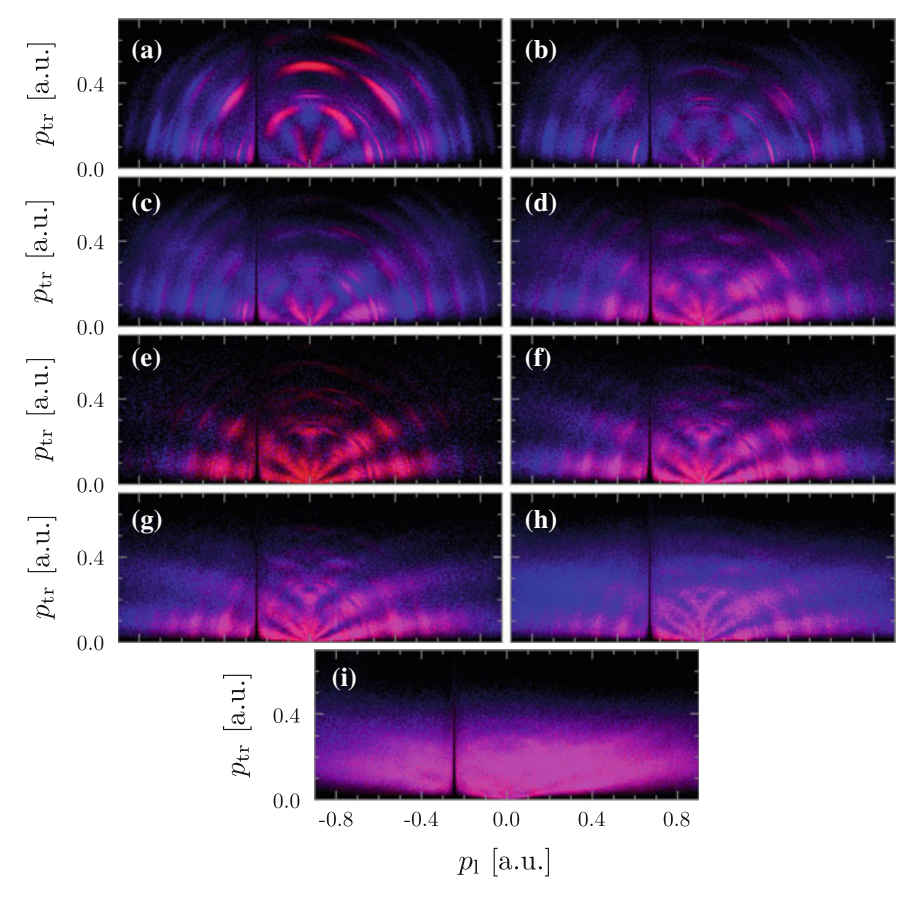


Fig. A.5 Combined electron momentum distributions obtained for the ionization channel (*red*) and the Coulomb explosion channel (*blue*). **a** 470 nm, **b** 498 nm, **c** 530 nm, **d** 570 nm, **e** 600 nm, **f** 630 nm, **g** 660 nm, **h** 790 nm, **i** 1300 nm

References

- W.E. Baylis, G.W.F. Drake, Units and constants (Chap. 1), in *Springer Handbook of Atomic, Molecular, and Optical Physics [online]*, ed. by G.W.F. Drake (Springer Science+Buisiness Media Inc., New York, 2006), pp. 1–6. doi:10.1007/978-0-387-26308-3
- J.S. Coursey et al., Atomic Weights and Isotopic Compositions (version 3.0) [Online] National Institute of Standards and Technology, Gaithersburg, MD (2010). http://physics.nist.gov/Comp, Accessed 9 Sep 2014
- 3. A. Fischer, Private communication (2014). Details about the methods used for the simulations may be found in: A. Fischer, Dissociative photoionization of molecular hydrogen—a joint experimental and theoretical study of the electron-electron correlations induced by XUV photoionization and nuclear dynamics on IR-laser dressed transition states. Ph.D. thesis. Ruperto-Carola University of Heidelberg, Germany. URN: urn:nbn:de:bsz:16-heidok-180165 (2015)

 A. Kramida et al., NIST Atomic Spectra Database (ver. 5.1) [Online]. National Institute of Standards and Technology, Gaithersburg, MD (2013). http://physics.nist.gov/asd, Accessed 5 Aug 2014

- P.J. Linstrom, W.G. Mallard (eds.) NIST Chemistry WebBook, NIST Standard Reference Database Number 69. National Institute of Standards and Technology, Gaithersburg MD, 20899 (2014). http://webbook.nist.gov, Accessed 12 Sep 2014
- P.J. Mohr et al., The 2010 CODATA Recommended Values of the Fundamental Physical Constants (Web Version 6.0). This database was developed by J. Baker, M. Douma, and S. Kotochigova. National Institute of Standards and Technology, Gaithersburg, MD 20899 (2011). http://physics.nist.gov/constants, Accessed 7 Sep 2014
- M. Protopapas et al., Atomic physics with super-high intensity lasers. Rep. Progress Phys. 60, 389–486 (1997). doi:10.1088/0034-4885/60/4/001